

# Magnetic Guidance for Linear Drives

Vom Fachbereich Elektrotechnik und Informationstechnik  
der Technischen Universität Darmstadt  
zur Erlangung des akademischen Grades eines  
Doktor-Ingenieurs (Dr.-Ing.)  
genehmigte Dissertation

von

**Phong C. Khong, M.Sc.**

Geboren am 10. April 1978 in Hanoi, Vietnam

Referent: Prof. Dr.-Ing. Peter Mutschler

Korreferent: Prof. Dr.-Ing. Mario Pacas

Tag der Einreichung: 11. 04. 2011

Tag der mündlichen Prüfung: 29. 08. 2011



## Erklärung laut §9 PromO

Ich versichere hiermit, dass ich die vorliegende Dissertation allein und nur unter Verwendung der angegebenen Literatur verfasst habe. Die Arbeit hat bisher noch nicht zu Prüfungszwecken gedient.

Darmstadt, den 08. April 2011.

---

Phong C. Khong





## Preface

This dissertation is the results of my 4-years study and research in the Department of Power Electronics and Control of Drives - Darmstadt University of Technology. Besides the personal works, the results are achieved by the contributed help directly or indirectly from many people to the dissertation. Therefore, I would like to give here my thanks to them.

Firstly, I would like to give my thanks to Prof. Dr.-Ing. Peter Mutschler, the supervisor and director of the Department. I would thank for his greatest support throughout my thesis with his supervision, inspiration and wonderful working plan during the 4-years. I would thank for his support in formalities and finance for my study in Germany.

To Prof. Dr.-Ing. Mario Pacas, I thank for his interest and for acting as the co-advisor.

I thank the DFG Deutsche Forschungsgemeinschaft for financially supporting my projects MU 1109.

I thank the 322 project of the Vietnamese Ministry of Education and Training (MOET) and Deutscher Akademischer Austausch Dienst (DAAD) for the financially supporting my basic living cost, formalities and the language course at the beginning.

I would like to thank all my colleagues in the institute for their supports and comments, a good working atmosphere, and many useful discussions. Especially, I would like to thank to Dr.-Ing Roberto Leidhold for his support since the beginning of my works in the Department.

Many non-scientific issues are important for an experimental project. I appreciate the work and advice of the institute's technical staff, and administrative staff.

I am very grateful to my parents and my wife for their support, encouragement and especially take care of my daughter during my study.

After all the help, I had been given, it was really wonderful in my preface to be able to express my thanks one more time, especially to my great supervisor who had shared his immense knowledge and precious time with me, and to my long-suffering family who had supported me through all the stress every step of the way!

Darmstadt, 08 April 2011.



## Abstract

Linear drives provide many new attractive solutions for the material transportation and processing in the manufacturing industry. With no mechanical transmission elements, they enable high dynamics and rigidity as well as low installation- and low maintenance-costs. That performance can give the linear motor system a better precision, a higher acceleration and a higher speed of the moving part. Therefore, the material transportation and processing using linear motors is studied and applied increasingly in manufacturing industry.

For these applications, the linear motor is typically with stationary long primary and a short moving secondary. As the secondary part is passive, no energy transmission is required between the moving and stationary part, avoiding the use of brushes or inductive transmission. The motor type best suited for the mentioned applications is the synchronous one with permanent magnets, because of its higher efficiency, compactness, but most important because it allows a higher air-gap.

In the usual approach, the linear motor is only used for thrust force production. The guidance is usually implemented by a mechanical assembly. The guidance constrains the movement to the longitudinal displacement, fixing the lateral and vertical displacement: yaw, roll and pitch. To achieve the necessary precision of the movement, accurate mechanical guidance is required. Such the mechanical assembly can be complex and source of high friction.

In this dissertation, a research of an active guiding system is presented. The purpose of this research is finding out a solution for the material transportation and processing applications. The target is a linear drive system, which can reduce the complicated mechanical structure. In additions, the passive vehicle is also necessary.

The result of the research is PM-synchronous linear motors with long and double-sided primaries. In the system, the lateral displacement and the yaw angle are controlled while a simple wheel-rail system fixes the vertical displacement. This combination of the magnetic and mechanical guidance offers a good trade-off among the complexity of the control, actuators and mechanics, when considering industrial applications. To allow multiple vehicles traveling simultaneously and independently on the guide-way (each vehicle is controlled by an individual part of the guide-way), the double side primary is separated into segments. With that structure, flexible-operating methods can be implemented. That is very useful in process-integrated material handling where different speeds of material carriers in each processing

station are necessary. Another advantage of segmented structure is the energy saving. The power is supplied only to the segment or the two consecutive segments in which the vehicle runs over. In one segment, each side of the primary is supplied by its own inverter, allowing the necessary degree of freedom to control the lateral position and the yaw angle in addition to the thrust control.

In order to make the vehicle completely passive, a capacitive sensor is proposed and implemented to measure the lateral position and the yaw angle. The sensor has active parts installed on the guide-way and passive parts on the vehicle.

The mathematical analysis and the finite element method (FEM) are used to analysis the proposed system. With the analysed results, the control for the system is investigated in detail. Hardware and software for the experimental system is developed and implemented.

The analysed results and the experimental results validate the proposed system. That gives a new solution for the material transportation and processing application using linear synchronous motors.

## Kurzfassung

Zum Transport und zur Bearbeitung von Gegenständen in der Verarbeitungsindustrie bieten die Linear- Direktantriebe zunehmend interessante Lösungen. Unter Wegfall mechanischer Übertragungselemente ermöglichen sie hohe Dynamik und Steifigkeit sowie Verschleiß- und Wartungsarmut. Diese Eigenschaften ermöglichen den Linearmotor-Systemen eine höhere Genauigkeit, höhere Beschleunigung und eine höhere Geschwindigkeit der beweglichen Teile. Daher wird der Transport und die Bearbeitung mit Linearmotoren in der Verarbeitungsindustrie zunehmend erforscht und eingesetzt.

Für diese Anwendungen werden normalerweise Linearmotoren mit langem stationären Primärteil und kurzem bewegenden Sekundärteil eingesetzt. Da der Sekundärteil passiv ist, wird keine Energieübertragung zwischen den beweglichen und stationären Teilen benötigt, und somit werden Bürsten oder induktive Übertragungssysteme vermieden. Der permanenterregte Synchronmotor ist der am besten passende Motortyp für die genannten Anwendungen, aufgrund seines höheren Wirkungsgrades und Leistungsdichte, aber vor allem weil er einen höheren Luftspalt ermöglicht.

Üblicherweise wird der Linearmotor nur für Erzeugung der Schubkraft eingesetzt. Die Spurführung ist in der Regel durch eine mechanische Konstruktion realisiert. Die Spurführung beschränkt die Bewegung auf die Längsachse. Bewegung auf der Transversal- und Vertikalachse (Gieren, Rollen und Nicken) ist durch die Spurführung nicht möglich. Um die notwendige Präzision der Bewegung zu erreichen, werden hochgenaue mechanische Führungen eingesetzt. Solche mechanische Führungen sind aufwendig und verursachen höhere Reibung.

Die Forschung eines aktiven Spurführungssystems wird in dieser Dissertation behandelt. Die Absicht dieser Forschung ist, Lösungen für Anwendungen des Materialtransports und Bearbeitung herauszufinden. Das Ziel ist ein Linearantrieb, der aufwendige mechanischer Strukturen vermeidet und dessen Fahrzeug passiv ist.

Das Ergebnis der Studie ist ein PM-Synchron-Linearmotor mit langen und doppelseitigen Primärteilen. Die seitliche Bewegung und der Gierwinkel werden geregelt, während die vertikale Bewegung von einem einfachen Rad-Schiene-System fixiert wird. Diese Kombination von magnetischer und mechanischer Führung bietet einen guten Kompromiss zwischen der Komplexität der Regelung, des Aktuators und

der Mechanik in dem Fall der industriellen Anwendungen. Um mehrere Fahrzeuge gleichzeitig und unabhängig auf dem Fahrweg führen zu können (jedes Fahrzeug wird durch einen individuellen Teil der Führung kontrolliert), ist der doppelseitige Primärteil in Segmente getrennt. Mit dieser Struktur können flexible Betriebsverfahren umgesetzt werden. Das ist sehr nützlich im integrierten Material-Handling, wo unterschiedliche Geschwindigkeiten des Materialträgers in jeder Bearbeitungsstation notwendig sind. Ein weiterer Vorteil der segmentierten Struktur ist die Energieeinsparung. Nur das Segment oder die zwei aufeinander folgenden Segmente die das Fahrzeug überfährt, werden gespeist. In einem Segment wird jede Seite des Primärteils von einem eigenen Wechselrichter versorgt, so dass der erforderliche Freiheitsgrad besteht, um die laterale Position, Gierwinkel und Schubkraft zu steuern.

Um das Fahrzeug vollständig passiv zu machen wird ein kapazitiver Sensor zur Messung der lateralen Position und des Gierwinkels vorgeschlagen und umgesetzt. Der aktive Teil des Sensors wird am Führungsweg und der passive Teil am Fahrzeug installiert.

Die mathematische Analyse und die Finite-Elemente-Methode (FEM) wurden verwendet um das vorgeschlagene System zu analysieren. Mit den analytischen Ergebnissen wurde die Regelung für das System im Detail untersucht. Hardware und Software für das experimentelle System wurde entwickelt und umgesetzt.

Die analytischen und experimentellen Ergebnisse bestätigen das vorgeschlagene System. Das gibt neue Lösungen für die Anwendungen in Materialtransport und Verarbeitung bei Nutzung von Linear-Synchronmotoren.

# Table of Contents

Erklärung laut §9 PromO.....	I
Preface .....	III
Abstract.....	V
Kurzfassung .....	VII
Table of Contents.....	IX
List of Symbols.....	XIII
Abbreviation .....	XVII
1. INTRODUCTION.....	1
1.1. Linear motor concept and applications .....	1
1.2. Linear drives for industrial material handling and processing.....	3
1.3. Aim of the study .....	5
1.4. Organization of the dissertation .....	6
2. PROPOSED SYSTEM.....	7
2.1. Topology of linear motors applied in industrial material handling and processing.....	7
2.2. State of the art .....	9
2.2.1. Research from other institutes.....	10
2.2.2. Research in our department.....	14
2.3. Proposed system.....	15
2.3.1. Target of research.....	15
2.3.2. Proposed structure .....	15
2.4. Program of the work.....	16
2.4.1. Control duty.....	16
2.4.2. Lateral position sensor and yaw angle sensor. ....	17
2.4.3. Work steps.....	18
3. EXPERIMENTAL SETUP .....	19
3.1. Mechanical structure .....	19
3.1.1. The motors.....	19
3.1.2. Construction .....	21
3.2. Electrical structure.....	23
3.2.1. Power supply .....	23
3.2.2. Inverter modules.....	24
3.2.3. Inverter interface .....	24
3.2.4. Sensor system.....	26
3.2.5. Controller .....	27
3.3. Software .....	29
3.3.1. Operating System .....	29
3.3.2. Real time control software .....	30
4. MATHEMATICAL MODEL .....	32
4.1. The magnetic guidance LSM model .....	32
4.1.1. The experimental system in the horizontal plane.....	32
4.1.2. Forces and torque on the vehicle.....	33
4.2. Forces and torque calculation.....	34

## Table of Contents

---

4.2.1.	Current density and flux distribution.....	35
4.2.2.	Magneto motive force and flux in the air-gap .....	39
4.2.3.	Magnetic energy and force calculation.....	42
4.2.4.	Linearization of the force and torque equations .....	44
4.3.	Equations of motion.....	46
4.4.	FEM simulation .....	47
4.4.1.	Finite element method .....	47
4.4.2.	FEM model of the experimental setup.....	48
4.4.3.	FEM results.....	49
4.5.	Practical measurement .....	53
5.	CONTROLLER DESIGN .....	57
5.1.	Control block diagram .....	57
5.1.1.	Proposed control method .....	57
5.1.2.	Block diagrams of the control system .....	59
5.2.	Controller design .....	65
5.2.1.	Current control loops .....	65
5.2.2.	Speed control loops.....	67
5.2.3.	Position control loops .....	68
5.3.	Control system simulation .....	69
5.3.1.	Simulation model.....	69
5.3.2.	Simulation results .....	71
6.	MAGNETIC GUIDANCE EXPERIMENTS.....	79
6.1.	Implementation of control method .....	79
6.2.	Lateral position control.....	81
6.3.	Yaw angle control.....	83
6.4.	Three DOFs control .....	86
6.5.	Perturbation in longitudinal traveling.....	89
7.	CAPACITIVE SENSOR .....	94
7.1.	Capacitive sensor structure .....	94
7.1.1.	Mechanical structure.....	94
7.1.2.	Electric circuit.....	96
7.2.	Mathematic model .....	98
7.2.1.	Ideal case analysis.....	98
7.2.2.	Calculation of the optimal value of $d$ . .....	101
7.3.	FEM simulation .....	104
7.3.1.	Parasitic capacitances .....	104
7.3.2.	Capacitive sensor performances .....	106
7.4.	Experimental setup and results .....	108
7.4.1.	Experimental setup .....	108
7.4.2.	Capacitive sensor calibration.....	109
7.4.3.	Control with capacitive sensor.....	110
7.4.4.	Quality of control with capacitive sensor. ....	111
8.	CONCLUSIONS .....	114
8.1.	Summary.....	114
8.2.	Future work.....	115
	Bibliography.....	117
	APPENDIX A .....	123



---

A1. Inverter interface board - IIB .....	123
A1.1 IIB structure.....	123
A1.2 Modulation in IIB.....	125
A2. Vehicle control interface - VCI .....	126
A3. The experimental communication bus .....	127
APPENDIX B .....	129
B1. The d-q projection.....	129
B2. Transformation of three phase currents .....	132
B3 Anti-windup current control.....	133
B4 Basics of designing controller for drives .....	135
B4.1 Amplitude optimum .....	136
a. Apply for current control loop with PI controller.....	137
b. Apply for position control loop with P controller .....	138
B4.2 Symmetrical optimum.....	138
APPENDIX C.....	141
C1. Review of electromagnetic field theory .....	141
C2. Permanent Magnet in PMLSM .....	142
Curriculum Vitae .....	145



# List of Symbols

SYMBOLS	MEANING
$a, a^2$	Complex unit vectors of the $b$ -axis and $c$ -axis unit vector in $abc$ frame
$b_s$	Slot width of linear motor primary.
$C_{FNx}$	Normal force constant values ( $x=1..5$ )
$C_{FTx}$	Thrust force constant values ( $x=1..2$ )
$C_M$	Leakage capacitance
$C_{xx}$	Capacitances of the capacitive bridge ( $xx = 11;12;21;...;42$ )
$d$	Coupling electrode horizontal gap
$d_L$	Distance between the permanent magnets and the armature
$d_{LL}, d_{LR}$	$d_L$ of the left- and right-side of the vehicle
$d_M$	Thickness of the permanent magnets
$E$	Electric field, Electric field intensity
$F$	Mechanical force
$F_\delta$	Force on the vehicle in $y$ -direction
$F_{\delta p}$	Perturbation force in $y$ -direction
$F_{Na}, F_{NPM}$	Normal force caused by the armature currents and the permanent magnet
$F_{NL}, F_{NR}$	The left- and right- normal force on the vehicle
$F_{TL}, F_{TR}$	The left- and right-side thrust on the vehicle
$F_{Tmax}$	Maximum thrust of the linear motor
$F_{Tn}$	Nominal thrust of the linear motor
$F_w(s)$	Transfer function of a closed loop
$F_x$	Electromagnetic thrust force along $x$ -axis,
$g$	Gap between primary and secondary back iron; Electrode stripes gap
$g_e$	Gap between sending- and receiving-electrode of the capacitive sensor
$\bar{g}$	Notation of space vector
$H$	Height of the coupling electrode
$h$	Height of electrode stripes
$H_B$	Height of the system basement

## List of Symbols

---

$h_e$	Height of the sending and receiving electrode
$H_V$	Height of the vehicle
$h_z$	Height of permanent magnets
$i_a$	Amplitude of the armature current
$i_d, i_q$	Current components in $dq$ -projection
$i_\delta$	Current for actuating $F_\delta$
$i_\gamma$	Current for actuating $T_\gamma$
$I_{\max}$	Max RMS current for 10s of the linear motor primary
$I_N$	Rate current (RMS) of the linear motor primary
$\vec{i}_1^s$	Primary current vector in static frame
$\vec{i}_1^m$	Primary current vector in moving frame
$i_x$	Current for actuating $F_x$
$K_c$	Converter gain
$K_e$	Electrical gain
$K_{\gamma p}$	Constant value of the perturbation torque on the vehicle
$K_p$	Gain constant of a controller
$k_{\omega v}$	Winding factor at harmonic frequency $\nu$
$K_x$	Forces constant values ( $x=1..4$ )
$K_{xp}$	Constant value of the perturbation force in $x$ -direction
$l$	Length of the capacitive sensor stripes
L1, L2, L3, N	Three phases four wires voltage system
$L_{am}$	Armature inductance
$L_B$	Length of the system basement
$L_V$	Length of the vehicle
$M$	Mechanical torque
$m$	Vehicle weight
$m_V$	Weight of the vehicle
$N_1$	Number of series winding turns per one primary slot
$p_a$	Number of primary poles

---

$P_i$	The internal power of the air-gap without stator losses
$p_m$	Number of secondary poles
$s$	Coupling electrode length
$T_D$	Converter delay
$T_\gamma$	Torque on the vehicle
$T_i$	Integral time value of a PI controller
$T_s$	Sampling time
$u$	Relative velocity between the magnet and the armature
$u_0$	Excitation voltage of the capacitive sensor
$u_1, u_2$	Output voltages of the capacitive sensor
$u_\delta, u_\gamma$	$\delta, \gamma$ output voltages from the capacitive sensor
$U_N$	Nominal voltage of the linear motor primary
$v_d, v_q$	Phase voltages presented in $dq$ -projection
$\vec{v}_1^s$	is the primary voltage vector in static frame
$W_B$	Width of the system basement
$W_{mag}$	Magnetic energy in the air-gap
$W_V$	Width of the vehicle
$x$	Longitudinal position of the vehicle (in $x$ axis)
$x_0$	Displacement between origins of the static- and moving-frame
$x_m$	Position presented in moving frame
$x_s$	Position presented in static frame
$y_0$	Air-gap of the vehicle when the vehicle in the middle of the guide-way
$\mathcal{A}_a$	Fundamental component of the armature current density
$\mathcal{A}_{PM}$	The equivalent current distribution of permanent magnet
$\mathcal{B}$	Magnetic field, Magnetic flux density
$\mathcal{B}_L$	Magnetic flux density of the air-gap
$\mathcal{B}_R$	Magnetic flux density of the permanent magnet
$\mathcal{B}_{RN}$	Remanent flux density of the permanent magnet
$\mathcal{D}$	Electric flux density
$\mathcal{F}$ or $\mathcal{M}$	Magneto motive force (MMF)
$\mathcal{F}_{PM}$	Fundamental component of the permanent magnet MMF

## List of Symbols

---

$\mathcal{H}$	Magnetic field intensity
$\mathcal{H}_c$	Coercive force
$\mathcal{J}$	Surface current density
$\mathcal{M}_{PM}$	Equivalent MMF of permanent magnet
$\Theta$	Inertial moment of vehicle
$\beta_m$	Angle between $dq$ -frame and $\alpha\beta$ -frame
$\delta$	Lateral position of the vehicle (in $y$ axis)
$\varepsilon$	Relative dielectric constant
$\varepsilon_0$	Dielectric constant of air
$\gamma$	Yaw angle of the vehicle
$\mu$	Permeability
$\mu_0$	Permeability of free space or vacuum permeability
$\mu_d$	Relative differential permeability
$\mu_M$	Permeability of the permanent magnet
$\mu_{Mr}$	Relative permeability of the permanent magnet
$\mu_r$	Relative permeability
$\phi$	Magnetic flux
$\phi_L$	Magnetic flux in the air-gap
$\phi_R$	Magnetic flux in the permanent magnet
$\theta_m$	Phase angle of the armature currents presented in moving frame
$\theta_s$	Phase angle of the armature currents presented in static frame
$\tau$	Pole pitch.
$\tau_p$	The magnet width.
$\tau_s$	Slot pitch of linear motor primary.
$\omega$	Angular frequency of the three phase voltage

# Abbreviation

ABBREVIATION	EXPLANATION
AD	Analog to Digital
ADC	Analog to Digital Converter
AMR	Anisotropic magneto-resistive
CNC	Computer Numerical Control
CPLD	Complex Programmable Logic Device
CSS	Capacitive sensor
DOF	Degree of Freedom
EMF	Electromotive Force
FEM	Finite Element Method
FOC	Field Oriented Control
FOCC	Field Oriented Control Converter
FPGA	Field-programmable Gate Array
IGBT	Insulated-gate Bipolar Transistor
IIB	Inverter Interface Board
ISR	Interrupt Subroutine Request
ISS	Inductive sensor
LIM	Linear Induction Motor
LSM	Linear Synchronous Motor
LUT	Look Up Table
MMF	Magneto Motive Force
PC	Personal Computer
PCI	Peripheral Component Interconnect
PDE	Partial Differential Equations
PI controller	Proportional–Integral controller
PM	Permanent Magnet
PM LSM	Permanent Magnet Linear Synchronous Motor
PWM	Pulse width modulation
RTAI	Real-Time Application Interface
SV-PWM	Space Vector Pulse Width Modulation
TF	Transfer function
VCI	Vehicle Control Interface





# 1. INTRODUCTION

## 1.1. Linear motor concept and applications

A linear motor can be defined as being the result of a cylindrical rotary electric machine, which has been mentally split along a radial plane, unrolled and flattened [1]. The result is an electrical machine in which the primary and the secondary are linear and parallel as shown in Figure 1.1. In contrast to a rotational electric motor, a linear motor generates a linear force (thrust force) along its length, i.e. there is no torque or rotation is produced by the relationship between electric currents and magnetic field. By supplying suitable currents to the primary with a suitable excitation in the secondary of a linear motor, they will move relatively in a linear path. This makes linear motors have a number of advantages over rotational motors in linear motion. Linear motors overcome most of the disadvantages of the most commonly used linear motion systems, which consist of rotational electric motors and ball screw systems. The advantages of linear motors are high speeds or acceleration rates, faster response, more stiffness, without backlash and cheaper maintenance free operation. Therefore, the linear motors are used in many application domains.

Invented in the early days of the electric motor, linear motor was firstly applied in public transportation area. The first linear motor applied in transportation was the “Axial Engine” developed by Charles Grafton Page (1812-1868) [2]-[4]. The later developments were inventions of Alfred Zehden (1905) [5], Hermann Kemper (1935) [6] and Eric Laithwaite (late 1940s). Nowadays, many transportation systems are using linear motors like the Maglev propulsion system, for instance, the Japanese Linimo magnetic levitation train or the German high-speed train Transrapid.

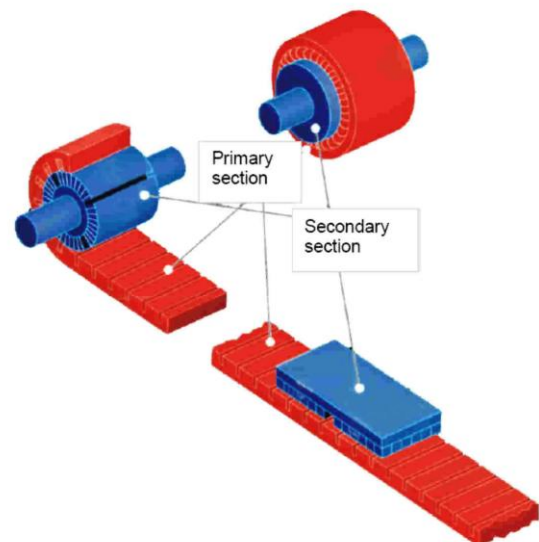


Figure 1.1 Imaginary process of splitting and unrolling a rotary machine to produce a linear motor [81]

Other transportation systems without magnetic levitation are Bombardier's Advanced Rapid Transit systems and number of modern Japanese subways. One more technology using linear motor is in the roller coasters [7].

Besides the public transportation applications, the linear motors are also applied in lifting mechanisms and many motion control applications. With small limitations of space and the required height, the vertical linear motors are suitable for skyscraper or deep mining elevators. Linear motors are also used in industrial or military lifting systems. In addition, they are offered to use on sliding doors of trams, buildings or elevators [8]-[12]. Dual axis linear motors also produced and applied to the applications that require X-Y motion, such as in precision laser cutting machines, automated drafting machines and others kind of CNC machine tools.

Many different types of linear motor exist due to a long period of developing time for different applications. If classified by structural geometry [13], the linear motors can be split into categories as shown in Figure 1.2. Depending on the primary and the secondary shape, a linear motor is called *tubular linear motor* when the primary and the secondary have coupling shape instead of flatbed shape in *flat linear motors*. In the two categories, the linear motors are built in *long stator*- (long primary) or *short stator*- (short primary) categories. The long stator linear motors have longer electrical supplied parts (primary, winding) in comparison with secondary parts. In this case, the secondary parts are moving (moving track – static forcer). In contrast, the short stator linear motors have longer secondary parts in comparison with primary parts and moving primaries (moving forcer – static track). The flat linear motors are further classified into *single side* linear motor or *double side* linear motor by the number and the arrangement of linear motor primary parts and secondary parts. If classified by electrical characteristic, linear motors have equivalent categories as rotational motors; linear induction motors (LIM), linear synchronous motors (LSM), linear DC motors, linear stepper motors, etc.

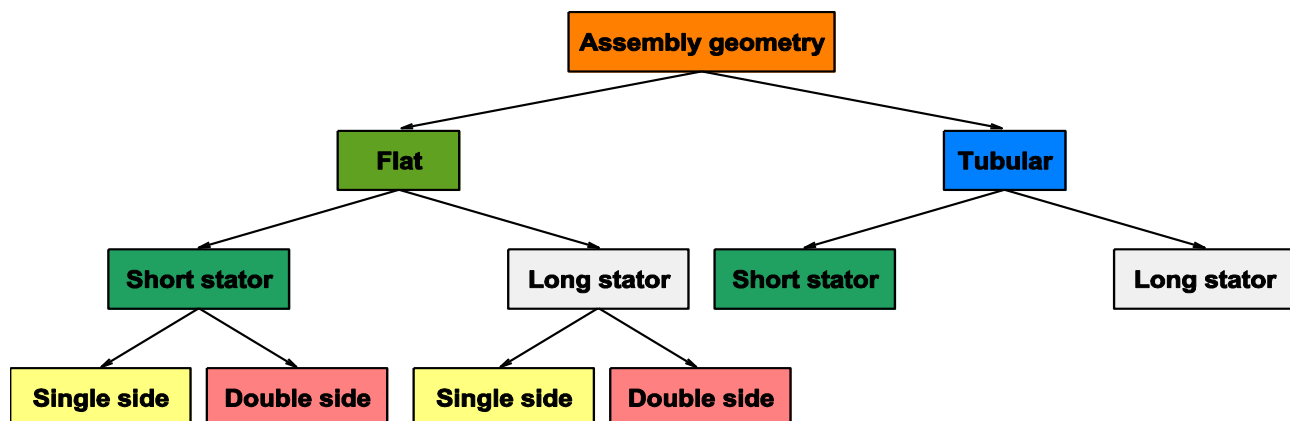


Figure 1.2 Linear motor categories [13]

Altogether, many types of linear motor have been developed for any applications until now. The researches to use the advantages of linear motors in practical applications are continuing. In this dissertation, a research to apply linear motor in the process integrated material handling will be presented.

## **1.2. Linear drives for industrial material handling and processing**

As mentioned above, the linear motors are used today more and more in industrial applications because of their advanced features. With their advanced mechanical structure over the rotational motors in linear motions, the linear motors have attracted many interests in the industrial material handling and processing applications.

In industrial production lines, materials must be processed and transported between processing stations. The raw materials are processed sequentially to transform from a raw state into finished parts or products. Each operation is done in one processing station. Within the processing stations, for high precise operation, materials need to be fastened when they are moving in and released when they are moving out. The final parts or products are completed at least after passing several stations. In between the stations, the raw materials are transported by conveyor belts, mobile vehicles or robots.

In traditional processing method, the materials are tightened and released in each operating station. That takes time of the process. In order to eliminate the significant time-consuming for tightening and releasing, material handling systems nowadays have a newly developing trend. That is using the high precise mobile mechanism, which can stop or move precisely within the processing stations. With that, the process can be operated on the mobile mechanism in each processing station. Therefore, the raw materials just need to be fastened to the mobile mechanism at the beginning of the processing chain and released at the end.

As the requirements mentioned above, the linear drive is a good option for the new trend of the industrial transportation and processing system. By using the linear drive [14] directly for processing and transportation without releasing and re-adjusting the work pieces, with a linear drive system will result in many benefits as follows:

- High productivity
- High dynamic and high precision (few  $\mu m$ )
- No mechanical transmission → reduced wear, assembling and maintenance costs

Figure 1.3 shows a simple example of combined transportation and processing of materials with a linear drive system. In such applications, the following properties are necessary for the linear drive system:

- On a guide-way (track), several vehicles travel with a high degree of independency.
- Each vehicle is controlled very precisely (few  $\mu m$ ) when the vehicle operates within a processing station.
- The carriage allows for movements following horizontal-, vertical- curves or closed paths.

A circular linear transport system for a concatenation of machine tools was proposed already by [18]. However, the transverse flux induction machine, which was designed for this project, needed very close air-gap tolerances, i.e. a high precision of the carriage way. Additionally, the reactive power of the inverter had to be rather large due to the large air-gap and thus the system was not optimal. In an application like in Figure 1.3, the track passes through processing stations (P1..P4). In the processing stations, typically high-precision positioning and high forces are necessary. For high-precision positioning, position sensors cannot be avoided. However, outside of the processing stations, typically a lower precision in positioning is sufficient. In these parts of the track, motion control without using sensors for speed or position should be realized.

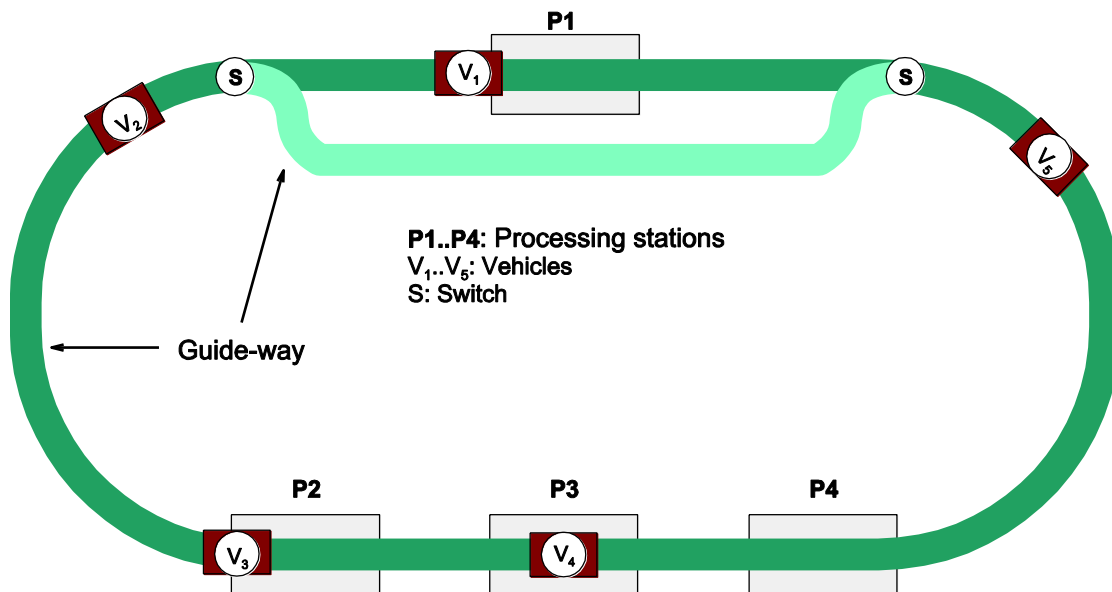


Figure 1.3 An example of proposed linear drive system for combined transportation and processing of material [44]

### 1.3. Aim of the study

With the advantages mentioned above, the linear drives provide many new solutions for material transportation and processing in the manufacturing industry. Instances of application can be found for stretching of plastic films [15] or in material handling [14][16][17]. For these applications, the linear motor is typically with stationary long primary part and a short moving secondary part [14]. As the secondary part is passive, no energy transmission is required between the moving and stationary part, avoiding the use of brushes or inductive transmission. The motor type best suited for the mentioned applications is the synchronous one with permanent magnets, because of its higher efficiency, compactness, but most important because it allows a higher air-gap.

In the usual approach, the linear motor is only used for thrust force production. The guidance is usually implemented by a mechanical assembly. The mechanical guidance constrains the movement to the longitudinal displacement, fixing the lateral and vertical displacement, yaw, roll and pitch. Such a mechanical assembly can be complex and source of high friction.

In this thesis, a study of an active guiding system is presented. The proposed guiding system is used for permanent magnet synchronous linear motors (PM SLM) with long and double-sided primary. The lateral displacement and the yaw angle are controlled while a simple wheel-rail system fixes the vertical displacement. This combination of magnetic and mechanical guidance offers a good trade-off among the complexity of the control, actuators and mechanics, when industrial applications are considered. To allow multiple vehicles traveling simultaneously and independently on the guide-way (each vehicle is controlled by an individual part of the guide-way), the double side primary is separated into segments. With that structure, flexible-operating methods can be implemented. That is very useful in process integrated material handling where different speeds of material carriers in each processing station are required. Another advantage of segmented structure is the energy saving. The power is supplied only to the segment or the two consecutive segments in which the vehicle runs over. In one segment, each side of the primary is supplied by its own inverter, allowing the necessary degrees of freedom to control the lateral position and the yaw angle in addition to the longitudinal position. With this arrangement, the mover can be kept passive avoiding any energy transmission system to it (besides for the sensors).

Together with the guiding system, the sensor system is also studied in order to make a complete passive vehicle. As the requirement of the guiding system, sensor

system must be able to supply three feedback parameters, namely: lateral position, yaw angle and longitudinal position. To eliminate either the supplying energy or the data transmission, the sensor system must have the active part on the guide-way, while the passive part is mounted on the moving vehicle.

### **1.4. Organization of the dissertation**

According to the aim of the study, the thesis will be introduced in the main chapters as follows:

In chapter 2, the topologies of the linear motors will be presented in order to find a suitable topology for the material transportation and handling applications. Based on the current state of art, a new system is proposed. Finally, a list of studying matters, which have to be solved in order to implement the proposed system, is established.

Chapter 3 is the descriptions of the experimental system. A prototype of the proposed system is realized with the combination of commercial products and institute-developed products.

The system is analyzed by mathematic calculations and finite element method (FEM) simulations in Chapter 4. The results are verified with the practical measurement in the experimental setup.

In chapter 5, the control method is proposed. Parameters of regulator units are calculated based on the proposed control method. The control system and regulator's parameter are then verified with a Matlab simulation model.

In chapter 6, the control method is implemented in the experimental setup. Verifying experiments are executed to test the proposed control method on a prototype system.

Finally, a new sensor system, which can make the vehicle passive, is studied and presented. The complete structure, mathematical analysis and practical experiment of the sensor system are introduced in chapter 7.

The conclusions are given in chapter 8. In the chapter, the summary of the works in the dissertation is presented, and suggestions for the future works are quoted.

## 2. PROPOSED SYSTEM

### 2.1. Topology of linear motors applied in industrial material handling and processing

After a long period of development, linear drives are manufactured in many different kinds, suitable for different applications. For industrial material handling and processing, the properties of linear drives need to be analyzed to make suitable choices. In this section, the two main distinguished categories of linear motor (short primary and long primary) are firstly analyzed. Then the suitable linear drive is chosen for the study in this dissertation.

In short-primary linear motors, the winding is mounted on the moving part. Hence, the short-primary linear drive requires active vehicles i.e. energy and information must be transmitted to the vehicle. The solutions for energy transmission can be running cables, sliding contacts or contact-less (inductive energy transmission). The running cable solution is not applicable in industrial material handling and processing, as the vehicle has to travel long distances and closed paths. In many industrial production environments, sliding contacts should be avoided because of the safety for workers, maintenance or exploding protection. In the short-primary category, the contact-less energy transmission is a suitable proposal. Figure 2.1 shows the contact-less energy transmission for short-primary linear motor proposed in [14]. In the figure, the static part supplies electric energy with constant frequency for the transmission system. On the moving part (vehicle), a power electronic system is used to supply the energy for the winding. Beside the energy transmission, a contact-less information transmission system is necessary. The benefits of this proposal are:

- The number of the converters and control units is equal to the number of vehicles plus the converter feeding the contact-less energy transmission.
- Position sensing is much easier and cheaper when auxiliary energy is available on board of the vehicle.
- The passive track plus contact-less energy transmission may cause lower costs than a long active track, especially when an induction machine is used.

The drawbacks of this system are:

- Because of the energy transmission system and the on board inverter, the vehicles have high weight and big volume.
- The power limitation of contact-less transmission system and the vehicle weight reduce the dynamic of the vehicle.

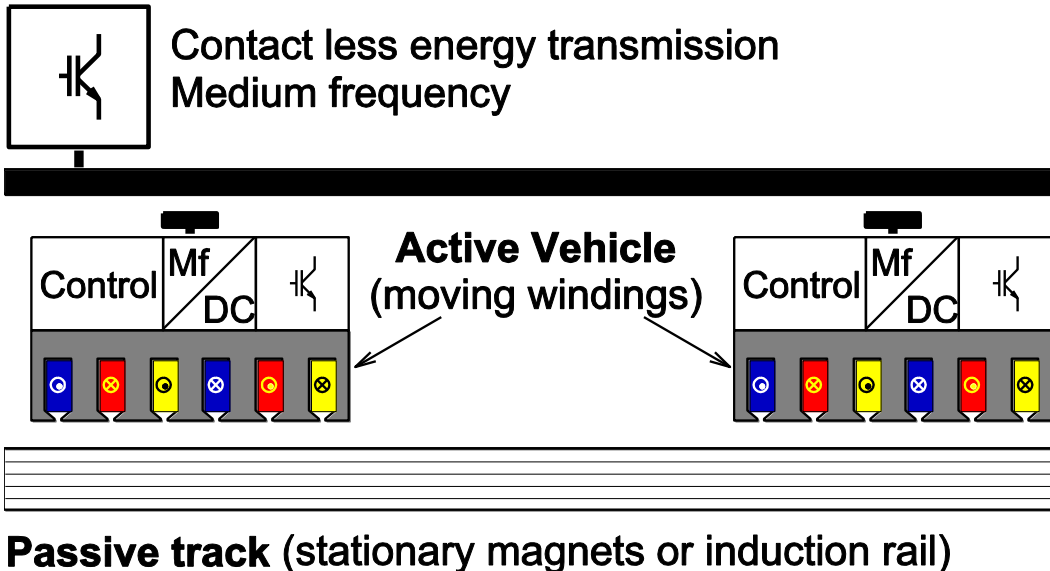


Figure 2.1 A short primary system with contact-less energy transmission [14]

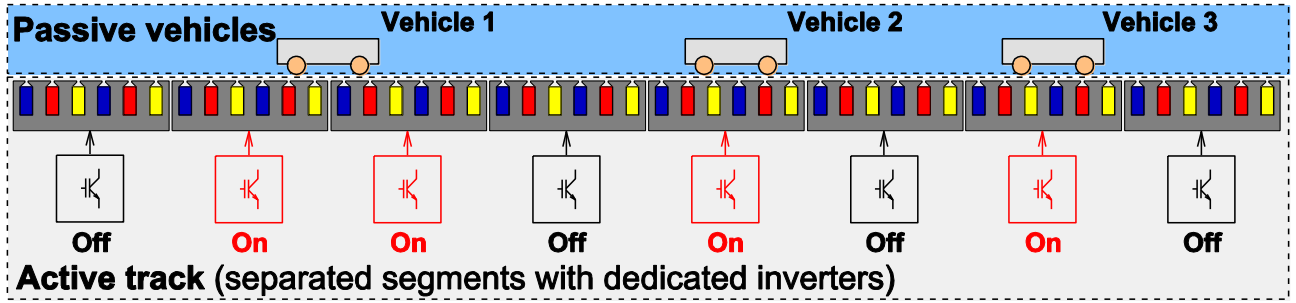
With the above characteristics, the short-primary linear drive can be a good solution for applications with a long track, low number of vehicles and low acceleration.

In order to overcome the drawbacks of the short-primary linear drive, the long-primary one can give solutions for high acceleration, passive, lightweight vehicles by using an active track. The system does not need energy or information transfer to the vehicles. Because of its higher efficiency, compactness, but most important because it allows a higher air-gap, permanent magnet excitations are usually used in the system. For use in industrial material handling and processing applications, the primary of the system is separated in to segments. This ensures that:

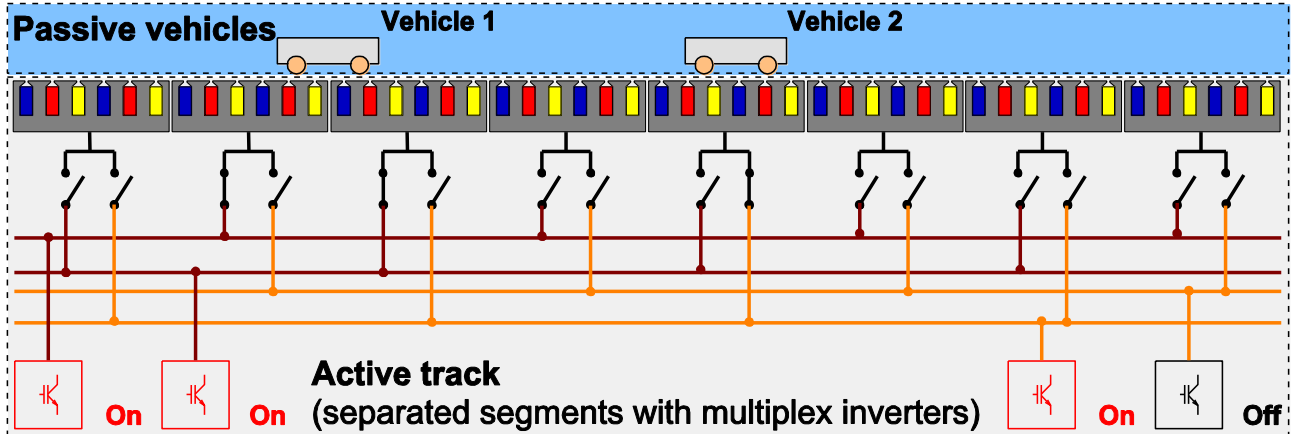
- Each vehicle can be controlled and moved independently by one or two contiguous primary segments.
- The reactive power can be reduced (save energy) by switching off the stator segments not carrying any vehicle.

The proposed long-primary systems are presented in Figure 2.2. In order to control the vehicles, each segment can be fed by dedicated-inverters (Figure 2.2 a) or multiplexed-inverters (Figure 2.2 b). With these structures, one vehicle is controlled independently by one feeding segment, when the vehicle is within the segment or by two feeding segments, when the vehicle in the transition area of the segments.





a) *Dedicated inverters*



b) *Multiplex inverters*

Figure 2.2 Proposed long primary topology [14]

As mentioned above, several suitable topologies are applicable for industrial material handling and processing. In this dissertation “Magnetic guidance for linear motor”, the research on long primary motors with dedicated inverters applicable to industrial material handling and processing is presented. The research is done with double side long-primary linear motor for high thrust force applications. Magnetic guidance is studied to avoid precise mechanical guidance.

## 2.2. State of the art

Regarding to the introduction in chapter 1, the research of this dissertation relates to the control of the magnetic thrust and lateral air-gap in a synchronous motor with long stator and “passive mover”. With no transmission between the environment and the vehicle (neither electric energy nor information), the “passive mover”, for example, can be used in material processing.

This topic is one part of the wide area of magnetic driving, levitation and guidance. We have to distinguish between rotating and linear drives. There are many interesting documents in literature of rotating drives, concerning magnetic bearing and bearing

less motors. They are also related to the research topic, but in this subsection, they are not discussed in detail.

With linear drive, these basic functions

- thrust force
- lift force and
- lateral force

generation can be realized in combination or be separated in subsystems. With combined realization, parts of the actuator (coil, magnet) are used jointly to generate some basic functions.

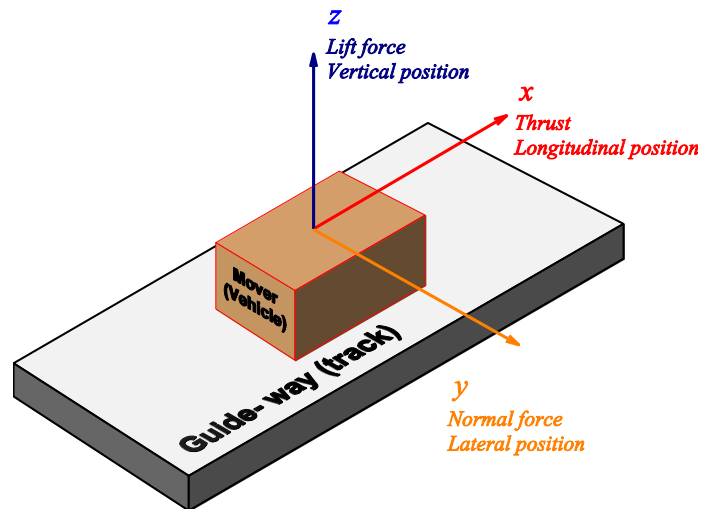


Figure 2.3 Basic functions of electrical linear motors

The lift force and lateral force can be generated with control, without control or with hybrid methods [19]-[24]. The realization without control is based on repulsive magnetic forces. These forces can be set up between the same polarity of poles of permanent magnets or with the aid of superconducting magnetic coils. By using electro-dynamic levitation or null-flux coils [19][20], passive magnetic guidance can be provided for one or more degrees of freedom. The drawback is the dependence on the longitudinal speed i.e. it does not provide guidance at standstill. The superconducting magnetic bearing [22] is a passive guidance method that works even in standstill, but it requires a cryogenic system instead. In addition, more destabilizing forces occur when the levitation is implemented [23]. Therefore, the levitation is not concerned in this dissertation in detail.

As mentioned above, the application of this research deals with linear drives for industrial material handling, consequently high-speed maglev trains are not dealt. The research is mostly related to machine tools and building applications. Research in this area will be discussed in the next subsections.

### 2.2.1. Research from other institutes

As already stated, studies based on only one basic function, e.g. on thrust generation only, such as [25], is not the focus of this work. Almost all the studies mentioned in this subsection try to handle with several basic functions.

In [26], a linear drive with active translator is handled as shown in Figure 2.4, in which three basic functions: thrust generating, vertical lifting and lateral force are

realized by separate components. In the active translator, four magnet modules assure the magnetic levitation and the guidance of the table. The levitation and the guidance here are implemented by a combination of permanent magnets and electrically excited magnet.

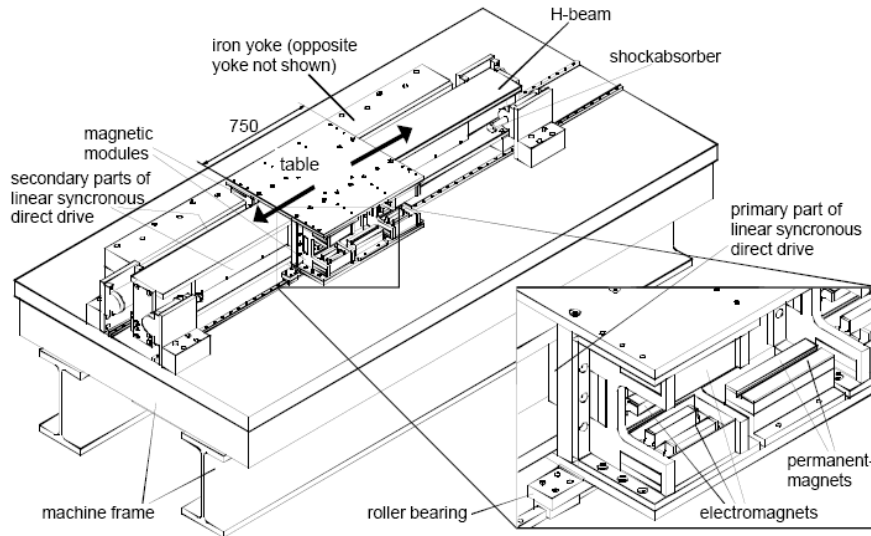


Figure 2.4 Linear drive with active translator [26]

As shown in Figure 2.5, a homopolar synchronous linear motor [27] is described with contact-less energy supply for the active translator. The upper part of Figure 2.5 shows a lifting magnet for the levitation together with basic function of lateral guidance. The combination of lift force and lateral force is also performed in [28], which is shown in Figure 2.6. However, the lateral guidance in [27] and [28] is uncontrolled.

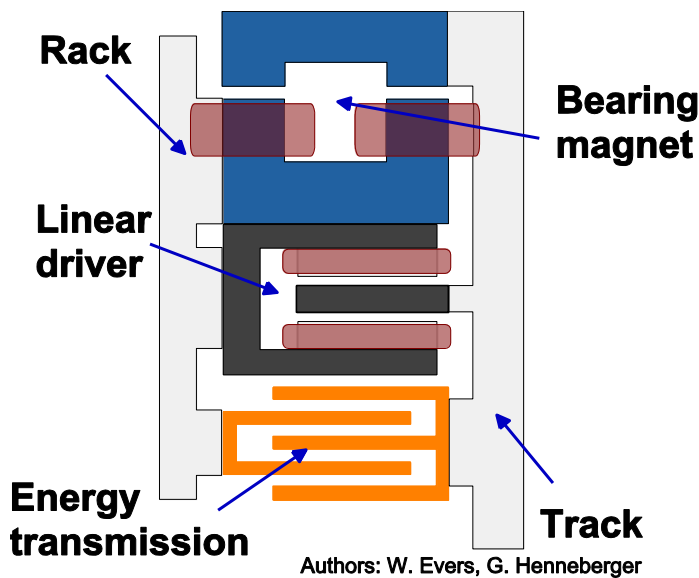


Figure 2.5 Non-contact energy supply [27]

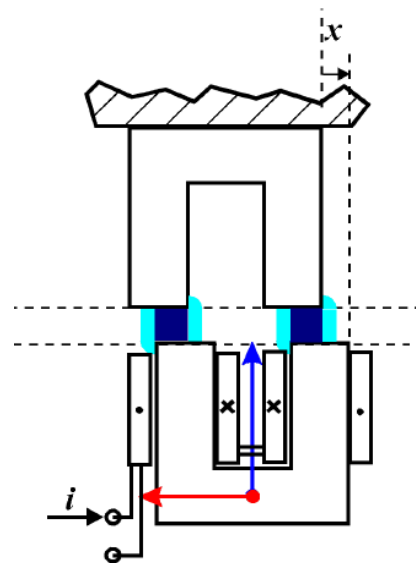


Figure 2.6 Lifting and guiding in [28]

The lifting and guiding functions are solved in Figure 2.7 of [29], where the permanent magnet is lifted in  $y$ -direction and guided in  $z$ -direction by controlling the electromagnets. In this approach, an active vehicle is required in order to supply power for the electromagnets and the control system.

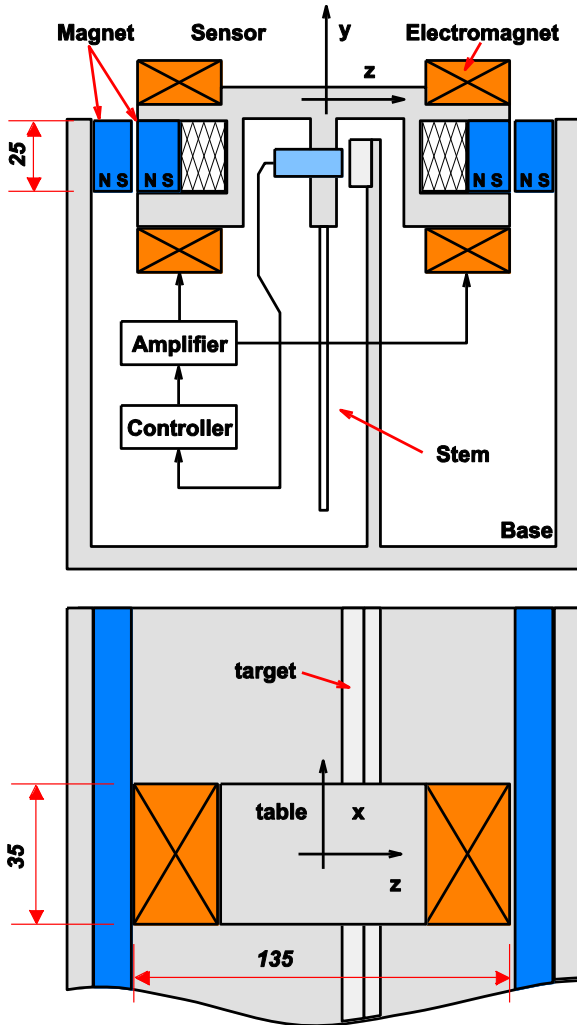


Figure 2.7 Lifting and guiding in [29]

The combination of the lift force due to attractive normal force and the thrust, which are generated by an asynchronous short stator motor with necessarily active vehicle as discussed in [30], is another solution. This is shown in Figure 2.8.

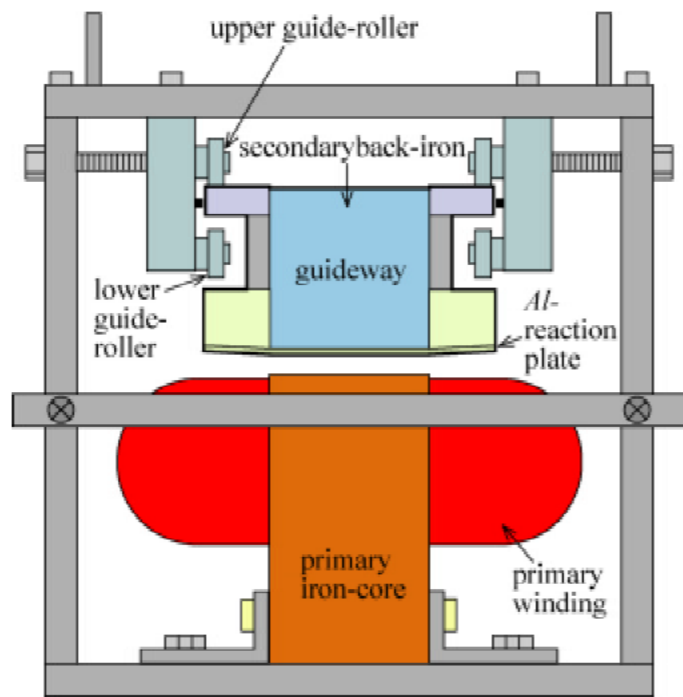
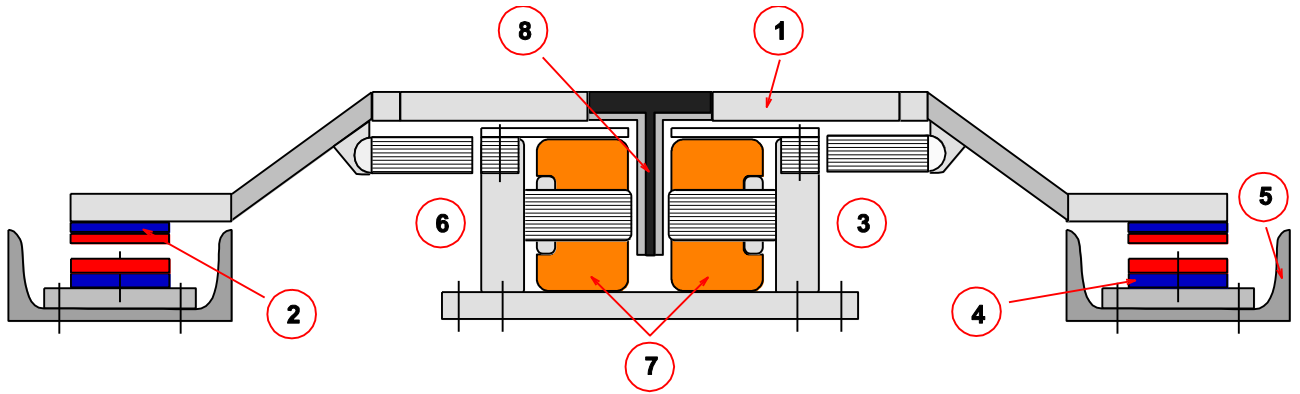


Figure 2.8 Lifting and guiding in [30]

In the arrangement of Figure 2.9 [31], [32], the repulsive force is applied by the same polarity of magnetic poles in order to lift the vehicle up (without control) ②④. Thrust is produced by a synchronous long stator double side linear motor with internal ironless permanent magnet cursor ⑧. Due to the ironless magnetic cursor and the permanent magnetic lifting system, the normal and the vertical rigidity of the guidance system are very low. Consequently, only small separated actuators ⑥ with sensor ③ are included in the vehicle (active vehicle) for lateral force generation. The actuators have to generate small forces in the directions orthogonal to the motion (normal force) to align the bogie.



① bogie, ② Magnetic guide (moving part), ③ lateral positioning sensor, ④ magnetic guide (unmoving part), ⑤ lateral reference guide, ⑥ electromagnetic actuator, ⑦ stator, ⑧ cursor

Figure 2.9 Lifting and guiding in [31][32]

In [33], an overview about the different arrangement of linear asynchronous is given. In contrast to the above studies, a long stationary primary is analyzed to generate the thrust and the normal force for a material transportation system with very high accelerating rate. The magnetic lift force is not necessary, because the vehicle is equipped with wheels.

In addition, supporting wheels and guiding wheels are used for the vehicles of the project “new rail technology Paderborn”, e.g. [34], [35], and [36] with a special feature. That is a double-sided linear asynchronous machine implemented in an active vehicle.

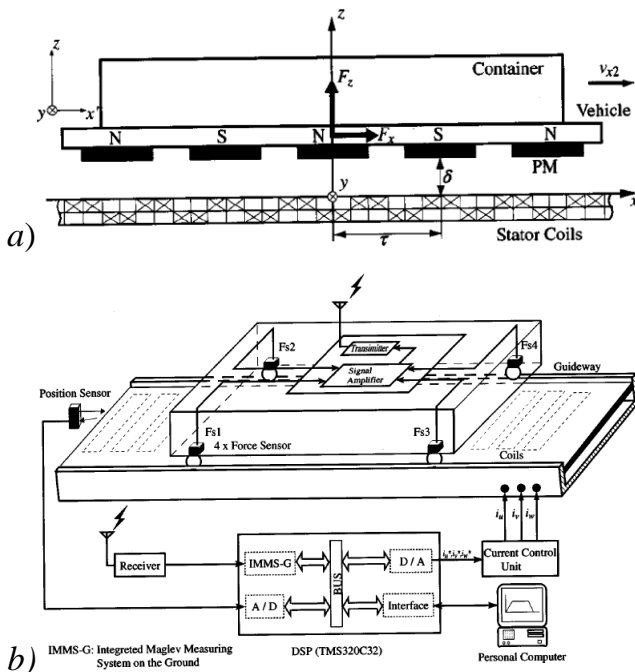


Figure 2.10 Supporting wheels in [37]

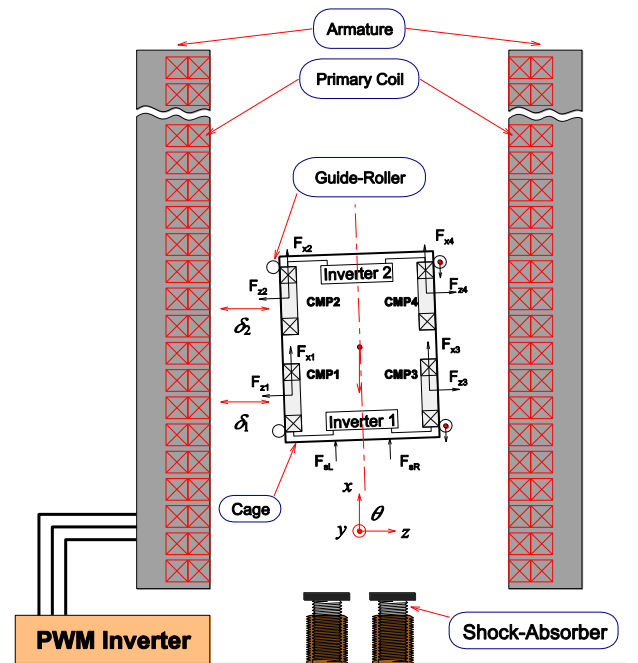


Figure 2.11 Elevator in [38]

Similarly, supporting wheels are used in the vehicle of [37]. The synchronous long stator linear motor generates thrust force and with the help of its ironless stator

winding a repulsive force to reduce the axle load. This principle is shown in Figure 2.10.a. In order to acquire feedback signals for the axle load control, force sensors and radio transmitters are inserted in the vehicle (Figure 2.10.b).

In Figure 2.11, the rope-less elevator from [38] is shown. The lateral position of elevator cage is guided in the elevator shaft by forces  $F_{z1} \div F_{z4}$ , which are produced by current supplied coils of controlled permanent magnets (CMP). The guidance is established by controlling the positions  $(\delta_1, \delta_2)$  simultaneously. The positions are controlled by actuating the currents of the CMPs. Nevertheless, in [38] not many results are shown. With the proposed structure, only simulation results for a sensor-less control of the lateral position is shown. In addition, an active translator (elevator cage) is necessary.

One of the first products has been already commercialized for material handling based on linear motors is shown in [39]. The synchronous long stator motor produces the thrust force. To produce lateral force, permanent magnets are used. The vertical force is supported by wheels. With them, the vertical force of the magnets boost the axle load i.e. friction and abrasion are increased. In [74], some other similar commercial products from MagneMotion are introduced.

### 2.2.2. Research in our department

The studies on linear direct drive have been realized in our institute in many years. In summary, these are as following works

- a) Parameter adaption for high dynamic control of short stator synchronous linear motors.[40][41][42][43]
- b) Modelling by Finite Element Method (FEM) to compensate the cogging forces and perturbation due to the segment transition of long stator linear motors [44][45][46].
- c) Speed sensor-less and position control of long stator linear synchronous motor [47][48][49][50][51].

In a), it is shown that, the parameter of a “dead beat” current control must follow a field of characteristics to make a fast optimal current control. Without that adaptation, the deadbeat control will be unstable by machine saturation. The required field of characteristics can be established by measurements or by results of FEM calculations.

In b), an example of a synchronous long stator linear motor was implemented to develop control methods and to get experimental verification. The linear motor can be controlled high dynamically and precisely even under the following conditions:

- strong and quick varying asymmetric phase windings,
- strong dependency of parameters and produced force on position.
- saturation.

The important thing is the compensation of varying forces, when the moving part passes between segments. Therefore, lookup tables, which are generated by field calculations, are used for calculating the reference values to compensate the influence of thrust forces. A control algorithm based on field oriented control technology is implemented in the experimental set-up in order to verify the method. Besides this a composed system of controller, interface bus, inverters etc. was developed.

In c), a highly important subject for linear drives - especially for long stator drives, is solved. It is well known that large research and development attempts to eliminate the sensors in rotating motors have been performed. Nevertheless, the position sensor of rotating motor is a relatively compact device. In contrary, the position sensor of a linear machine extends along the guide-way through a typically harsh environment. The cost for the linear position sensor (encoder), especially for passive vehicles, is disproportionately high. This is a strong motivation for sensor-less control. In addition, the difficulties of sensor less methods are solved in PM rotating machine with surface mounted magnets. Thus in c), the main study is finding solutions to solve problems caused by end effect, low coverage of the stator magnetic carrier and the transition between the stator segments.

## **2.3. Proposed system**

### **2.3.1. Target of research**

This study deals with production and control of the thrust force and the lateral guiding of synchronous long stator linear drives with passive and wheel-supported vehicles, which can be used in material handling and processing. The lateral guiding of the vehicle is controlled by electromagnetic forces. That will simplify the mechanical structure of the long roadway, as no lateral precision guidance is required anymore. By the double-sided stator, no vertical force is created.

### **2.3.2. Proposed structure**

The proposed approach is shown in Figure 2.12. In the guide-way, two long double-sided stators are integrated. The double stators are applied to produce thrust and guiding force. It is not like conventional double side motors, which are arranged tightly to both sides, our linear motor have a larger distance between the two stator

sides. Due to this, not only the lateral position  $\delta$  but also the vehicle yaw angle  $\gamma$  (heading angle) can be influenced by the proposed control.

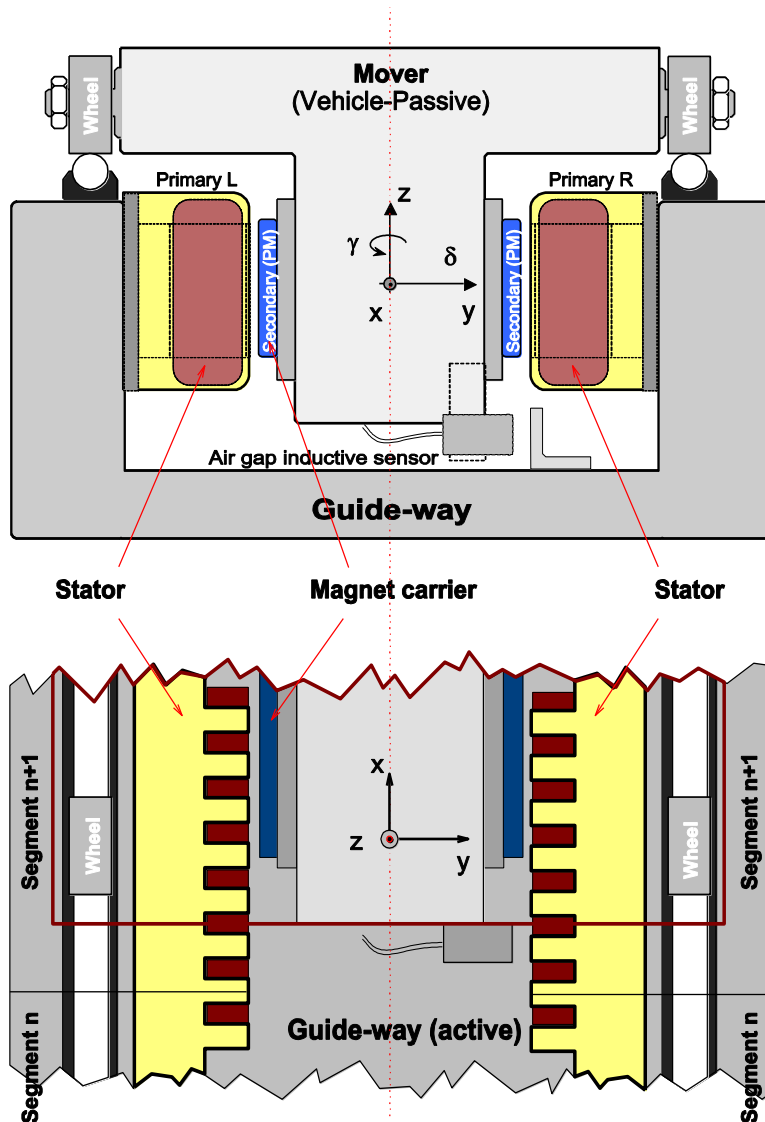


Figure 2.12 Proposed approach

As in Figure 2.12, the long stator is divided into many segments. For each segment, there are two inverters, one supplies power for the left side and the other supplies the right side of the stator. The segmented arrangement allows many vehicles moving independently in a guide-way. In order to reduce the energy losses, only the stators of the segments, in which vehicles are located at the observing moment, are supplied with power. The others are in standby mode.

In the initial part of this work, the lateral position and yaw angle sensors are commercially available inductive sensors mounted in front and back of the

vehicle. Later on, they will be replaced by a new type of capacitive sensors, which are developed in this work. As mentioned before, this is only one of several possible constructions to study the magnetic guidance and the new capacitive sensor design. The study can lead to further considerations on advantages and disadvantages of various designs to find the cheapest solution.

## 2.4. Program of the work

### 2.4.1. Control duty.

With the proposed structure mentioned in the previous section, the individual  $dq$ -axis currents are supplied to the both primaries. The  $q$ -axis currents, on one hand,



produce the thrust following the guide-way direction ( $x$ -direction). On the other hand, they control the yaw angle of the vehicle by controlling the difference of both feeding thrusts around zero. That control can keep the vehicle parallel to the guide-way axis. With  $d$ -axis currents, the normal forces are produced to keep the center of vehicle coincide with guide-way center (middle of the stators - e.g. lateral position  $\delta=0$ ).

Altogether, there are three coupled control duties to realize

- $x$ -position,
- lateral control  $\delta=0$  and
- yaw control  $\gamma=0$ .

During the movement of the vehicle from one feeding segment to the next, it covers two-stator segments simultaneously, where the coverage of the vehicle's magnets at the old segment decreases and the coverage at the new segment increases. At that time both segments are supplied, that means controls for both segments (i.e. four stators, eight current components) must be coordinated together, such that the three control duties are produced co-ordinately 1.  $x$ -position, 2. Lateral control ( $\delta=0$ ), 3. Yaw control ( $\gamma=0$ ). These three control duties have to be fulfilled not only in one stator segment but also during the transition between two stator segments.

### **2.4.2. Lateral position sensor and yaw angle sensor.**

In the above outline, to implement control duties, beside the available actuators (inverters + stators) the actual value of controlled qualities i.e.  $x$ ,  $\delta$ ,  $\gamma$  are required. In this thesis, a basic sensor system was developed and investigated.

One difficult condition of the sensor is the demand that neither information nor auxiliary power is transferred between vehicle and stationary environment (passive vehicle). To fulfil the duty, only sensors for lateral- and yaw- control are tested and examined. For the  $x$ -position sensor, one of the methods studied in [52][53] can be applied.

To get the lateral position  $\delta$  and yaw angle  $\gamma$ , we can use many different sensor principles, particularly inductive or capacitive. In this thesis, a new capacitive sensor will be introduced later on. Furthermore, other principles (not in this thesis) are possible i.e. inductive sensor method, sensor-less method. The best solution may be found when the advantages and disadvantages of different sensors are compared together.

### **2.4.3. Work steps**

With the duties mentioned above, the study program was arranged in following steps:

- Linear motor prototype assembly: Stator selection, Inverter components, Position sensor for  $x$ -direction, Mechanical design and construction.
- Control parameters calculation.
- Development of the control method: Implementation and test.
- Design of the new capacitive sensor for lateral position and yaw angle control.
- Documentation.

## 3. EXPERIMENTAL SETUP

To implement the experimental setup as proposed in chapter 2, a combination of the available equipment in the market and self-developed products of the institute was implemented. In this chapter, the experimental setup system is introduced in three main parts: Mechanical structure, Electrical system and Control system.

### 3.1. Mechanical structure

#### 3.1.1. The motors

The linear motor, which is used in the experimental system, is a commercial industrial linear motor. The motor is an assembly kit motor, i.e. the motor components consisting of separate primary-sections (LSE10G 0614) and secondary-sections (LSM10G 0615) as in Figure 3.1 are separate parts. The primary-section consists of an iron core and distributed three-phase windings. It is completely enclosed by composite material. The main parameters of the primary-sections are presented in Figure 3.2.a and Table 3.1.

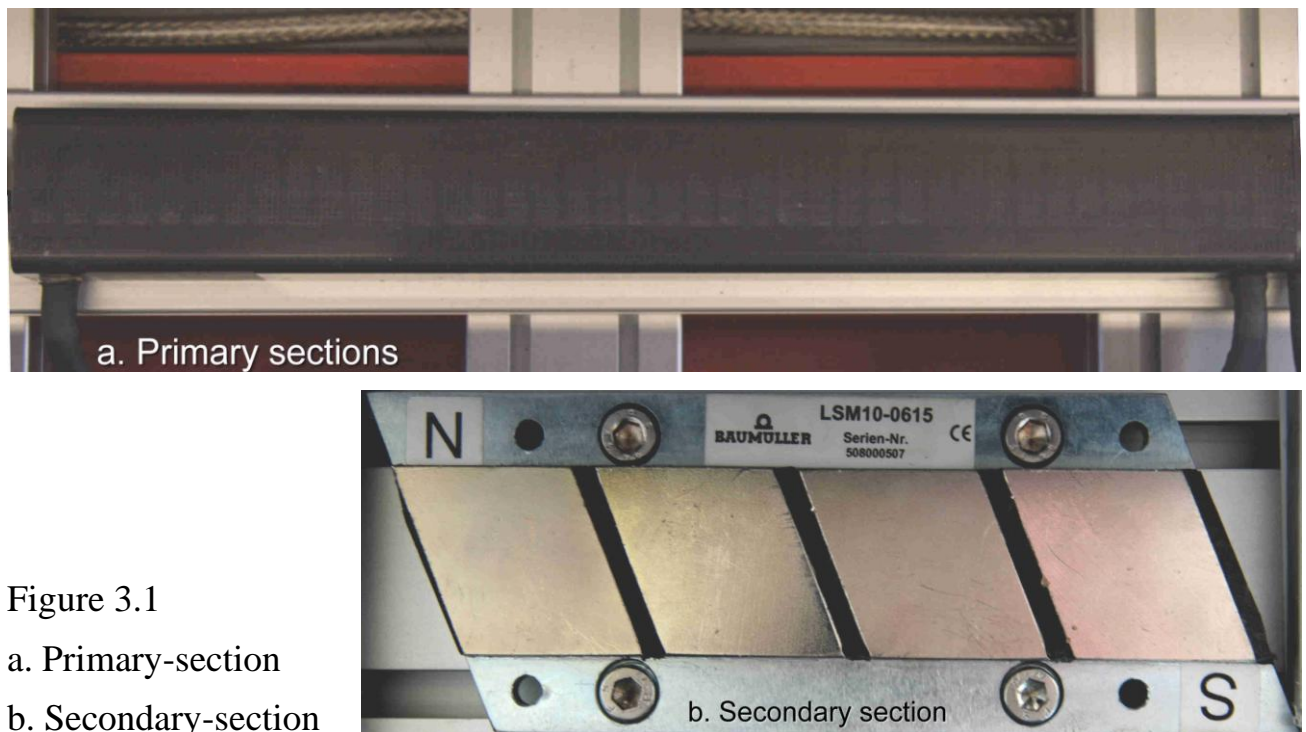


Figure 3.1

a. Primary-section

b. Secondary-section

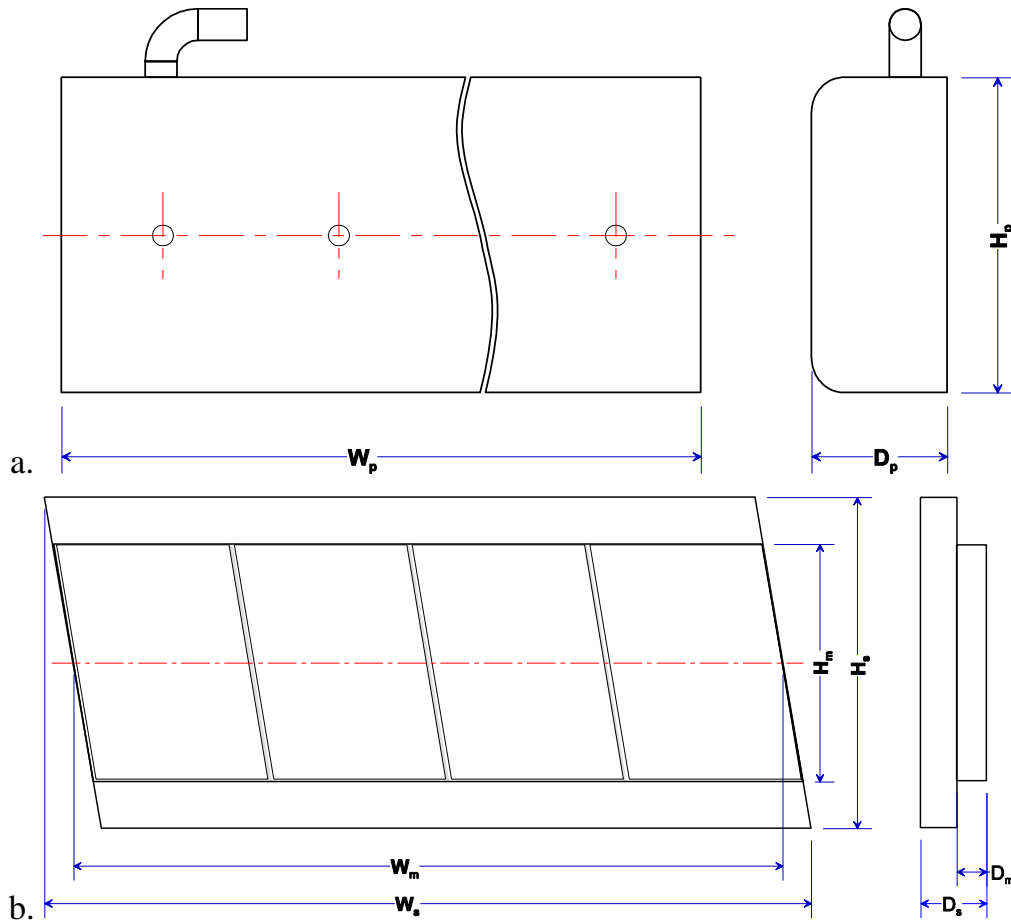


Figure 3.2 Linear motor dimensions a. Primary b. Secondary

A segment of the secondary-sections consists of a galvanized base steel body, which serves as magnetic return path. The permanent magnets are bonded to it. In this design, the secondary-sections with four poles (four magnet pieces) were chosen. Detailed parameters are presented in Figure 3.2.b and Table 3.1.

TABLE 3.1 LINEAR MOTOR PARAMETERS

Parameter	Value	Parameter	Value
<b>Primary section</b>		Slots per section	42
$W_p \times H_p \times D_p$ (mm)	504x65x42	Winding arrangement	Distributed
Nominal voltage $U_N$ (V)	540	Number of coils per phase	13
Nominal current $I_N$ (A)	2.9	Number of turns per coil	30
Peak current $I_{\max}$ (A)	21.3	Pole pitch (mm)	36
Thrust force $F_{Tn}$ (N)	210	Tooth pitch (mm)	12
Maximal thrust $F_{T\max}$ (N)	1270	<b>Secondary section</b>	
Resistance ( $\Omega$ )	2.34	$W_s \times H_s \times D_s$ (mm)	144x60x12
Inductance (mH)	11.0	Nr. of magnets per section	4
Weight (Kg)	7.6	Magnet material	NdFeB
Pole per section	14	$W_m \times H_m \times D_m$ (mm)	34x30x4

### 3.1.2. Construction

The structure of the experimental system was designed and built in the institute, based on the proposed system and the available commercial components in the market. Following the proposal, the experimental structure is designed, as a long stator double-sided linear motor. The aluminium profiles are used to build the machine frame in order to reduce the processing and installation time. Figure 3.3 is the drawing of the mechanical structure. In Figure 3.4, the photo of the experimental structure is shown. With that structure, the experimental set-up consists of two main parts: The system basement (guide-way) and the vehicle (mover).

The system basement is a frame to fit the components of the experimental setup, e.g. primary-sections, stationary parts of the air-gap sensors and of the incremental longitudinal position sensor. In addition, the system basement has a function to

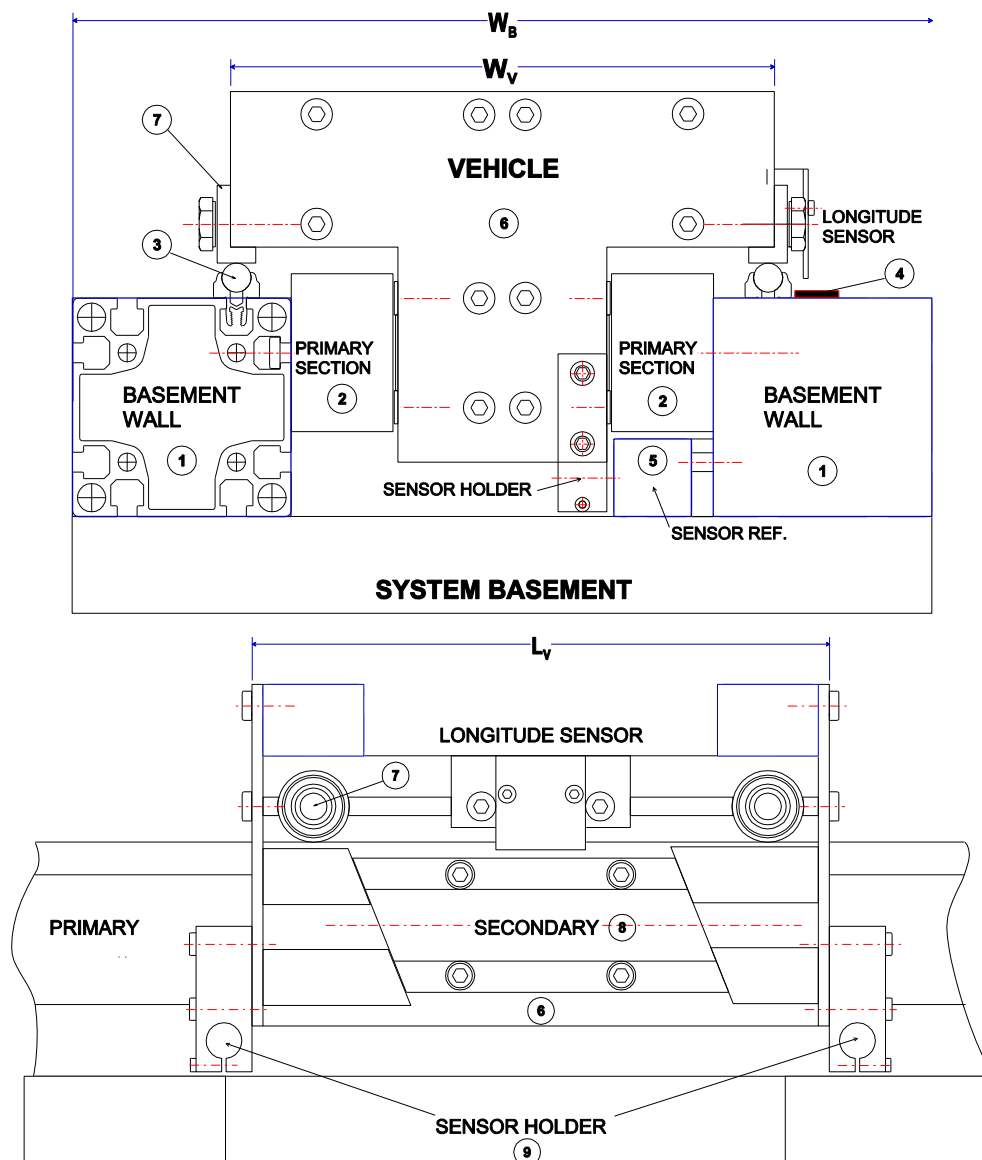


Figure 3.3 Drawing of mechanical structure

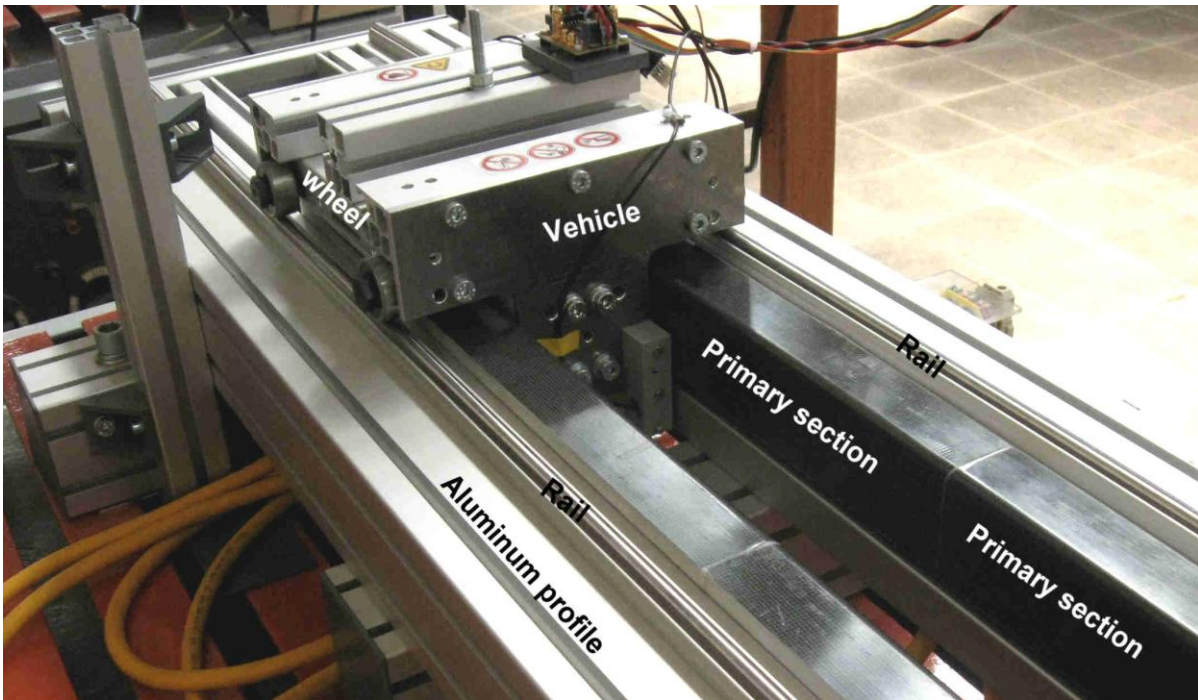


Figure 3.4 Mechanical structure of the experiment setup

constrain the vehicle in the vertical movement. The system basement was built with two parallel aluminium walls ① along the guide-way of the vehicle. On each wall side, the primary sections ② were fastened consecutively to make a line. Each pair of primary sections, in opposite, composes a primary segment. The experimental setup here was constructed with two primary segments. On the top of the aluminium walls, two round iron rods ③ were attached to make a running way for the vehicle. A magnetic incremental tape ④ was pasted on the top of the left wall to give the measuring reference for the longitudinal position sensor. Under the left primary sections, a small aluminium wall ⑤ was installed in order to give a reference for inductive air-gap sensors.

The chassis ⑥ of the vehicle was built from aluminium profile. It has four wheels ⑦, which allow the vehicle move freely in the horizontal plane created by the guiding rods when the vertical displacement is fixed. In the lower part of the vehicle, there are two secondary-sections ⑧ facing the primary-sections. That arrangement forms a synchronous linear motor with double-sided stators. In the middle of the vehicle's left side, the longitudinal position sensor was installed. The air-gap sensors ⑨ were fixed in the front and the back of the vehicle opposite to the small aluminium wall.

With the structure described above, the experimental setup allows to implement the proposed experiment with magnetic guidance for the vehicle described in the later chapter of this document. The main parameters of the mechanical structure are in Table 3.2.

TABLE 3.2 MAIN PARAMETERS OF MECHANICAL STRUCTURE.

Parameters	Value	Parameters	Value
<b>System basement</b>		Length $L_V$ (mm)	238
Width $W_B$ (mm)	354	Weight $m_V$ (kg)	6.5
Length $L_B$ (mm)	1764	Wheels distances (mm)	183x219
Height $H_B$ (mm)	194.5	Lateral sensor distance (mm)	263
Nr. of primaries per side	2	Nominal air-gap (mm)	1.5
<b>Vehicle</b>		Max air-gap (mm)	2.4
Width $W_V$ (mm)	224	Max longitudinal position (mm)	1008
Height $H_V$ (mm)	152.5		

### 3.2. Electrical structure

#### 3.2.1. Power supply

The power supply for the experimental setup is fed by a three phase four wires

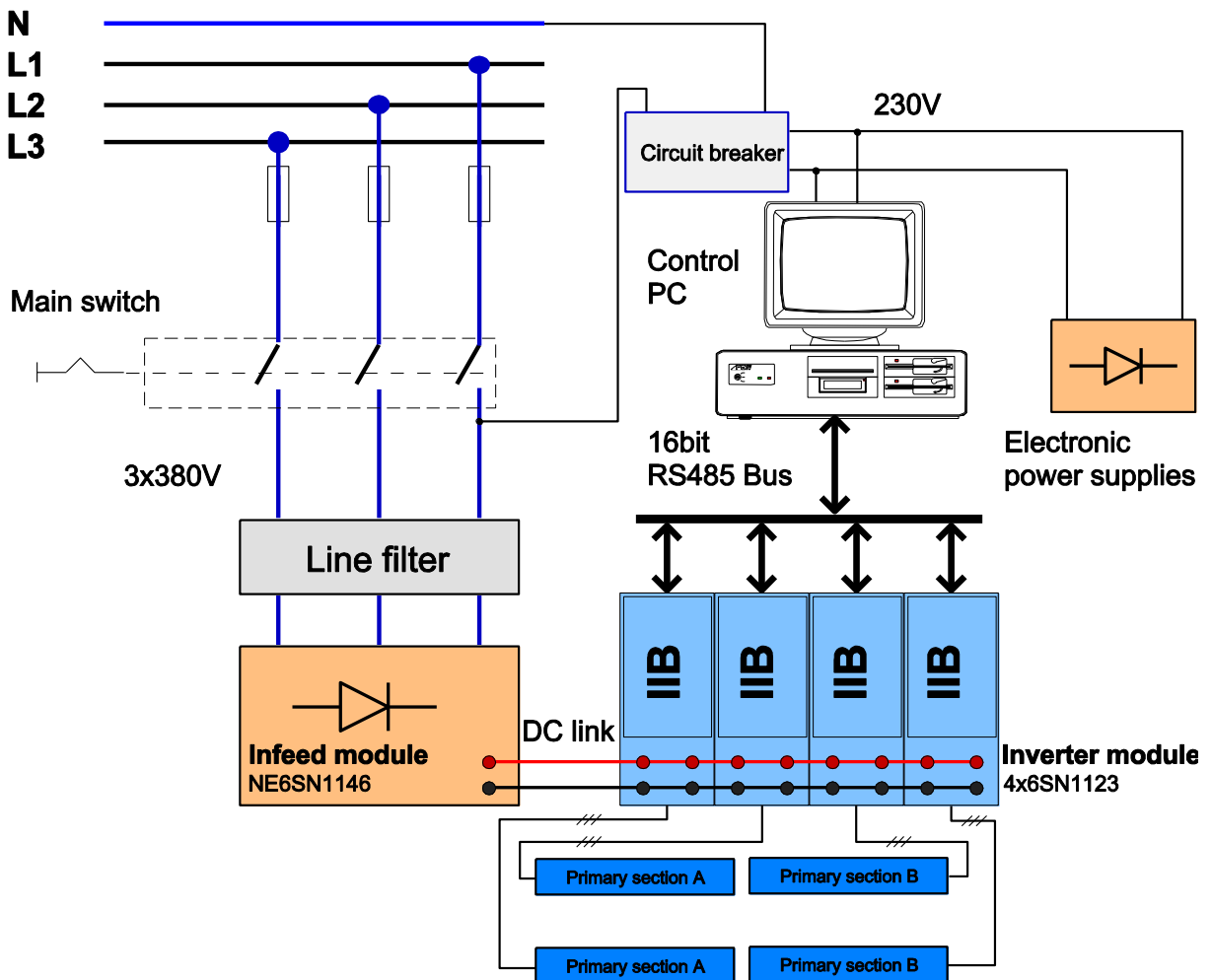


Figure 3.5 Power supply for experimental setup



(with neutral) power in the laboratory. It has the duty to supply power to the inverter system, controller system and electronic system as show in Figure 3.5.

First, the three-phase voltages are supplied through three fuses, which are used to protect the completely experimental setup from over current. The three-phase voltages are then fed to a three-phase main switch. After the main switch, the three-phase voltages are connected to a three-phase line filter and then supplied to the inverter system. Another part of the power supply, after the main switch, is to feed the control system and electronic power suppliers (DC adapters). The voltage between phase L1 and the neutral is supplied to one phase line filter. Output voltage of the filter is used by the controller system and the electronic power suppliers.

### **3.2.2. Inverter modules**

Most of the power for the experimental setup is supplied to the inverter system. The inverter system then generates suitable output voltages to feed the linear motor. Normally, it supplies two primary-sections. When the vehicle crosses the junction point of two segments, it feeds four primary-sections simultaneously.

As described in subsection 3.2.1, the inverter system has a main function to feed the four primary-sections of the LSM. Further, the inverter system must have the ability to communicate with the controller in order to form a closed control loop for the proposed experiment.

In order to supply the four primary-sections, the inverter system has one rectifier module (in-feed module) NE6SN1146 and four inverter-modules (power module) 6SN1123 from Siemens. The details of the modules are presented in [75].

The communication of the inverter module is executed by an electronic board. The board is a self-developed interface board mounted in the inverter module. The interface board also replace of the original commercial control unit in each inverter module. Functions of the interface board are presented clearly in the next subsection.

### **3.2.3. Inverter interface**

The inverter interface has the duties to control the inverter module, to communicate and transfer information to the controller. Therefore, the inverter interface needs four main functions:

- Generate PWM signals for the power module (IGBT) gates,
- Acquire measured data,
- Communicate with the controller,



- Protect the inverter (over current, over temperature etc.).

Because of experimental requirements, all the calculations and the regulation tasks are done by a central controller (a PC) instead of microprocessors for each inverter module. That requirement could not be satisfied by any commercial inverter control unit. Therefore, in the experimental setup, each inverter module has one inverter interface board (IIB), which was developed by colleges in our institute [13][54].

Replacing the control unit in the inverter module, the IIB has a function to generate PWM signals. The PWM signals are generated by using the time values received from the controller. The signals are used to drive six IGBTs of the inverter module.

In the IIB, there are three AD channels in order to acquire the measured data. The data include two phase-current values and a position value. They are acquired and sent to the controller via the communication bus.

As mentioned in the two previous functions, the IIB has to receive the timing values from the controller and send the acquired data to the controller. That requires the IIB needs to be able to communicate with the controller. Therefore, a communication module is implemented in the IIB. The module communicates with the controller by a 16-bit parallel bus. Each bit of the bus is transferred by one pair of wires using RS485 transceivers.

The main protected functions of the IIB are the over current and the over temperature. They protect the system from serious damages. In addition, the IIB gives also some other protections i.e. the communication is broken; one of requirement signals from the rectifier module is missed.

The photo of the IIB is shown in Figure 3.6, and the details are described in appendix A1.

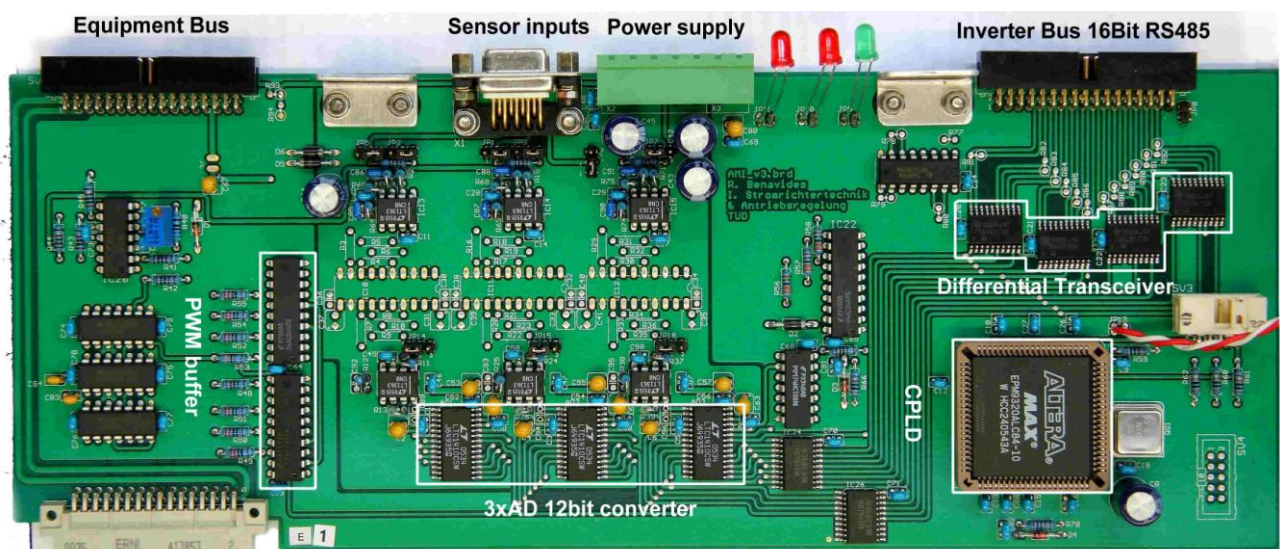


Figure 3.6 Photo of an Inverter interface board (IIB)

### 3.2.4. Sensor system

The information required for the system to execute the control is

- Information about vehicle's position,
- Information about electric currents.

To control the vehicle's motion (guidance) in the plane, which is generated by the guide-way, the information about vehicle positions needs to be evaluated. In the proposed system, they are the positions in  $x$  direction (longitudinal position), in  $y$  direction (lateral position) and the yaw angle.

In the first part of the experiments, the lateral position and the yaw angle are measured by two inductive air-gap sensors. These air-gap sensors are eddy current displacement sensors from LION precision with ECA100 amplifier and U18 probe, shown in Figure 3.8a. The sensors have 0-10V nonlinear outputs and 100 kHz bandwidth. The U18 probe can measure in a range from  $0.75\text{ mm}$  to  $5.0\text{ mm}$  with a resolution 0.02% i.e. precision  $0.85\ \mu\text{m}$ .

The two air-gap sensors are arranged in front and rear of the vehicle. They measure the distances to the aluminium reference wall mentioned in subsection 3.1.2 and generate output voltages which are nonlinear function of the distances. The voltages result in nonlinear values in the control programme by AD converters. The nonlinear values are then linearized by a lookup table, which is generated by calibrating the sensors with practical measurements. The calibration is performed with precision feeler gauges. Blades of the gauges are inserted in between the vehicle and the primary. That gives high-precision references for the air-gap between the vehicle and the primary. At each reference position, output values of the air-gap sensors are captured. The position references values and the captured values are the calibration data of the sensors. The calibration data are then interpolated in Matlab in order to generate the lookup table. The two air-gap sensors with the look-up table can give the linearized values of the vehicle front and rear air-gaps. The mean values of the front and rear air-gaps are used as the reference for calculating the vehicle lateral positions. The different values of the front and rear air-gaps are used as the reference for calculating vehicle yaw angles. In chapter 7, these sensors will be replaced by a capacitive sensor in order to implement a total passive vehicle.

The longitudinal position is measured with a magnet incremental sensor ELS29-200I-SST03-01 from Sensitec, shown in Figure 3.8.b. The sensor contains an anisotropic magneto-resistive (AMR) length sensor and a 13-bit interpolation-IC. In use with a magnetic linear measurement scale with 1 mm pitch, the electronic

delivers two 90-degree phase shifted rectangular signals A and B. The resolution can be configured up to 8192 increments per pole through the configuration interface of the processing unit. In a typical application like the experimental setup, the resolution is set to 200 increments per pole i.e. the sensor's resolution is  $5\mu\text{m}$ . The sensor provides the longitudinal position for the vehicle position control and reference information for the field oriented control (FOC) method. In addition, the time derivative of the vehicle position is used as the feedback value for the speed control loop.

The three phase supply currents in the output of one inverter module are measured by current sensors. The current sensors used in the experimental setup are current transducers LAH 25-NP from LEM, shown in Figure 3.8.c. The sensor has 25A primary nominal current and 25mA secondary nominal current with the accuracy  $\pm 0.3\%$  of the full scale. In the experiment, only two of three phase currents of each inverter module are measured. The two output signals from current sensors are fed to two analogue channels of the IIB. They are amplified, converted to digital values and are sent to the controller of the system. In the controller, the third current of the three phase currents is calculated from the two other current values.



Figure 3.7 Sensors used in the set-up

### 3.2.5. Controller

The controller of the experimental system has the duty to acquire feedback signals from the plant and send the control signals according to control algorithms to the inverter interface board. To simplify the system configuration, the system parameter setting, the control algorithm, the data acquisition etc., a personal computer (PC) is



used as a controller. The PC executes the control function and communicates with the other equipment by an interface card.

The control PC used in the experiment system is a normal commercial computer. As other closed loop control systems, the PC has functions to receive feedback signals from the system plant. The feedback signals consist of three phase currents of inverter modules, the lateral and longitudinal positions of the vehicle and the vehicle's yaw angle. Moreover, the PC receives also reference values from the user interface.

With the feedbacks and references mentioned above, the PC calculates required output currents for linear motor primaries. The required currents are outputs of P and PI control loops implemented in a PC control program. The control loops are standard cascade loops of position controls, speed controls and current controls in the lateral position control, the longitudinal position control and the yaw control. In addition, there are some coupling values added to correct the required currents. The required currents are then realized by corresponding PWM time values, which are then sent to inverter modules for PWM modulations.

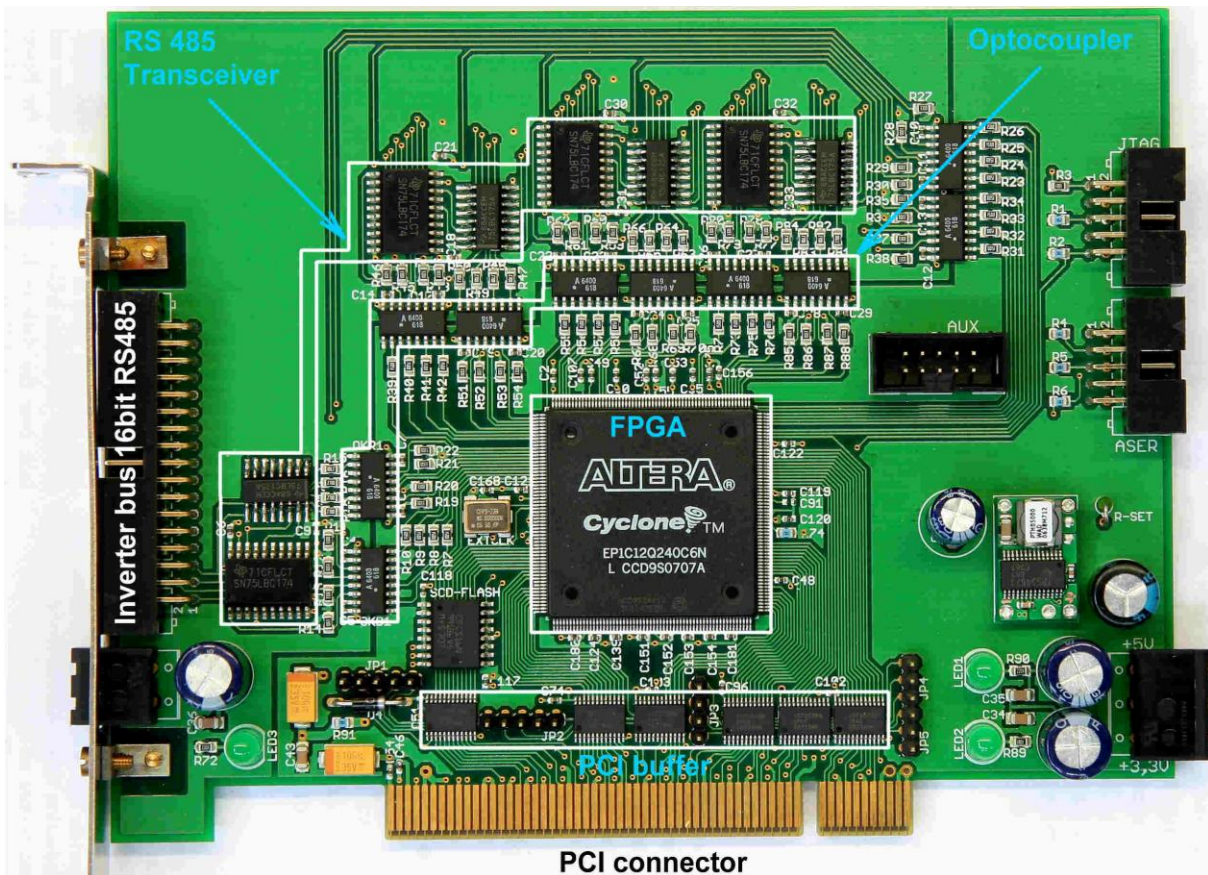


Figure 3.8 Photo of VCI board

In order to perform the communication function for the controller, an auxiliary circuit board is used. The board is a department self-developed product named Vehicle Control Interface (VCI) [54][46], shown in Figure 3.10. The VCI helps the

control PC to transmit and receive information from the IIBs. In addition, it acquires longitudinal position directly from the position sensors. In a control process, the VCI transfers data to each IIB in every  $100\mu s$ . The transfer protocol has a time slot of  $10\mu s$ , so in  $100\mu s$  the VCI can transfer data to maximum 10 IIBs.

## 3.3. Software

### 3.3.1. Operating System

Based on the basic requirements of the experimental setup, Linux operating system has many advantages in comparison with the others. Therefore, Linux was chosen as the operating system for the experimental control PC. The Linux operating system, which is used in the system, is a Vector-Linux Soho distribution using the Kernel 2.6.18.

First, the experimental operating system in this setup must have the ability to support basic software functions. For this requirement, Linux can support:

- Documentary read-write software with Open office, KDE (PDF file reading),
- Analysis Software (Matlab, Scilab),
- Programming Software (C, C++ with GNU compiler, Interface with GTK+, GTKmm, CLX...)

These are all the basic requirements of a control PC for the experimental-execution, documentation and analysis.

Another important characteristic of the control system is the stability and the real-time control. In this aspect, Linux has many advantages in comparison with other operating systems. Because Linux is open-source software, Linux has fewer system crash problems as the others do. On the other hand, Linux has less attack from virus and malware because of its character and number of Linux user. Therefore, Linux is stable operating software. To be open-source software, Linux allows the users interfere with its kernel. Hence, it is easy to implement the real time control applications in Linux by adding a real time extension module to Linux kernel. There are some different approaches to transform Linux into a real-time operating system. In this thesis, the Real-Time Application Interface (RTAI) was used as the solution for the Linux real-time operating system.

### 3.3.2. Real time control software

An important function of the digital control system is the real-time control i.e. the sample time is critical. The real-time control of the experimental setup executes within a sample time. In one sample period, the VCI sends requests to get information of the inverters and the vehicle. The information sent back by the IIBs is transferred to the PC. Last, the PWM timing values for the inverter modules responded from the PC are sent to the IIBs. In the setup, all those real-time control works are implemented by the VCI firmware, the IIB firmware and a RTAI patch [46][54].

The real-time communication of the system is performed by the VCI and IIB firmware. In the communication system, the VCI has functions of the bus master, and the IIBs have functions of bus clients. The bus master and clients implement data transfers in every 100µs. A set of data transfer is implemented in 10µs slot, so the VCI can manage 10 IIBs. All the data then transferred to the control PC by 100µs interrupt subroutines. With the communication, the system can implement a 100µs sampling real-time control.

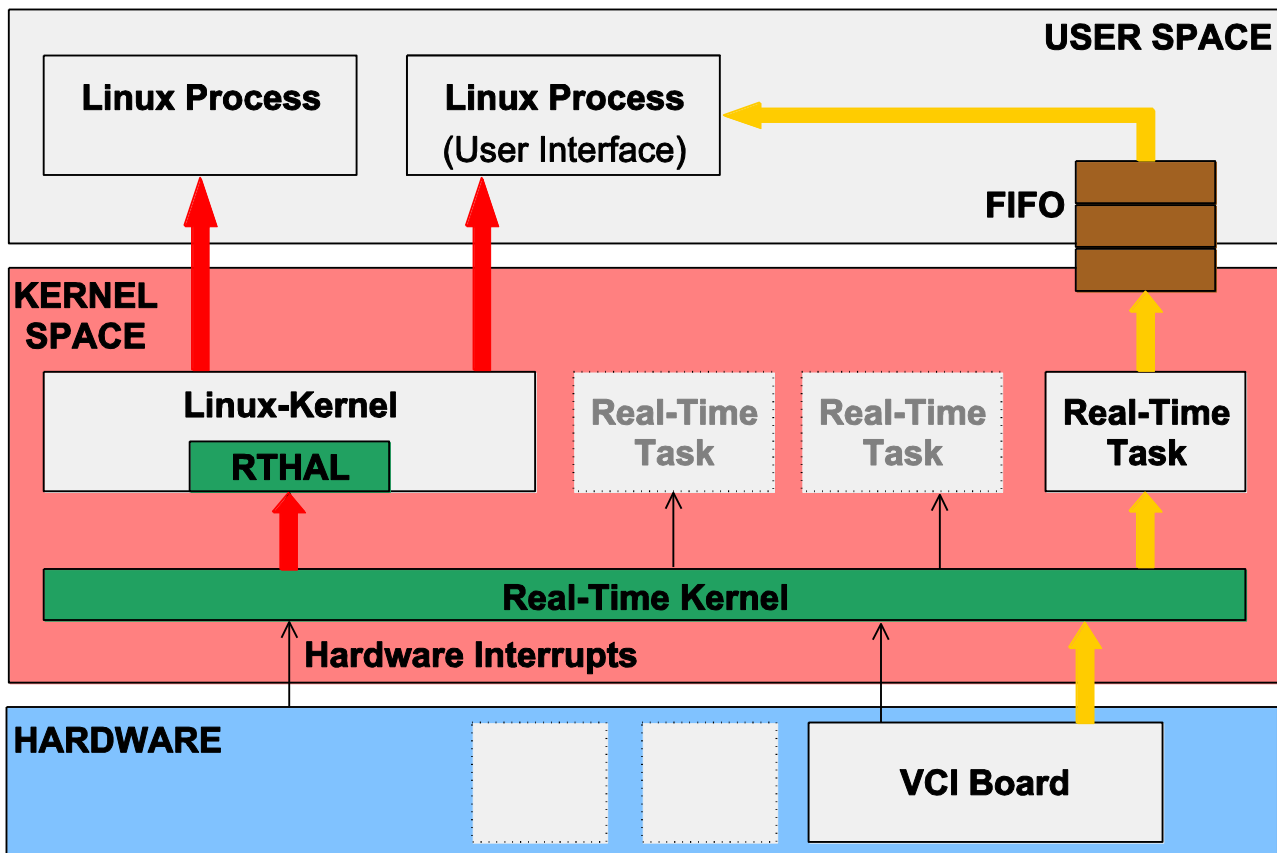


Figure 3.9 Linux RTAI architecture



In addition to the communication system, the real-time is performed by the real-time operating system Linux-RTAI [55]. By adding a patch into the Linux kernel, all the hardware interrupts are transferred directly to the user programme without delay. The system architecture is presented in Figure 3.9. That allows implementing a real-time control programme in the system.

With all the firmware and the software mentioned above, the experimental setup was implemented a real-time control system. The complete system is presented in photos in Figure 3.10.

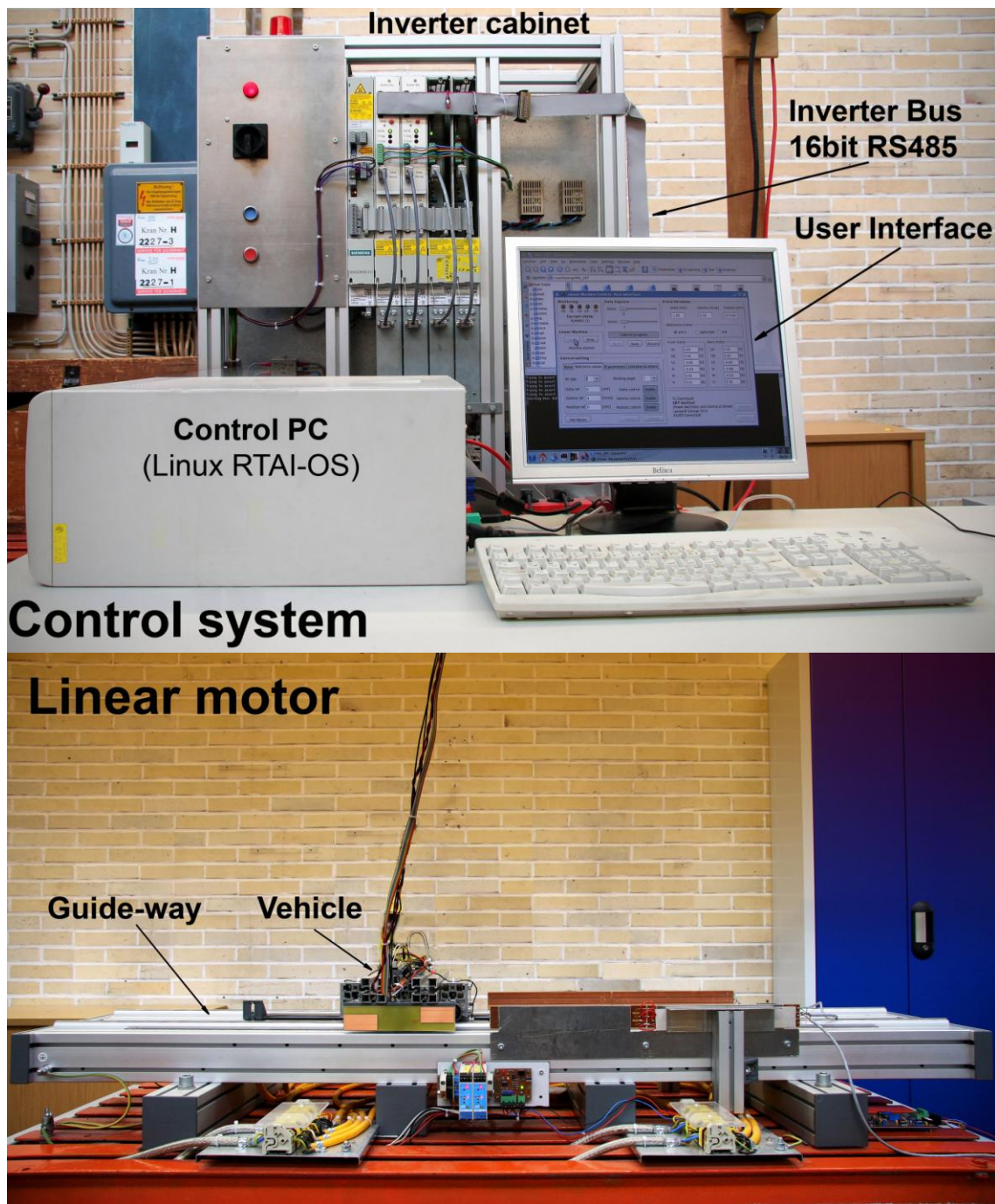


Figure 3.10 Complete experimental system

## 4. MATHEMATICAL MODEL

The mathematical model is the basic requirement for the analysis of the experimental system, the simulation and the controller designs. In this chapter, the geometrical and physical-characteristics of the experimental system are analyzed and presented in equations. The results are then compared with the Finite Element Method (FEM) simulation results and experimental measurements.

### 4.1. The magnetic guidance LSM model

#### 4.1.1. The experimental system in the horizontal plane

As in the experimental structure presented in chapter 3, the vehicle can freely move on the horizontal plane formed by the guiding rails while the vertical movement is constrained. With that structure, the setup can be simply presented in the horizontal plane by a geometrical figure as presented in Figure 4.1. In that figure, the main parameters of the experimental setup and also forces and torques acting on the vehicle are presented.

The figure describes the vehicle simply as a light blue rectangle. The sections of the secondary (magnet) are depicted by black lines on both sides. The two parallel red lines represent the primary sections. All geometrical parameters of the experimental system required for the model analysis and calculation are presented in corresponding symbols. The orange rectangle shows the desired position of the vehicle in the control process. At that position, the vehicle is in the middle and parallel with the guide-way i.e. the left-side air-gap ( $d_{LL}$ ) and the right-side air-gap ( $d_{LR}$ ) are equal, or the vehicle's centerline coincides with the guide-way centerline.

In order to determine the vehicle's position, a coordinate system  $xOy$  is used, as shown in the Figure 4.1. The origin of the coordinate system is placed on the centerline of the guide-way. The vertical axis ( $Ox$ ) is parallel to the guide-way, and the horizontal axis ( $Oy$ ) is perpendicular to the guide-way. The vehicle's center position is referred to this coordinate system. The center position of the vehicle referred to  $Oy$  axis is called lateral position ( $\delta$ ). The center position referred to  $Ox$  axis is called longitudinal position ( $x$ ). The angle between the vehicle's centerline and the guide-way's centerline is called yaw angle ( $\gamma$ ). The aim of the control process is to control the lateral position and the yaw angle to zero ( $\delta=0$ ,  $\gamma=0$ ) and to change the longitudinal position  $x$  according to control requirements.



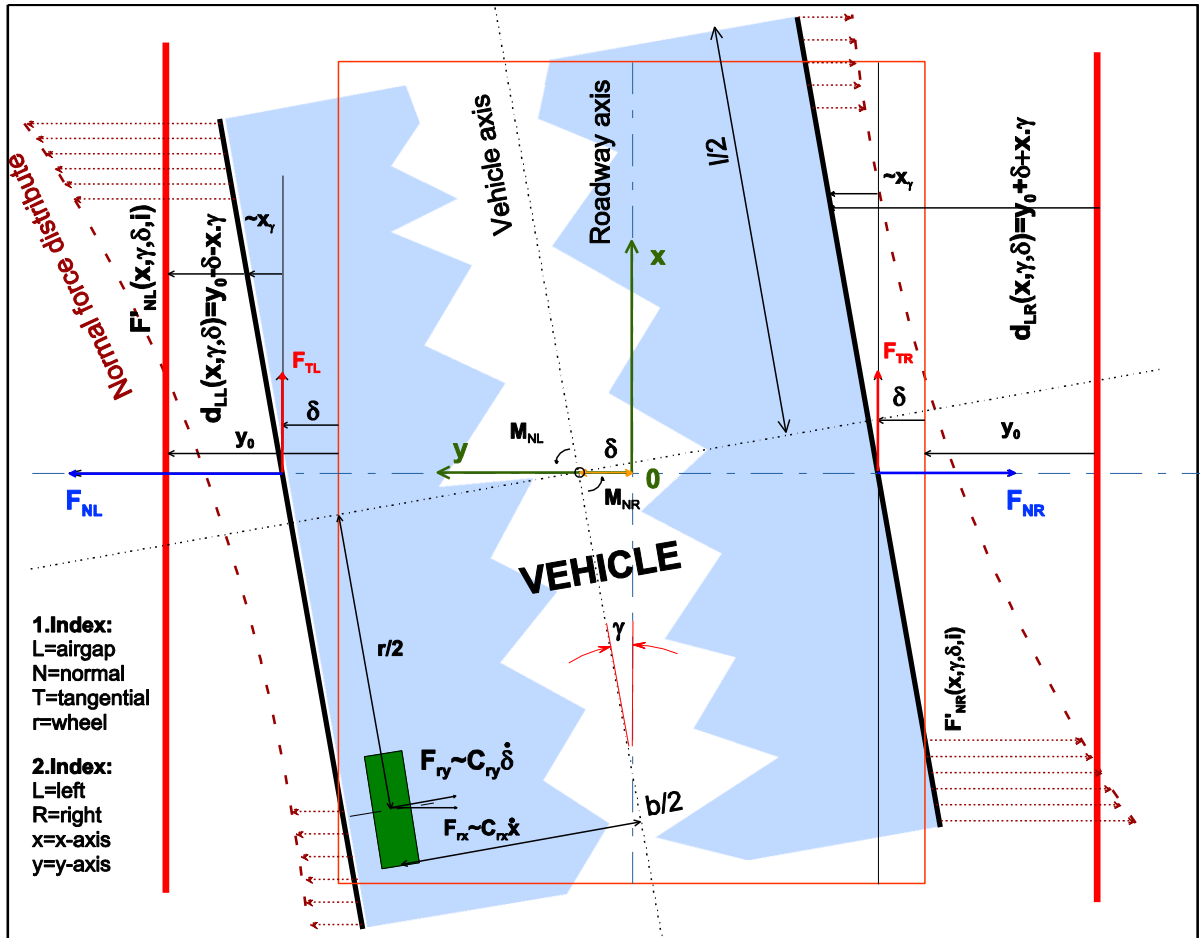


Figure 4.1 Forces and Torques on the vehicle

### 4.1.2. Forces and torque on the vehicle

Except the vertical forces, which are constrained by the rails, all the other forces acting on the vehicle are presented in Figure 4.1. All these forces make the vehicle move and rotate in the horizontal plane. Therefore, the performance and analysis of these forces and torque are necessary in order to design suitable controllers for the vehicle.

In parallel to the guide-way, the tangential forces comprise the left-side tangential force ( $F_{TL}$ ) and the right-side tangential force ( $F_{TR}$ ). They are formed by the interaction between the magnets and the three-phase currents. The intensities of these forces depend on the magnets, the air-gap between primary sections and secondary sections and the primary currents. Consequently, these forces can be controlled by changing the currents in order to push and pull the vehicle in the  $Ox$  direction. In addition, the torque generated by these tangential forces can be used to control the yaw angle of the vehicle.

The forces, which are perpendicular to the guide-way, are named normal forces. These forces have opposite direction on the  $Oy$  axis with  $F_{NL}$  on the left side and with  $F_{NR}$  on the right side. Each normal force here includes three components: the normal force caused by the permanent magnet on the primary iron; the normal force caused by the primary currents on the back iron; and the normal force caused by the primary currents on the permanent magnet. The first component depends on the magnet and the air-gap ( $d_{LL}$  and  $d_{LR}$ ). It is uncontrollable and need to be compensated in the control process. The second and third components are dependent on the currents and the air-gap. They can be varied by controlling the primary currents. Hence, the vehicle's movement in  $Oy$  direction can be controlled by the two current dependent components of the normal forces.

An uncontrolled torque appears on the vehicle when the vehicle is not parallel to the guide-way. In this condition, the air-gap between the magnet and primary section is not homogeneous along the magnet's length. Consequently, the normal force distribution, which depends on the air-gap at each position, is varying along the magnet's length as presented in Figure 4.1 by brown curve. This produces the torque  $M_{NL}$  and  $M_{NR}$  on the vehicle. This torque can be compensated by the difference in thrust forces as mentioned above.

## 4.2. Forces and torque calculation

As a result of the progress in the field of power and signal processing electronic, the field oriented control (FOC) is applied widely in the alternating current (AC) motor drives. FOC techniques realized by fast microprocessors have made possible applications of induction-motor and synchronous motor drives for high-performance applications. Therefore, in this thesis, the FOC method [56][57][58] is used to analyze the linear motors and control the linear motor system like in the case of rotating drives. The control is based on projections, which transform a three-phase coordinate system into a two coordinate ( $d$  and  $q$  coordinates) system moving with the PM of the machine.

In the following analysis, all calculations of the forces and torque are based on three-phase currents transformed to a current vector in the  $dq$  coordinate system in order to reduce the number of variables of the experimental setup. This simplifies the calculations and cut down the number of controllers of current control loops (from 3 to 2). The projection of a three phase symmetrical component into the  $dq$  coordinates is presented in appendix B1.

### 4.2.1. Current density and flux distribution

The high-accuracy calculation of the forces and torque acting on the vehicle is difficult and requires a lot of computing power. It can be done, nowadays, with high-power computers and simulation software. In order to compute the forces of the linear motor, required for controller parameters design, the calculating process is simplified by several assumptions.

The analysis is done with the structure presented in Figure 4.2. Because both sides

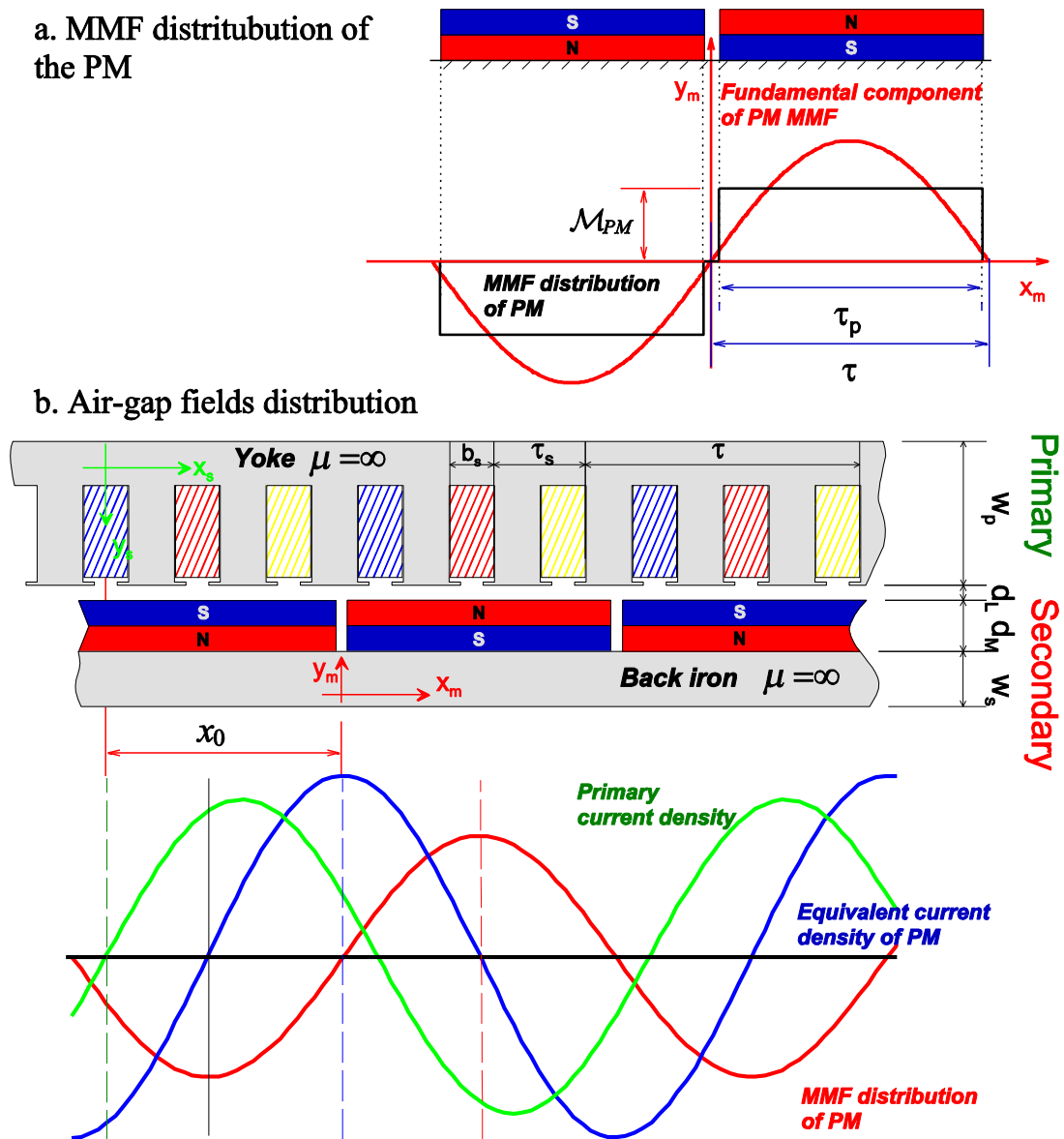


Figure 4.2 Fields distribution in the air-gap of the linear synchronous motor of the vehicle are symmetrical, the analytical structure presents only one side of the vehicle. It can be considered like a single flat linear permanent magnet synchronous motor (LPMSM). The analysis will be referred to two directions ( $x$ ,  $y$ ) and two

coordinate axes  $(x_m 0y_m, x_s 0y_s)$ . The coordinate  $x_s 0y_s$  is the static frame fixed to the linear motor primary and the coordinate  $x_m 0y_m$  is the moving frame, fixed to the permanent magnet of the linear motor.

First, the slotted structure of the LPMSM is simplified by assuming smooth structure, i.e. the primary of the linear motor has isotropic magnetic properties. Moreover, in order to simplify the magnetic circuit calculations, the primary iron and the secondary back iron are assumed to have an infinite permeability ( $\mu_r = \infty$ ). Therefore, the primary permeability is infinite ( $\mu_a \approx \infty$ ), i.e. the primary reluctance is zero. The magnetic circuit is simplified in the area defined by  $d_L + d_M$ , from the primary surface to the secondary back iron surface as shown in Figure 4.2. In addition, the regions containing magnets are considered isotropic, with

$$\mu_{PM} = \mu_M \mu_0 \approx \mu_0 \text{ with } \mu_M \approx 1 \quad (4.1)$$

Second, the field distributions of the linear motor are assumed sinusoidal. Therefore, in the analysis, only the fundamental components of current distributions and magneto motive force (MMF) are considered. With the assumption that the permanent magnet is a constant MMF source as presented in Figure 4.2.a and appendix C2, the fundamental component of MMF distribution  $\mathcal{F}_{1PM}$  caused by the PM is given by

$$\mathcal{F}_{1PM}(x_m) = \frac{4}{\pi} \mathcal{M}_{PM} \sin \frac{\pi \tau_p}{2\tau} \sin \frac{\pi}{\tau} x_m \quad (4.2)$$

where  $\tau$  is the pole pitch,  
 $\tau_p$  is the magnet width,  
 $\mathcal{M}_{PM} = \mathcal{H}_c \cdot d_M$  is the equivalent MMF of the PM per pole,  
 $\mathcal{H}_c$  is coercive force.

The corresponding equivalent current distribution along the longitudinal permanent magnet,  $x$ -axis, is given by

$$\mathcal{A}_{PM}(x_m) = \frac{d\mathcal{F}_{1PM}}{dx_m} = \frac{4}{\tau} \mathcal{M}_{PM} \sin\left(\frac{\pi \tau_p}{2\tau}\right) \cos\left(\frac{\pi}{\tau} x_m\right) \quad (4.3)$$

Consequently, the remanent flux density of the magnet is also assumed to have sinusoidal distribution. It is defined as follows.

$$\mathcal{B}_R(x_m) = \mathcal{B}_{RN} \frac{4}{\pi} \sin\left(\frac{\pi}{\tau} x_m\right) \quad (4.4)$$

where:  $\mathcal{B}_{RN}$  is the actual remanent flux density of the magnets.

To analyze the reaction forces between a primary and a PM, the displacement between the origins of the primary coordinates (static frame  $x_sOy_s$ ) and of the PM coordinates (moving frame  $x_mOy_m$ ) is called  $x_0$ . Hence, the remanent flux density of the magnet presented in the static frame is

$$\mathcal{B}_R(x_s) = \mathcal{B}_{RN} \frac{4}{\pi} \sin\left(\frac{\pi}{\tau}(x_s - x_0)\right) \quad (4.5)$$

where:  $x_s = x_m + x_0$ ,

$x_0$  is the displacement between origin points of the static and the moving frames as shown in Figure 4.2.

Third, the calculations with the entire harmonic of the MMF are complicated, and they take a lot of computing time. They are necessary only in the linear motor design calculations in order to optimal the power losses, the ripple, the noise, etc. However, with the aim to design controllers, only the fundamental component of the MMF time-space distribution is used for forces and torque analyses in this dissertation. Hence, the analysis assumes that only the fundamental component of the primary MMF generates forces on the secondary.

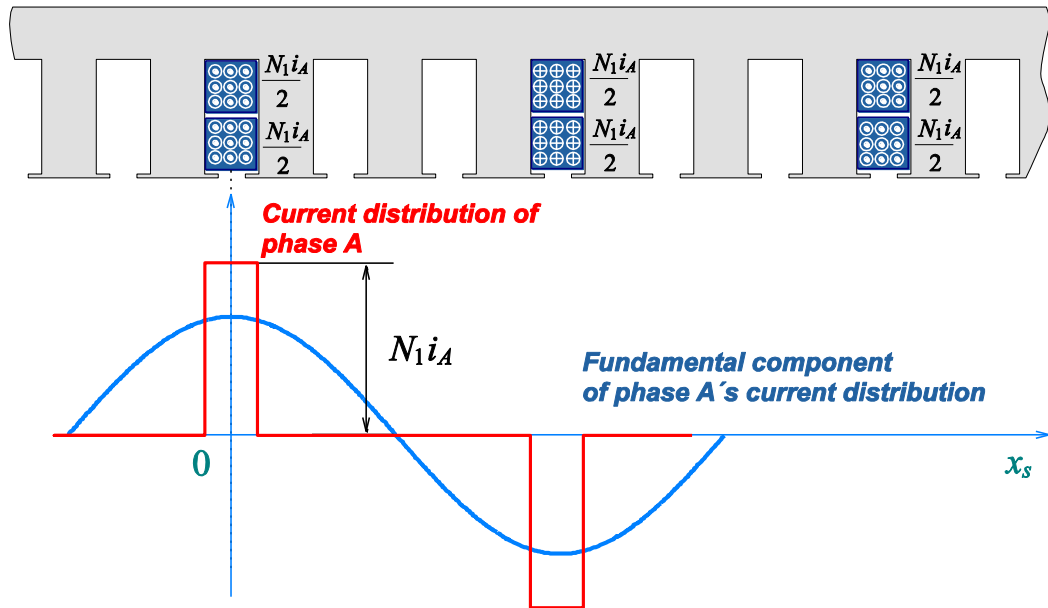


Figure 4.3 MMF generated by one phase current.

The fundamental current distribution of the primary in one phase (phase A) is presented in Figure 4.3, and the fundamental components of the three-phase current distributions are expressed in equations (4.6)-(4.8).

$$\mathcal{A}_A(x_s) = \frac{2N_1 i_A}{\pi} k_{\omega 1} \cdot \cos\left(\frac{\pi}{\tau} x_s\right) \quad (4.6)$$

$$\mathcal{A}_B(x_s) = \frac{2N_1 i_B}{\pi} k_{\omega 1} \cdot \cos\left(\frac{\pi}{\tau} x_s - \frac{2\pi}{3}\right) \quad (4.7)$$

$$\mathcal{A}_C(x_s) = \frac{2N_1 i_C}{\pi} k_{\omega 1} \cdot \cos\left(\frac{\pi}{\tau} x_s - \frac{4\pi}{3}\right) \quad (4.8)$$

where  $i_A, i_B, i_C$ : are instantaneous values of the primary currents,  
 $N_1$ : is the number of series turns per primary slot,  
 $k_{\omega 1}$ : is the winding factor at fundamental wave,  
 $\tau$ : is the pole pitch.

In general, the three-phase currents are arbitrary. However, in this thesis, the three phase currents are modulated by the field oriented control (FOC) method i.e. the three phase currents are transformed from a  $dq$  current vector without zero component by inverse Park's transformation as it is presented in appendix B2. The fundamental component of the primary current distribution is the algebraic sum of the three-phase current distributions, as presented in (4.9).

$$\begin{aligned} \mathcal{A}_a(x_s) &= \mathcal{A}_A(x_s) + \mathcal{A}_B(x_s) + \mathcal{A}_C(x_s) \\ &= \frac{2N_1 i_a}{\pi} \cdot \cos(\theta_s) \cdot k_{\omega 1} \cdot \cos\left(\frac{\pi}{\tau} x_s\right) \\ &\quad + \frac{2N_1 i_a}{\pi} \cdot \cos\left(\theta_s - \frac{2\pi}{3}\right) \cdot k_{\omega 1} \cdot \cos\left(\frac{\pi}{\tau} x_s - \frac{2\pi}{3}\right) \\ &\quad + \frac{2N_1 i_a}{\pi} \cdot \cos\left(\theta_s - \frac{4\pi}{3}\right) \cdot k_{\omega 1} \cdot \cos\left(\frac{\pi}{\tau} x_s - \frac{4\pi}{3}\right) \end{aligned} \quad (4.9)$$

where  $i_a$  is the instantaneous value of the primary current vector,  
 $\theta_s$  is the instantaneous phase of the primary currents in the static frame.

Reducing the right expression of the equation (4.9), a simple current distribution equation is presented in (4.10).

$$\begin{aligned} \mathcal{A}_a(x_s) &= \frac{2N_1 i_a k_{\omega 1}}{\pi} \cdot \frac{1}{2} \left\{ \cos\left(\theta_s + \frac{\pi}{\tau} x_s\right) + \cos\left(\theta_s - \frac{\pi}{\tau} x_s\right) \right. \\ &\quad \left. + \cos\left(\theta_s + \frac{\pi}{\tau} x_s - \frac{4\pi}{3}\right) + \cos\left(\theta_s - \frac{\pi}{\tau} x_s\right) \right. \\ &\quad \left. + \cos\left(\theta_s + \frac{\pi}{\tau} x_s - \frac{8\pi}{3}\right) - \cos\left(\theta_s - \frac{\pi}{\tau} x_s\right) \right\} \\ &= \frac{3N_1 i_a k_{\omega 1}}{\pi} \cos\left(\theta_s - \frac{\pi}{\tau} x_s\right) \end{aligned} \quad (4.10)$$

The fundamental component of primary current distribution can be rewritten in the moving frame  $x_m 0 y_m$  by

$$\mathcal{A}_{1a}(x_m) = \frac{3N_{1a}k_{\omega 1}}{\tau} \cos(\theta_m - \frac{\pi}{\tau}x_m) \quad (4.11)$$

where:  $\theta_m = \theta_s - \frac{\pi}{\tau}x_0$  is phase of the current distribution in the moving frame.

In order to calculate the fundamental component of the MMF, the primary core is assumed non-saturating. Therefore, the MMFs generated by the fundamental current density are sinusoidal, and the primary MMF has a relationship with the current density as in equation (4.12).

$$\mathcal{A}_{1a}(x_s) = \frac{d\mathcal{F}_{1a}(x_s)}{dx_s} \quad (4.12)$$

Consequently

$$\mathcal{F}_{1a}(x_s) = \int \mathcal{A}_{1a} dx_s = -\frac{3N_{1a}k_{\omega 1}}{\tau} \sin(\theta_s - \frac{\pi}{\tau}x_s) + C \quad (4.13)$$

The integration constant  $C$  is determined the condition of Gauss's law for magnetism; the integral of the flux along the air-gap is zero. In the next subsection, the MMF  $\mathcal{F}_{1a}(x_s)$  will be used to calculate flux along the air-gap. Solving the Gauss's equation for the magnetism in the air-gap will give the value of  $C$ .

### 4.2.2. Magneto motive force and flux in the air-gap

In Figure 4.4 the simplified model of one side of the linear motor, based on the current distribution (current coverage), is presented. In this figure, the current coverage wave  $\mathcal{A}$  and the MMF wave  $\mathcal{F}$  along the x-axis are represented in red and green color respectively. The secondary flux density wave  $\mathcal{B}_R$  is represented in blue color.

In this model, the two axes as mentioned above are used: the  $x_s$ -axis in the primary and the  $x_m$ -axis in the secondary. The secondary displacement ( $x_0$ ) defines the distance between the origin of both axes:

$$x_m = x_s - x_0 \quad (4.14)$$

(for the  $x_s$  to  $x_m$  axis transformation the angle of the secondary will be neglected)

Using the simplified model, the MMF and flux in the air-gap are defined and calculated as following.

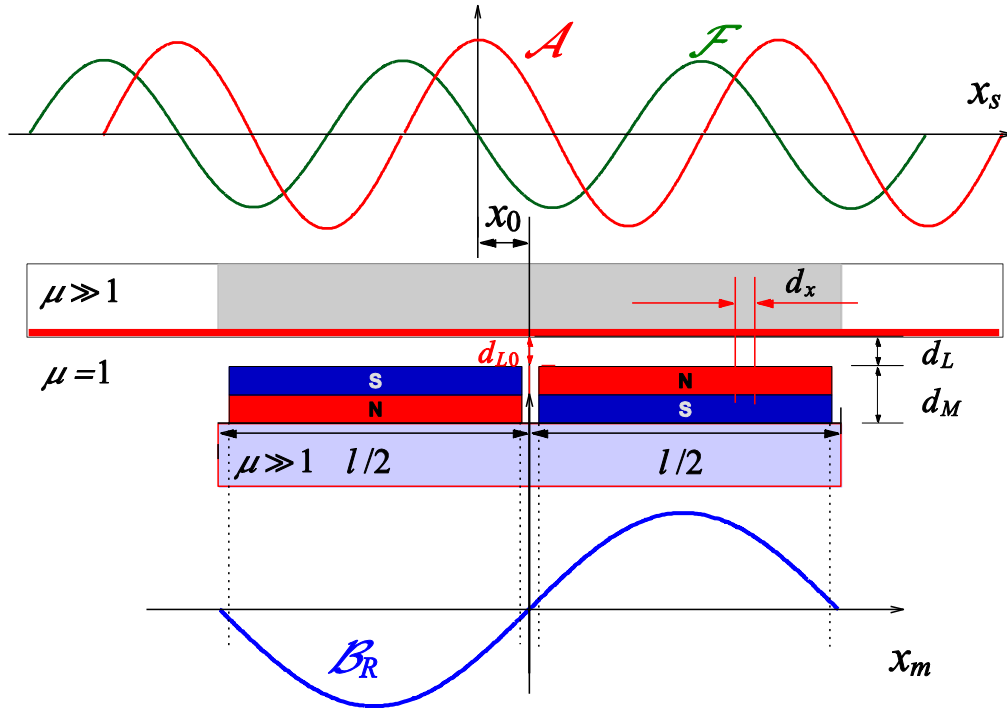


Figure 4.4 Simplified model of one side of the linear motor, based on the current density.

**a. The air-gap**

The air-gap along the  $x_m$ -axis is the function of position:

$$d_L \ x_m = d_{L0} + m \cdot x_m \quad \text{with} \quad -p\tau \leq x_m \leq p\tau \quad (4.15)$$

where  $d_{L0}$  is the air-gap at the center of the secondary,  $m$  is the slope of the secondary ( $m = \sin \gamma$ ) and  $l = 2p\tau$  is the length of the secondary. The values of  $d_{L0}$  and  $m$  are limited to the condition where the secondary hits the primary, i.e. it must be  $d_L \ x_m \geq 0$ .

The air-gap referred to the  $x_s$ -axis yields:

$$d_L \ x_s = d_{L0} + m \cdot (x_s - x_0) \quad \text{with} \quad -p\tau \leq x_s - x_0 \leq p\tau \quad (4.16)$$

**b. Flux of the air-gap and secondary**

The flux in the air-gap is assumed similar to free vacuum space all along the primary and the permeability of the primary and secondary yoke is assumed  $\mu \approx \infty$ . Then, the air-gap flux density is,

$$\mathcal{B}_L = \mu_0 \mathcal{H}_L \quad (4.17)$$

and the flux density in the magnet is,

$$\mathcal{B}_M = \mathcal{B}_R(x) + \mu_0 \mu_M \mathcal{H}_M \quad (4.18)$$



Where  $\mathcal{H}_L$  and  $\mathcal{H}_M$  are the air-gap and PM magnetizing field, respectively,  $\mu_0$  is the vacuum permeability, and  $\mu_M$  is the PM's relative permeability. Due to the former assumptions,

$$\mathcal{B}_M = \mathcal{B}_L \quad (4.19)$$

Assuming a differential slice of the magnetic system (motor) shown in Figure 4.4, having a width  $dx$ , an equivalent magnetic circuit can be considered as shown in Figure 4.5 ( $\phi$  denotes flux,  $\mathcal{R}$  reluctance and  $h_z$  the stack height).

The MMF over the air-gap and the magnet is:

$$\mathcal{F} x_s = d_L x_s \mathcal{H}_L + d_M \mathcal{H}_M \quad (4.20)$$

By substituting (4.17) and (4.18) into (4.20), it yields

$$\mathcal{F} x_s = \frac{d_L x_s}{\mu_0} \mathcal{B}_L + \frac{d_M}{\mu_0 \mu_M} \mathcal{B}_L - \mathcal{B}_R x_s \quad (4.21)$$

Solving the equation (4.21) for the air-gap flux density, the result is

$$\mathcal{B}_L x_s = \frac{\mathcal{F}(x_s) \mu_M \mu_0 + d_M \mathcal{B}_R(x_s)}{\mu_M d_L(x_s) + d_M} \quad (4.22)$$

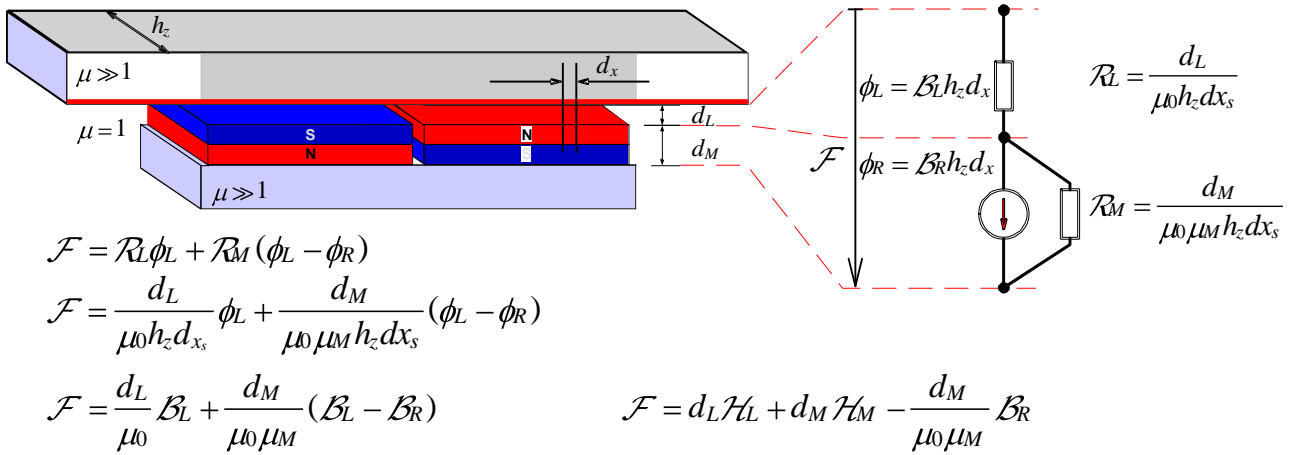


Figure 4.5 Equivalent magnetic circuit.

Now, as mentioned earlier, the integral of the flux along the air-gap must be zero, i.e.

$$\int_{-p\tau+x_0}^{+p\tau+x_0} \mathcal{B}_L(x_s) dx_s = 0 \quad (4.23)$$

The air-gap MMF ( $\mathcal{F}$ ) equals the MMF generated by the fundamental current density shown in (4.13). Therefore, by using  $\mathcal{F} = \mathcal{F}_{1a}$  in (4.22) and substituting into (4.23), the equation (4.23) can be solved in order to obtain the integration constant  $C = f(\gamma, \theta_s)$ . For a constant air-gap, i.e.  $m=0$ , it results in  $C=0$ . For non-constant air-gaps, the closed form of  $C$  is too complex. Thus, the numerical computation is a

good solution for solving the equation (4.23). Moreover, the yaw angle  $\gamma$  of the experimental system changes in a small boundary because of the mechanical limit. Hence,  $m$  is assumed zero, i.e. yaw angle is neglected, in the following mathematical analysis in order to simplify the calculation.

### 4.2.3. Magnetic energy and force calculation

The force, in this subsection, will be computed by a virtual work principle on a  $x$ -differential slice of the motor.

Generally, the energy stored in a magnetic field is defined by the volume integral

$$w = \frac{1}{2} \int \mathcal{H} \mathcal{B} dv \quad (4.24)$$

Based on the calculation in subsection 4.2.2, the assumption (4.1) and the neglect of the yaw angle effect on the air-gap  $d_L(x_s)$  (assume  $m=0$ ), the air-gap flux density is represented by

$$\mathcal{B}_L(x_s) = \frac{\mathcal{F}(x_s)\mu_0 + d_M \mathcal{B}_R(x_s)}{d_{L0} + d_M} \quad \text{with } \mu_M = 1 \quad (4.25)$$

The magnetic energy on a differential slice along the  $x_s$ -axis calculated following (4.24) and (4.25) is:

$$\begin{aligned} dw &= \frac{1}{2} \iint \mathcal{H}_L \mathcal{B}_L dy_s dx_s + \frac{1}{2} \iint \mathcal{H}_M (B_L - B_R(x_0)) dy_s dx_s \\ &= \frac{1}{2} h_z (\mathcal{H}_L \mathcal{B}_L d_L + \mathcal{H}_M (B_L - B_R(x_0)) d_M) dx_s \end{aligned} \quad (4.26)$$

where  $h_z$  is the magnetic stack width

$B_R(x_0)$  is the remanent flux density defined in (4.5) as the function of  $x_0$ .

The density (per length unit) of the magnetic energy is:

$$w' = \frac{dw}{dx_s} = \frac{1}{2} h_z (\mathcal{H}_L \mathcal{B}_L d_L + \mathcal{H}_M (B_L - B_R(x_0)) d_M) \quad (4.27)$$

Substituting  $\mathcal{H}_L$  and  $\mathcal{H}_M$  in (4.17)-(4.18) to (4.27), it yields:

$$w' = \frac{1}{2\mu_0} h_z (\mathcal{B}_L^2 d_L + (B_L - B_R(x_0))^2 d_M) \quad (4.28)$$

The force densities (per length unit) are obtained by derivations of (4.28) with respect to the movement directions and in constant flux condition. For the longitudinal movement  $x_0$  along  $x_s$ -axis, it yields the tangential force density:

$$F'_T = -\left. \frac{dw'}{dx_0} \right|_{\mathcal{B}_L = \text{const}} = \frac{h_z d_M}{\mu_0} \mathcal{B}_L - \mathcal{B}_R \frac{d\mathcal{B}_r}{dx_0} \quad (4.29)$$

$$F'_T = -\frac{h_z d_M}{\mu_0} \mathcal{B}_L - \mathcal{B}_R \mathcal{B}_{RN} \frac{4}{\tau} \cos\left((x_s - x_0) \frac{\pi}{\tau}\right) \quad (4.30)$$

And for the lateral movement  $d_L$ , it yields the normal force density:

$$F'_N = -\left. \frac{dw'}{dd_L} \right|_{\mathcal{B}_L = \text{const}} = -\frac{h_z}{2\mu_0} \mathcal{B}_L^2 \quad (4.31)$$

The total tangential and normal force on one side of the motor is obtained by integrating (4.30)-(4.31) along the active area of the stator:

$$F_T = p \int_{x_0-\tau}^{x_0+\tau} F'_T dx_s = \frac{12p \mathcal{B}_{RN} N_1 d_M h_z k_{\omega 1} i_a}{\pi d_L + d_M} \sin\left(\theta_s - \frac{\pi}{\tau} x_0\right) \quad (4.32)$$

$$F_N = p \int_{x_0-\tau}^{x_0+\tau} F'_N dx_s = -\frac{ph_z \tau}{2\pi^2 \mu_0 d_L + d_M} \times \left(16 \mathcal{B}_{RN}^2 d_M^2 + 9 N_1^2 \mu_0^2 k_{\omega 1}^2 i_a^2 + 24 \mathcal{B}_{RN} d_M k_{\omega 1} \mu_0 i_a \cos\left(\theta_s - \frac{\pi}{\tau} x_0\right)\right) \quad (4.33)$$

The equations (4.32) and (4.33) are represented simply with constant values  $K_1$ ,  $K_2$ ,  $K_3$ ,  $K_4$  in follows.

$$F_T = \frac{K_4}{d_L + d_M} i_a \sin\left(\theta_s - \frac{\pi}{\tau} x_0\right) = \frac{K_4}{d_L + d_M} i_q \quad (4.34)$$

$$F_N = \frac{1}{(d_L + d_M)^2} \left( K_3 + K_1 i_a^2 + K_2 i_a \cos\left(\theta_s - \frac{\pi}{\tau} x_0\right) \right) \\ = \frac{1}{(d_L + d_M)^2} K_3 + K_1 (i_d^2 + i_q^2) + K_2 i_d \quad (4.35)$$

Where  $i_d = i_a \cos\left(\theta_s - \frac{\pi}{\tau} x_0\right)$ ,  $i_q = i_a \sin\left(\theta_s - \frac{\pi}{\tau} x_0\right)$ ,

and

$$K_1 = \frac{9}{2\pi^2} N_1^2 k_{\omega 1}^2 h_z p \tau \mu_0, \quad K_2 = \frac{12}{\pi^2} \mathcal{B}_{RN} d_M N_1 k_{\omega 1} h_z p \tau,$$

$$K_3 = \frac{8}{\pi^2 \mu_0} \mathcal{B}_{RN}^2 d_M^2 h_z p \tau, \quad K_4 = \frac{12}{\pi} \mathcal{B}_{RN} d_M k_{\omega 1} N_1 h_z p.$$

#### 4.2.4. Linearization of the force and torque equations

The forces on equation (4.34) and (4.35) are a non-linear function of the variables: the air-gap ( $d_L$ ) and the primary currents. In order to develop a control block diagram and to design suitable controllers, it is useful to linearize the equations regarding to the movement of the vehicle in longitudinal direction ( $x$ -direction) and lateral direction ( $y$ -direction).

##### a. The total normal force

As represented in Figure 4.1, the variation of the lateral position  $\delta$  causes the changing of the left and the right air-gaps in opposite direction. Therefore, the linearization below is executed separately for the left and right sides regarding to the change of the lateral position.

##### Calculation for the right side

Replacing variables in (4.35) with the variables of the right side and with the right air-gap  $d_{LR} = y_0 + \delta$  the linearized right normal force is

$$\begin{aligned} F_{NR,lin} &= F_{NR}|_{\delta=0} + \left. \frac{\partial F_{NR}}{\partial \delta} \right|_{\delta=0} \delta \\ &= K_3 + K_1 i_{aR}^2 + K_2 i_{dR} \left( \frac{1}{(y_0 + d_M)^2} - \frac{2\delta}{(y_0 + d_M)^3} \right) \end{aligned} \quad (4.36)$$

##### Calculation for the left side

In the same way, the linearized normal force of the left side is calculated with the left variables and the left air-gap  $d_{LL} = y_0 - \delta$ .

$$\begin{aligned} F_{NL,lin} &= F_{NL}|_{\delta=0} + \left. \frac{\partial F_{NL}}{\partial \delta} \right|_{\delta=0} \delta \\ &= K_3 + K_1 i_{aL}^2 + K_2 i_{dL} \left( \frac{1}{(y_0 + d_M)^2} + \frac{2\delta}{(y_0 + d_M)^3} \right) \end{aligned} \quad (4.37)$$

where:  $F_{Nx,lin}$  are the linearized normal forces of (L) left side, (R) right side,  
 $i_{dx}$ ,  $i_{qx}$  are the  $dq$ -currents of left- and right-primary,  
 $i_{ax} = \sqrt{i_{dx}^2 + i_{qx}^2}$  are the primary currents of left- and right-primary,  
 $y_0$  is the air-gap of left- and right-side, when the vehicle is in the middle of the guide-way.

The total normal force acting on the vehicle is the difference of normal forces on the left- and right-side in opposite directions. From equation (4.36) and equation (4.37), the total normal force acting upon the vehicle is

$$F_{NL,lin} - F_{NR,lin} = \frac{4K_3}{d_M + y_0^3} \delta + \frac{K_1}{d_M + y_0^2} i_{aL}^2 - i_{aR}^2 + \frac{K_2}{d_M + y_0^2} i_{dL} - i_{dR} \\ + \frac{2K_1}{d_M + y_0^3} i_{aL}^2 + i_{aR}^2 \delta + \frac{2K_2}{d_M + y_0^3} i_{dL} + i_{dR} \delta$$

And presented in a simple way

$$F_{NL,lin} - F_{NR,lin} = C_{FN1} \delta + C_{FN2} i_{aL}^2 - i_{aR}^2 + C_{FN3} i_{dL} - i_{dR} \\ + C_{FN4} i_{aL}^2 + i_{aR}^2 \delta + C_{FN5} i_{dL} + i_{dR} \delta \quad (4.38)$$

where:  $C_{FN1} = \frac{4K_3}{d_M + y_0^3}$ ;  $C_{FN2} = \frac{K_1}{d_M + y_0^2}$ ;  $C_{FN3} = \frac{K_2}{d_M + y_0^2}$ ;

$$C_{FN4} = \frac{2K_1}{d_M + y_0^3}$$
;  $C_{FN5} = \frac{2K_2}{d_M + y_0^3}$ .

### **b. The total thrust and torque**

Besides the normal forces, which are perpendicular to the PM, the tangential forces lie on the surface of the PM and along the guide-way. On the vehicle, the two tangential forces of both sides produce the motion and the rotation of the vehicle on the  $x_0y$  plane. Therefore, the sum of two tangential forces produces a thrust force and the difference of them produces a torque.

As assumed in the previous subsection, the influence of a small yaw angle  $\gamma$  can be neglected. With the yaw angle  $\gamma = 0$ , the air-gap is constant along the longitudinal  $x$ -position, so the tangential forces can be calculated as it is presented in (4.34). Therefore, the thrust forces on both sides are presented simply as

$$F_{TL} = K_4 \frac{i_{qL}}{d_M + y_0 - \delta} \quad (4.39)$$

$$F_{TR} = K_4 \frac{i_{qR}}{d_M + y_0 + \delta} \quad (4.40)$$

where:  $F_{Tx}$  are the thrust forces of left- and right-side.

Using the same linearized process as for normal forces, the linearized tangential forces of left and right sides are

$$F_{TL,lin} = \frac{K_4}{d_M + y_0} i_{qL} + \frac{K_4}{d_M + y_0}^2 i_{qL} \delta \quad (4.41)$$

$$F_{TR,lin} = \frac{K_4}{d_M + y_0} i_{qR} - \frac{K_4}{d_M + y_0}^2 i_{qR} \delta \quad (4.42)$$

The equations (4.41) and (4.42) are simplified by means of the constant coefficients:

$$C_{FT1} = \frac{K_4}{d_M + y_0}; \quad C_{FT2} = \frac{K_4}{d_M + y_0}^2$$

The thrust force and the torque impact on the vehicle are the functions of difference and sum of linearized tangential forces presented by

$$F_{TL,lin} - F_{TR,lin} = C_{FT1} i_{qL} - i_{qR} + C_{FT2} i_{qL} + i_{qR} \delta \quad (4.43)$$

$$F_{TL,lin} + F_{TR,lin} = C_{FT1} i_{qL} + i_{qR} + C_{FT2} i_{qL} - i_{qR} \delta \quad (4.44)$$

All the linearized equations in this subsection are used in the next chapter in order to design controllers for the experimental system.

### 4.3. Equations of motion

In following, equations of motion are the basic dynamic equations of the vehicle presented in the Figure 4.1. With all the forces acting on the vehicle, which are defined in section 4.2, the dynamic equations of vehicle's motion can be presented in three degrees of freedom like below:

$$\text{Yaw rotating motion: } \Theta \ddot{\gamma} = -\frac{b}{2} F_{TL} - F_{TR} - \frac{r}{2} 4F_{rr} \quad (4.45)$$

$$\text{Lateral motion: } m \ddot{\delta} = F_{NL} - F_{NR} - 4F_{ry} \quad (4.46)$$

$$\text{Longitudinal motion: } m \ddot{x} = F_{TL} + F_{TR} - 4F_{rx} \quad (4.47)$$

where:  $\Theta$ : is the moment of inertia of the vehicle,  
 $m$ : is the mass of the vehicle,  
 $b$ : is the width of the vehicle,  
 $r$ : is the distance from the centre of the vehicle to the wheels,  
 $F_{rr}$ ,  $F_{rx}$ ,  $F_{ry}$ : Friction forces in rotation,  $x$ - and  $y$ -axis.

## 4.4. FEM simulation

### 4.4.1. Finite element method

The finite element method (FEM) [60] is a numerical technique for finding approximate solutions of partial differential equations (PDE) as well as of integral equations. The solution approach is based either on eliminating the differential equation completely (steady state problems), or discretizing the PDE into an approximating system of ordinary differential equations, which are then numerically integrated using standard techniques such as Euler's method, Runge-Kutta, etc. With that characteristic, the method is useful to solve many technical problems, including electromagnetic problems. In this section, the electromagnetic forces on the vehicle are simulated by Maxwell 2D program.

In solving PDE, the main challenge is to produce an equation that approximates the equation needs to be studied. However, the solution of the equation has to be numerically stable, i.e. errors in the input and intermediate calculations do not accumulate and do not cause the resulting output to be meaningless. The FEM is a good selection for solving partial differential equations over complicated domains like the electromagnetic one. Therefore, the FEM together with real experimental measurement was used in this research in order to verify the reliability of the theoretical calculations above.

Maxwell® is the premier electromagnetic field simulation software from Ansoft for engineers tasked with designing and analyzing 3-D and 2-D electromagnetic and electromechanical devices such as motors, actuators, transformers, sensors and coils [59]. Maxwell uses the accurate finite element method to solve static, frequency-domain and time varying electromagnetic and electric fields. A key benefit of Maxwell is its automated solution process where users are only required to specify geometry, material properties and the desired output. From this point, Maxwell will automatically generate an appropriate, efficient and accurate mesh for solving the problem. This proven automatic adaptive meshing process removes complexity from the analysis process and allows engineers to benefit from a highly efficient, easy-to-use design flow. For these reasons, the simulation used Maxwell 2D for analyzing the electromagnetic forces influencing the vehicle of the designed experimental setup. The analytical work is simplified by supplying the software with the geometries and the material properties of the experimental machine, which are presented in chapter 3.

### 4.4.2. FEM model of the experimental setup

The geometries of the simulation are taken from the real parameters of the experimental setup in Table 3.1. With these parameters, a FEM model was drawn in Maxwell 2D as shown in Figure 4.6. Instead of regarding many particular parts of the experimental machine as presented in chapter 3, the simulation figure here concentrates only the electromagnetic parts, which generate the magnetic forces on the vehicle. They are the PMLSM primaries and secondary. The primaries consist of the primary iron and the primary winding mounted on the guide-way. The secondary consist of the PMs and the back iron mounted on both sides of the vehicle.

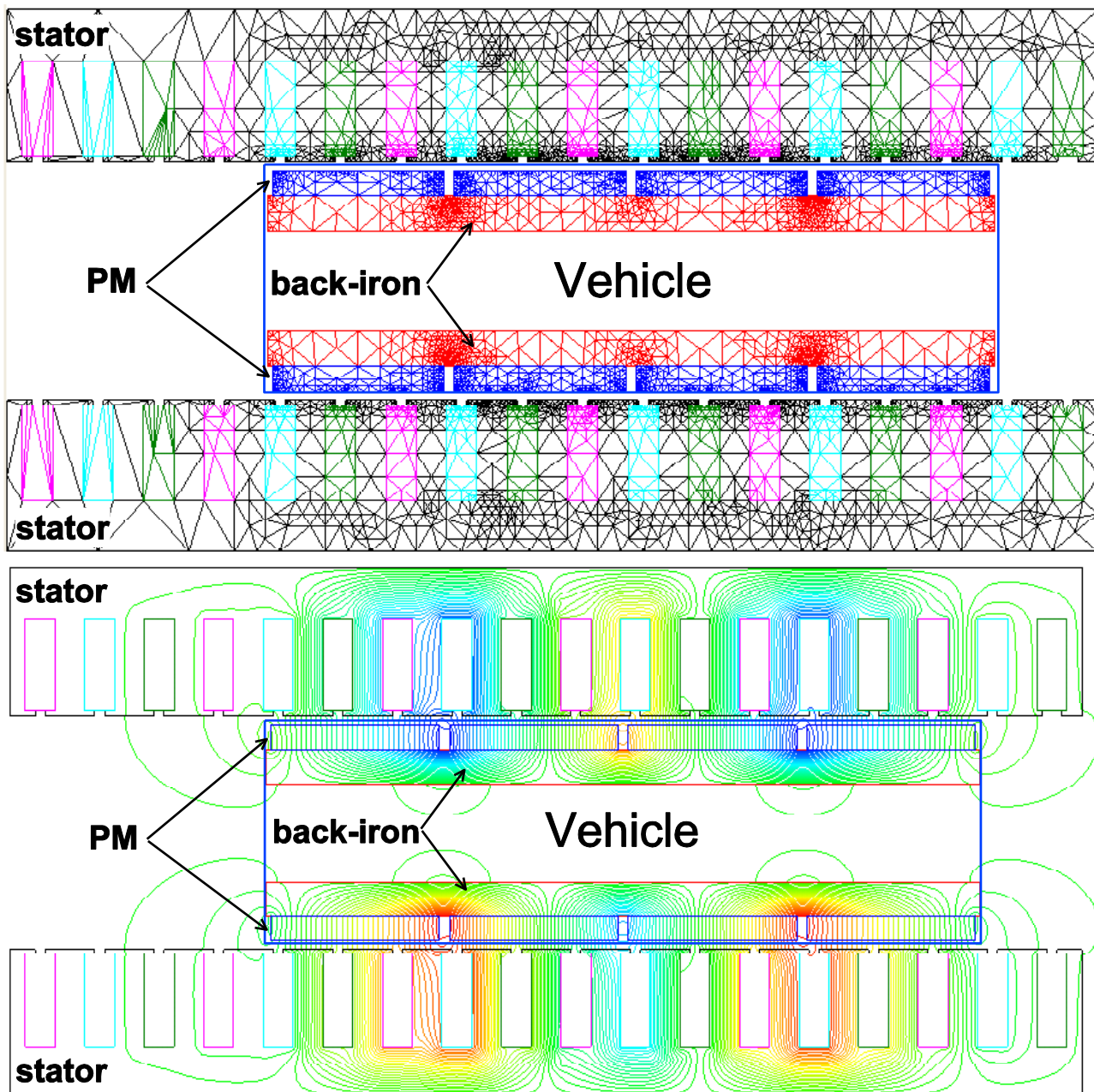


Figure 4.6 LPMSM model for FEM simulation



The primaries in the model include two stator cores and three phase windings on the left- and right-side of the guide-way. The simulation uses the drawing in the horizontal plane with the parameters taken from the experimental system. The material set for the stator cores is non-oriented steel 1008 with the B-H curve as in Figure 4.7. The windings are set up as pure copper, and the surrounding area of the PMLSM was set as air environment.

In the vehicle, there are two secondary segments at both sides. Each segment consists of a back iron and four permanent magnets, which are arranged in an array along the vehicle. The back iron is also set up as steel 1008, and the permanent magnets are set up as NdFeB. In the PM array, the magnet directions of two closed magnets are put in inverted directions.

The FEM model depicted in Figure 4.6 was used to simulate the characteristic of the experimental LPMSM. The simulation results were used to verify the validity of previous analytical model.

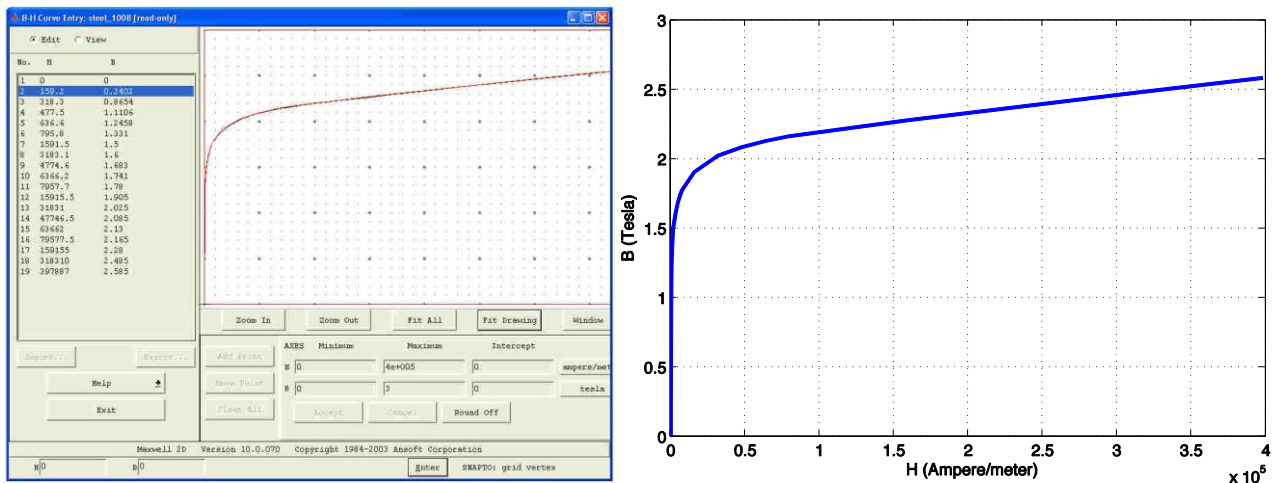


Figure 4.7 B-H curve: a. Editing interface b. Curve

### 4.4.3. FEM results

With the model described above, the simulations were done for three different cases in order to verify the forces' calculation in section 4.2. The three simulation cases are the change in the lateral position, the change in the angular phase ( $\theta_s$ ) of the primary currents and the change in the longitudinal position ( $x$ ). The simulations are described further in detail as following.

First, the effect of the vehicle's lateral position was implemented. In the simulation, the stators of the simulation model were established with no current. The vehicle position in the  $y$  direction (lateral position  $\delta$ ) was changed from  $-1.2mm$  to  $1.2mm$ , when the yaw angle  $\gamma$  was constrained at zero. Due to the changing of

lateral position, the normal forces generated by the PMs of the left- and right-side are not balanced. Therefore, the normal force influencing the vehicle is nonzero and depends on the lateral position. The result is presented in Figure 4.8 with normal force as the function of  $\delta$ . The normal force changing line generated by the simulation is shown in green colour. The simulation result is linear as expected in the theoretical calculation presented in the blue colour line. The difference between the two lines is caused by the simplifying assumptions in the analytical calculation and simulation material.

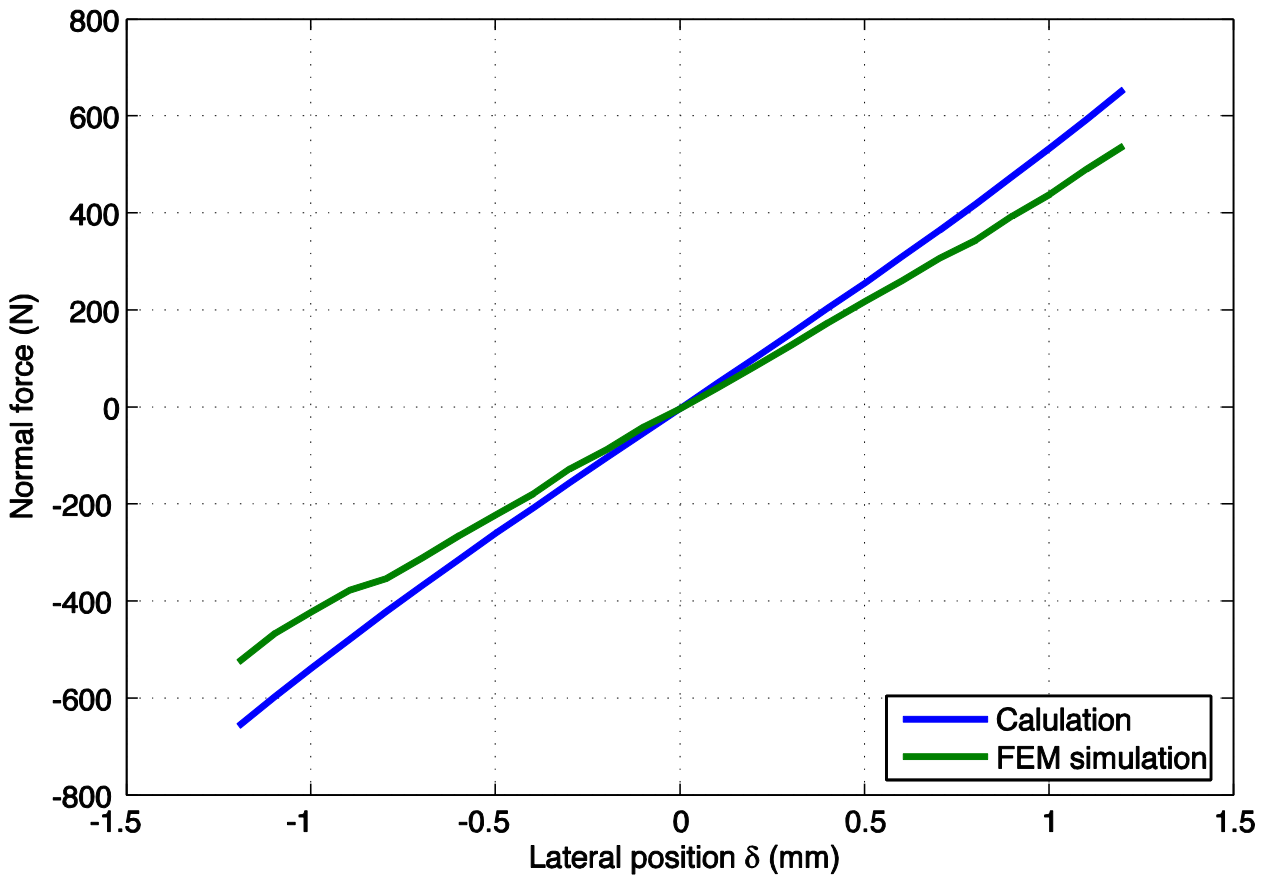


Figure 4.8 Normal force generated by the PM, as the function of lateral position  $\delta$

Second, the simulations were implemented to verify the validity of the normal force and the thrust calculations in the moving reference frame.

At the beginning, the vehicle's right stator was supplied with symmetrical three phase currents:

$$i_A = i_a \sin(\theta_s),$$

$$i_B = i_a \sin(\theta_s - 120^\circ),$$

$$i_C = i_a \sin(\theta_s - 240^\circ),$$

while the left stator currents were set to zero.

The simulation was done by fixing the vehicle at several lateral positions ( $\delta = 0\text{mm}$ ;  $\delta = 0.5\text{mm}$  and  $\delta = 1.0\text{mm}$ ). At each lateral position, the electrical phase  $\theta_s$  of the three phase currents was changing from  $0^0$  to  $360^0$ . The vehicle's position was arranged at a longitudinal position so that the normal force was highest, when  $\theta_s$  equals zero, i.e.  $x_0 = 0$ . This means the  $i_d$  approximately equals  $i_a$  and  $i_q$  approximately equals zero. With this setting,  $i_d$  and  $i_q$  vary correspondingly to cosine- and sine-function when the electrical angle  $\theta_s$  changes, i.e. the normal- and thrust-force will change accordingly.

The simulation results of normal forces presented in green lines are shown in Figure 4.9. They are compared with the theoretical calculation results presented in blue lines. In both cases, the results are quite similar with the changing of the electrical phase. The difference of the results is caused by the selected PM material of the FEM simulation. Because the software library has no material, which has exact parameters like in analytical calculation, the PM material was selected with nearest parameters. Therefore, the normal force generated by the PM in the FEM simulation is less than the one in the analytical calculation while the normal force generated by

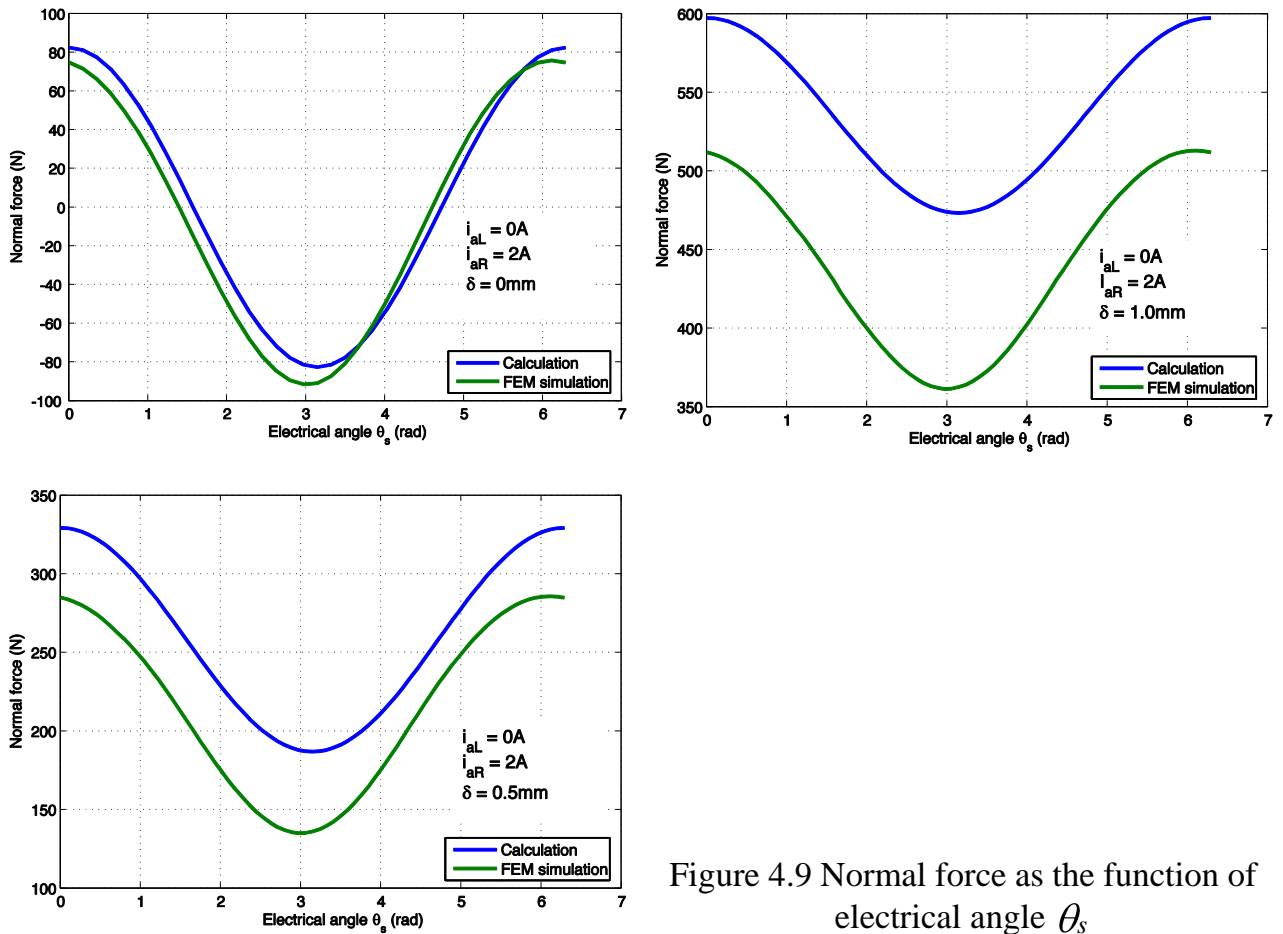


Figure 4.9 Normal force as the function of electrical angle  $\theta_s$

the primary current almost matches with the analytical calculation. That why, there are differences in the offset of the normal force results while the amplitudes are similar. It is clearer when the results in Figure 4.8 are considered. The difference of the normal forces generated by the PM in the analysis and simulation is small when the absolute value of the lateral position ( $\delta$ ) is small. As a result, the difference of the normal forces resulted in Figure 4.9a is not considerable when the lateral position is zero. The greater lateral position ( $\delta=0.5mm$  and  $\delta=1.0mm$ ) is the bigger difference in the results of the normal forces, as shown in Figure 4.9b and c.

To have more notions about the effect of  $i_d$  and  $i_q$ , the change of the normal- and thrust-force according to the electric angle was simulated. The simulation was done at  $\delta=0mm$ ,  $x_0=0mm$  and  $\theta_s = 0 \div 360^\circ$ . The results show the forces as the function of  $\theta_s$  in Figure 4.10.

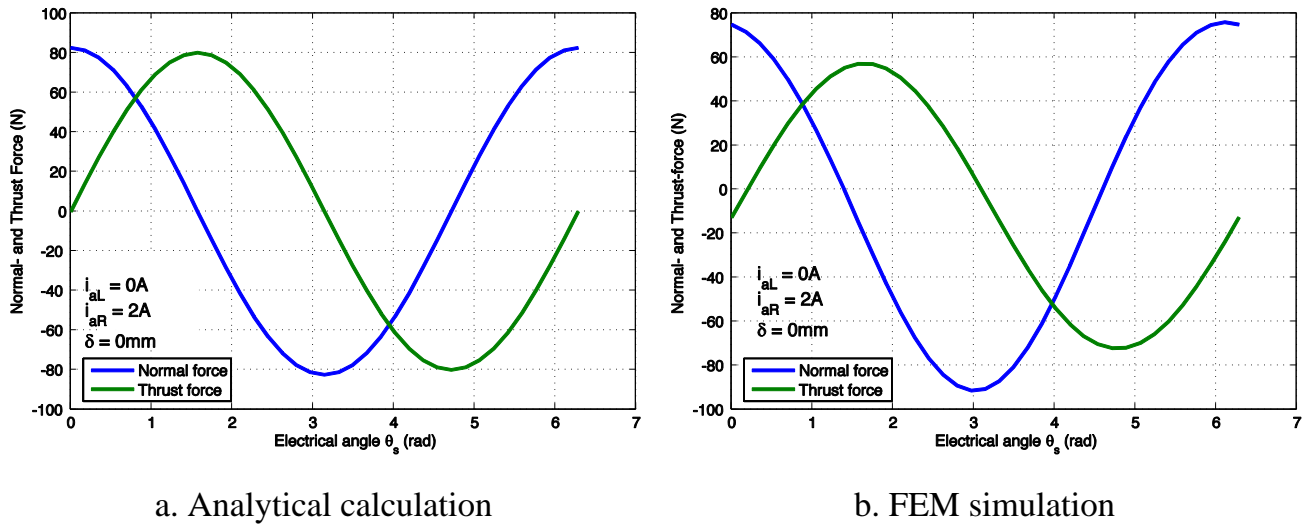


Figure 4.10 Varying of Normal- and Thrust-force

As the longitudinal position ( $x_0$ ) is zero, the changing of the current's phase ( $\theta_s$ ) results in the changing of the  $dq$  currents as following:

$$i_d = i_a \cos(\theta_s - \frac{\pi}{\tau} x_0) = i_a \cos(\theta_s) \quad (4.48)$$

$$i_q = i_a \sin(\theta_s - \frac{\pi}{\tau} x_0) = i_a \sin(\theta_s) \quad (4.49)$$

By substituting the equations (4.48), (4.49) into equations (4.34) and (4.35), the normal force and thrust force can be drawn as functions of the current's phase in Figure 4.10a. The simulation results in Figure 4.10b show the same characteristic as the mathematical analysis. The difference in the amplitude of the forces is caused by the material parameters as mentioned in the previous simulation.

The last simulation was done with an unchanging current ( $\theta_s = 0$  or DC), when the vehicle moves along  $x$ -direction in the middle of the guide-way from 0 to  $-2\tau$  ( $-72\text{mm}$ ). This causes the variation in  $dq$ -currents as sinusoidal functions:

$$i_d = i_a \cos(\theta_s - \frac{\pi}{\tau} x_0) = i_a \cos(-\frac{\pi}{\tau} x_0) \quad (4.50)$$

$$i_q = i_a \sin(\theta_s - \frac{\pi}{\tau} x_0) = i_a \sin(-\frac{\pi}{\tau} x_0) \quad (4.51)$$

Therefore, the analytical forces and simulation forces should be the same as the results in Figure 4.10. However, the simulation results presented in Figure 4.11a are different. In comparison with the analytical force lines and the previous simulation force lines, the simulation force lines here are not smooth because of the cogging force generated by the stator teeth. This effect is seen more clearly in the simulation results in Figure 4.11b, when the primary currents equal zero.

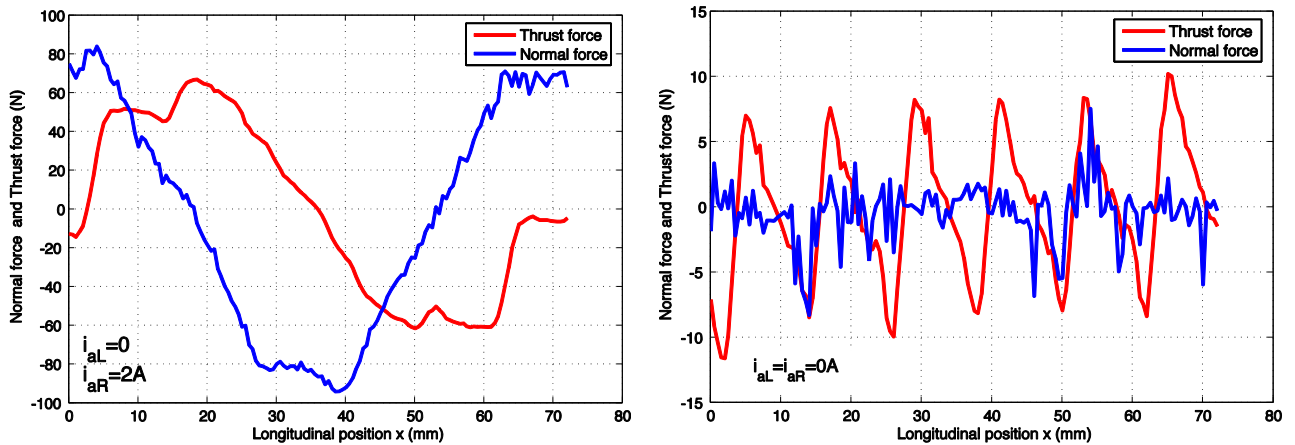


Figure 4.11 FEM-Simulation of Normal- and Thrust-Force vs. longitudinal position  $x$

The analytical calculations show some deviations from the FEM-simulation results but they can be used for the control design, as for the control goal, i.e.  $\delta=0$  agreement is acceptable.

## 4.5. Practical measurement

In order to verify the validity of the calculations and simulation above, an experimental setup was constructed. Due to the installation cost, the experiment was implemented to measure only the normal force as the function of lateral position and stator currents instead of all three experiments as the FEM simulation had done.

In Figure 4.12, the structure of the verifying experiment is described. There, an aluminium arm (2) is mounted on an axle (1) placed in the middle of the guide-way. The arm can rotate easily around the axle. At the end of the arm, the vehicle (3) is

fixed with two screws. By this, the vehicle moves mostly in  $y$ -direction inside the limitation generated by two primary stators (4), whereas the movement in  $x$ -direction is almost zero. Because of the small space limited by the stators and the length of the arm, the rotating angle of the vehicle referring to  $Ox$  axis is very small. Therefore, the vehicle in the experiment can be assumed parallel to the stator. In the middle of the vehicle, a force sensor was attached to measure the normal force in some experimental cases. The photo of the experimental setup is shown in Figure 4.13.

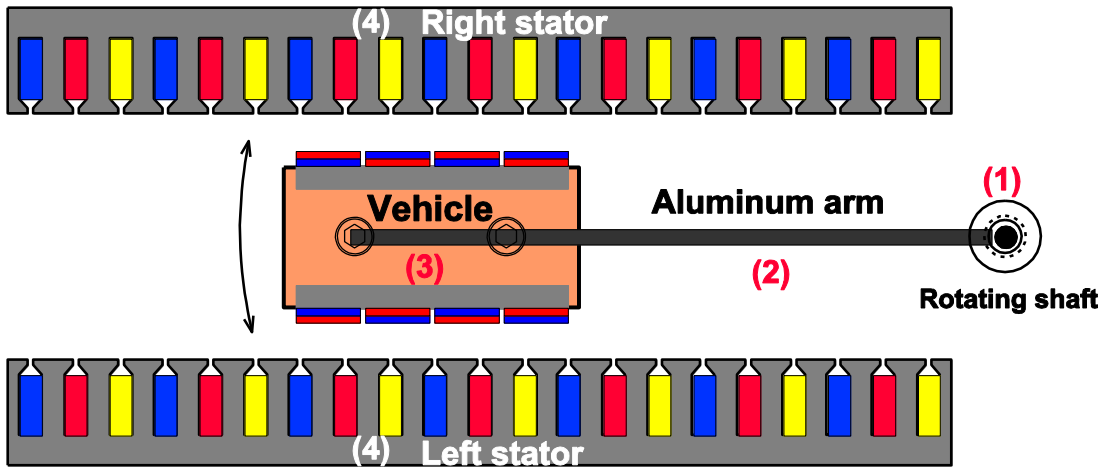


Figure 4.12 Verifying experiment structure.

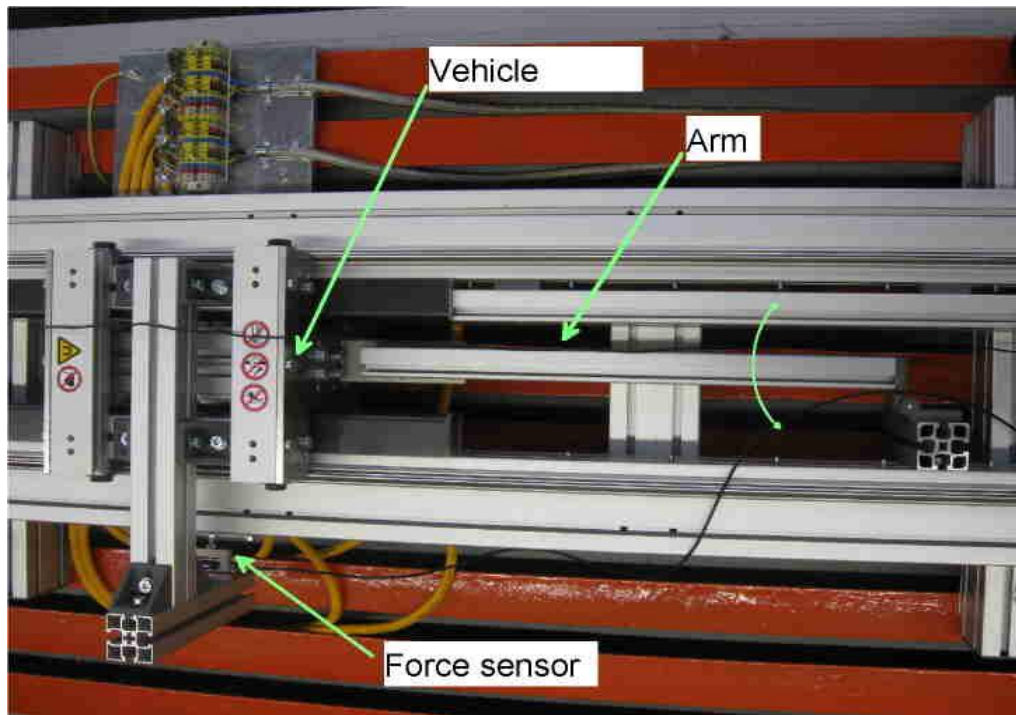


Figure 4.13 Verifying experiment photo.

First, a verifying experiment was done with no primary current when the vehicle moved in the  $y$ -direction from 0 to  $1.5mm$  (the other side is mirrored). At nonzero lateral positions ( $\delta \neq 0mm$ ), a normal force on the vehicle occurred because of the

unbalance between left- and right- normal forces. The result presented in Figure 4.14 is the normal force as the function of lateral position  $\delta$  (red line). The output normal force is proportional to the lateral position. The slope of the measured line in Figure 4.14 is about in the middle of the slope of the FEM-result in Figure 4.8 and the slope of the analytical calculation, i.e. FEM result and analytical result both deviate from measurement, but in opposite direction.

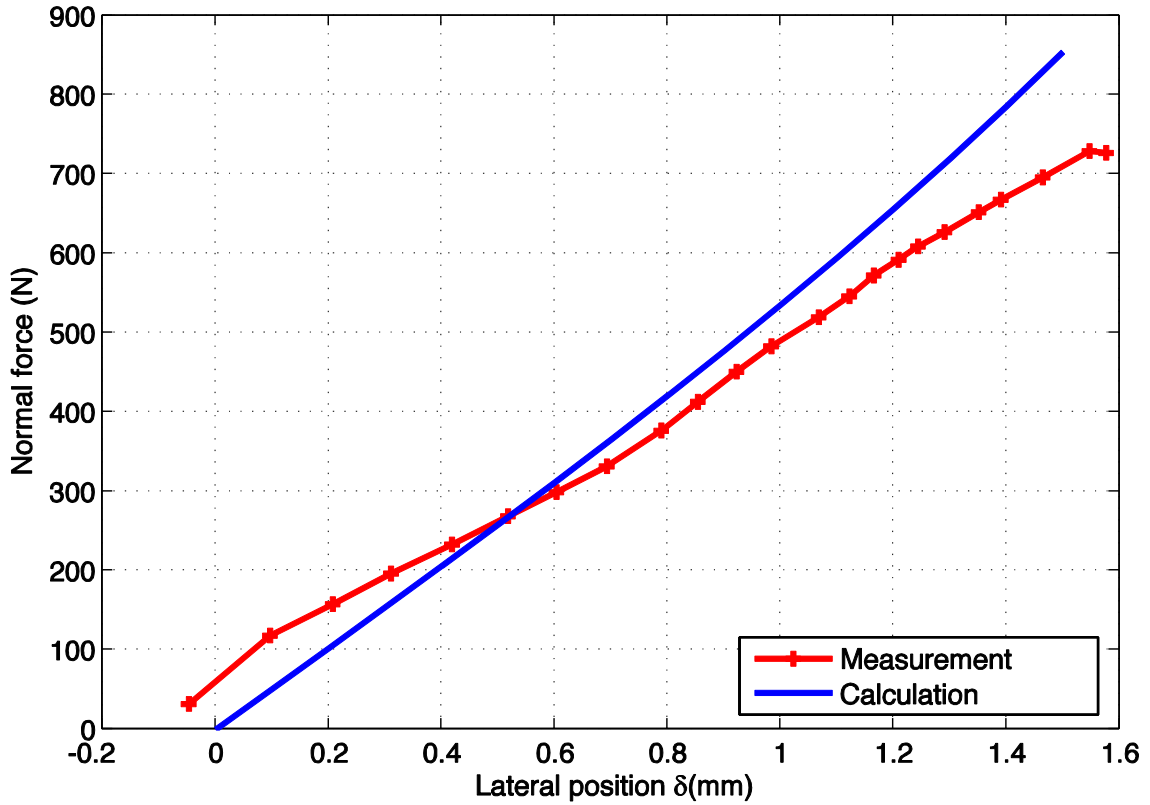


Figure 4.14 Relation between force and gap at current is zero.

Second, experiments were done in some fixed lateral positions with changing currents. In the experiments, the lateral position was fixed at  $\delta=1.0mm$  and  $\delta=0.54mm$ , when the electrical angle of the primary current (2A amplitude) changed from  $0^0$  to  $360^0$ . The results are presented in Figure 4.15. The results show the same performance of the normal force on the vehicle regarding to the changing of primary currents. The differences between the analytical calculation results and the experimental results are caused by the simplified assumptions mentioned in 4.2.1. As in the assumption, the linear motor has a smooth slot structure i.e. the normal force generated by a constant current vector in  $dq$ -coordinates ( $\vec{i}_m = const$ ) is constant when the vehicle moving along the primary. However, the real slot structure caused different normal forces with constant  $\vec{i}_m$  in different longitudinal positions, and the experimental results here are measured in only one longitudinal position. In addition, the aim of the experiment is measuring the qualitative performance of the system.



Thus, the mechanical structure was not well designed to measure the force with high precision.

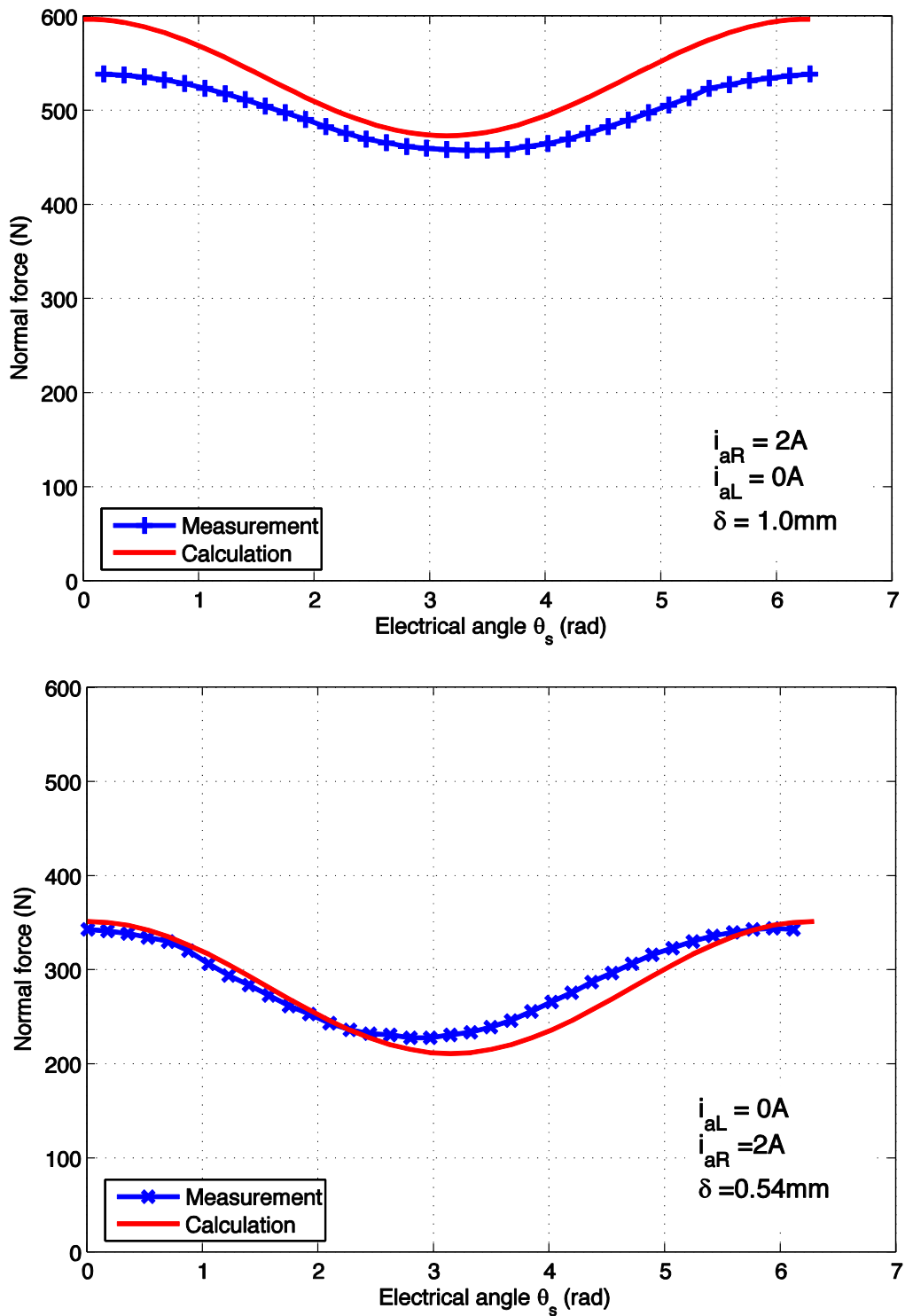


Figure 4.15 Relationship between normal force and electrical angle  $\theta_s$



## 5. CONTROLLER DESIGN

The main target of the controller in this dissertation is the ability to guide the vehicle in the horizontal plane by a magnetic guiding system without any extra mechanical or magnetic structure. With reference to the mathematical model analyzed and examined in chapter 4, a control method will be proposed in this chapter. The block diagram and calculation will be presented in the following sections.

### 5.1. Control block diagram

#### 5.1.1. Proposed control method

The proposed control method of each plant must be based on the plant's characteristic. Thus, the PM LSM force and torque equations in the previous chapter will be analysed and rearranged in this subsection in order to derive a proposed control method.

In chapter 4, the system was analysed, calculated and presented by mathematical equations. The equations were then verified by the FEM simulations and experimental measurements. The simulation and experimental results agree with the calculated results; therewith the validity of the mathematical equations is confirmed. With the limitations of the real experimental setup, the linear equations (4.38), (4.43), (4.44) give the approximate behaviour of the system. In the description of the experimental system, the vehicle has three degrees of freedom (DOF) to move on the horizontal plane created by the two guiding rails. They are the longitudinal movement in the  $x$ -axis, the lateral movement  $\delta$  in the  $y$ -axis and the yaw rotation  $\gamma$  around the  $z$ -axis. In order to propose a control method for the system, the three equations (4.38), (4.43), (4.44) were rearranged to present the three-motion axes as the functions of the currents  $i_x, i_\delta, i_\gamma$ .

The thrust force is derived from the equation (4.44), and the results is

$$F_x = F_{TL} + F_{TR} = K_x \cdot i_x + K_{xp} \cdot i_\gamma \cdot \delta \quad (5.1)$$

where  $F_x$  is the force impacting the vehicle in  $x$ -axis (thrust force),  
and  $K_x = C_{FT1}$ ,  $F_{xp} = C_{FT2}$ .

The lateral force is the difference of the normal forces presented in (4.38)

$$F_\delta = F_{NL} - F_{NR} = K_\delta \cdot i_\delta + F_{\delta p} \delta, \gamma, i_\delta, i_\gamma \quad (5.2)$$

where  $K_\delta = C_{FN3}$  and

$$F_{\delta p}(\delta, \gamma, i_\delta, i_\gamma) = C_{FN1}\delta + C_{FN2} i_{dL}^2 - i_{dR}^2 + C_{FN4} i_{dL}^2 + i_{dR}^2 \delta + C_{FN5} i_{dL} + i_{dR} \delta$$

Derived from the equation (4.43), it attains the torque ( $T_\gamma$ ) impacting the vehicle from the tangential forces

$$T_\gamma = F_{TL} - F_{TR} \frac{b}{2} = K_\gamma \cdot i_\gamma + K_{p\gamma} \cdot i_\delta \cdot \delta \quad (5.3)$$

where  $b$  is the gap in between the two PMs of the vehicle,

$$K_\gamma = \frac{bC_{FT2}}{2}, \quad K_{p\gamma} = \frac{bC_{FT1}}{2}.$$

In these equations, the forces and torque impacting the vehicle in  $x$ -axis ( $F_x$ ),  $y$ -axis ( $F_\delta$ ) and yaw ( $T_\gamma$ ) are presented by proportional relations with the current variables  $i_x$ ,  $i_\delta$ ,  $i_\gamma$  and the nonlinear functions  $K_{xp} \cdot i_\gamma \cdot \delta$ ,  $F_{\delta p} \delta, \gamma, i_\delta, i_\gamma$ ,  $K_{p\gamma} \cdot i_\delta \cdot \delta$ . The current variables ( $i_x$ ,  $i_\delta$ ,  $i_\gamma$ ) have relations with the  $dq$ -currents of the LM primaries presented in (5.4) and (5.5). The  $dq$ -currents of the primaries are distinguished by subscript  $L$  for the left primary and subscript  $R$  for the right primary.

$$i_{qL} = \frac{i_x + i_\gamma}{2}; \quad i_{qR} = \frac{i_x - i_\gamma}{2}; \quad (5.4)$$

$$i_{dL} = \frac{i_\delta}{2}; \quad i_{dR} = -\frac{i_\delta}{2}; \quad (5.5)$$

Therefore,

$$i_\delta = i_{dL} - i_{dR}; \quad i_\gamma = i_{qL} - i_{qR}; \quad i_x = i_{qL} + i_{qR}; \quad (5.6)$$

In addition, with the linear dynamic equations of the vehicle's motions (4.45)-(4.47), the controllers for the three DOFs suggest the use of standard cascaded PI control method. Assume that the inverters are used to generate the required currents in a very short time in comparison with the dynamic motions. The cascaded PI controllers of the vehicle motions are presented in equations from (5.7) to (5.12).

$$i_x^* = k_{pv}(v^* - v) + \frac{k_{pv}}{T_i} \int_0^t (v^* - v) dt \quad (5.7)$$

$$i_\delta^* = k_{p\varepsilon}(\varepsilon^* - \varepsilon) + \frac{k_{p\varepsilon}}{T_i} \int_0^t (\varepsilon^* - \varepsilon) dt \quad (5.8)$$

$$i_\gamma^* = k_{p\omega}(\omega^* - \omega) + \frac{k_{p\omega}}{T_i} \int_0^t (\omega^* - \omega) dt \quad (5.9)$$

$$v^* = k_{px}(x^* - x) \quad (5.10)$$

$$\varepsilon^* = k_{p\delta}(\delta^* - \delta) \quad (5.11)$$

$$\omega^* = k_{p\gamma}(\gamma^* - \gamma) \quad (5.12)$$

where:  $i_x^*, i_\delta^*, i_\gamma^*$  are reference values of current for three DOF motion,  
 $v^*, \varepsilon^*, \omega^*$  are the reference values of three DOF motion velocity,  
 $x^*, \delta^*, \gamma^*$  are the reference values of three DOF motion position,  
 $k_{p\dots}, T_i$  are the constant parameters of the PI controllers.

In the proposed control method above, the nonlinear parts of equation (5.1), (5.2) and (5.3) are considered as perturbations. This consideration can cause a reduction in the control quality of the system, especially when the values of  $\delta$  and  $\gamma$  are significant. In order to improve the control quality, compensation of the perturbations needs to be implemented by decoupling and feed forward calculations in the controllers. Detail of the methods is clearly represented in the next subsection by block diagrams.

### 5.1.2. Block diagrams of the control system

In this subsection, the control system is described by block diagrams. In the block diagram, the LSM characteristics presented by the equations in chapter 4 are represented as a set of elementary blocks. The proposed control methods and the limitations for the system are also presented in three different block diagrams.

Using the dynamic equations of the vehicle's motions and the linearized equations of forces and torque with regard to  $\gamma$  and  $\delta$  in chapter 4, the LSM block diagram is produced and presented in the right part (yellow area) of Figure 5.1. The small friction forces on the wheels have been greatly simplified to be proportional with vehicle velocities in the horizontal plane. The instability of the open loop caused by lateral offset distance  $\delta$  and yaw angle  $\gamma$  is not difficult to recognize by the positive feedback through the coefficients  $C_{FN1}, C_{FN3}, C_{FN4}, C_{FN5}, C_{FT1}$  and  $C_{FT2}$ . Consequently, the closed cascaded control loops as mentioned above need to be employed.

The basic structure of the control system for each of the three DOF motion ( $x, \delta, \gamma$ ) presented in the Figure 5.1 is a cascaded control system. The internal loops of the system are the current control loops using field oriented control (FOC) method ( $d$ - and  $q$ -currents). The superposed control loops of the current control are the speed

( $dx/dt$ ,  $d\delta/dt$  and  $d\gamma/dt$ ) control loops. It is assumed here that the sensor signals of the positions  $x$ ,  $\gamma$  and  $\delta$  are available. The lateral position ( $\delta$ ) and yaw angle ( $\gamma$ ) signals are supplied by industrial inductive sensors and afterwards supplied by a self-developed capacitive sensor. Beside  $\delta$  and  $\gamma$ , the longitudinal position ( $x$ ) is supplied by the incremental magnet position sensor. The time derivatives of the positions, which provide feedback speed information ( $\dot{x}$ ,  $\dot{\delta}$  and  $\dot{\gamma}$ ), are obtained by either approximate differentiate or by an observer structure, that is described in the right-hand side of the block diagram in Figure 5.1.

The output signal of the controller for the longitudinal velocity ( $dx/dt$ ) is the reference value for the sum of current values in the  $q$ -axis of the left- and right-primary ( $i_x^*$ ). The combination of real  $q$ -currents caused by  $i_x^*$  leads the vehicle with  $\delta=0$  moving by the total forces in  $x$ -direction  $F_{TL} + F_{TR}$ .

The controller for yaw angle velocity  $d\gamma/dt$  sends out the reference value for the difference between the current values in the  $q$ -axis of the left- and right-primary ( $i_\gamma^*$ ). The accompanying real  $q$ -currents caused by  $i_\gamma^*$  in the primaries control the difference between the left and the right tangential forces to generate a rotational moment on the vehicle around a z-axis in the middle of the vehicle.

The reference values of the  $q$ -currents ( $i_{qL}^*$ ,  $i_{qR}^*$ ) are determined from the relationship in equation (5.4) and presented in the block diagram.

The controller of the lateral velocity ( $d\delta/dt$ ) returns the reference value for the difference of  $d$ -currents in the primaries to control the lateral position. From the output of  $d\delta/dt$  controller, the  $d$ -current references are extracted to generate the corresponding normal forces on the left- and right-side of the vehicle against the lateral motion. In this approach, the two  $d$ -axis currents ( $i_{dL}^*$ ,  $i_{dR}^*$ ) are simply mapped to half of the difference value with inverted signs as in (5.5).

The external control loops are the position control loops ( $\delta$ -,  $\gamma$ -,  $x$ - controller). The position controllers receive position reference values ( $\delta^*$ ,  $\gamma^*$ ,  $x^*$ ) from the user interface and feedback values ( $\delta$ ,  $\gamma$ ,  $x$ ) from system sensors to calculate the speed references. The references are then supplied to the corresponding speed controllers.

Because of the strong coupling and positive feedback with regard to the lateral offset distance  $\delta$  and the yaw angle  $\gamma$ , the proposed control system discussed till now can work only at poor dynamics. Hence, extra signals are added to the reference signals of the current controllers in Figure 5.2. The signal are the estimated values of

the perturbations  $K_{xp} \cdot i_\gamma \cdot \delta$ ,  $F_{\delta p} \delta, \gamma, i_\delta, i_\gamma$  and  $K_{p\gamma} \cdot i_\delta \cdot \delta$  mentioned in (5.1)-(5.3). They are used to counteract the positive feedback in the control system and decouple the effect of  $\delta$ ,  $\gamma$ ,  $x$  on the control qualities of the others. In the decoupling blocks,  $C_{FN1} C_{FN2} \dots C_{FT1} \dots$  are the estimated constants of the system. The currents  $\hat{i}_{dR}, \hat{i}_{qR}, \hat{i}_{dL}, \hat{i}_{qL}$  are estimated from the feedback currents of two phases, instead of three phases as usual.

In the block diagram Figure 5.2 described above, the control system of the vehicle is assumed a linear circuit according to the linearized coefficients. The current controllers are assumed to have a very small delay time. It is also useful to consider that the current controllers can generate the combination of  $dq$ -currents linearly proportional to the reference value. With these assumptions, the control signals of the velocity controllers ( $d\delta/dt$ ,  $d\gamma/dt$  and  $dx/dt$ ) can be implemented to guide the vehicle as presented in the block diagram Figure 5.2.

With the limited current supplies of the inverters, the limitations of current values are also added as in Figure 5.3. Here, the  $d$ -currents are given higher priorities versus the  $q$ -currents, i.e. in operating under the current limitation, most current is used in the  $d$ -axis to produce enough normal force against the magnetic attraction between the permanent magnets and the primaries.

$$|i_{dx}| \leq I_{\max} \quad (5.13)$$

$$|i_{qx}| \leq \sqrt{I_{\max}^2 - i_{dx}^2} \quad (5.14)$$

where  $i_{dx}, i_{qx}$  are the  $dq$ -currents of the left and right primary,  
 $I_{\max}$  is the limited current of the inverter.

However, the normal forces must be high only at the beginning when the vehicle leaves the rest position, from one side of the guide-way to the middle of the guide-way. When the vehicle is in the middle of the guide-way, the required  $d$ -currents are small; most current can be used in the  $q$ -axis to guide the vehicle moving in the longitudinal direction.

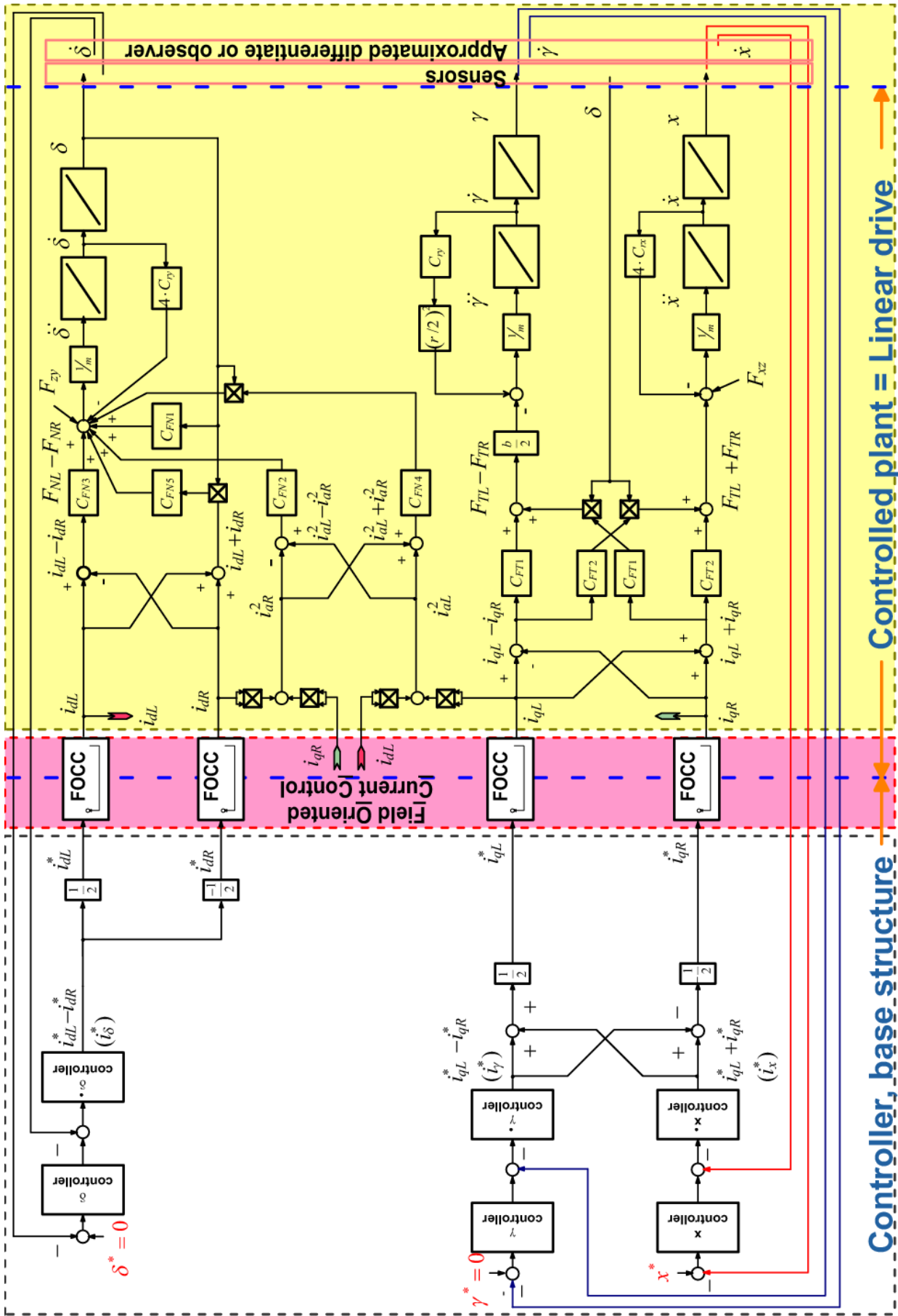


Figure 5.1 Basic control structure with PI controllers

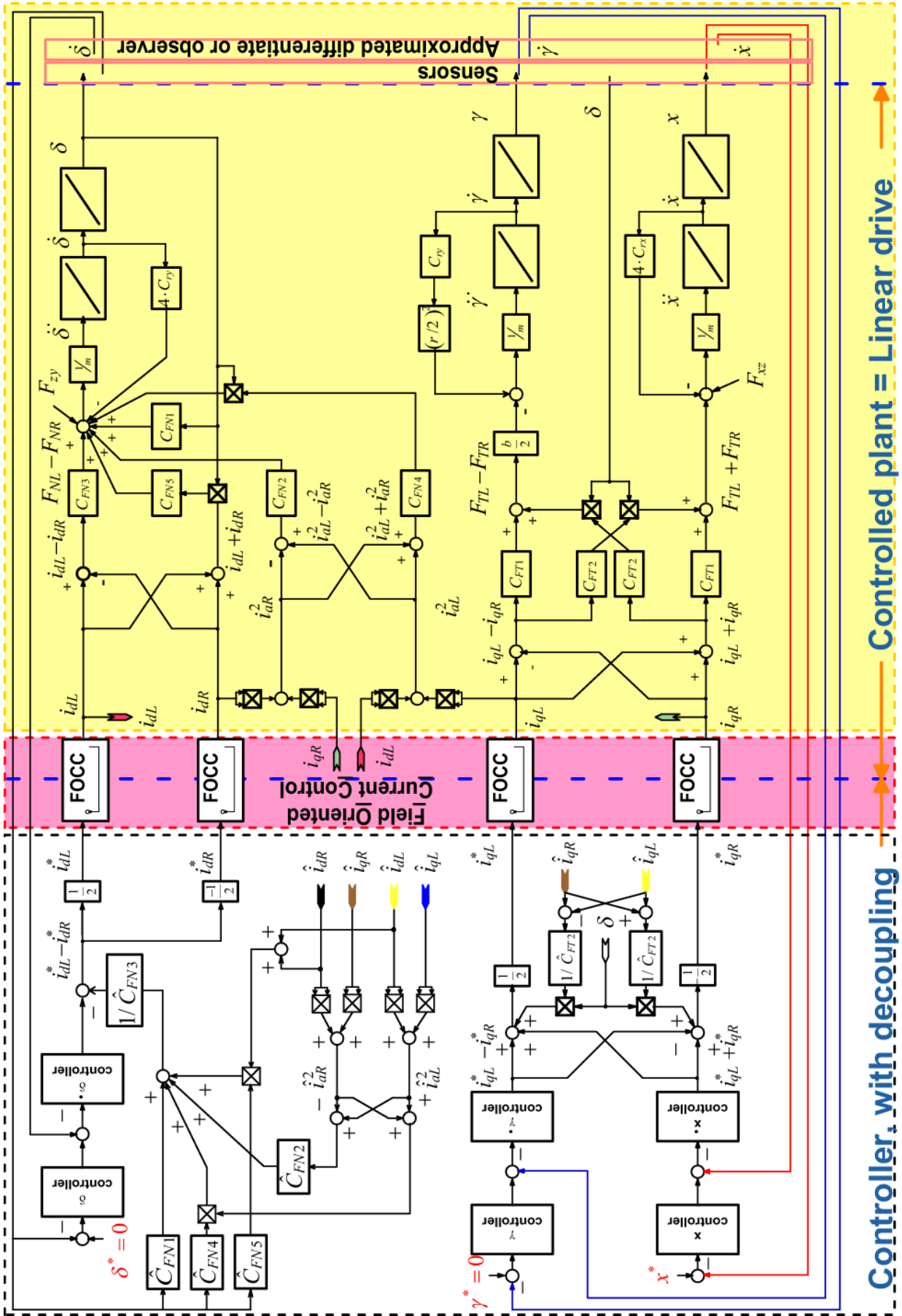


Figure 5.2 Decoupling control structure

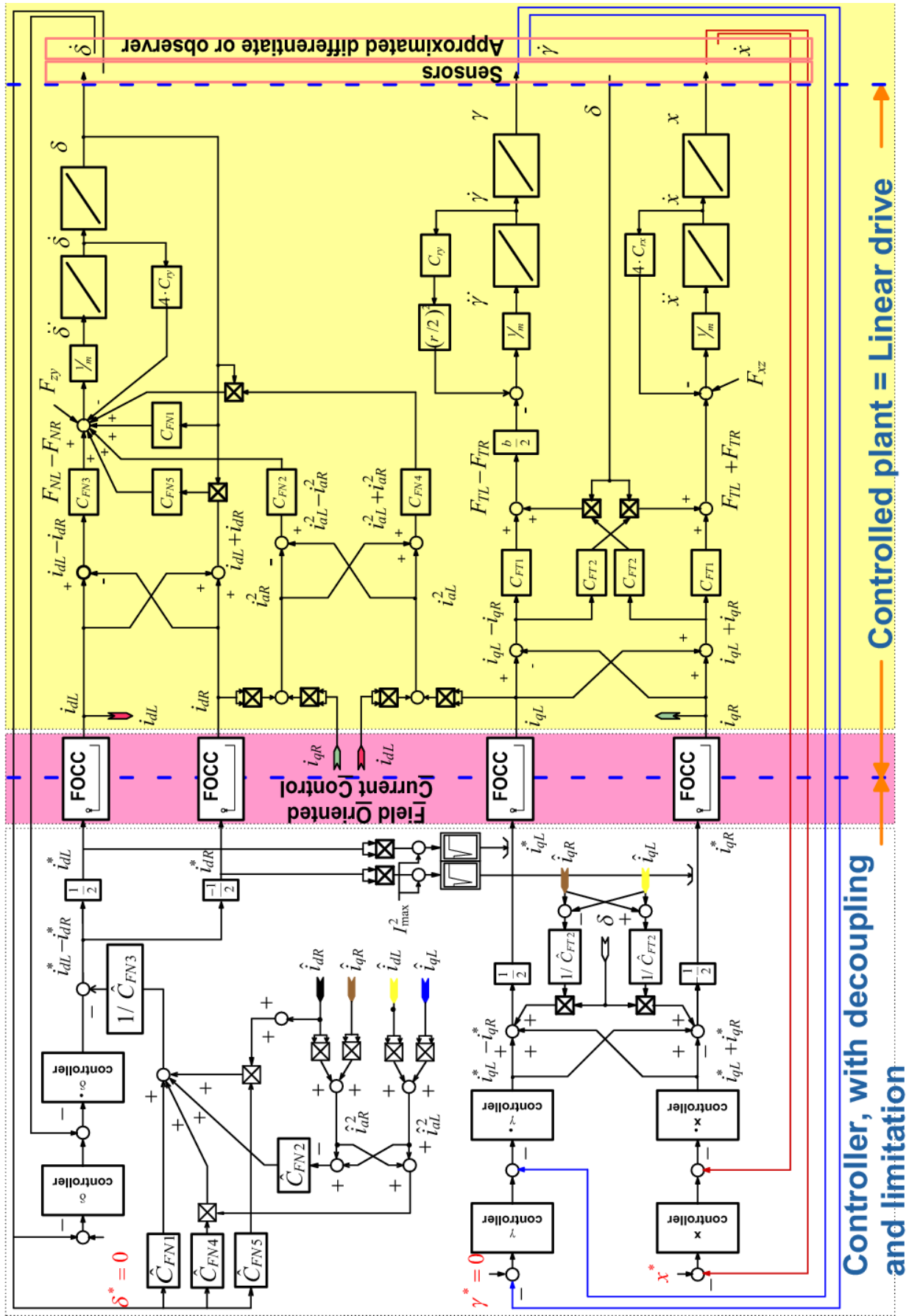


Figure 5.3 Decoupling control structure with current limitation



## 5.2. Controller design

The motions of the vehicle must be controlled in the horizontal plane. The control structure as mentioned in the block diagrams is a field oriented control (FOC) without (Figure 5.1) and with decoupling (Figure 5.3). The standard cascade PI control structure of the rotating machine is also used in this LSM system.

The equipment and the structure of the control system were described in chapter 3. The controller and the control algorithm were implemented on a PC running Linux RTAI operating system. The sampling frequency of the control system is 10 kHz (100  $\mu$ s per sample). Although a digital controller is used, the design and the tuning of the controller are still performed in the s-domain (continuous) using the theory of linear control system. The controller is discrete using the Tustin linear transformation given by (5.15).

$$s \approx \frac{2}{T_s} \frac{z-1}{z+1} = \frac{2}{T_s} \frac{1-z^{-1}}{1+z^{-1}} \quad (5.15)$$

### 5.2.1. Current control loops

According to the previous subsection, the control system uses a field oriented control method to control the three DOF motions. In Figure 5.4 is the block diagram of the implemented current control algorithm. The control algorithm is used to control independently the current  $i_d$  and  $i_q$  of the linear motor in the  $dq$ -reference frame. The outputs of the current PI controllers ( $v_d^*, v_q^*$ ) are transformed to three phase reference voltages. The reference voltages are fed to a Space Vector Pulse Width Modulation (SV-PWM) to generate the inverter switching times. The switching times are then sent to the inverter interface board to generate the desired currents.

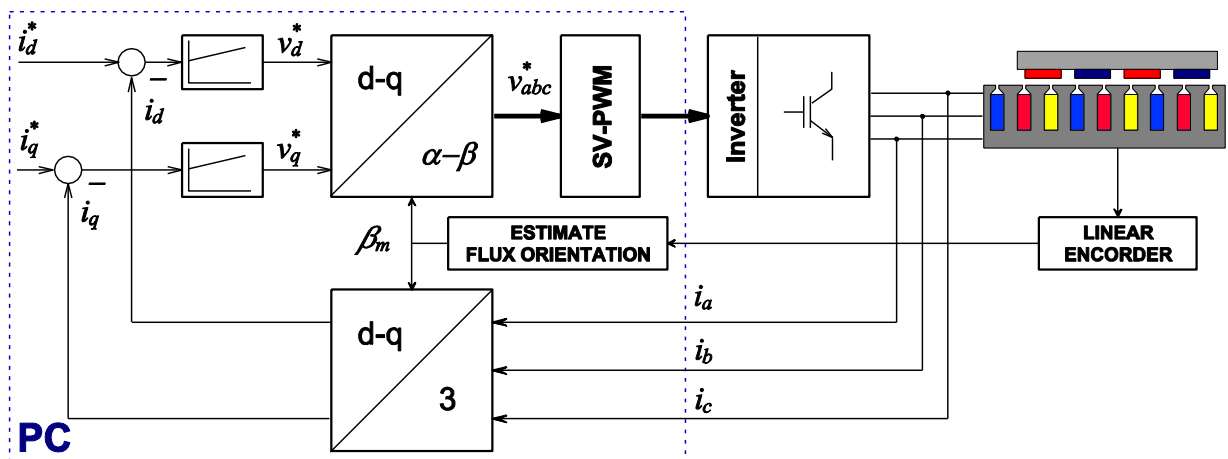


Figure 5.4 Current FOC block diagram

With the structure of the current control presented above, the current control loops in each segment consist of two  $d$ -current loops and two  $q$ -current loops of the left- and right-primary. Figure 5.5 shows the simplified current control loops of one primary segment using a PI controller, where the couplings between  $dq$ -axis are assumed to be compensated. Here, the control's time delay (including inverter reaction time) is modelled as a first order lag element with a time constant  $T_D = 1.5T_s$ , where  $T_s$  is the sampling time [56]. The converter gain  $K_c$  is the relationship between the numerical evaluation in the computer (digital controller) and the real output voltage. In the experiment, the used resolution scale was 4000 for the complete line to line voltage ( $2/3$  DC-link voltage). The experimental LSM also gives  $L_d = L_q = L_s$ . Then,  $K_c$ ,  $K_e$ ,  $T_e$  are obtained from (5.16).

$$K_c = \frac{2}{3} u_{dc} \cdot \frac{1}{4000}; \quad K_e = \frac{1}{R}; \quad T_e = \frac{L_d}{R} = \frac{L_q}{R} = \frac{L_s}{R} \quad (5.16)$$

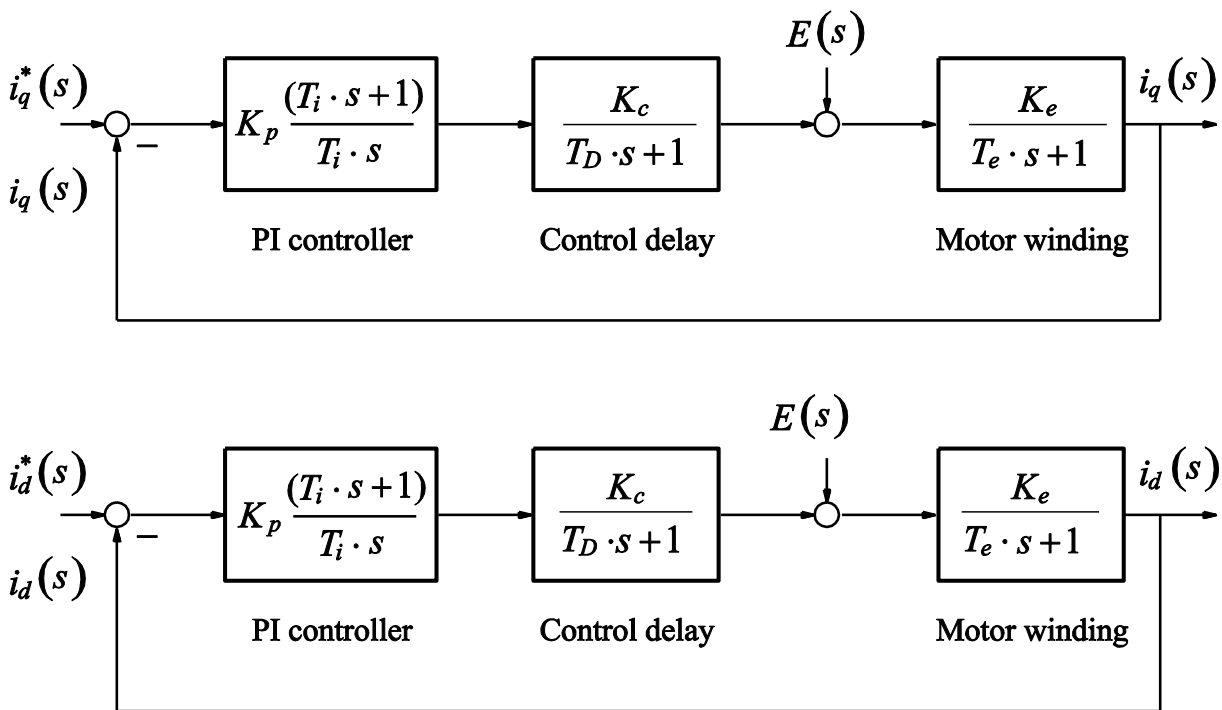


Figure 5.5 Simplified current control loops.

The PI's parameters of both current loops are calculated by the criteria of amplitude optimum [61][62]. The results are similar as given in (5.17)

$$T_{i\_i} = T_e; \quad K_{p\_i} = \frac{L_s}{2 \cdot K_c \cdot K_e \cdot T_D}; \quad (5.17)$$

With the calculated PI's parameters, the current control loops can be simplified as a first order lag element in (5.18)

$$F_{w\_id}(s) = F_{w\_iq}(s) = \frac{1}{2T_D^2 \cdot s^2 + 2T_D \cdot s + 1} \approx \frac{1}{2T_D \cdot s + 1} \quad (5.18)$$

### 5.2.2. Speed control loops

The speed control loops are here concerned with the three DOFs control loops. They consist of a longitudinal speed control loop ( $\dot{x}$ -control), a yaw speed control loop ( $\dot{\gamma}$ -control) and a lateral speed control loop ( $\dot{\delta}$ -control). Due to the decoupling network, each control loop is assumed to be independent of the others and has its own controller.

In the cascaded control method, the speed control loops are superposed on current control loops. The speed controllers provide the reference signals to current control loops. From the block diagrams in the previous subsection and the simplified current control loop in (5.18), the speed control loops are presented in Figure 5.6. In the figure, the friction forces are assumed as disturbance.

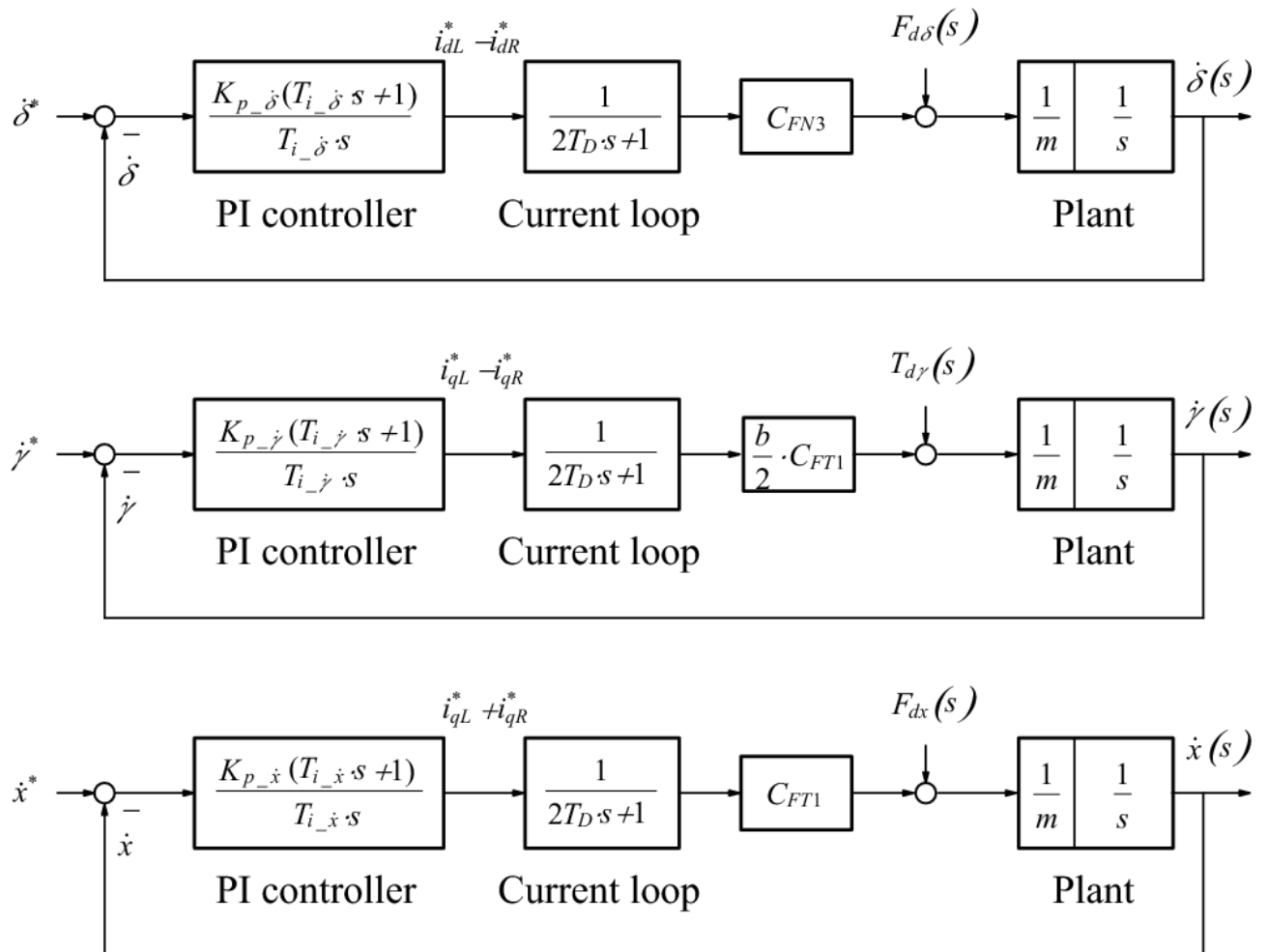


Figure 5.6 Speed control loops

With this structure, PI controllers are proposed to control the speed loops. The open loops have integrating behaviours. Therefore, the PI controller parameters are tuned for symmetrical optimum. The PI parameters are presented in (5.19)-(5.21).

$$T_{i_{-\delta}} = 4 \cdot 2T_D = 8 \cdot T_D; \quad K_{p_{-\delta}} = \frac{m}{8 \cdot C_{FN3} \cdot 2T_D} = \frac{m}{16 \cdot C_{FN3} \cdot T_D}; \quad (5.19)$$

$$T_{i_{-\dot{\gamma}}} = 4 \cdot 2T_D = 8 \cdot T_D; \quad K_{p_{-\dot{\gamma}}} = \frac{m}{8 \cdot \frac{b}{2} \cdot C_{FT1} \cdot 2T_D} = \frac{m}{8 \cdot b \cdot C_{FT1} \cdot T_D}; \quad (5.20)$$

$$T_{i_{-\dot{x}}} = 4 \cdot 2T_D = 8 \cdot T_D; \quad K_{p_{-\dot{x}}} = \frac{m}{8 \cdot C_{FT1} \cdot 2T_D} = \frac{m}{16 \cdot C_{FT1} \cdot T_D}; \quad (5.21)$$

The PI controllers, with the parameters above, reduce the speed control loops acting as first order lag elements, which are given by (5.22)

$$F_{w_{-\delta}}(s) = F_{w_{-\dot{\gamma}}}(s) = F_{w_{-\dot{x}}}(s) \approx \frac{1}{1 + 8 \cdot T_D \cdot s} \quad (5.22)$$

### 5.2.3. Position control loops

The position control loops are the superposed loops on the speed control loops. The controllers of the position control loops generate reference signals ( $\delta^*$ ,  $\dot{\gamma}^*$ ,  $\dot{x}^*$ ) for the speed control loops. The transfer functions of all speed control loops are the same; the block diagram of the position control loops is presented simply as in Figure 5.7.

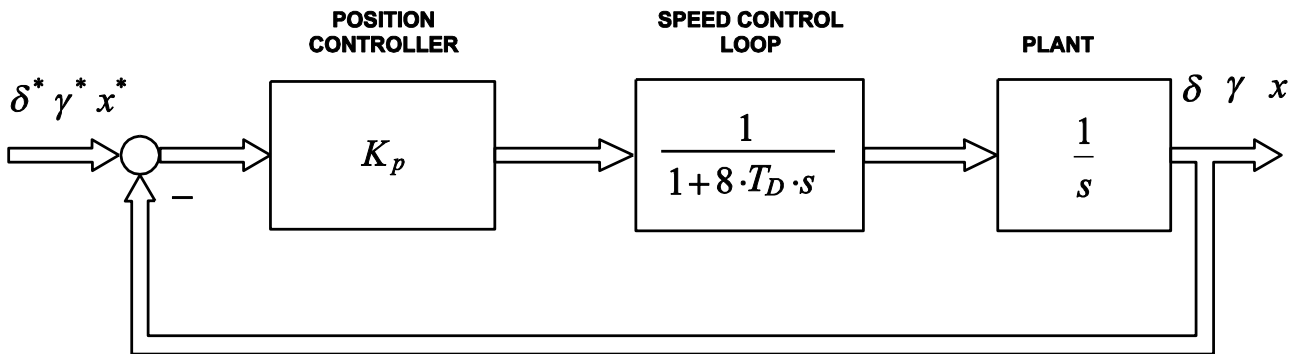


Figure 5.7 Position control loops

As position controllers, P type controllers are used. The gain values of the controllers are obtained by criteria of amplitude optimum presented in (5.23).

$$K_{p_{-\delta}} = K_{p_{-\gamma}} = K_{p_{-x}} = \frac{1}{2 \cdot (8T_D)}; \quad (5.23)$$

### 5.3. Control system simulation

In order to check the viability of the proposed system, a simulink simulation was modelled in MATLAB following the mathematical calculations. Then controllers with the parameters calculated according to the previous subsection were implemented. The whole system with controller was simulated to verify the proposed LSM.

#### 5.3.1. Simulation model

To get the characteristics of the vehicle's reaction with the control currents, a linear motor model is created in MATLAB Simulink as in Figure 5.8. The model was created based on the mathematical model of the proposed system in the  $dq$ -coordinate system. Inputs of the model are the  $d$ - and  $q$ -currents of the PM LSM primaries. The input currents are firstly used to calculate amplitudes of the armature currents in the left- and right- primary ( $i_{dL}$ ,  $i_{dR}$ ). In addition to the primaries currents and the output values ( $\delta$ ,  $\gamma$ ), the input  $dq$ -currents are then the inputs of the simulation model, which are supplied to a multiplex block (MUX-black bar). In the model, the normal forces and the tangential thrusts are calculated by the nonlinear equation (4.34) and (4.35). They are represented by four function blocks  $f(u)$  in the middle of the figure. The thrusts and forces make the vehicle move in three degrees of freedom as presented in dynamic motion equations (4.45)÷(4.47). Outputs of the

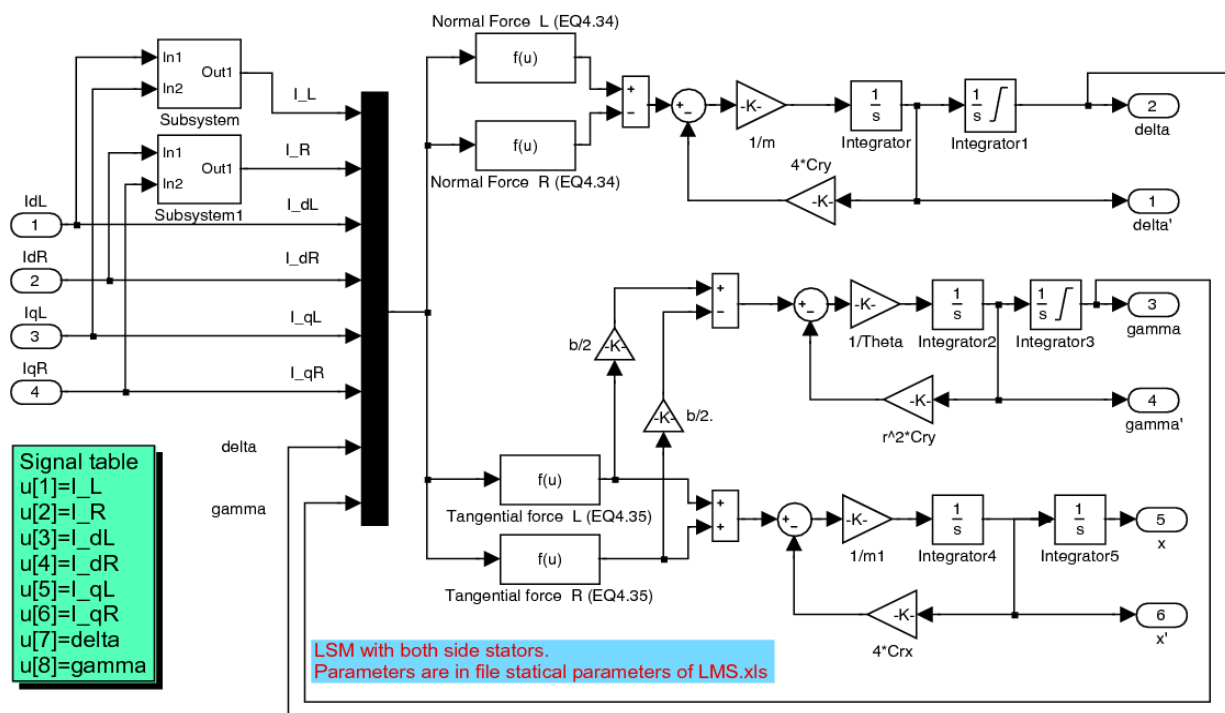


Figure 5.8 The simulation model of the experimental LSM system

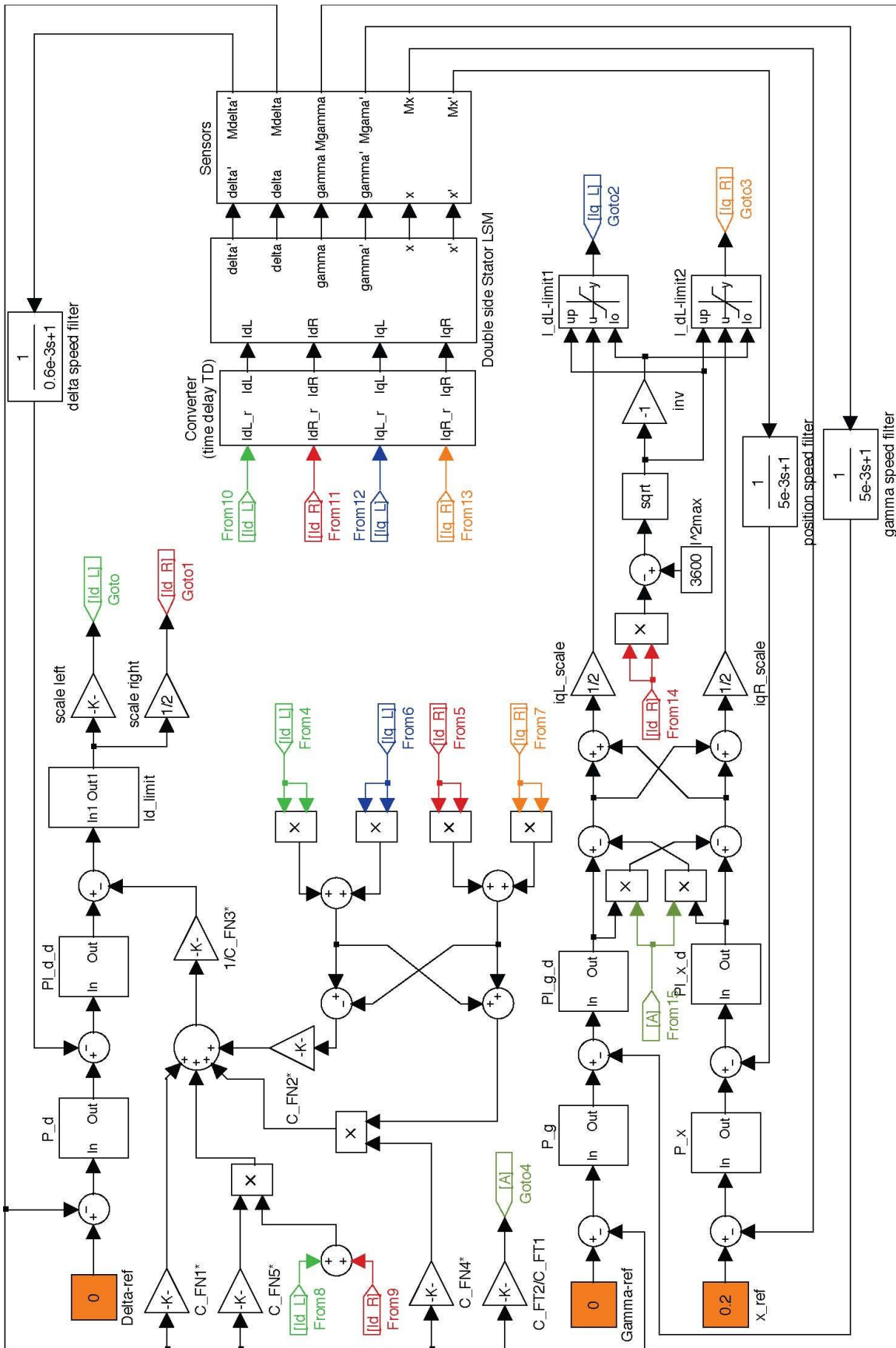


Figure 5.9 Completed simulating model system

model are lateral position ( $\delta$ ), yaw angle ( $\gamma$ ), longitudinal position ( $x$ ) and their corresponding speeds.

The whole-system model is developed to study some characteristics of the PM SLM and the ability of the designed controller. In the completed model in Figure 5.9, the PM SLM model in Figure 5.8 is packed as a block with four current input signals ( $i_{dL}$ ,  $i_{dR}$ ,  $i_{qL}$ ,  $i_{qR}$ ) and six motor state variable outputs ( $\delta$ ,  $\dot{\delta}$ ,  $\gamma$ ,  $\dot{\gamma}$ ,  $x$ ,  $\dot{x}$ ). The PM SLM is connected with the converter block (input) and the measurement block (output). Here, they are simplified as first order lag elements. The measurement system has a duty to supply feedback signals for the control system, and the converter receives desired current values from the control system.

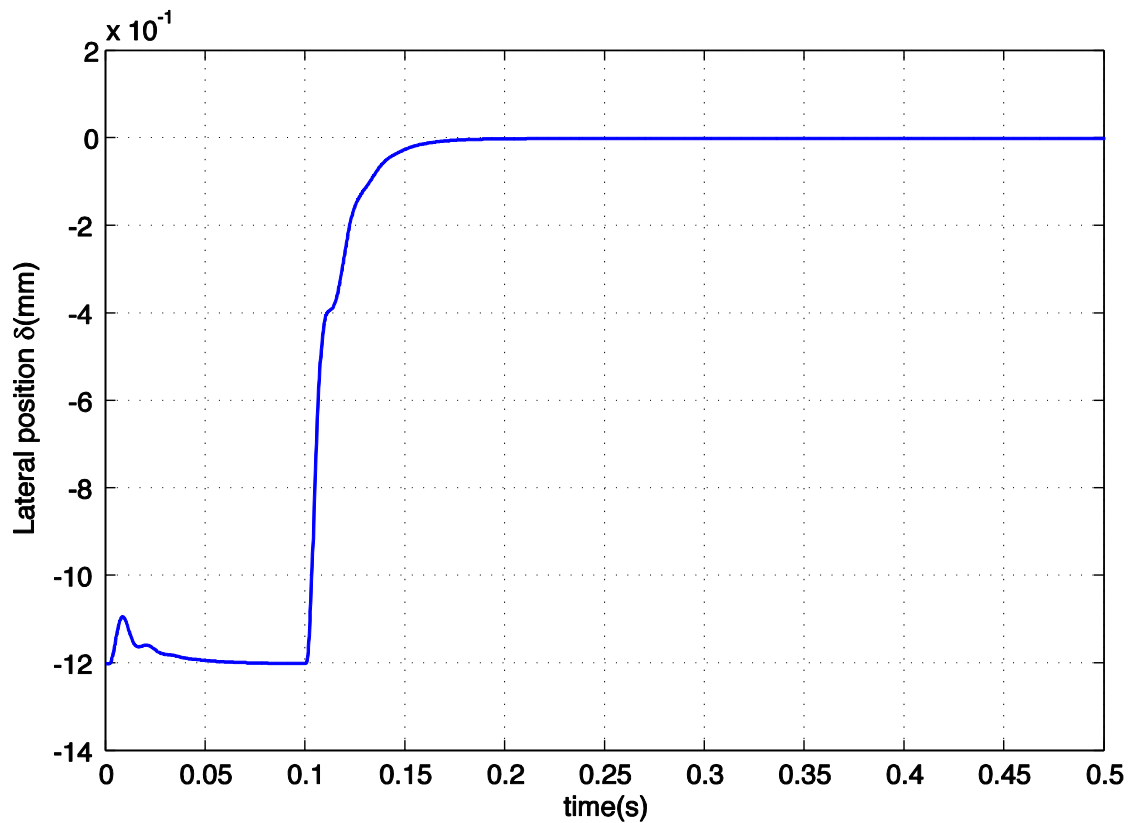
The model of the control system is built according to the left part of the block diagram Figure 5.3. The control model is separated into three control loops to control three DOFs independently with feed forward control to compensate the coupling between the control values. The feed forward block diagram is based on the estimated parameters of linearized equation (4.38), (4.43) and (4.44). Each DOF is controlled by three cascaded control loops: current control loop, speed control loop and position control loop.

### 5.3.2. Simulation results

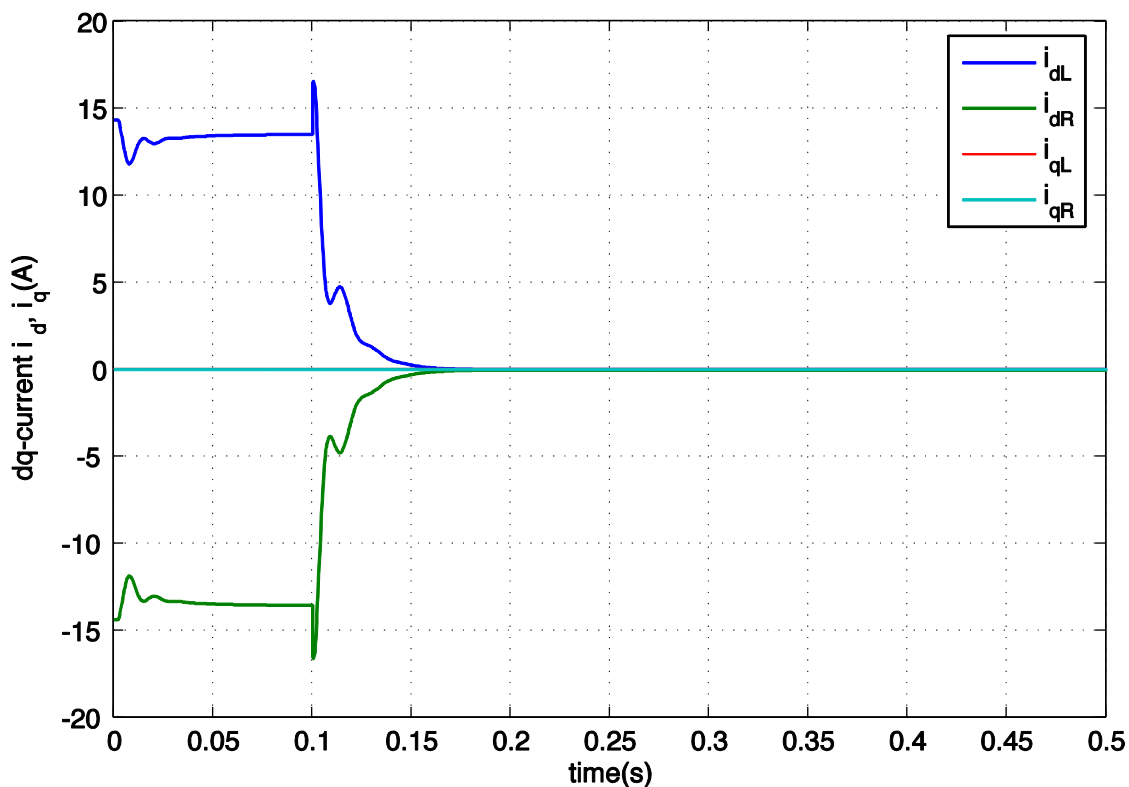
With the simulation model mentioned above, simulations were done to verify the proposed control method on the mathematical model of the PM LSM. The simulations consist of separated controls and simultaneous control as follows.

At first, the simulation was done with separated controls. Each DOF of the vehicle was controlled from starting value (rest position) to desired control values while the two other controls were constrained, i.e. only one position ( $\delta$  or  $\gamma$  or  $x$ ) is controlled, the other two positions were modelled to be constant. At the beginning, the system was started with one position at rest value ( $\delta = -1.2mm$  or  $\gamma = -8.0mrad$  or  $x = 0mm$ ), and the two others were constrained at zero ( $\delta = 0mm$ ,  $\gamma = 0mrad$ ,  $x = 0$ ). At  $t = 0.1s$ , the control position was set for desired value ( $\delta^* = 0mm$  or  $\gamma^* = 0mrad$  or  $x^* = 200mm$ ). The simulation results are presented in turn in Figure 5.10-Figure 5.12. In the figures, the lateral position ( $\delta$ ), yaw angle ( $\gamma$ ) and longitudinal ( $x$ ) are shown as functions of time.

In Figure 5.10, the lateral position was controlled from the rest position  $\delta = -1.2mm$  to the reference position  $\delta^* = 0$ . In this control, only the  $d$ -currents are



a.



b.

Figure 5.10 Three DOFs in separated control – Lateral position.

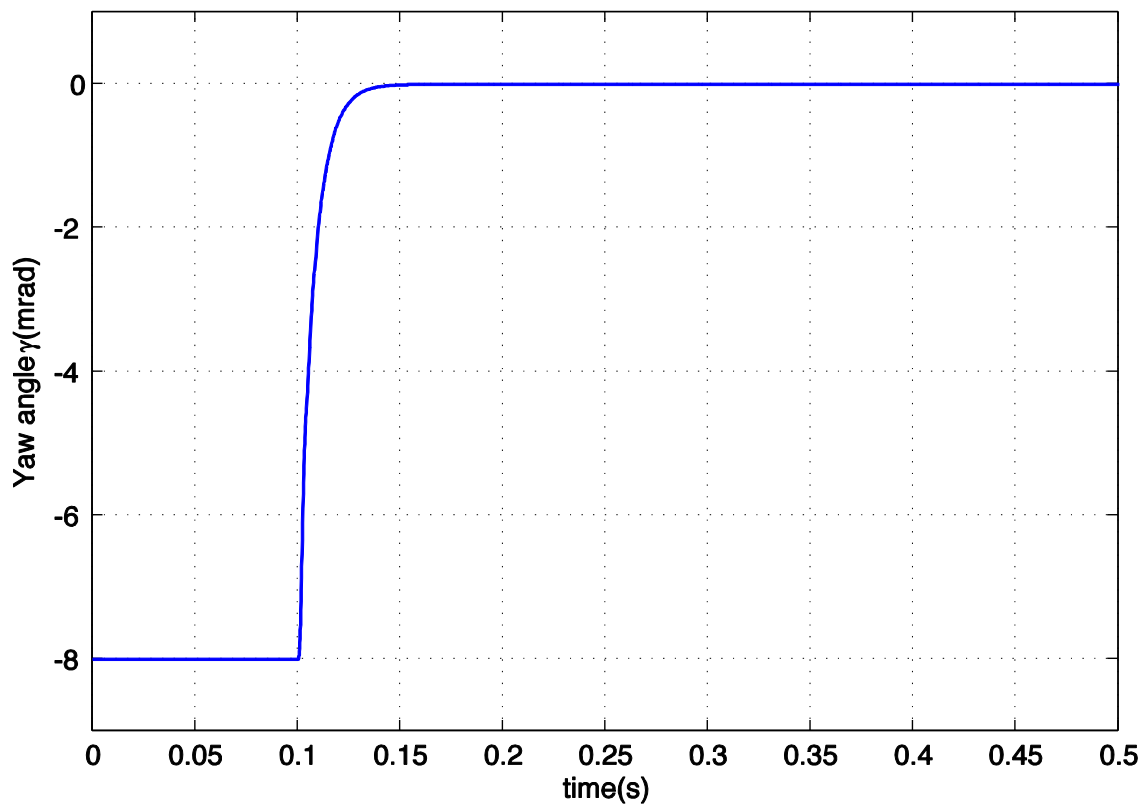
a. Lateral position; b.  $dq$ -currents.



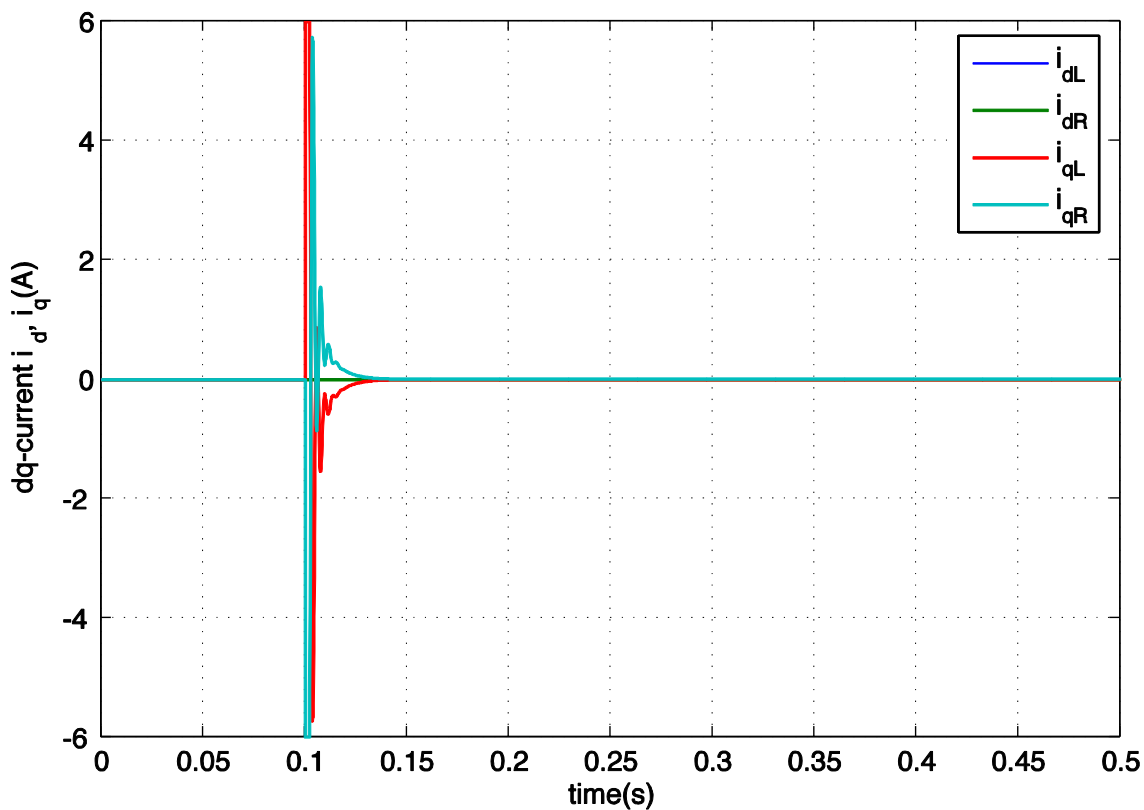
required to control the lateral position, while the  $q$ -currents are zero, as shown in Figure 5.10b. The simulation results show a good control quality in lateral position control (Figure 5.10a). There was a disturbance at the beginning of the simulation when the vehicle was in the rest position. The phenomenon is caused by the compensation currents from the decoupling structure. The currents make the vehicle move toward the centre of the guide-way, i.e. the lateral position ( $\delta$ ) trends toward zero. However, this reduces the compensation currents. Therefore, the vehicle moves back to the rest position, and the system here establishes a balance between the normal forces generated by the compensation currents and the other forces.

The simulation results of yaw angle ( $\gamma$ ) control are presented in Figure 5.11. The yaw angle was controlled from  $\gamma = -8.0\text{mrad}$  to  $\gamma = 0\text{mrad}$  with a high-performance, as shown in Figure 5.11a. In the simulation, only the difference of the  $q$ -currents is used in order to control the yaw angle as the  $q$ -currents ( $i_{qL}$ ,  $i_{qR}$ ) are symmetrical with respect to the horizontal axis, i.e. the sum of the  $q$ -currents is zero. The  $d$ -currents are also not necessary in this case. These are shown in Figure 5.11b.

The longitudinal position ( $x$ ) control ability was considered in the third simulation. The results are shown in Figure 5.12. The controller leads precisely the vehicle to the desired position  $x^* = 200\text{mm}$  (Figure 5.12a). The slow dynamic of this control in comparison with the two other controls is the aim of the design. In order to limit the acceleration of the vehicle, the absolute value of maximum  $q$ -current is restricted under 12A. This causes a reduction in the control dynamic. Moreover, a low-pass filter used in the speed loop is another cause. The filter is used to eliminate noises of speed feedback signal, which is the derivative of an incremental sensor signal. Therefore, a high time-constant filter is required. Finally, the dynamic of the longitudinal position control must be lower than the two other in order to improve the qualities of the motion control. Figure 5.12b shows the  $dq$ -currents of the simulation. The  $d$ -currents are not necessary for longitudinal position control ( $i_{dL} = i_{dR} = 0$ ). The  $q$ -currents are the same in order to generate thrust force by the sum of the tangential forces and not generate torque on the vehicle. In the figure, the limit of  $q$ -current can also be recognized.



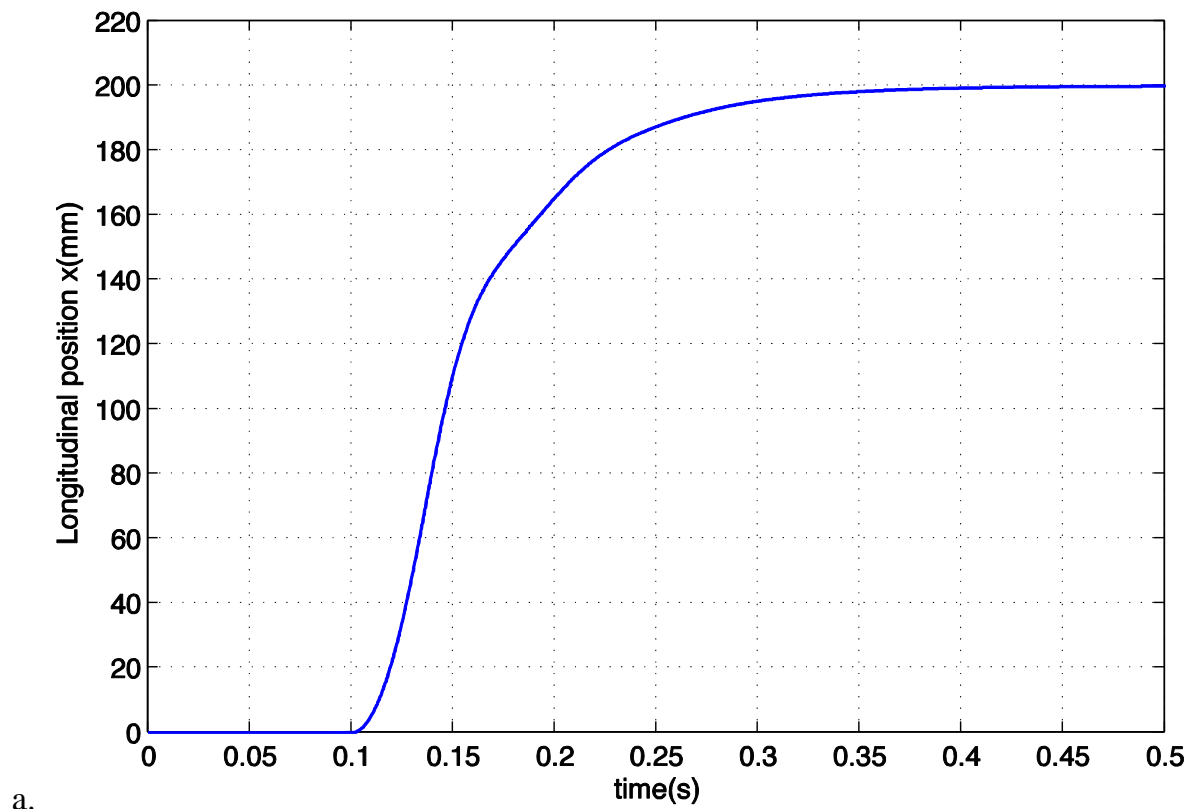
a.



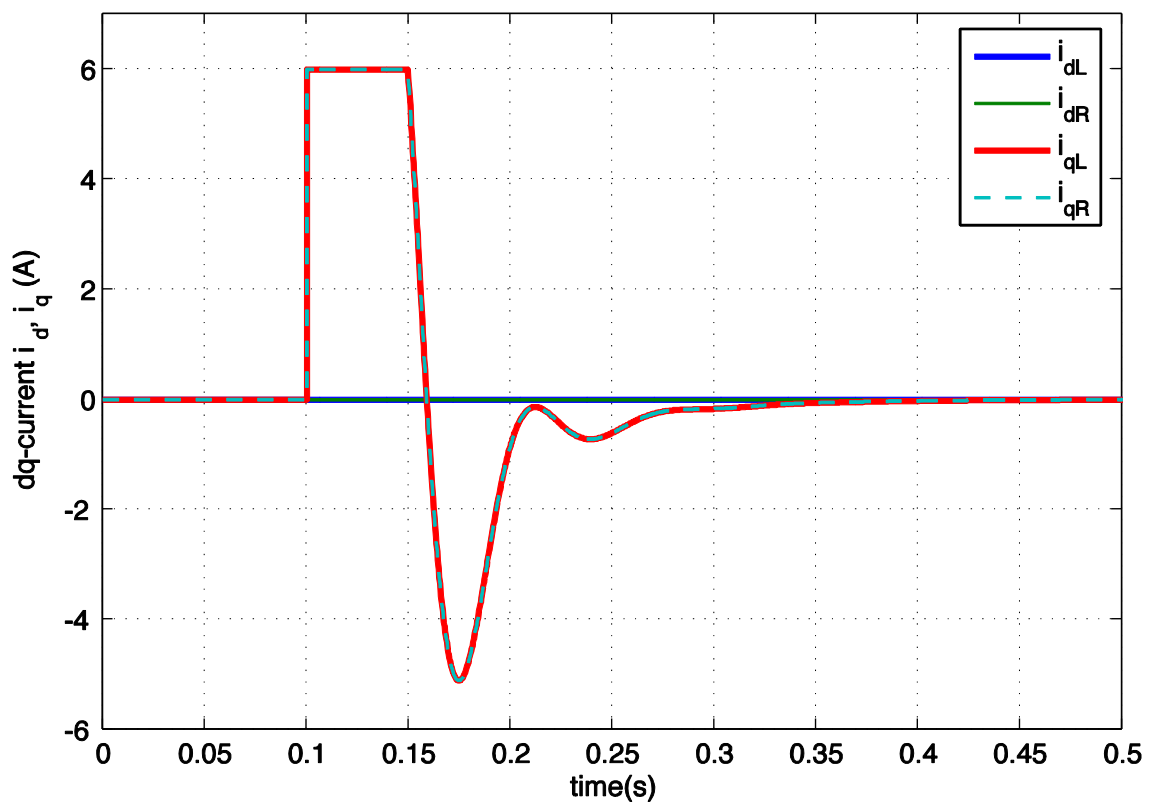
b.

Figure 5.11 Three DOFs in separated control – Yaw angle control.

a. Yaw angle; b.  $dq$ -currents.



a.



b.

Figure 5.12 Three DOFs in separated control – Longitudinal control.

a. Longitudinal position; b.  $dq$ -currents.

Second, the simulation results in the case of simultaneous control were performed. In this simulation, all DOFs are controlled simultaneously from the rest positions to desired positions. The parameters here were set for the same parameters like in the case of the separated controls. At the beginning, the vehicle was at the rest positions ( $\delta = -1.2mm$ ,  $\gamma = -8.0mrad$  and  $x = 0mm$ ). At  $t = 0.1s$ , all the control positions were set for desired values ( $\delta^* = 0mm$ ,  $\gamma^* = 0mrad$  and  $x^* = 200mm$ ). The vehicle was controlled to move centrally and parallel to the middle of the guide-way. The results display the response of the vehicle position in three DOFs as functions of time in Figure 5.13-Figure 5.15.

In Figure 5.13, all the three controlled variables are presented. They show the same performance as the results of separated controls do. That means the proposed control method can eliminate the coupling of the three DOFs of the simulation model. Each control variable ( $\delta$  or  $\gamma$  or  $x$ ) can be controlled independently.

In Figure 5.14 and Figure 5.15, the response currents of the primaries in the  $d$ - and  $q$ -axis with regards to the simultaneously control simulation are presented. Here, all the  $dq$ -currents are required instead of using the currents of only one axis (the  $d$ - or  $q$ -axis). As in the figures, the  $d$ -currents are required when the vehicle is controlled to move from the rest position to the middle of the guide-way. The  $d$ -currents are zero when the vehicle is in the middle of the guide-way ( $\delta = 0$ ). The difference of  $q$ -currents is necessary when the controller is steering the vehicle parallel to the guide-way ( $\gamma = 0$ ), and the sum of  $q$ -currents is used to push the vehicle along the guide-way.

As the results of the simulation presented here and many other simulations, the proposed control method could be suitable for the mathematical model of the PM LSM system. The linearized decoupling parameters in (4.38), (4.43) and (4.44) can compensate well for the nonlinear equations (4.34) and (4.35) used in the vehicle model. This leads to the well-controlled results of three DOFs control. Altogether, the simulation results are the foundation to implement the control method of the real experimental system in the next chapter.

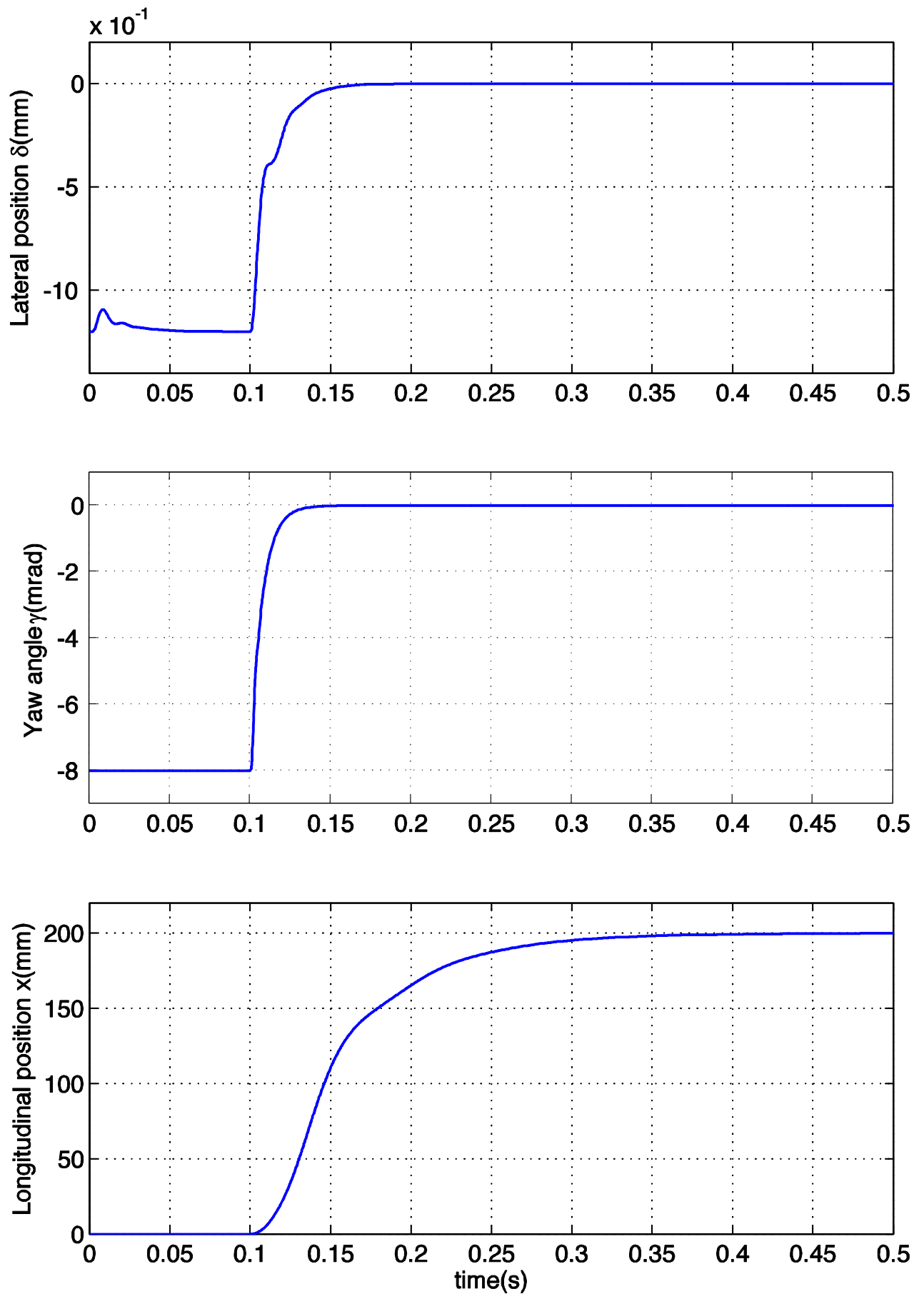


Figure 5.13 Three DOFs in simultaneous control.

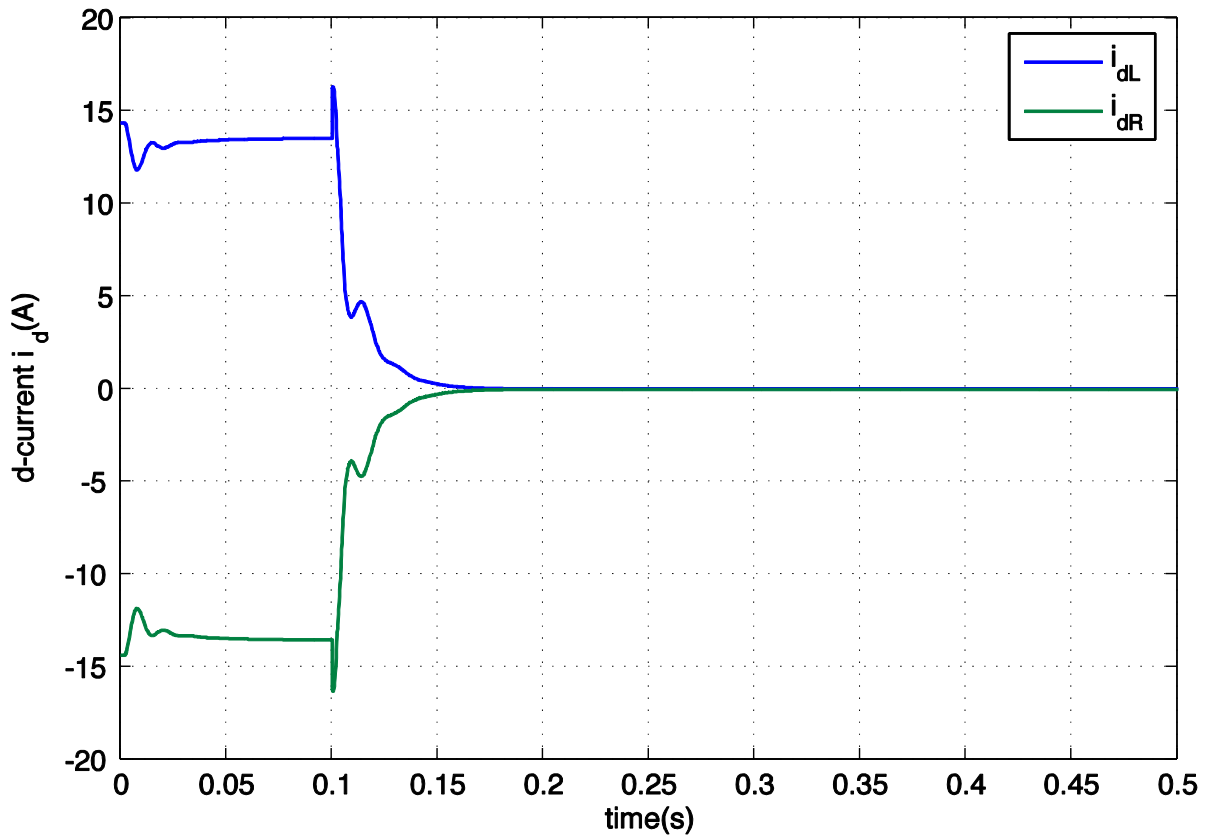


Figure 5.14 Primaries  $d$ -currents

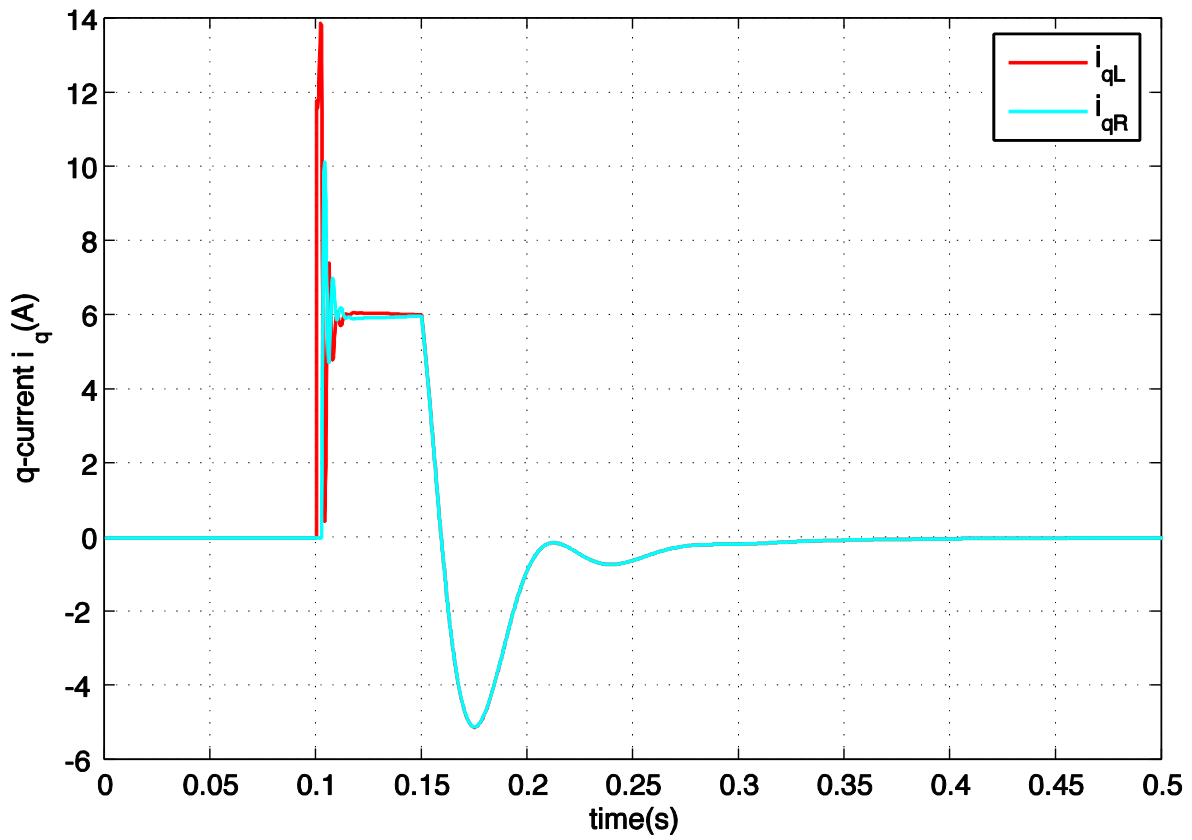


Figure 5.15 Primaries  $q$ -currents

## 6. MAGNETIC GUIDANCE EXPERIMENTS

The simulation model of the plant in chapter 5 is based on the analytical model, which was derived in chapter 4 using several simplifications. The proposed control method shows acceptable results in the simulations employing this simplified analytical model. In this chapter, the control method will be implemented in the real experimental setup presented in chapter 3. The implementation and the experimental results will be shown in the following.

### 6.1. Implementation of control method

Figure 6.1 presents the structure of the experimental setup, the implemented software and control method used for the four aspects: structure, hardware, software and control algorithm. The experimental equipment and setup were already outlined in chapter 3. In this section, the implementations of the equipment and the software will be shown.

The real experimental setup was initially assembled with one primary at each side of the guide-way. These two primaries compose a guiding segment for the vehicle as in Figure 6.1. This structure allows executing the experiments in three DOFs control. Later, another segment was added in order to conduct experiments with the vehicle in the transition area. One inverter supplies each primary a three-phase voltage using a 5 kHz switching frequency. The switching intervals are generated by the inverter interface board (IIB) with timing values transferred from the vehicle control interface (VCI) through the addressed bus communicating system. The timing values are sent to each IIB separately with its own address every  $100\mu s$ . In each IIB there are three AD converter channels. The first two channels (channel 1 and channel 2) of each IIB are used for current feedback signals from each primary. The third channel (channel 3) of the two IIBs are used for air-gap sensors. These current signals and air-gap signals are sent by IIBs to the VCI after receiving timing values (every  $100\mu s$ ).

All the inverters mentioned above are controlled by one PC based controller. The controller is a standard PC with INTEL 1.7 GHz processor. The control signals for the inverters and the feedback signals are transferred through the Vehicle Control Interface board (VCI) in a standard PCI slot. The VCI sends switching times to the inverters and receives the feedback currents from each inverter, together with air-gap values of the two inductive sensors through 16 bits communicating bus. It also

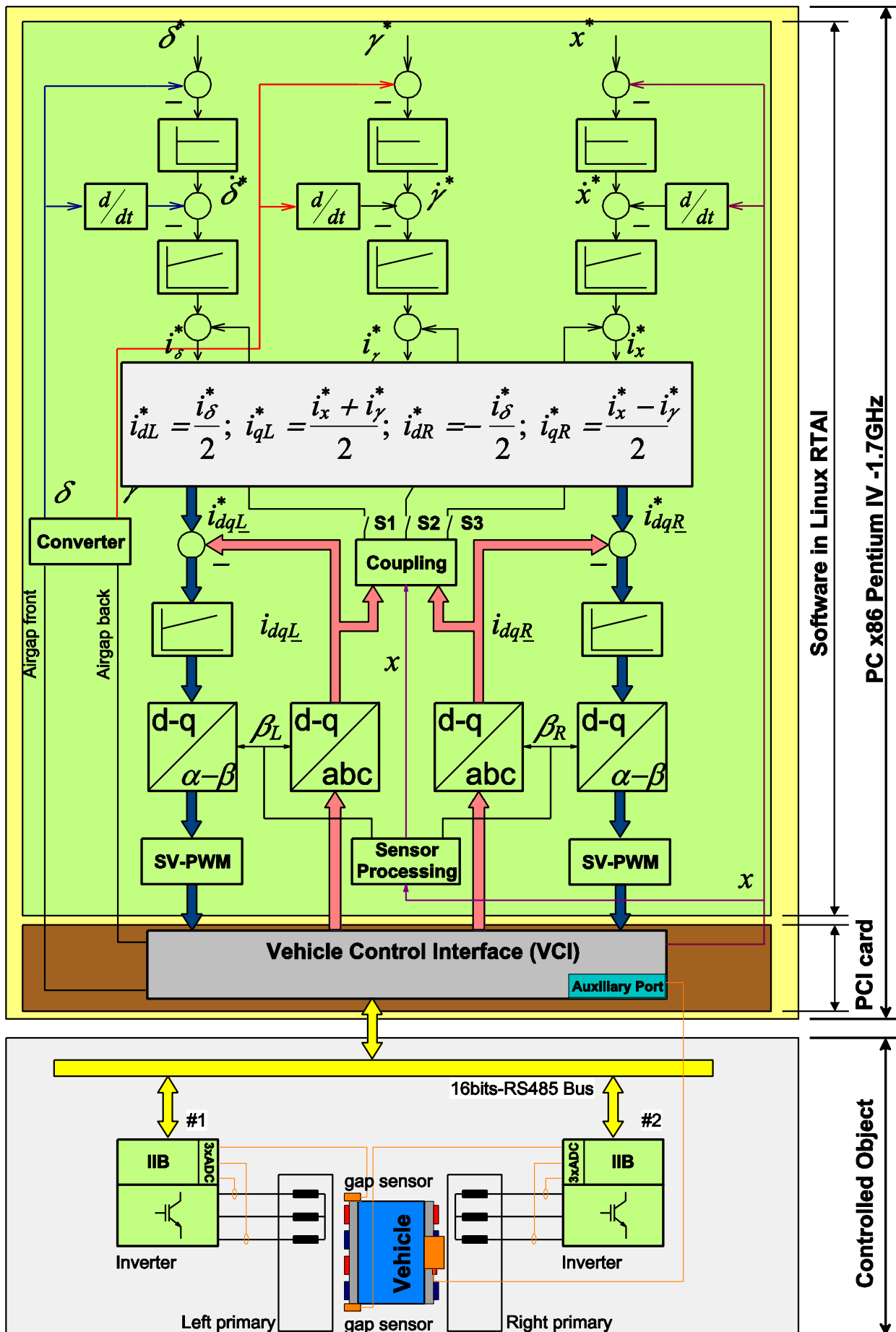


Figure 6.1 Implementation of experimental setup.



receives incremental signals from the position encoder through an auxiliary port. This exchange of data with inverters of one segment and the control software takes place every  $100\mu s$  under control of an interrupt service routine (ISR). The VCI generates one interrupt request (IRQ) to communicate with inverters of each segment every  $100\mu s$ . Therefore, the sampling time of each inverter control loop is  $100\mu s$ .

The control PC works under Linux Soho kernel 2.6.18 operating system with RTAI patch. The control program was written in C language. The user interface was programmed by Glade program for GTK+ toolkit. Regarding the control software, the algorithm was implemented as shown by the light green area in Figure 6.1. As mentioned in the previous chapter, the current controls were implemented by using the field oriented control algorithm with anti-windup PI controllers. The details are depicted in appendix B3. The other superposed control loops were also implemented with PI controller for speed loops and P controller for position loops as shown in the figure. Decoupling control can be applied by enabling switches S1, S2 and S3.

## 6.2. Lateral position control

With the implemented prototype above, the proposed control method was implemented and tested step by step. At first, the controller for each DOF was implemented in the control program. In this section, the experiment with the controllers in lateral position control loops will be presented.

In this experiment, the vehicle was kept parallel with the guide-way in a longitudinal position by the same mechanical structure used for the normal force measuring experiment (Figure 4.12, Figure 4.13). Only the lateral position ( $\delta$ ) of the structure could move freely in the  $y$ -direction under the limitation of two stators. The two other DOFs ( $\gamma$  and  $x$ ) were constrained in fixed positions. This arrangement enables the lateral position controller to be tested independently in the experimental system.

The control method was implemented only in lateral position loops with P controller for lateral position and PI controller for lateral speed as presented in chapter 5. The reference values for current control loops were implemented by the left- and right-  $dq$  currents:

$$i_{dL} = -i_{dR} = \frac{i_{\delta}^*}{2} \quad (6.1)$$

$$i_{qL} = i_{qR} = 0 \quad (6.2)$$

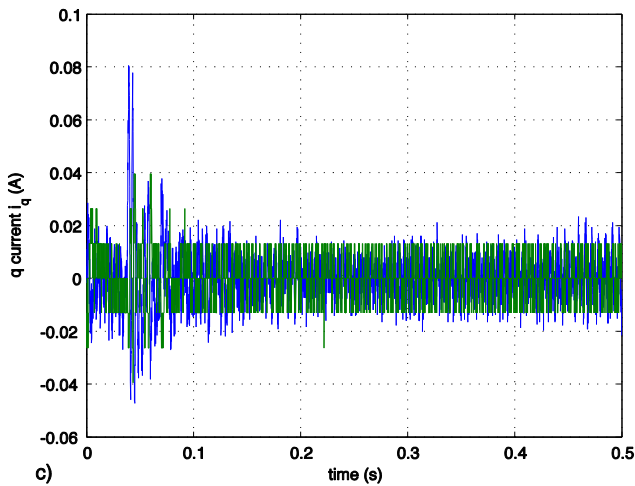
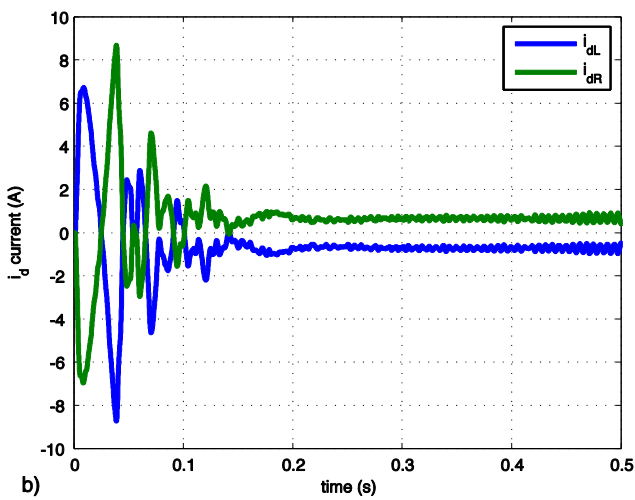
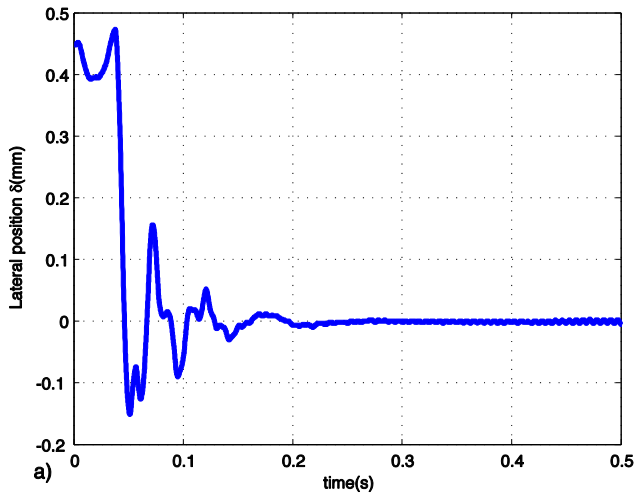


Figure 6.2 Lateral position control results from left rest side. *a) Lateral position  $\delta$ ; b) d-current of left- and right primary; c) q-current of left- and right primary.*

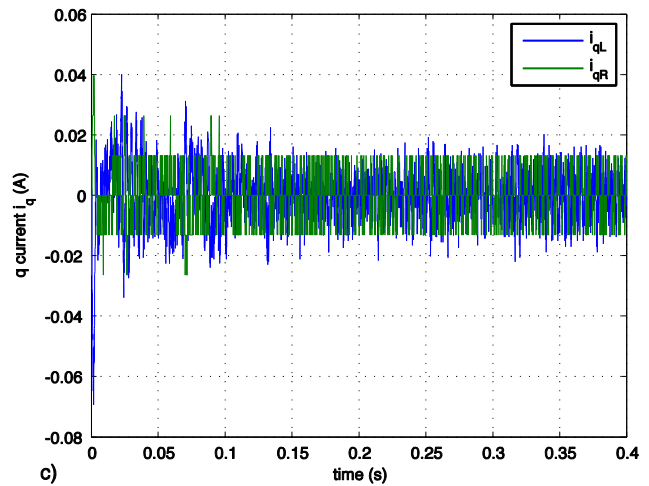
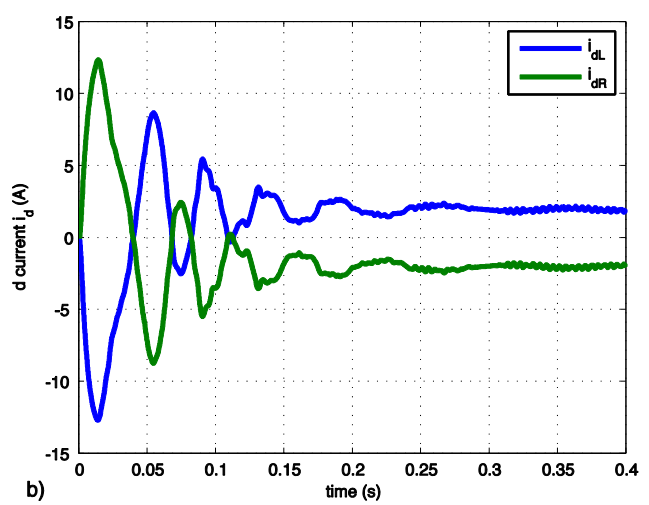
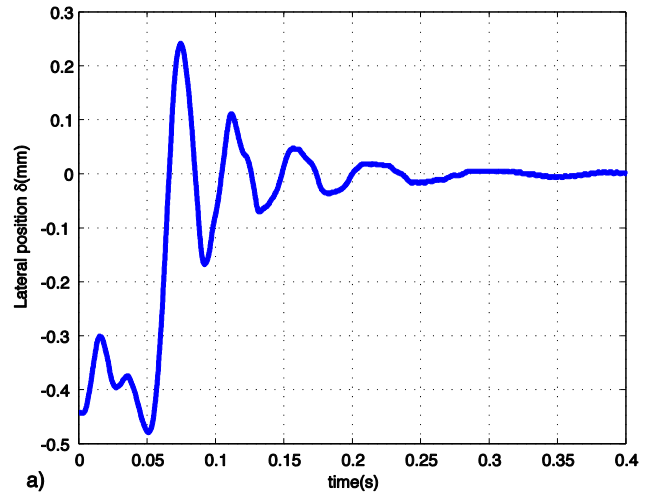


Figure 6.3 Lateral position control results from right rest side *a) Lateral position  $\delta$ ; b) d-current of left- and right primary; c) q-current of left- and right primary.*

The experiment was conducted by with the vehicle starting in the rest position on one side of the guide-way. At  $t=0$ , the controller started, and the lateral position reference  $\delta^*$  was set to zero. The control system guided the vehicle movement to the middle of the guide-way ( $\delta=0$ ). The experimental results are presented in Figure 6.2 and Figure 6.3 as the results of the vehicle moving from the left- and right-sides of the guide-way. In the figures, the  $dq$ -currents of the primaries are also presented. All the results are plotted as a function of time.

The experimental results show the independent lateral control ability as the simulation in chapter 5 did, in the qualitative aspect. The system can control the vehicle leaving the rest position to the middle of the guide-way. In the experiment, also only the difference of  $d$ -currents was required in order to generate the normal force while the  $q$ -currents were zeros. These show the ability of the controller in the case of independent lateral position control.

However, the experimental control quality here has a big difference in comparison with the simulation results shown in Figure 5.10. In this experiment, the controlled lateral position ( $\delta$ ) has several oscillations before the steady state. In  $dq$ -currents figures, the  $d$ -currents are not zero when the vehicle in the middle of the guide-way ( $\delta=0$ ). These caused by the imperfect mechanical structure. The experimental holding structure (Figure 4.12, Figure 4.13) cannot keep the vehicle absolutely parallel to the guide-way. Therefore, the rest position of the vehicle was changed to  $\delta=\pm 0.4mm$  in order to improve this condition. The structure also changes the parameters of the control system. Nevertheless, the controller designed with the ideal condition of the vehicle was used in the experiment, i.e. the vehicle can move freely and parallel to the guide-way at  $x=0$ . This causes the oscillation in the lateral position control. In addition, the imperfect mechanical structure makes the normal force generated by the PMs is not equal zero when the vehicle is in the middle of the guide-way ( $\delta=0$ ). Hence, the lateral current ( $i_\delta$ ) is required to generate a force balance with then PM's normal force at  $\delta=0$ , i.e.  $d$ -currents are not zero.

### 6.3. Yaw angle control

In the experiment to verify yaw angle control loops, the lateral position was fixed in the middle of the guide-way. The motion of the vehicle in the longitudinal direction was also constrained when the yaw angle ( $\gamma$ ) could change freely. This was realized using the mechanical structure shown in Figure 6.4. In the structure, the centre of the vehicle was fixed with an axle. The axle was arrested in the longitudinal

position in the middle of the guide-way by a ball-bearing that allowed the vehicle to only rotate around its centre.

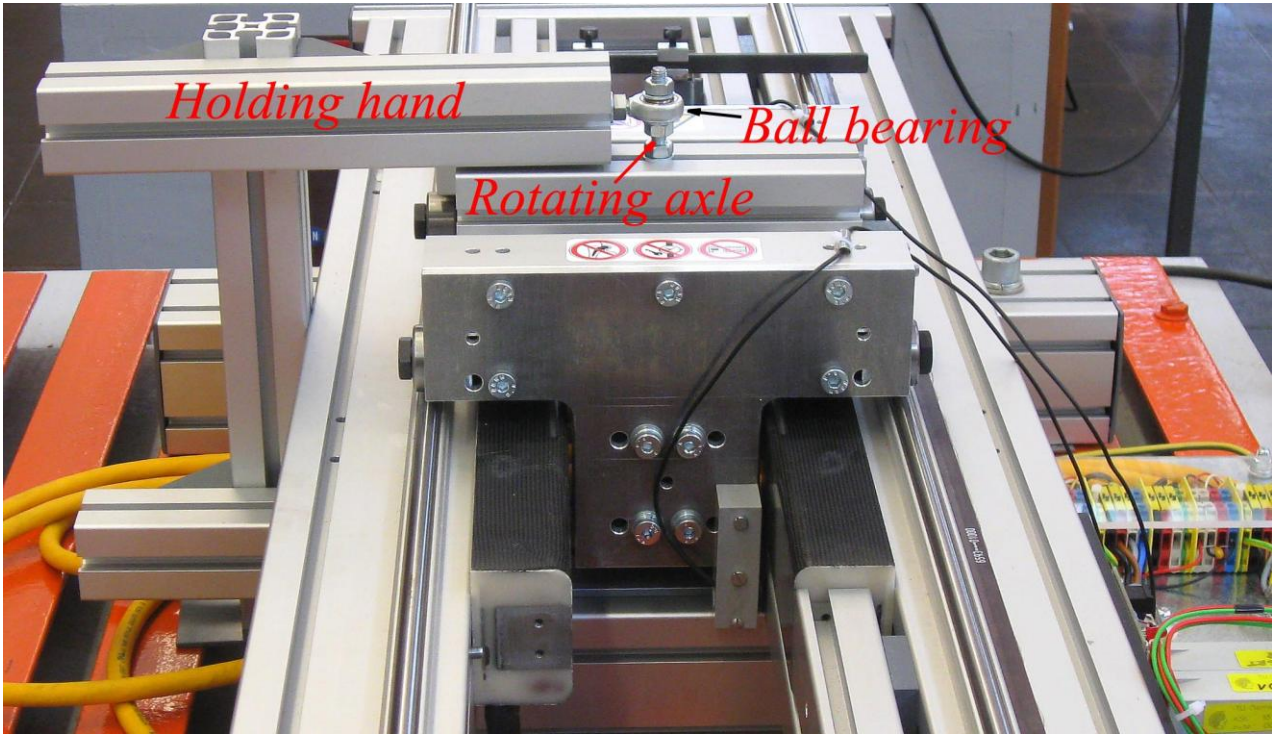


Figure 6.4 Testing set-up of yaw angle control

Similar to the lateral position control experiment, the control program here implemented only the controller for yaw angle control loops. The current reference values in this case were obtained by (6.3) and (6.4).

$$i_{dL} = i_{dR} = 0 \quad (6.3)$$

$$i_{qL} = -i_{qR} = \frac{i_{\gamma}^*}{2} \quad (6.4)$$

The experiment was done by controlling the yaw angle from the rest position ( $\gamma \approx 10\text{mrad}$ ) until the desired value ( $\gamma = 0$ ). Experimental results are displayed in Figure 6.5 with yaw angle ( $\gamma$ ) and  $dq$ -currents as a function of time. The results show good control quality in yaw angle control using  $q$ -currents.

In this experiment, the yaw angle was controlled well from the rest position to the desired value, as shown in Figure 6.5a. The control quality here is almost the same as the simulation result in Figure 5.11a is. The mechanical structure in this case causes not much problem as it does in the experiment with the lateral position control. The structure does not change the vehicle parameters, e.g. moment of inertial. Therefore, the controller parameters designed with ideal condition of the vehicle are used in this case without any effect to the control quality.

The experimental results in Figure 6.5b and c show the role of the  $q$ -currents in yaw angle control while the  $d$ -currents are zero as expected from the simulation and analysis.

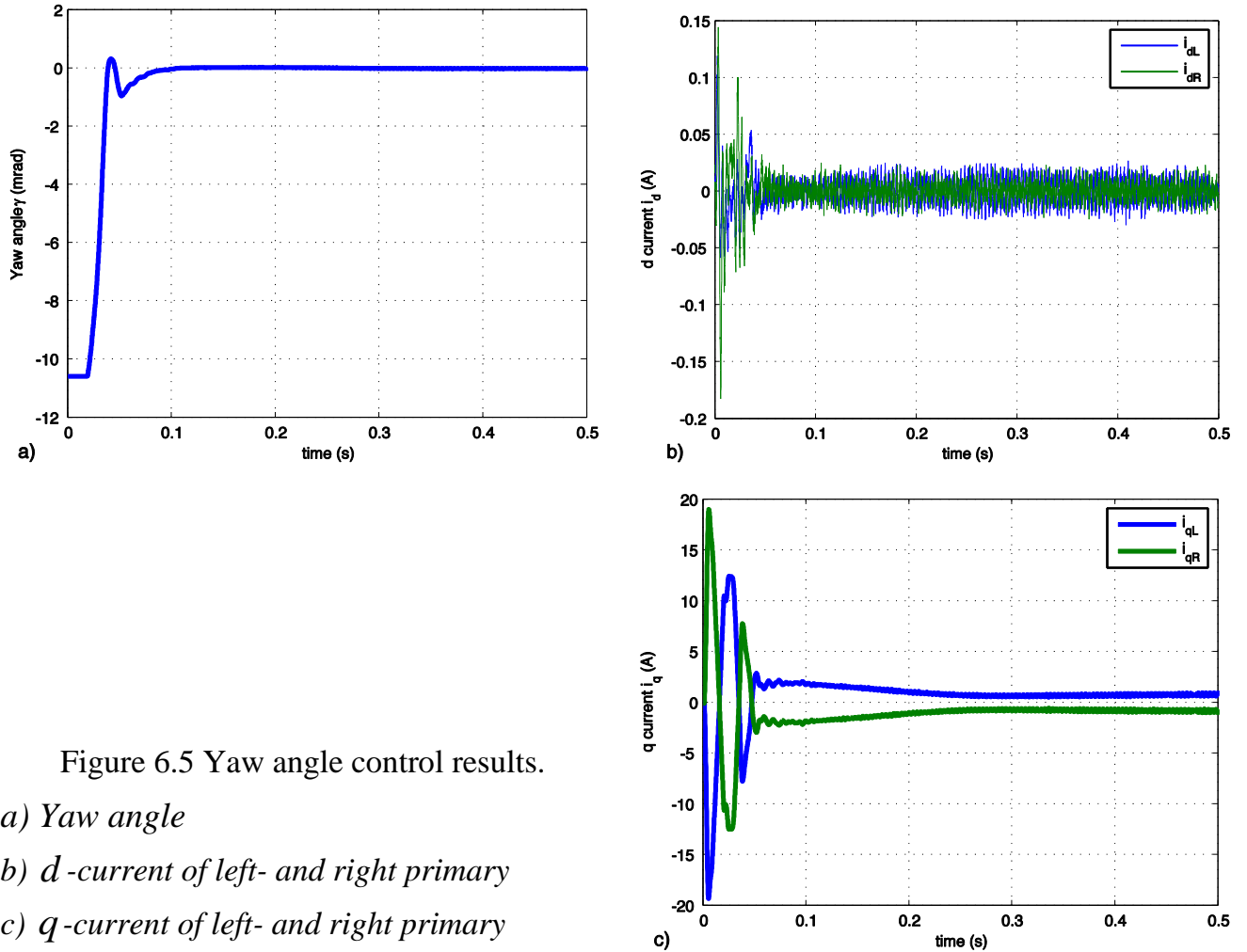


Figure 6.5 Yaw angle control results.

- a) Yaw angle
- b)  $d$ -current of left- and right primary
- c)  $q$ -current of left- and right primary

There are two small differences in this experiment results in comparison with the simulation results in Figure 5.11. First, there is a delay at the beginning of the control process. It is caused by the control electronic system. When the controller is not active, the VCI card does not communicate with the IIB cards. Therefore, all the feedback signals are at random values. This makes the output of the PI controller saturate at a limited value. At the moment, that the controller is started, the output of the PI controller feeds immediately the saturated value to current controllers. The current controllers react with that signal by generating an opposite yaw current ( $i_\gamma$ ) in the direction that increases the yaw angle. However, the mechanical structure constrains the vehicle not to rotate more. After a short delay time caused by the yaw speed filter and time constants of the controllers, the controllers regulate yaw current ( $i_\gamma$ ) to the correct direction. The yaw angle starts changing toward zero when the yaw current crossing zero. Thus, the yaw angle is constant in a short time at the beginning.

Second, the  $q$ -currents return to zero when the vehicle parallel to the guide-way ( $\gamma=0$ ) as the simulation results in Figure 5.11b shows. The reason is the imperfect mechanical structure like in the case of the lateral position control. Because of the imperfect structure, there is a small torque affecting the vehicle when the yaw angle ( $\gamma$ ) is zero. Hence, the  $q$ -currents are necessary in order to compensate the torque.

## 6.4. Three DOFs control

Experimental results in three DOFs control were obtained with the described experimental setup. A test was executed to check the control performance of the proposed method on the prototype system. In the test, all the motions of the vehicle in the horizontal plane were free moving. The controls of the three DOFs ( $\delta$ ,  $\gamma$  and  $x$ ) were simultaneously implemented. The four  $dq$ -current reference values of the left- and right-primary were implemented as in (6.5) and (6.6).

$$i_{dL} = -i_{dR} = \frac{i_{\delta}^*}{2} \quad (6.5)$$

$$i_{qL} = \frac{i_x^* + i_{\gamma}^*}{2}; i_{qR} = \frac{i_x^* - i_{\gamma}^*}{2} \quad (6.6)$$

The system was started with the vehicle in the rest position with the highest absolute value of delta ( $\delta_{\max}$ ) at the longitudinal position  $x=100mm$ . At  $t=0.1s$ , the references values  $\delta^*$  and  $\gamma^*$  were set to zero and  $x^*=100mm$ , the mover was controlled to parallel the guide-way and to move to the middle of the guide-way. At  $t=0.4s$ , the reference for the longitudinal position was set to  $x^*=300mm$ . At  $t=0.9s$ , the reference  $\gamma^*$  was established to a new value of  $0.5rad$ .

To identify differences between the standard cascade controller and the compensated cascade controller, the experiments were implemented with and without decoupling. Without decoupling, the controller considers only the force and torque terms  $K_{\delta} \cdot i_{\delta}$ ,  $K_x \cdot i_x$ ,  $K_{\gamma} \cdot i_{\gamma}$ , the couplings in the plant, i.e.  $K_{xp} \cdot i_{\gamma} \cdot \delta$ ,  $F_{\delta p}$ ,  $K_{\gamma p} \cdot i_{\delta} \cdot \delta$  were assumed as perturbations. With decoupling control, the couplings were compensated by feed-forward calculations as mentioned in chapter 5. The measured lateral position, the yaw angle and the longitudinal position of the first case are shown in Figure 6.6 as a function of time. The results of the second case are shown in Figure 6.7.

As the experimental results in Figure 6.6 and Figure 6.7 show, it is easy to recognize that the control system can work without compensation. However, the

control quality is poor, particularly at the beginning when the lateral displacement  $\delta$  is high, causing the perturbation  $F_{\delta p}$  to considerably effect the control quality. The control quality is much better when compensation is used.

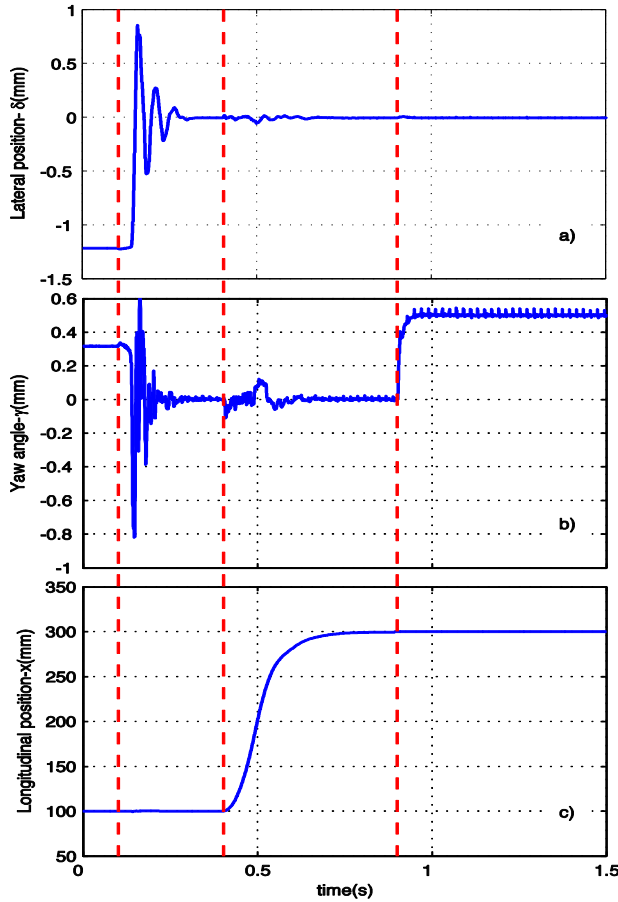


Figure 6.6 Start-up and movement control (experimental); a) lateral position, b) yaw angle and c) longitudinal position without compensation

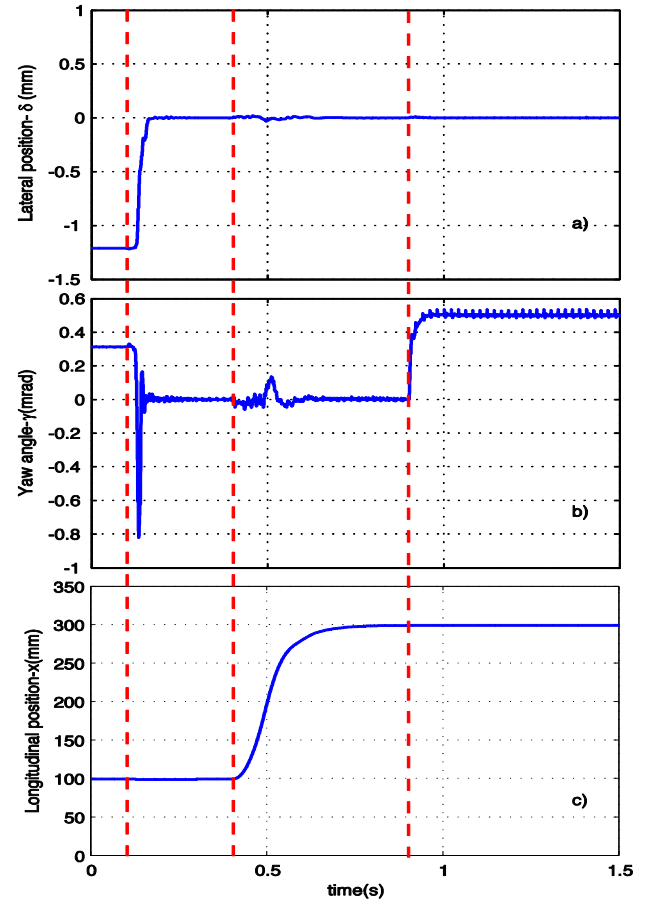


Figure 6.7 Start-up and movement control (experimental); a) lateral position, b) yaw angle and c) longitudinal position with compensation

The current  $i_d$ , used for  $\delta$  control, and the current  $i_q$ , used for  $\gamma$  and  $x$  control, are components of the same current vector. As a result of the inverters' limitation, the magnitude of the current vector must be limited by limiting each of its components. However, the attractive force between the primary iron-core and the PM (lateral force) is very high. Therefore, in the control algorithm, a higher priority was given to the current component of lateral position  $\delta$  control ( $i_d$ ) while the other component ( $i_q$ ) was limited as shown in chapter 5. This is the reason why after  $t=0.1s$  lateral position ( $\delta$ ) is well controlled and yaw angle ( $\gamma$ ) oscillates in a short time. However, at  $t=0.9s$  when the vehicle is in the middle of the guide-way, the lateral force remains balanced. Consequently,  $i_d$  was small at that time, thus a step up in  $\gamma$  reference responded with higher quality.



During the movement of the vehicle from  $100\text{mm}$  to  $300\text{mm}$ , there was some disturbance in  $\gamma$  and  $\delta$  measurement results. The disturbance in the yaw angle result was high in areas of acceleration or deceleration of longitudinal movement, since the system gave these areas high thrust generating priority, as there was nearly no demand for d-axis current. As the presented results illustrate, the ability to start-up from the rest position shows that the controller was able to guide the vehicle within the guide-way. The decoupling control could compensate all couplings between delta and gamma control loops to improve the control quality.

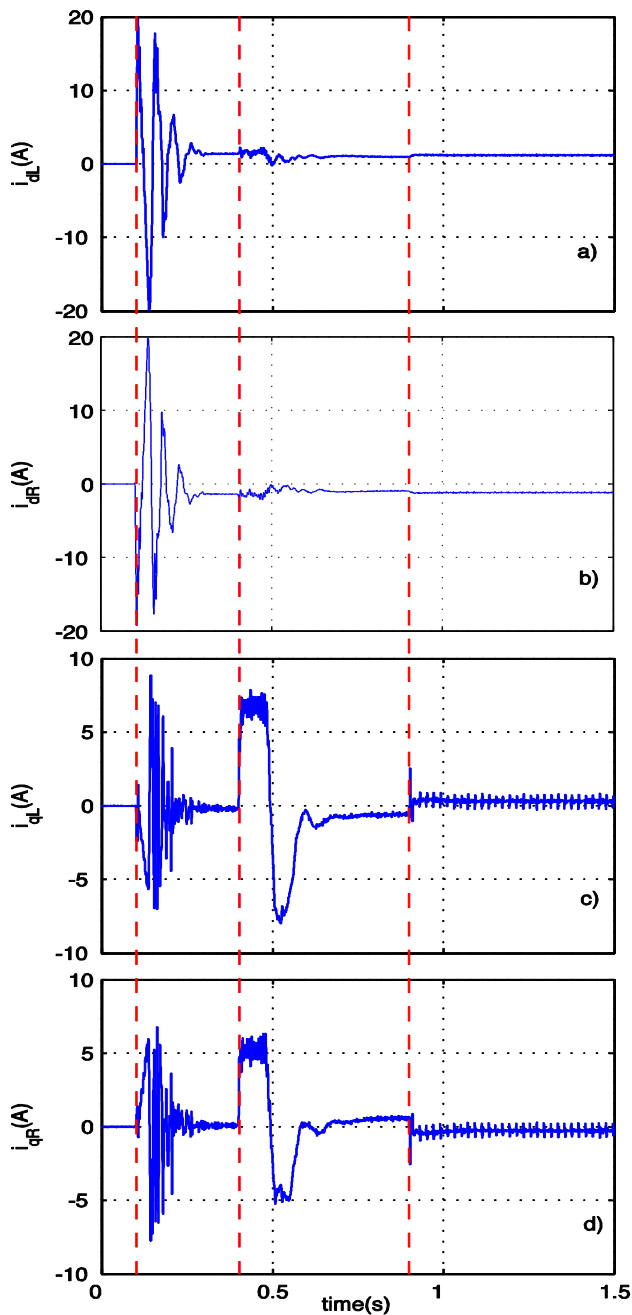


Figure 6.8 Field oriented control current  $i_d$ ,  $i_q$  of left and right side without compensation.

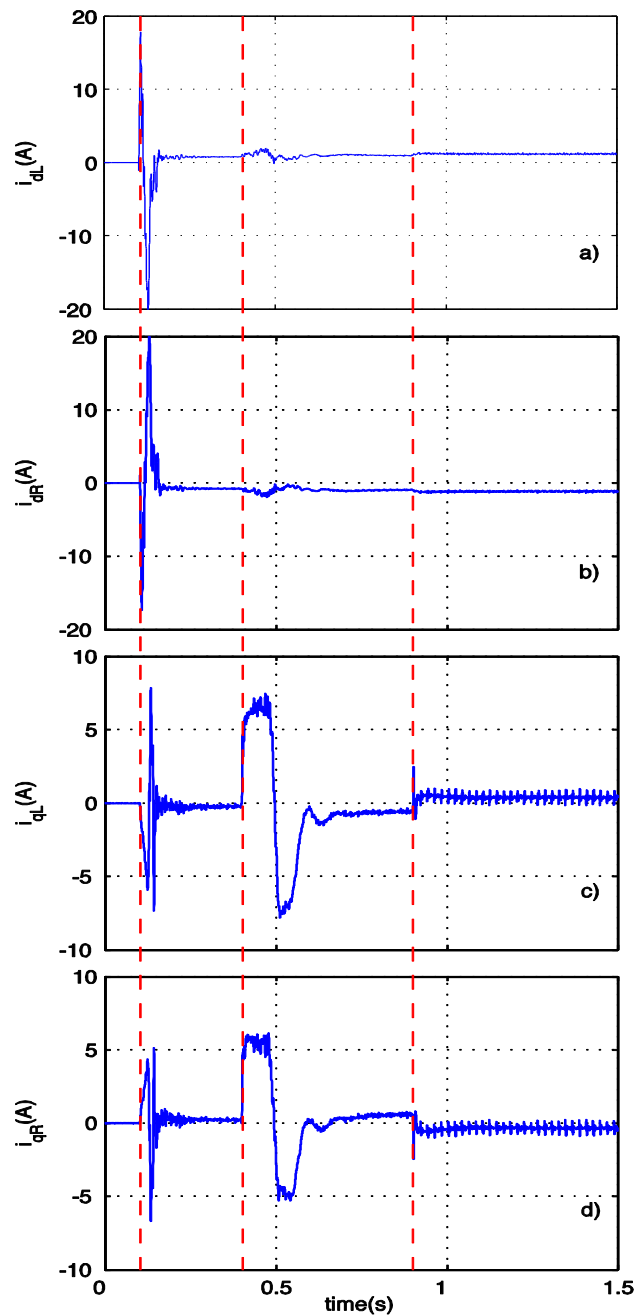


Figure 6.9 Field oriented control current  $i_d$ ,  $i_q$  of left and right side with compensation.



The resulting measurements of current  $i_d$  and  $i_q$  are presented in Figure 6.8 and Figure 6.9 as functions of time. In Figure 6.8a-b and Figure 6.9a-b, the current  $i_{dL}$  and  $i_{dR}$  were symmetrical. They were very high when the delta position of the vehicle was controlled from the rest position to zero. When the vehicle was in the middle of the guide-way, the required currents  $i_d$  were much smaller (almost zero). The currents  $i_{qL}$  and  $i_{qR}$ , which are shown in Figure 6.8.c-d and Figure 6.9.c-d, generated the thrust force and rotational torque for the vehicle. Consequently, the total and difference of  $i_{qL}$  and  $i_{qR}$  changed correlatively when the vehicle was moving or rotating. They changed in the same direction when thrust force was required, and they changed in opposite direction when torque was required.

## 6.5. Perturbation in longitudinal traveling

In this experiment, a test was carried out to check the effect of  $x$ -axis motion on the lateral motion and the yaw rotations. In addition, the viability of guiding the vehicle across a junction between two segments was also tested. By moving the vehicle position from one segment to the next segment at different speeds, the measurement results will show the effect of the longitudinal speed on the lateral- and yaw-control qualities. The junction area between two segments also affects control qualities, as presented in the results of this section.

The experiments were implemented with the experimental structure presented in Figure 6.10. In the structure, one more segment was added in order to test the guiding viability of the vehicle when it crosses the junction area between two segments. This requires two additional inverters. All four inverters (#1 ÷ #4) were controlled by the control PC via the VCI card. To communicate with the inverters, the VCI generated one communicating IRQ every  $100\mu s$  for every inverter in each segment. With the experimental structure, the inverters of each segment receive a command to run or standby depending on the vehicle position. The command is determined by the address decoding block. When the vehicle is in segment  $n$  (or  $n+1$ ), the inverters of segment  $n$  (or  $n+1$ ) are active and the inverters of the other segment are on standby. When the vehicle is in the junction area, all four inverters are active to guide the vehicle through the area.

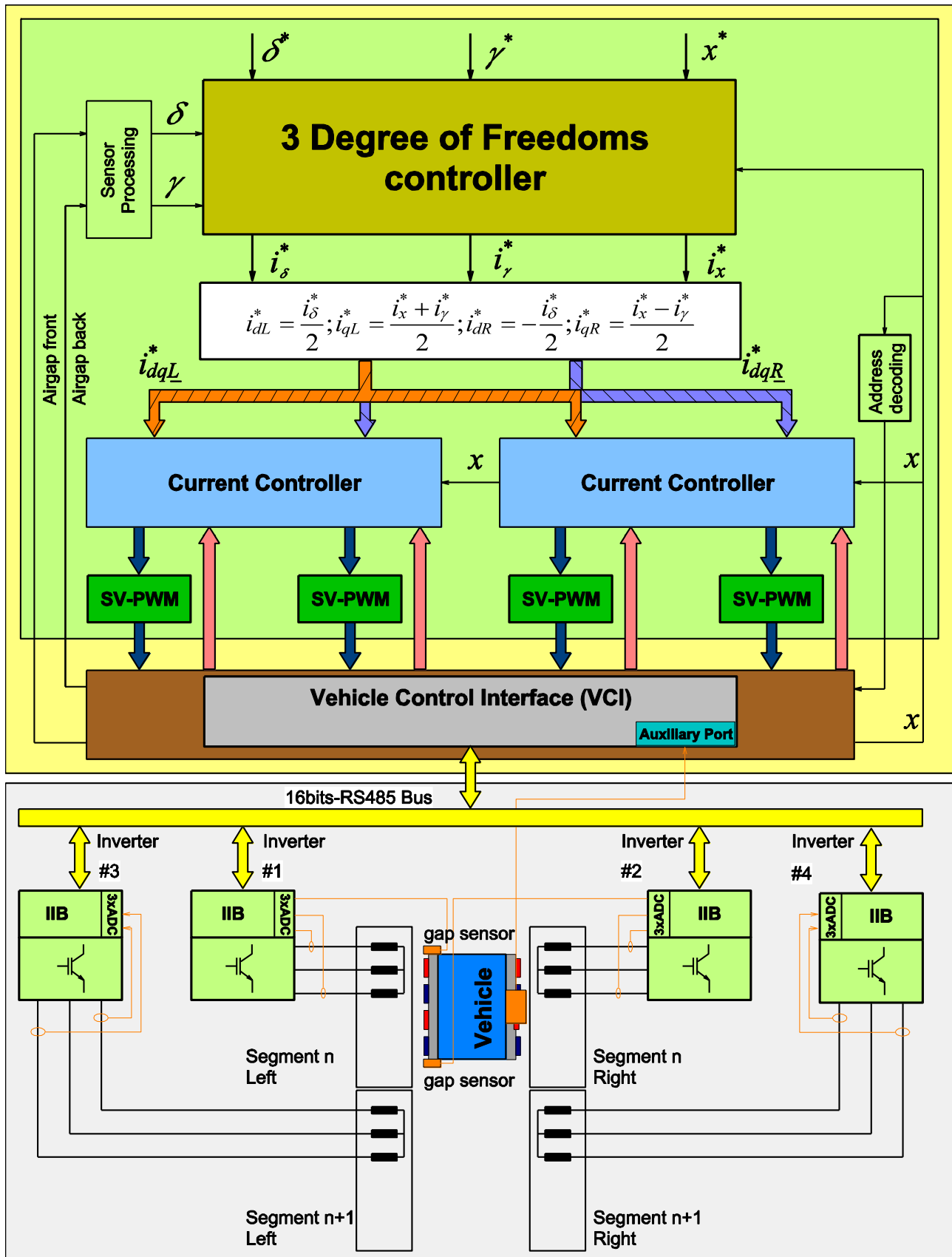


Figure 6.10 Multi segments structure

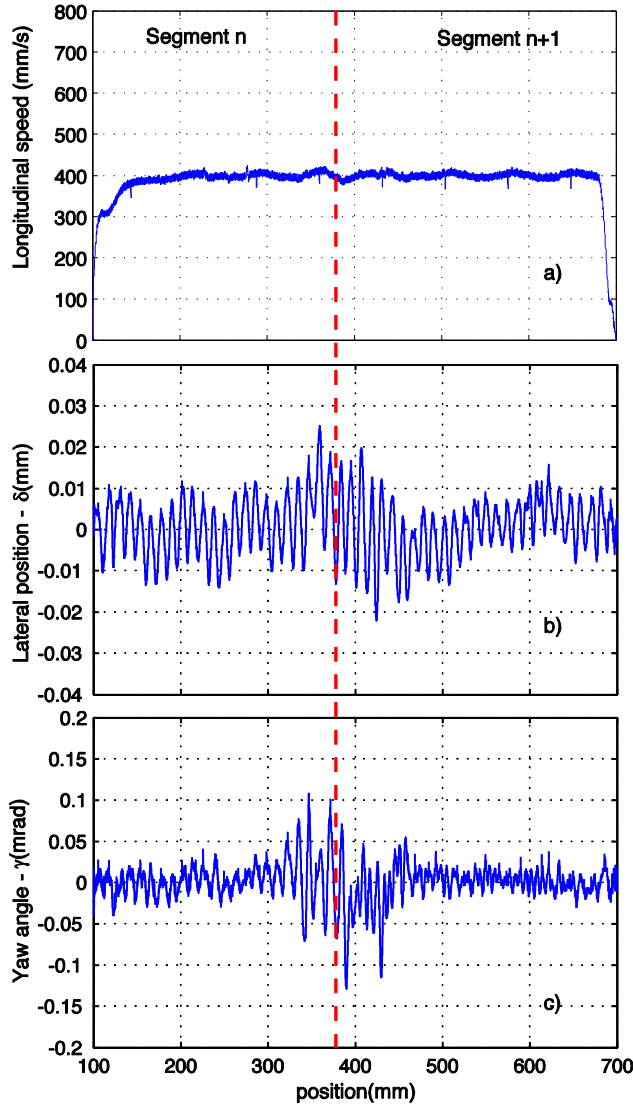


Figure 6.11 The speed, delta, gamma of the vehicle as functions of position

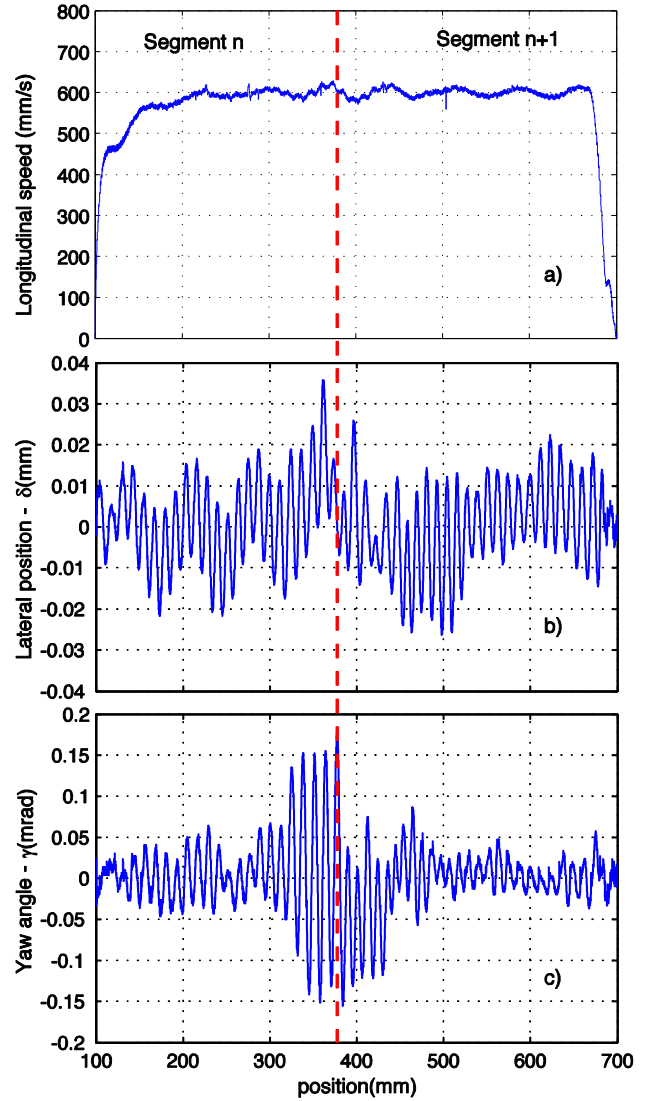


Figure 6.12 The speed, delta, gamma of the vehicle as functions of position

Using the structure in Figure 6.10, the experiments were executed as follows. At the beginning, the vehicle was controlled to stay in the middle of the guide-way at position  $x^* = 100\text{mm}$  (segment 1). At  $t = 0.1\text{s}$ , the reference position was set to  $x^* = 700\text{mm}$  (segment 2). The experiments were implemented with different longitudinal speed references. Figure 6.11 and Figure 6.12 show results of speed, delta and gamma as a function of position. In Figure 6.11, the vehicle was set to run at the speed of  $400\text{mm/s}$  and in Figure 6.12 at  $600\text{mm/s}$ . The results firstly show the ability of the controllers to guide the vehicle moving from one segment to the other. Secondly, the results show that the speed of the vehicle affects the quality of the lateral position ( $\delta$ ) and yaw angle ( $\gamma$ ) control. A higher speed results in lower qualities of the lateral position ( $\delta$ ) and yaw angle ( $\gamma$ ) control. The reason of these low qualities is the cogging force caused by the primary tooth structure mentioned in

the simulation results in Figure 4.11. The inhomogeneous structure of the tooth and slots structure makes the flux density in the air-gap is not smooth along the guide-way. Hence, the normal force is rippled when the vehicle moves. At low speed, the PI controllers can compensate the ripple. However, at high speed, the normal force ripples with higher frequency that the controller cannot compensate well. This results low qualities in the lateral position ( $\delta$ ) and yaw angle ( $\gamma$ ) control.

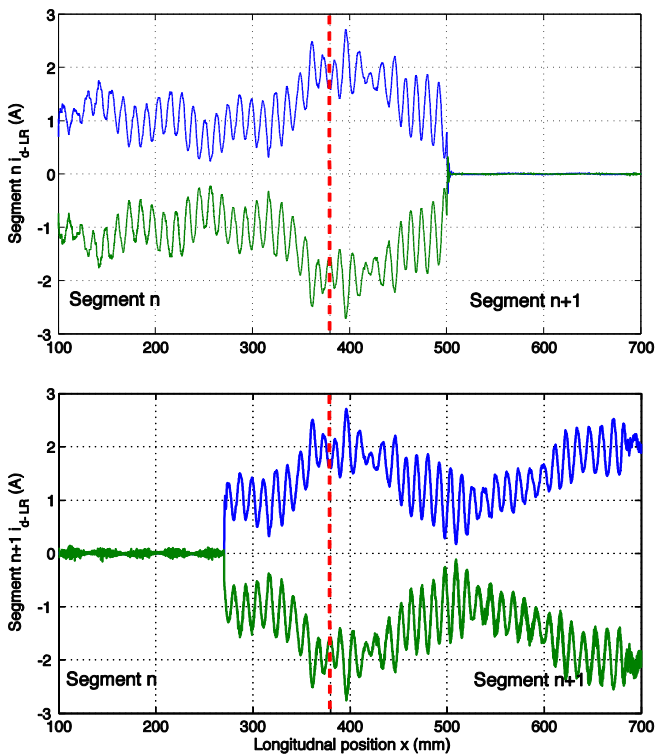


Figure 6.13  $d$ -currents when the vehicle crosses two consecutive segments

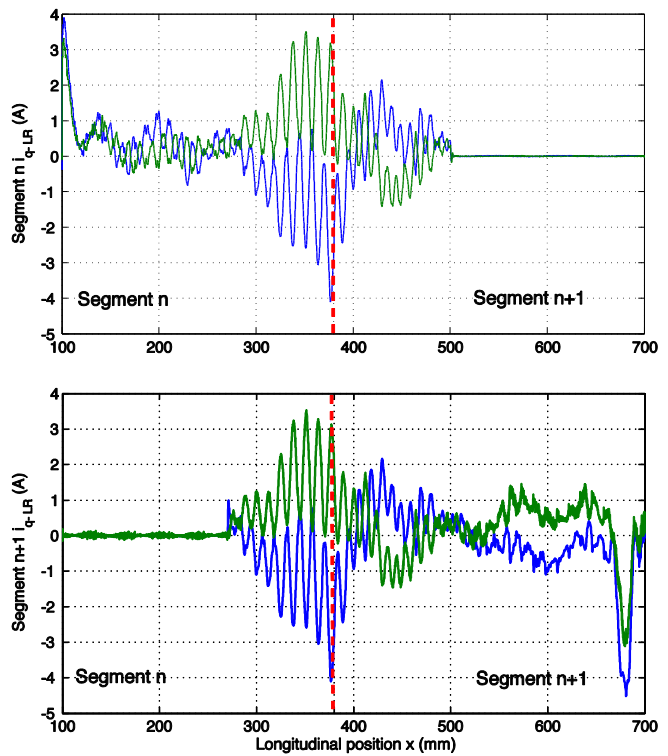


Figure 6.14  $q$ -currents when the vehicle crosses two consecutive segments

As shown in Figure 6.11 and Figure 6.12, the  $\delta$  and  $\gamma$  signals vibrated more when the vehicle moved through the junction point of two segments (position  $x = 380\text{mm}$ ). In this area, the flux density generated by the primaries currents is weakened because of the end-effect phenomenon. This changes the parameters of the control system and causes the poor control quality in the area. The detail of this phenomenon and the methods to improve the control quality in this area can be referred in [13].

In order to save energy, only the inverters of the segment with the moving vehicle are activated. The other inverters are inactive. This function is presented in Figure 6.13 and Figure 6.14. The  $dq$ -currents, as a function of longitudinal position ( $x$ ) in Figure 6.13 and Figure 6.14, show the active inverters depending on the vehicle position. The currents of the inverters were active when the vehicle was in the junction areas of their segment or inside their segment. The results also present the high requirement of current when the vehicle is in the junction area (highest at the

junction point presented by red dash line). This is the result of the reduced magneto motive force (MMF) in the first and last pole of each primary, due to a lack of windings [45]. The ripple in control currents is caused by the primaries' tooth ripple force.

## 7. CAPACITIVE SENSOR

In the magnetic guidance of the mover in a long-primary linear motor, the vehicle, which was proposed as the short secondary of the linear motor, is controlled to run in the middle of the guide-way by the primary magnet. The feedback signals required for the control system are the lateral position  $\delta$ , the yaw angle  $\gamma$  and the vehicle's longitudinal position  $x$ . The signals are provided by the sensors mounted in the linear motor system.

With the desire to have a passive vehicle for industrial processing and material handling applications, the active parts of the sensors must be mounted on the guide-way: the static part of the system. That means neither information nor auxiliary power between the surrounding environment and the vehicle must be exchanged. But the inductive, eddy current based sensors which were used in the previous chapters need both: energy and information transfer between the stationary and the moving parts of the system. For this reason, a new sensor prototype for measuring lateral and yaw values was designed and implemented in the magnetic guiding system. The new sensor prototype does not need energy and information transfer between the stationary and the moving parts of the system and was developed in order to replace the industrial inductive sensors, which are used in the previous discussed experiments. For longitudinal measurement, the sensor proposed in [52] and [53] can be used.

To determine the lateral position  $\delta$  and the yaw angle  $\gamma$ , we can use many different sensor principles, particularly with the inductive principle or the capacitive principle. In theory, several possible sensor prototypes can be used. In this dissertation, we further develop the capacitive sensor concept to obtain a new solution.

### 7.1. Capacitive sensor structure

#### 7.1.1. Mechanical structure

In order to simultaneously measure the lateral position  $\delta$  and the yaw angle  $\gamma$  as the vehicle moves along the guide-way, the designed capacitive sensor is proposed to consist of two symmetrical parts: the static part and the moving part. As mentioned, the static part of the sensor was designed to be active with a connecting cable to supply energy and to receive measuring signals. The moving part is simply a couple

of electrodes on a passive printed circuit board. The overview of the capacitive sensor is presented in Figure 7.1. At the left side of the figure is the front cross-section of the linear motor system with the desired capacitive sensor and on the right side is the simple 3D drawing of the capacitive sensor.

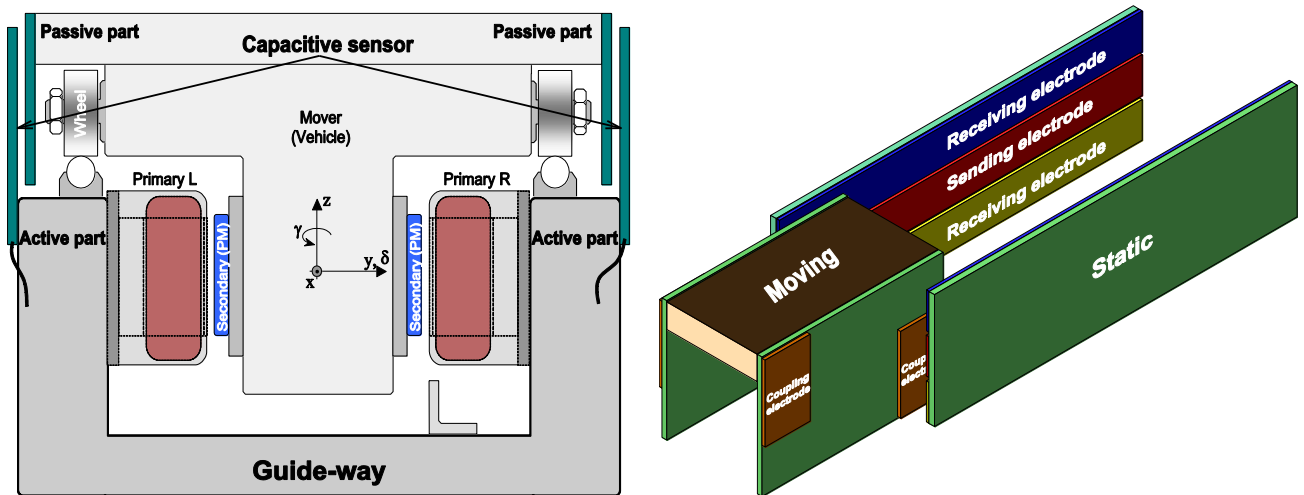


Figure 7.1 Overview of the capacitive sensor

As seen in Figure 7.1, the static part of the sensor includes two similar printed circuit boards mounted symmetrically on the left and right of the guide-way with the two printed circuit boards are extended over the whole length. In each printed circuit board, there are three copper electrode strips arranged in parallel to the guide-way. The middle strip is assigned as the sending electrode, and the two others are assigned as receiving electrodes. All the excitation signals and the output signals of the capacitive sensor are connected to these electrodes on the guide-way of the linear motor system. Therefore, the static part of the capacitive sensor is also called an “active part”. The detail of the printed circuit board in the static part is presented in Figure 7.2.

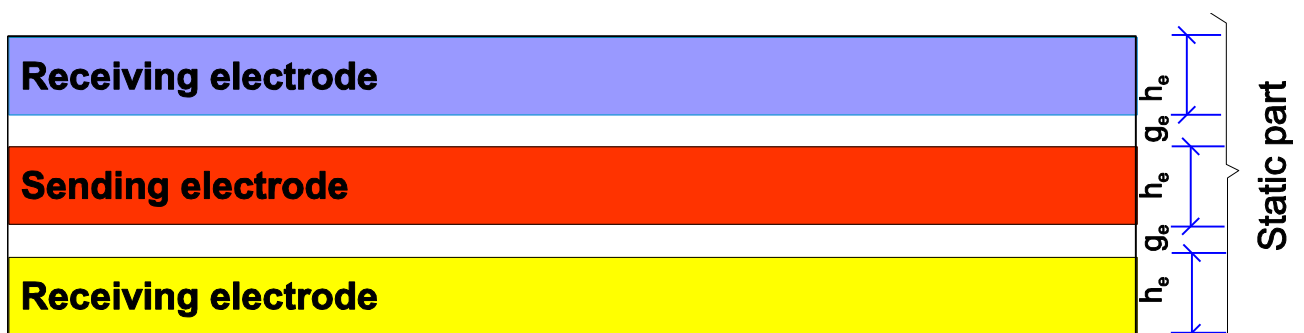


Figure 7.2 Static part of the capacitive sensor

The moving part (passive) mounted on the vehicle also has two symmetrical printed circuit boards on the sides of the vehicle. The printed circuit boards extend over the length of the vehicle, and there are two rectangular copper coupling

electrodes on each one. The two coupling electrodes are symmetrical with respect to the center of the printed circuit board. They are situated in two corners of the board. Each coupling electrode covers one sending electrode and one of the two receiving electrodes. With this arrangement, a capacitor is generated between each sending electrode - coupling electrode - receiving electrode, which is made up by two single capacitors in serial connection. In total, there are four capacitances generated between the sending electrodes, the receiving electrodes and the coupling electrodes. The printed circuit board in the moving part of the capacitive sensor is presented in detail in Figure 7.3. The figure describes only one side, the other side is mirrored to the centerline of the vehicle.

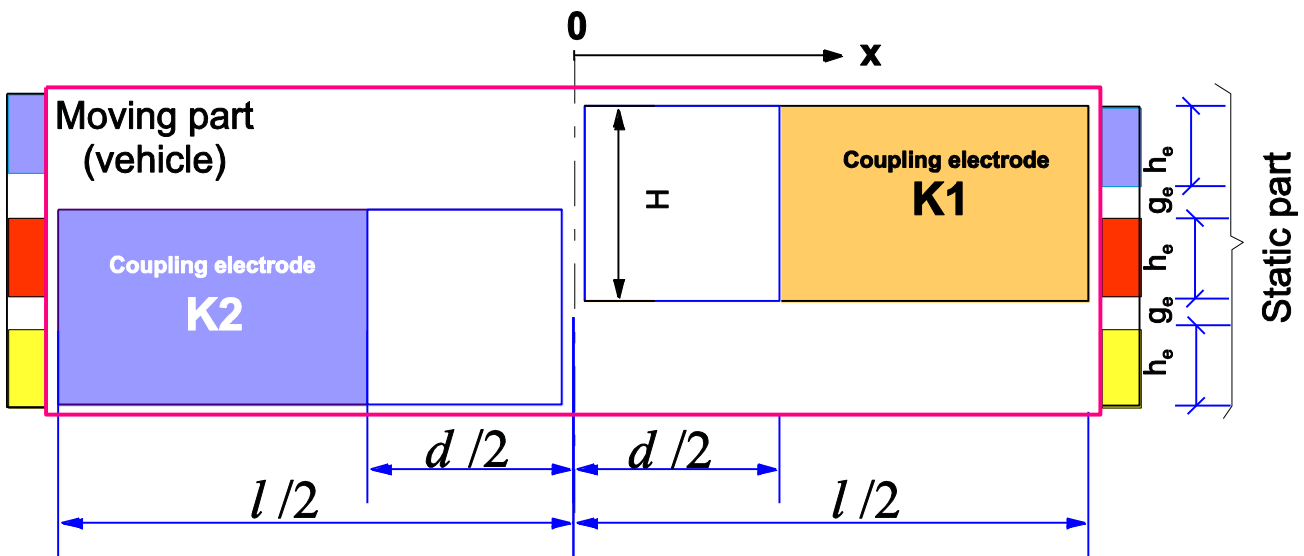


Figure 7.3 Moving part of the capacitive sensor

### 7.1.2. Electric circuit

With the mechanical arrangement presented in the previous subsection, the coupling electrodes generate four capacitors  $C_1$  to  $C_4$  between the sending and receiving electrodes. These capacitors have capacitances that vary with the change of lateral position  $\delta$  and yaw angle  $\gamma$  of the vehicle. The idea of the capacitive sensor is to determine  $\delta$ ,  $\gamma$  values by measuring capacitances  $C_1$  to  $C_4$ . However, measuring the absolute values of such small capacitances is a difficult matter. Therefore, a bridge circuit was created by connecting the varying capacitors, as in Figure 7.4.a. The circuit can be represented simply as in Figure 7.4.b with an additional resistor branch. The resistor branch is added to generate a reference voltage. The resistors used in the branch have the same values in order to generate a reference voltage of  $u_{ref} = u_0 / 2$ . The bridge circuit has output voltages  $(u_1, u_2)$  with regard to the reference voltage. These output voltages  $(u_1, u_2)$  are sensitive to the ratio of the



capacitances (not to their absolute values) in the capacitive branches. In other words, the output voltages are sensitive to variations of lateral position  $\delta$  and yaw angle  $\gamma$  of the vehicle.

The sending electrodes ( $S12$  and  $S34$ ) in the circuit are powered by a high frequency sinusoidal voltage. The receiving electrodes  $E1 \& E3$  as well as  $E2 \& E4$  are connected together to define the measured voltages  $u_1$  and  $u_2$ .

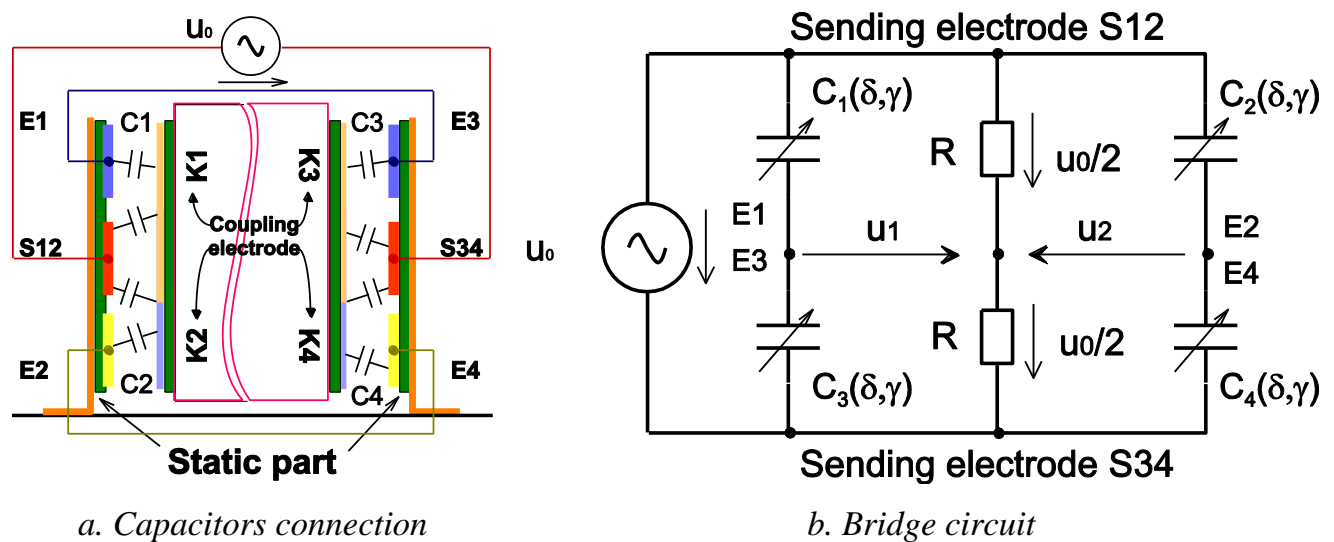


Figure 7.4 Capacitive bridge

The output voltages ( $u_1$ ,  $u_2$ ) of the capacitive bridge are collected and routed to the controller via an electronic circuit, as presented in the block diagram Figure 7.5. In the figure, the signal generator produces a  $100kHz-10V$  sinusoidal signal. The signal is supplied to sending electrodes  $S12$  and  $S34$  of the capacitive bridge as an exciting signal for the sensor system. The output voltages, which carry the information of the lateral position and the yaw angle from the bridge, are sent to the input channels of a sensor adapter board. The voltages are similarly processed in both channels. In the sensor adapter channels, the low frequency noise is filtered from the voltages with high-pass filters. The filtered voltages are then amplified and sent to synchronous demodulators. Here, the voltages are synchronously demodulated with the synchronous signal, which is phase shifted from the exciting voltage. The synchronous demodulator eliminates the carrying frequency from the voltages to obtain the valuable DC output signals. After that, the high noise frequency is filtered from the demodulated signals and then amplified one more time to obtain smooth suitable signals for the next signal processing step. Finally, they are sent to the output of the adapter as voltages  $u'_1$  and  $u'_2$ , carrying information of the lateral position  $\delta$  and the yaw angle  $\gamma$ . The output signals of the adapter are fed to the third AD converter channels of the inverter interface boards (IIB) mentioned in chapter 6.

Here, these signals are converted to  $12\text{bits}$  digital data and sent to the controller (PC) through a connecting bus. In the control PC, the data is processed to extract the values of  $\delta$  and  $\gamma$ .

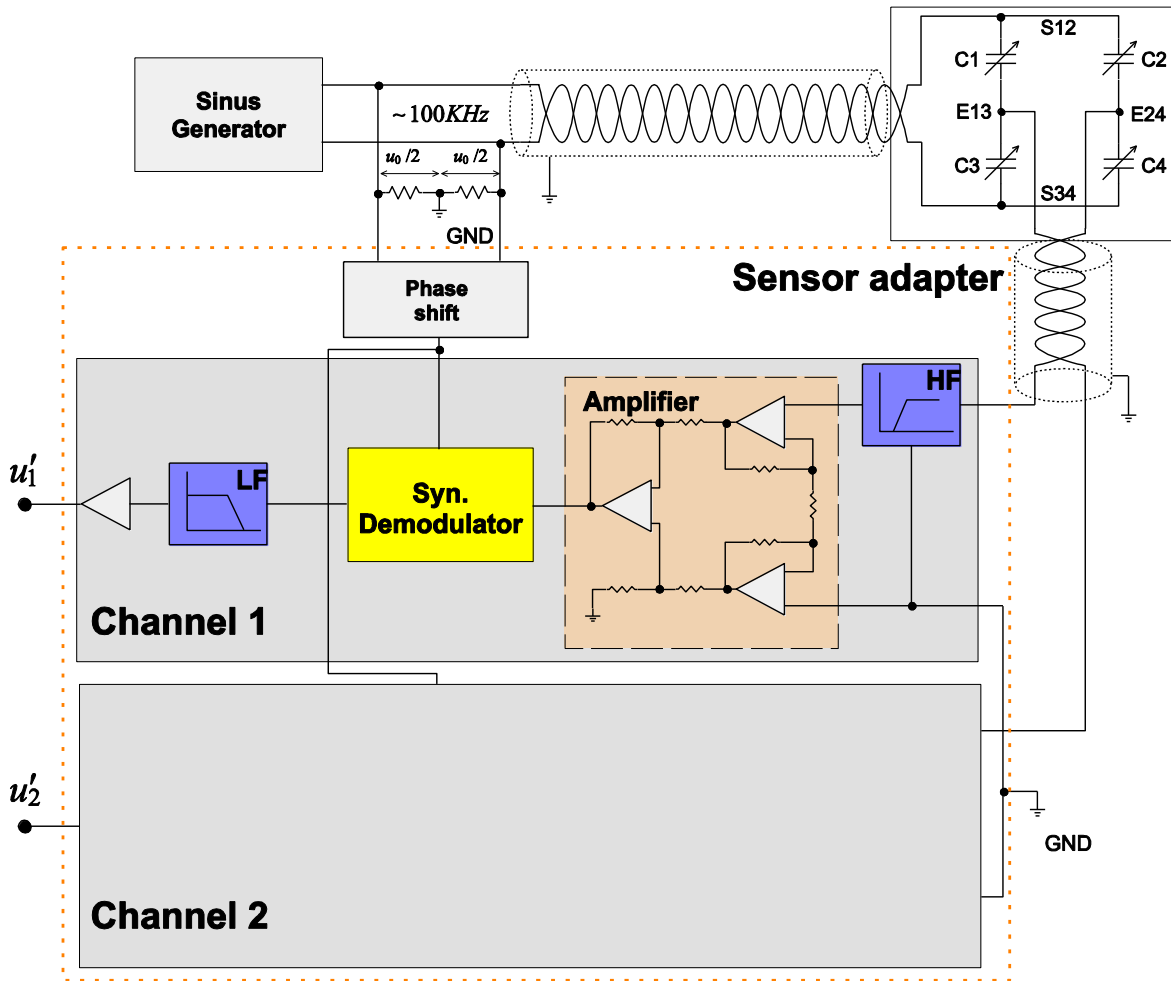


Figure 7.5 Capacitive sensor block diagram

## 7.2. Mathematic model

### 7.2.1. Ideal case analysis

In order to analyze the sensitivity of the capacitive sensor, the capacitive sensor system model shown in Figure 7.6 was used. The figure shows the effect of the lateral position  $\delta$  and the yaw angle  $\gamma$  on the capacitances of  $C_1$  to  $C_4$ . The capacitances of this model were analyzed and calculated as follows.

Firstly, the capacitance  $C_1$  was analyzed and calculated with the model as in Figure 7.7. To simplify the calculation, the following suppositions are used:  $C_{11}$  is the capacitance between the sending electrode  $S12$ , the receiving electrode  $E1$  and the coupling electrode  $K11$  spreading from  $0$  to  $d/2$ ;  $C_{12}$  is the capacitance between the sending electrode  $S12$ , the receiving electrode  $E1$  and the coupling

electrode  $K12$  spreading from  $0$  to  $l/2$ . With these suppositions, the capacitance  $C_1$  between the sending electrode  $S12$ , the receiving electrode  $E1$  and the coupling electrode  $K1$  is  $C_1 = C_{11} - C_{12}$ . With a top view arrangement of the electrodes as in Figure 7.6, an approximation of  $C_{11}$  can be analyzed and calculated as presented in equation (7.1).

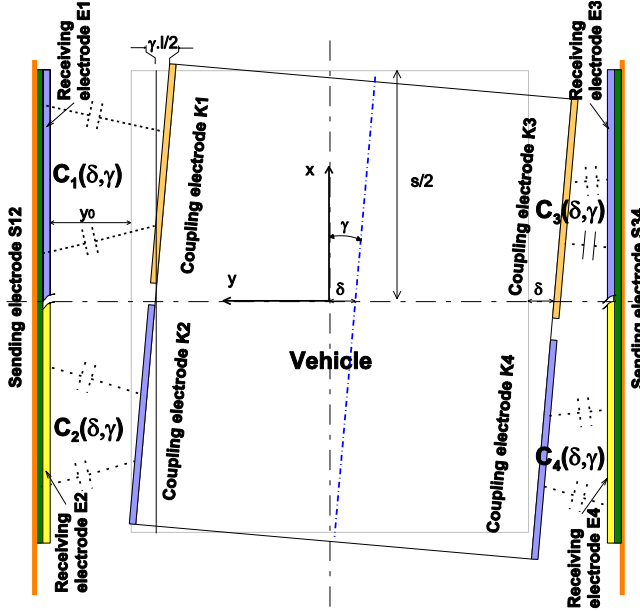


Figure 7.6 Electrode arrangement

$$C_{11}(\gamma, \delta) \approx \frac{\epsilon \epsilon_0 h_e l}{2\gamma} \log\left(\frac{y_0 + \delta + \frac{l}{2}\gamma}{y_0 + \delta}\right) \quad (7.1)$$

Where  $\epsilon_0$  is the dielectric constant of air,  $\epsilon$  is the relative electric constant,  $s$  is the length of the capacitance moving part,  $y_0$  is the air-gap when  $\delta=0$  and  $\gamma=0$ , and  $h_e$  is the height of the electrode strips.

By linearization around the working point  $\delta=0$ ,  $\gamma=0$ , we get:

$$C_{11, Lin} = \frac{\epsilon \epsilon_0 h_e l}{2y_0} \left(1 - \frac{\delta}{y_0} - \frac{\gamma l}{4y_0}\right) \quad (7.2)$$

Similarly calculating, we get:

$$C_{12, Lin} = \frac{\epsilon \epsilon_0 h d}{2y_0} \left(1 - \frac{\delta}{y_0} - \frac{\gamma d}{4y_0}\right) \quad (7.3)$$

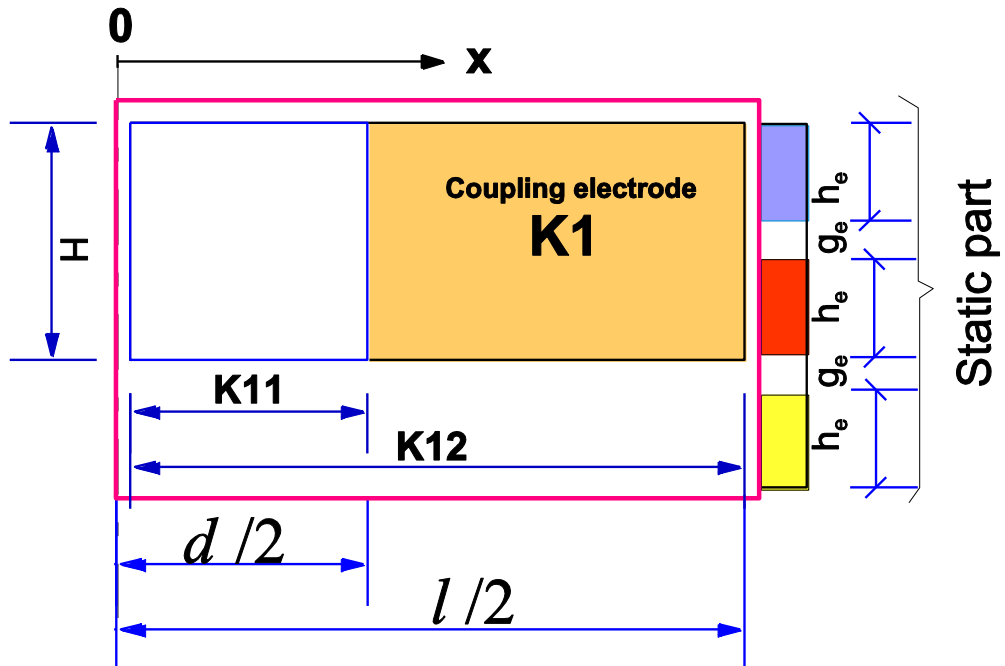


Figure 7.7 Capacitance  $C_1$  analysis

The linearized value of  $C_1$  is the difference between  $C_{11,Lin}$  and  $C_{12,Lin}$ :

$$C_{1,Lin} = C_{11,Lin} - C_{12,Lin} = \frac{\varepsilon\varepsilon_0 h_e}{2y_0} (l - d - (l - d) \frac{\delta}{y_0} - (l^2 - d^2) \frac{\gamma}{4y_0}) \quad (7.4)$$

Simplifying equation (7.4) we get:

$$C_{1,Lin} = \frac{\varepsilon\varepsilon_0 h_e (l - d)}{2y_0} (1 - \frac{\delta}{y_0} - (l + d) \frac{\gamma}{4y_0}) \quad (7.5)$$

The expressions for the other capacitors  $C_{2,Lin}$  to  $C_{4,Lin}$  are:

$$C_{2,Lin} = \frac{\varepsilon\varepsilon_0 h (l - d)}{2y_0} (1 - \frac{\delta}{y_0} + (l + d) \frac{\gamma}{4y_0}) \quad (7.6)$$

$$C_{3,Lin} = \frac{\varepsilon\varepsilon_0 h_e (l - d)}{2y_0} (1 + \frac{\delta}{y_0} + (l + d) \frac{\gamma}{4y_0}) \quad (7.7)$$

$$C_{4,Lin} = \frac{\varepsilon\varepsilon_0 h_e (l - d)}{2y_0} (1 + \frac{\delta}{y_0} - (l + d) \frac{\gamma}{4y_0}) \quad (7.8)$$

The measured voltages  $u_1$  and  $u_2$ , as in Figure 7.4.b, depend on the ratios of the bridge capacitances as follows.

$$u_2 = u_0 \left( \frac{1}{1 + C_4 / C_2} - \frac{1}{2} \right) \quad (7.9) \quad u_1 = u_0 \left( \frac{1}{1 + C_3 / C_1} - \frac{1}{2} \right) \quad (7.10)$$

Substituting the linearized capacitances  $C_{1,Lin} \div C_{4,Lin}$  into (7.9) and (7.10) results in the linearized voltages:

$$u_{1,Lin} = \frac{-u_0}{2y_0} \left( \delta + \gamma \frac{l + d}{4} \right) \quad (7.11) \quad u_{2,Lin} = \frac{-u_0}{2y_0} \left( \delta - \gamma \frac{l + d}{4} \right) \quad (7.12)$$

Solving the set of equations (7.11) and (7.12) results in  $\delta_{Lin}$  and  $\gamma_{Lin}$  as the function of  $u_{1,Lin}$  and  $u_{2,Lin}$

$$\delta_{Lin} = -y_0 \frac{u_{1,Lin} + u_{2,Lin}}{u_0} \quad (7.13) \quad \gamma_{Lin} = \frac{4y_0}{l + d} \frac{u_{2,Lin} - u_{1,Lin}}{u_0} \quad (7.14)$$

For the lateral position and yaw angle control, the actual values are required as DC-signals, i.e. the AC signals of equation (7.13) and (7.14) must be demodulated (and will be indicated by “Demod” or presented as  $u'_1$  and  $u'_2$ ).

$$\delta_{ist,Lin} = -y_0 \frac{u_1 + u_2}{\hat{u}_0} \text{ Demod} \quad (7.15) \quad \gamma_{ist,Lin} = \frac{4y_0}{l + d} \frac{u_2 - u_1}{\hat{u}_0} \text{ Demod} \quad (7.16)$$

To simplify the equations,  $u_\delta$  and  $u_\gamma$  will be used to take the place of sum and difference of  $u_1$ ,  $u_2$  from now on.

$$u_{\delta} = (u_1 + u_2)_{Demod} \quad (7.17)$$

$$u_{\gamma} = (u_2 - u_1)_{Demod} \quad (7.18)$$

### 7.2.2. Calculation of the optimal value of $d$ .

The yaw sensitivity of the capacitive sensor, which is the changing of the output voltage  $u_{\gamma}$  corresponding to the varying of the yaw angle  $\gamma$ , was small in FEM simulation results and practical measurements,. That makes poor quality in yaw angle control. In order to improve the control quality, optimisation of the capacitive sensor for high sensitivity to yaw angle is required for the system. Therefore, the capacitive sensor was analyzed to determine the optimal design for the sensor with priority given to high yaw angle sensitivity.

From the equations (7.5) to (7.16) we can recognize that the yaw angle sensitivity of the capacitive sensor depends on

- the sum  $(l + d)$ ,
- the exciting signal amplitude  $u_0$  and
- the air-gap value  $y_0$  when the vehicle is in the middle of the guide-way.

With the amplitude of the exciting signal  $u_0$  and desired value of lateral position  $y_0$  are limited (by electronic circuit and mechanical structure), the sensitivity of the sensor can increase by raising the sum  $(l + d)$ . When the sum is raised, two factors need to be considered:

- A raise in  $l$  value increases the length of the capacitor moving part that can cause the mechanical structure to be unstable.
- A raise in  $d$  value reduces the capacitances of  $C_{1,lin}$  to  $C_{4,lin}$  thus increasing sensor impedance and causing interference with noise.

To obtain mechanical structure stability and high yaw angle sensitivity, the capacitive sensor length  $l$  should be limited by the vehicle length. Consequently, the capacitive sensor length was fixed by the vehicle's structure. The yaw angle sensitivity was optimized by the distance between coupling electrodes ( $d$ ).

As presented in ideal equations (7.11), (7.12) and (7.16), which do not consider any leakage field, the greater the  $d$  value is, the greater is the sensitivity of the capacitive sensor to yaw angle. However, in practice, when the  $d$  value increases, the capacitances of  $C_1$  to  $C_4$  are reduced. This can cause a reduction in capacitive sensitivity when the capacitances reach a limiting value, where the leakage field can no longer be neglected. The leakage capacitors here are parasitic capacitors formed between; 1) electrodes and 2) electrodes-ground, as presented in Figure 7.8.

Neglecting the effect of very small capacitors  $C_{K13}$  and  $C_{K24}$ , the capacitor circuit in Figure 7.4b will be augmented as shown in Figure 7.9. Transforming the circuit and presenting all parasitic capacitors as equivalent capacitors  $C_M$ s, the capacitive circuit was simplified as in Figure 7.10. In order to develop something similar to circuit Figure 7.4b, the circuit was represented as shown on the right of Figure 7.10 with  $C'_i = C_i + C_M \Big|_{i=1:4}$ . The measured voltage  $u_1$  and  $u_2$  now are

$$u_2 = u_0 \left( \frac{1}{1 + C'_4 / C'_2} - \frac{1}{2} \right) \quad (7.19)$$

$$u_1 = u_0 \left( \frac{1}{1 + C'_3 / C'_1} - \frac{1}{2} \right) \quad (7.20)$$

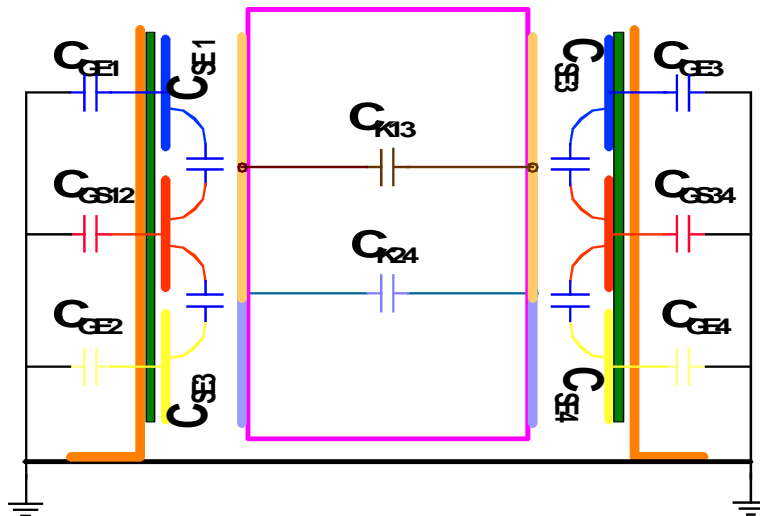


Figure 7.8 Parasitic capacitors

Linearized equation (7.11) and (7.12) become

$$u_{1, Lin} = \frac{-u_0}{2y_0} \left( \frac{\delta + \gamma \frac{l+d}{4}}{1 + \frac{2y_0 C_M}{\epsilon_0 \epsilon h_e (l-d)}} \right) \quad (7.21)$$

$$u_{2, Lin} = \frac{-u_0}{2y_0} \left( \frac{\delta - \gamma \frac{l+d}{4}}{1 + \frac{2y_0 C_M}{\epsilon_0 \epsilon h_e (l-d)}} \right) \quad (7.22)$$

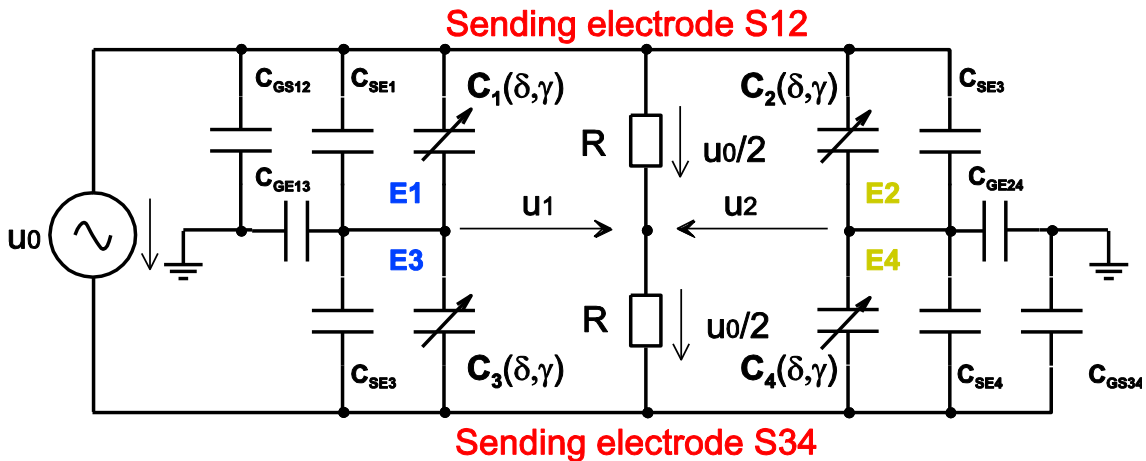


Figure 7.9 Capacitive sensor circuit with parasitic capacitors

Output voltages of the lateral position and the yaw angle are proportional to  $\gamma$  with the sensitive factor presented in (7.23) (7.24)

$$u_{\delta, Lin} = u_{1, Lin} + u_{2, Lin} = -\delta \frac{u_0 \varepsilon_0 \varepsilon h_e}{y_0} \frac{l-d}{\varepsilon_0 \varepsilon h_e \cdot (l-d) + 2y_0 C_M} \quad (7.23)$$

$$u_{\gamma, Lin} = u_{2, Lin} - u_{1, Lin} = \gamma \frac{u_0 \varepsilon_0 \varepsilon h_e}{4y_0} \frac{l^2 - d^2}{\varepsilon_0 \varepsilon h_e \cdot (l-d) + 2y_0 C_M} \quad (7.24)$$

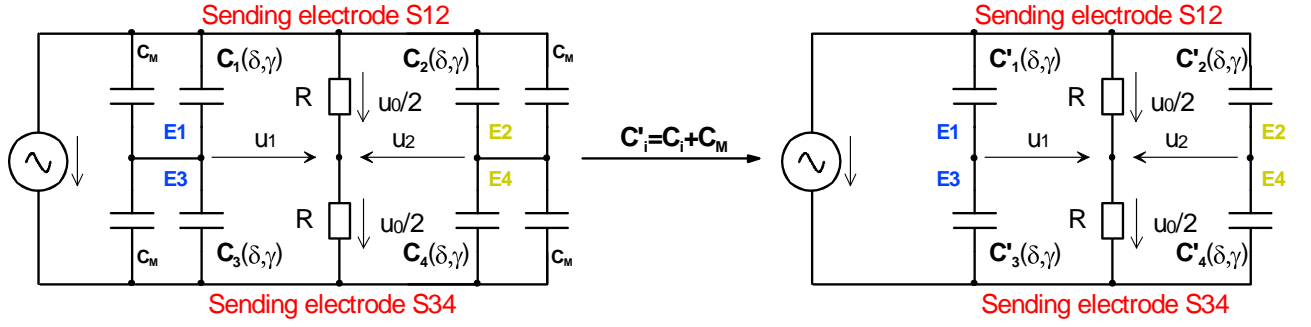


Figure 7.10 Simplified circuit

In order to find the optimal value of  $d$ , the yaw sensitivity factor (i.e. the gain) of the capacitive sensor in (7.24) is defined as a function of  $d$  in (7.25)

$$f(d) = \frac{u_0 \varepsilon_0 \varepsilon h_e}{4y_0} \frac{d^2 - l^2}{\varepsilon_0 \varepsilon h_e \cdot d - (\varepsilon_0 \varepsilon h_e l + 2y_0 C_M)} = \frac{d^2 - l^2}{A \cdot d - B} \quad (7.25)$$

with  $A = \varepsilon_0 \varepsilon h_e$ ;  $B = \varepsilon_0 \varepsilon h_e \cdot d + 2y_0 C_M = A \cdot s + 2y_0 C_M$ .

The first order derivative with respect to  $d$  of the factor is

$$f'(d) = \frac{2d(A \cdot d - B) - A(d^2 - l^2)}{(A \cdot d - B)^2} = \frac{A \cdot d^2 - 2B \cdot d + A l^2}{(A \cdot d - B)^2} \quad (7.26)$$

The  $f(d)$  reaches extreme values when  $f'(d) = 0$  at optimal value of  $d$

$$d_{opt} = \frac{B \pm \sqrt{B^2 - A^2 l^2}}{A} = l + \frac{2y_0 C_M \pm \sqrt{B^2 - A^2 l^2}}{A} \quad (7.27)$$

Since  $0 \leq d \leq l$ , the final optimal value of  $d$  value is

$$d_{opt} = l + \frac{2y_0 C_M - \sqrt{B^2 - A^2 l^2}}{A} = l + \frac{2y_0 C_M - \sqrt{4\varepsilon_0 \varepsilon h_e y_0 l C_M + 4y_0^2 C_M^2}}{\varepsilon_0 \varepsilon h_e} \quad (7.28)$$

As in (7.28), the optimal value of  $d$  depends on other parameters of the capacitive sensor, especially on the parasitic capacitance  $C_M$ . In the ideal case,  $C_M = 0$ , the optimal value equal the length of the moving part of the capacitive sensor,  $l$ . With  $C_M > 0$ , the optimal value always smaller than  $l$ . The meaning of this optimal value will be presented in the next subsection.

## 7.3. FEM simulation

In order to verify the theoretical calculation, the 2D FEM simulation software Maxwell from Ansoft was used. With this software, the simulations were executed to calculate the parasitic capacitances and to verify the capacitive sensor's principle of operation.

### 7.3.1. Parasitic capacitances

At first, the parasitic capacitance of the capacitive sensor was calculated with a FEM model, which has a cross-section shown in Figure 7.11. Parameters used in the simulation model were the same as those used for the designed prototype in Table 7.1. In this simulation, the sending electrodes (red) and the receiving electrodes (pink) were set up as copper material. The material between the electrodes and the aluminium base was set up as woven glass and epoxy FR-4 (material of printed circuit board). The electrode strip lines were connected as in the capacitive sensor circuit in Figure 7.4.  $E1$  and  $E3$  were connected together in a group object.  $E2$  and  $E4$  formed another group object. Power was supplied to  $S12$  and  $S34$ . The parasitic capacitances  $C_M$  between each group object to sending electrodes,  $S12$  and  $S34$ , were calculated by running the simulation model.

TABLE 7.1 CAPACITIVE SENSOR DIMENSIONS

Parameters	Value [mm]
Electrode strip height ( $h$ )	12
Electrode strip gap ( $g$ )	2
Electrode strip length ( $l$ )	580
Coupling electrode height ( $H$ )	28
Balanced state air-gap ( $y_0$ )	1.35
Coupling electrode horizontal gap ( $d$ )	80
Coupling electrode length ( $s$ )	200
Aluminium body grounded	

The aim of this simulation was to find a means to reduce the parasitic capacitances in order to improve the sensitivity of the capacitive sensor. To meet this aim, three varying simulations were conducted: non-grounded aluminium base, grounded aluminium base, grounded aluminium base with grounded barriers. In the first case, the aluminium base was set to be floating with the voltage system. The aluminium base was connected to the ground of the system in the second simulation. In addition to the grounded aluminium base, the small grounded-barrier copper strip lines (blue)



were put between the electrode strip lines in the third case. Simulation results ( $C_M$ ) were  $15.86\text{pF}$ ,  $7.93\text{pF}$  and  $2.76\text{pF}$  in sequence. The simulation results showed that; the grounded aluminium base can reduce the parasitic capacitances in the capacitive sensor system and the best case is the grounded aluminium base with grounded barriers.

The effect of these parasitic capacitors on the capacitive sensor sensitivity is presented in Figure 7.12. A set of sensitive curves with different  $C_M$  are displayed.

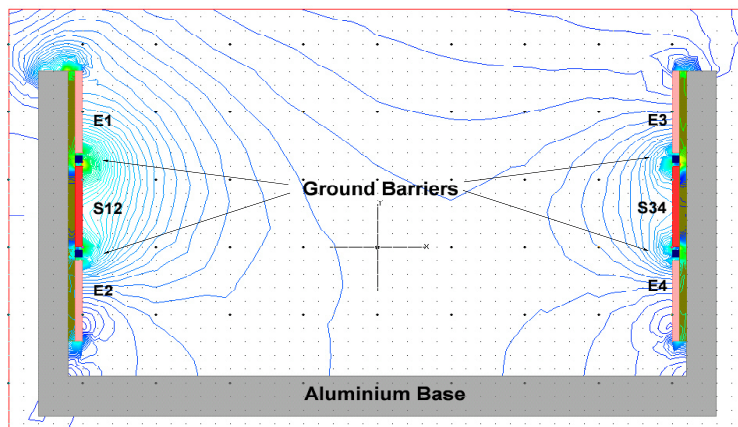


Figure 7.11 FEM parasitic capacitance model in cross-section (without vehicle).

Each curve is a  $f(d)$  curve plotted by changing the  $d$  value from zero to the  $l$  value (0.2m in this case) with one constant  $C_M$ . The results, which are presented in Volt/rad as yaw angle sensitivity, show that: the smaller the parasitic capacitor is, then the higher is the yaw sensitivity of the capacitive sensor. In the ideal case ( $C_M = 0$ ), the higher the  $d$

value, then the higher the resulting capacitive sensor sensitivity will be. When the parasitic capacitances are considered, with each value of parasitic capacitance  $C_M$ , there is one optimal value of  $d$  that gives the highest sensitivity for the capacitive sensor (dot in graph of Fig 7.12).

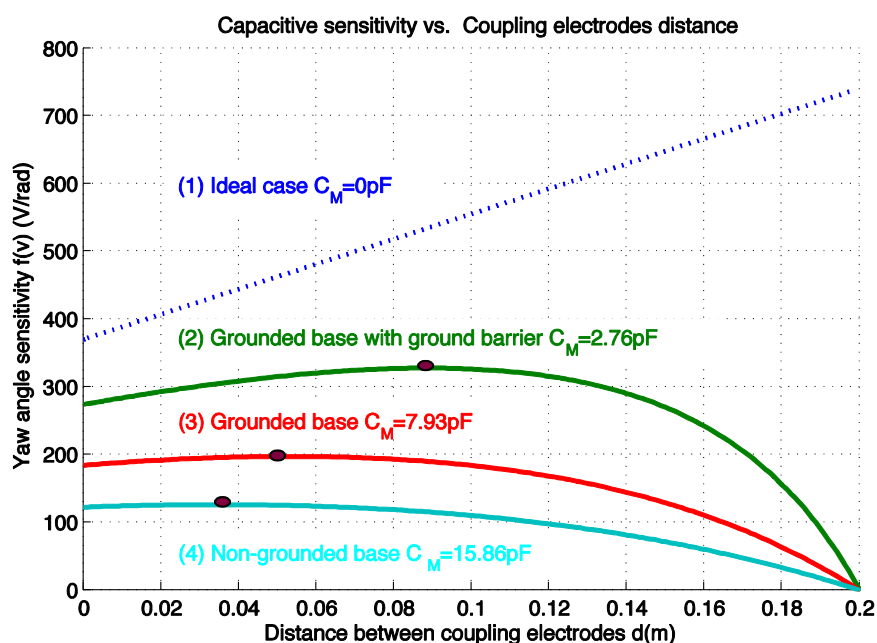


Figure 7.12 The set of yaw angle sensitivity curves as a function of  $d$  value.

### 7.3.2. Capacitive sensor performances

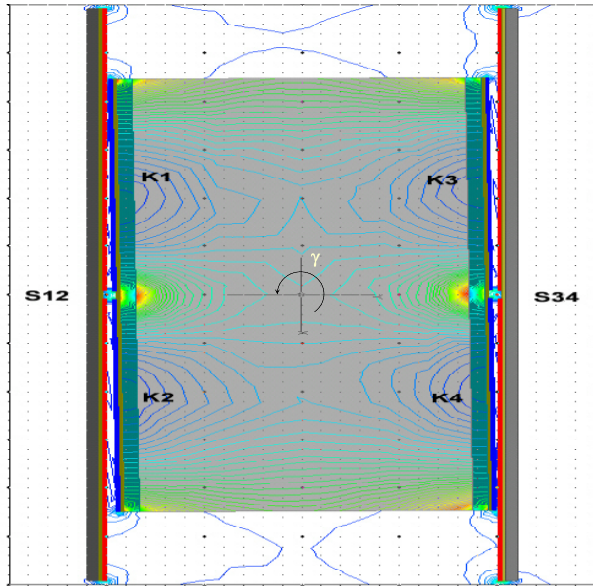


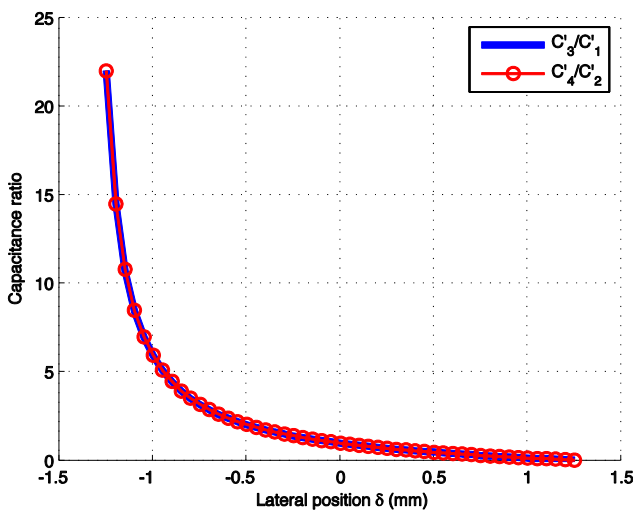
Figure 7.13 FEM model of capacitive sensing in top view.

In this subsection, the concept of capacitive sensor is simulated. The FEM model in Figure 7.13 with the main parameter in Table 7.1 was implemented. In this model, the electrodes are arranged from a top view. The effect of lateral position  $\delta$  and yaw angle  $\gamma$  on the capacitances and output voltages are presented in succession as follows: Firstly, yaw angle was constrained to zero ( $\gamma=0$ ) when the lateral position  $\delta$  was varied from  $-1.25\text{mm}$  to  $1.25\text{mm}$ .

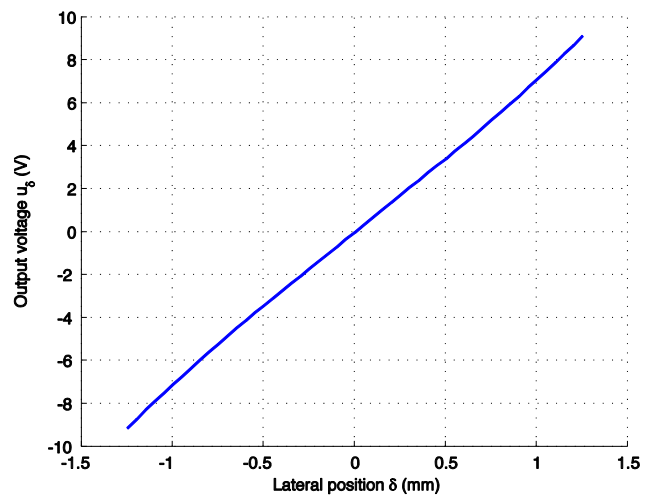
The capacitances  $C_1'$  to  $C_4'$  varied correspondingly with the change in lateral position. The simulated results are illustrated in Figure 7.14.a with the capacitive ratios  $C_3'/C_1'$ ,  $C_4'/C_2'$  as a function of lateral position  $\delta$ . The output voltages  $u_\delta$  calculated from the ratios following equations (7.19) and (7.20) as in (7.29) is presented in Figure 7.14.b.

$$u_{\delta, \text{Lin}} = u_{2, \text{Lin}} + u_{1, \text{Lin}} = u_0 \frac{1 - XY}{(X + 1)(Y + 1)} \quad (7.29)$$

with  $X = C_3' / C_1'$ ;  $Y = C_4' / C_2'$



a. Capacitive ratios

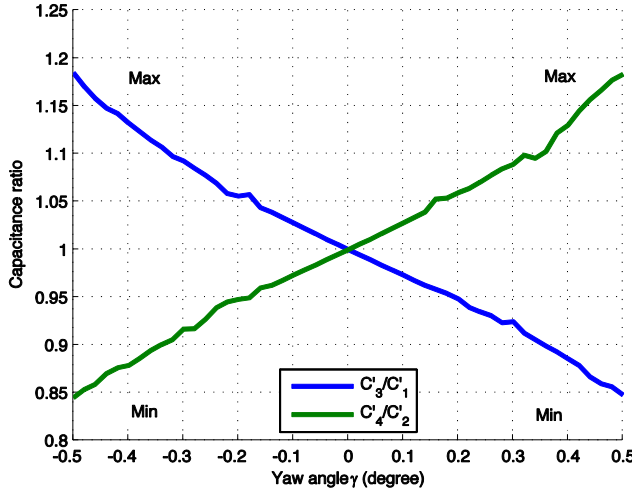


b. Output voltage  $u_\delta$

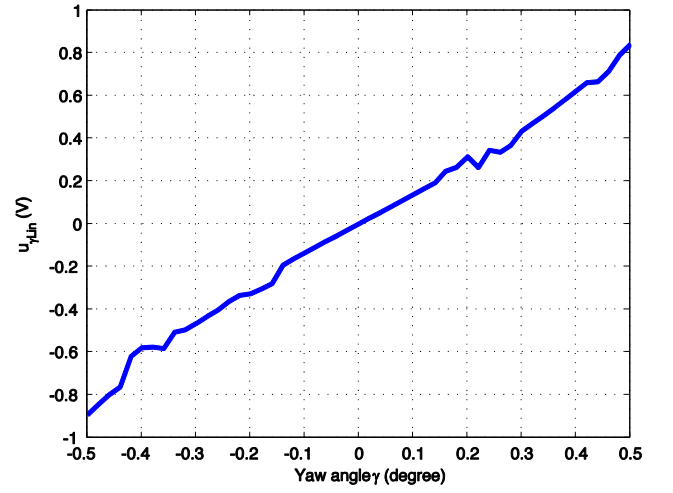
Figure 7.14 Capacitive sensor outputs as functions of  $\delta$

Secondly, the capacitances between  $S12$ ,  $S34$  and  $K1$  to  $K4$  were calculated with the yaw angle of the vehicle changing from  $-0.5$  deg to  $0.5$  deg when the lateral position was zero. The resulting capacitance ratios as a function of yaw angle are presented in Figure 7.15.a. The output voltage of the capacitor bridge dependence on yaw angle can be calculated with (7.30) and represented as Figure 7.15.b.

$$u_{\gamma, Lin} = u_{2, Lin} - u_{1, Lin} = u_0 \frac{Y - X}{(X + 1)(Y + 1)} \quad (7.30)$$



a. Capacitive ratios



b. Output voltage  $u_{\gamma}$

Figure 7.15 Capacitive sensor outputs as functions of  $\gamma$

In both cases, output voltages  $u_{\delta}$  and  $u_{\gamma}$  were calculated with capacitance ratios used in (7.29) and (7.30) with  $u_0 = 10V$ . As presented in the FEM result figures, output voltages show a linear relationship with lateral position change and yaw angle of the vehicle.

In order to confirm that our optimal value calculation in (7.28) is indeed optimal, a simulation of equation (7.28) using different  $d$  values ( $4mm$ ,  $140mm$ ) and the optimal  $d$  value ( $d_{opt} = 35mm$ ) was executed. The simulation was done with  $C_m = 15.86pF$  and the parameters were the same as those in Table 7.1. The yaw angle was changed from  $-0.5$  deg to  $0.5$  deg. The FEM results are capacitance ratios in

Table 7.2. From (7.23) and (7.25) the sensitivity  $f(d)$  can be calculated with (7.31). The sensitivity results in the last column of

Table 7.2 show the highest sensitivity is obtained with  $d$  optimal.

$$f(d) = \frac{\Delta u_{\gamma, Lin}}{\Delta \gamma} = \frac{u_{\gamma, Lin}(X_{max}, Y_{min}) - u_{\gamma, Lin}(X_{min}, Y_{max})}{\Delta \gamma} \quad (7.31)$$

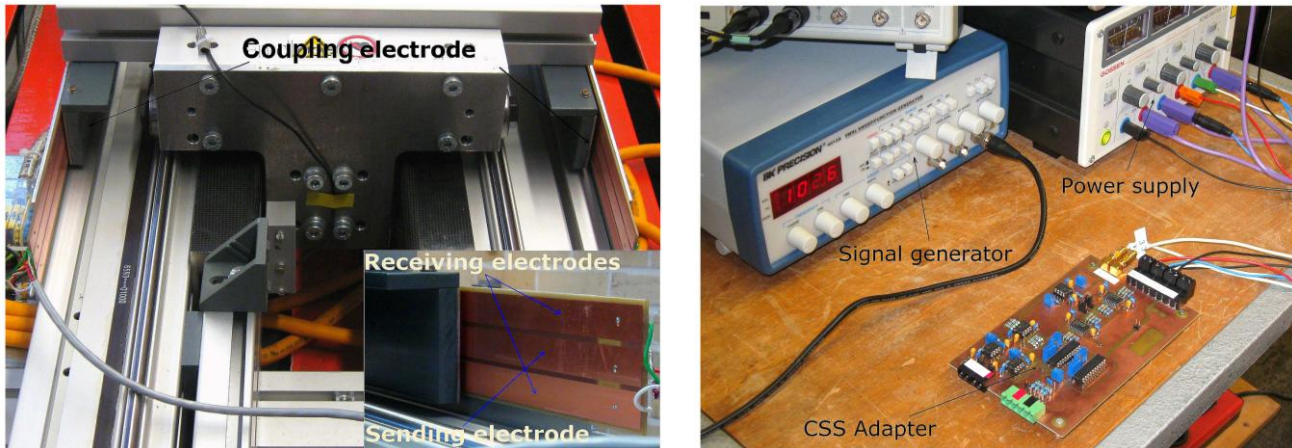
TABLE 7.2 CAPACITIVE SENSOR SENSITIVITY

Simulation case	$X = C_3' / C_1'$		$Y = C_4' / C_2'$		f (V/rad)	Note
	Min	Max	Min	Max		
$d = 4mm$	0.849	1.155	0.845	1.185	87.2	Long
$d = 35mm$	0.848	1.185	0.823	1.183	99.6	Optimal
$d = 140mm$	0.887	1.127	0.894	1.121	66.6	Short

## 7.4. Experimental setup and results

### 7.4.1. Experimental setup

According to the theoretical calculation and simulation above, two prototypes of capacitive sensor were realized. The real experimental setup was implemented as in Figure 7.5 using the parameters in Table 7.1. The experimental setup is presented in the photos in Figure 7.16.



a. Capacitive sensor's electrodes

b. Capacitive sensor adapter

Figure 7.16 The real experimental setup of the capacitive sensor.

In the experimental setup, the excitation signal was generated with a sinus generator Precision 4012A. The signal was supplied to the sending electrodes of the capacitive sensor's static part, which was self-designed and produced in our institute. The output voltages from the capacitive bridge were fed to the capacitive adapter, which was also a self-made product. The output signals of the adapter were  $u_1'$  and  $u_2'$  carrying the information of the lateral position  $\delta$  and the yaw angle  $\gamma$ . These analog signals ( $u_1'$  and  $u_2'$ ) were then sent to two reserved ADC channels of the inverter interface boards (IIB) mentioned in chapter 3. The analog signals were converted in IIB's ADC to digital data. The data was then processed in the control PC to determine the value of the lateral position  $\delta$  and the yaw angle  $\gamma$ .

## 7.4.2. Capacitive sensor calibration

As mentioned above, the capacitive sensor data was processed in the control PC. The sum of the two ADC data values is proportional to the vehicle's lateral position ( $\delta$ ). The difference of the two ADC output values is proportional to the vehicle's yaw angle ( $\gamma$ ).

To use the data as feedback signals for the air-gap and yaw angle controller, calibrations need to be performed. At first, the vehicle was controlled to change one variable (the lateral position or the yaw angle) slowly and smoothly when the other was constrained at zero. The calibration control process was executed using the feedback signal from the industrial inductive sensor mentioned in chapter 6. The results measured from the high precision industrial inductive gap sensors and the ADC outputs of the capacitive sensor are captured in the process. The captured results are displayed in Figure 7.17.a and Figure 7.17.b. The figures present the output voltages ( $u_\delta$ ,  $u_\gamma$ ) of the capacitive sensor in ADC unit as a function of the lateral position ( $\delta$ ) and the yaw angle ( $\gamma$ ). Consequently, with each measured value of the lateral position or the yaw angle, there was an appropriated value of the sum or the difference from the capacitive sensor ADC value. The measuring data from the inductive sensors was combined with the capacitive sensor data to generate look up tables (LUT) for the capacitive sensor. One LUT is generated by the lateral positions measured by the inductive sensor and the corresponding sums of the capacitive sensor ADC values. The other is generated by the yaw angles and the corresponding differences of the capacitive sensor ADC values. These LUT are embedded in the control program in order to calculate the feedback lateral position ( $\delta$ ) and yaw angle ( $\gamma$ ) from the capacitive sensor ADC values.

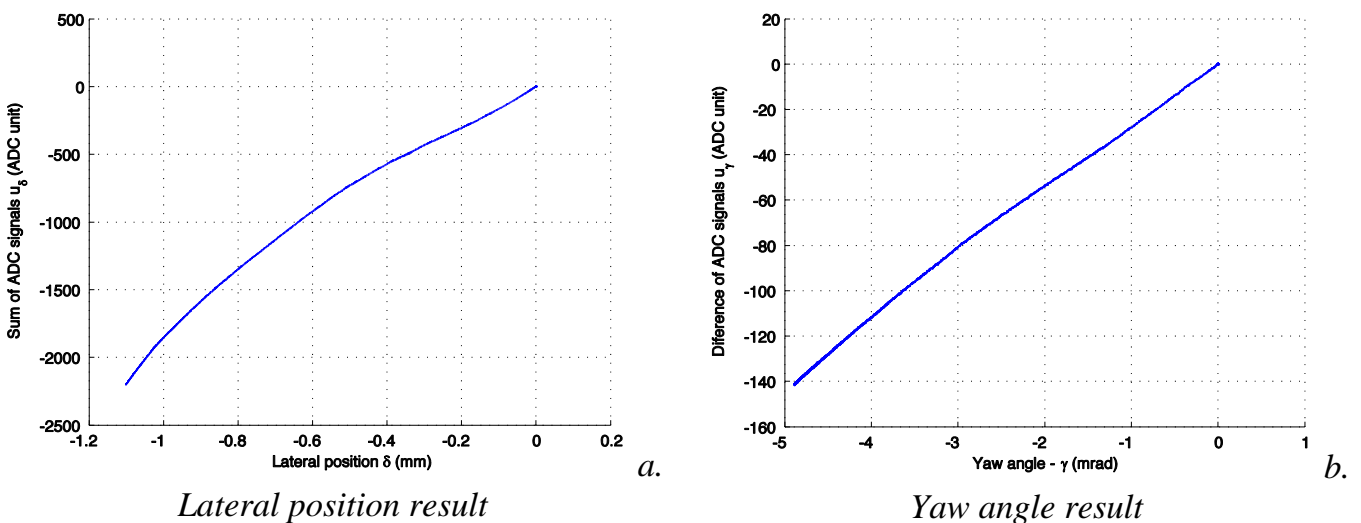


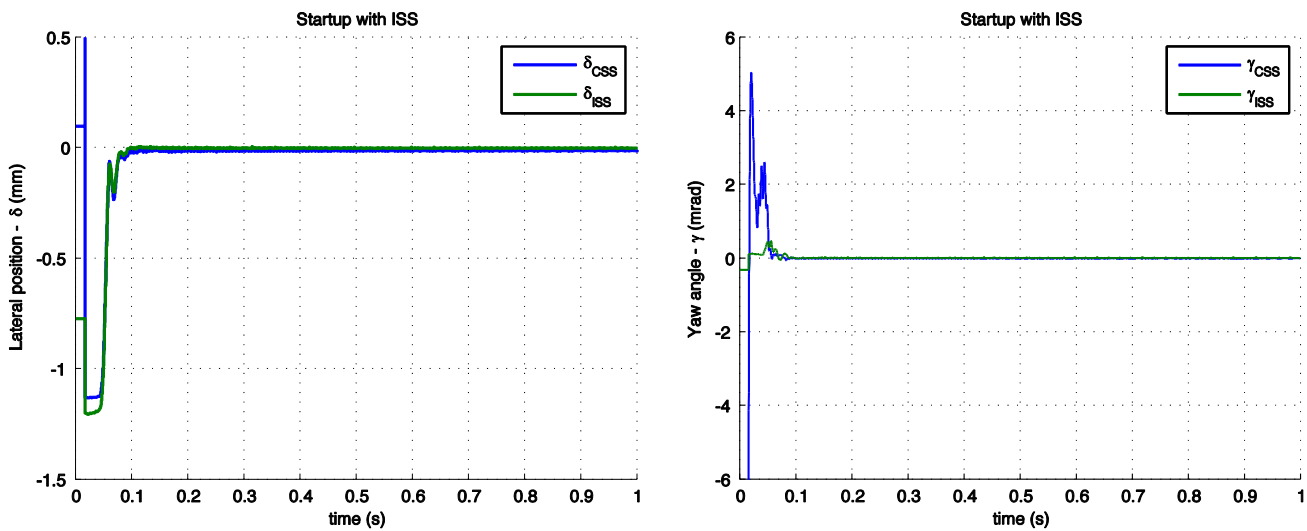
Figure 7.17 Capacitive sensor calibration results



As shown in Figure 7.17.a and Figure 7.17.b, the relationships of the sum and the difference of ADC signals are quite linear. This agrees with the theoretical calculations in equations (7.23) and (7.24) and the results of the FEM simulation in subsection 7.3.2; the output voltages of the capacitive sensor are linearly proportional to  $\delta$  and  $\gamma$ .

### 7.4.3. Control with capacitive sensor

At first, the capacitive sensor signals (CSS) must be tested in order to verify its quality for high dynamic conditions. In this experiment, the vehicle was controlled to move from the rest position at longitudinal position  $x=0$  centrally and parallel to the middle of the guide-way ( $\delta=0$  and  $\gamma=0$ ). The control was implemented with feedback signals from the inductive sensor signals (ISS). The results are shown in Figure 7.18.a and Figure 7.18.b with the measured values of the CSS and the ISS. The displayed results are the lateral position and the yaw angle as functions of time. The blue curves are the measured results from the CSS and the green ones are the measured results from the ISS. As shown in the figures, the CSS signals match those of the ISS. The minor differences at the start-up period are caused by the mounting position of the two sensor systems. In addition, the mechanical structure of the CSS system caused additional disturbance due to the rolling vibration of the vehicle.



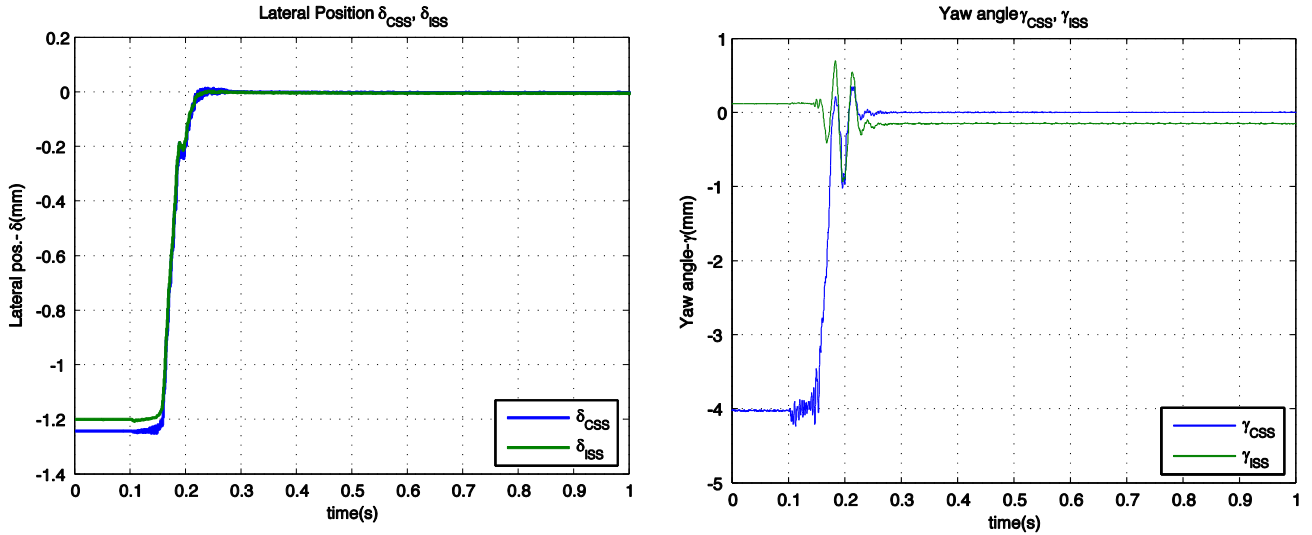
a. Lateral position response

b. Yaw angle response

Figure 7.18 CSS signal testing experiment - control with ISS signal

With the good results obtained in the quality verifying experiment, the measured signals from CSS were used as the feedback value for  $\delta$ - and  $\gamma$ - controller. The control results are shown in Figure 7.19.a and Figure 7.19.b. The resulting control

quality was similar to that obtained when the ISS feedback signals were used. Duplicate tests resulted in almost duplicate values of CSS and ISS, especially in the lateral position measurement. This shows that the control of the system with capacitive sensor signals is possible.



a. Lateral position response

b. Yaw angle response

Figure 7.19 Control with CSS signal

#### 7.4.4. Quality of control with capacitive sensor.

In the start-up experiments, priority is given to lateral position control in order to override the high normal force when the vehicle is attached to one of the stators. However, this deteriorates the yaw angle control quality. To ascertain the control quality for each individual degree of freedom (DOF), step control experiments were implemented. In the step control experiment, step references were applied separately for each DOF starting at the system's steady state with longitudinal position at  $x=0$ , lateral position at  $\delta=0$  and  $\gamma=0$ . The results are presented in Figure 7.20 to Figure 7.22.

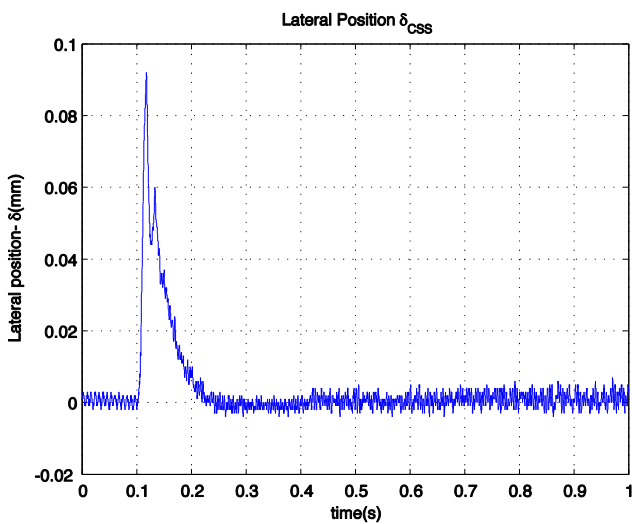
In the results, the control qualities of the system with capacitive sensor show high performance as the control qualities of the system with inductive sensor do. The controller can give fast responding to the step control in the lateral position and yaw angle control. The higher noise in the capacitive sensor results in comparison with inductive sensor results is caused by the design and quality of the realization. As mentioned, the capacitive sensor is completely designed and produced in our institute instead of using an industrial product like the inductive sensor. Hence, this problem can be improved when the sensor is produced under industrial condition. Altogether,

using the capacitive sensor in order to make the vehicle passive is significantly feasible.

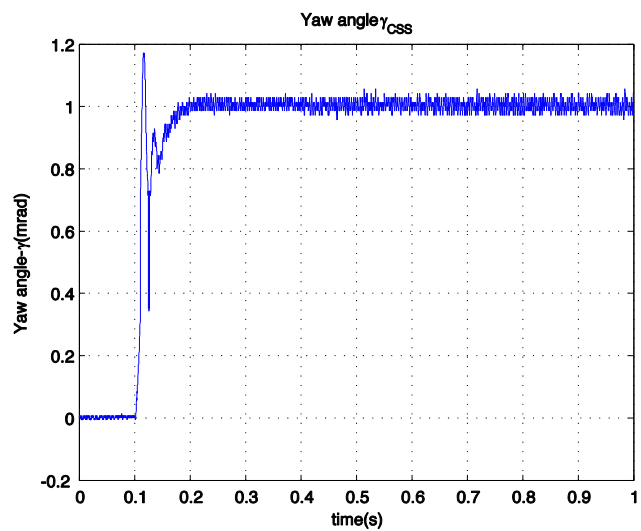
The conditions for the following figures are given in the table below:

TABLE 7.3 STEP CONTROL RESULT

		Step of commanded value in		
		$\delta$	$\gamma$	$x$
Reaction of	$\delta$	Figure 7.21.a	Figure 7.20.a	Figure 7.22.a
	$\gamma$	Figure 7.21.b	Figure 7.20.b	Figure 7.22.b
	$x$			Figure 7.22.c

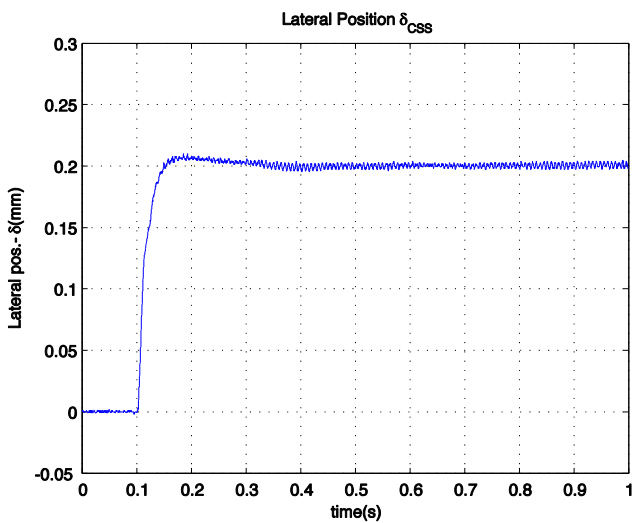


a. Lateral position response

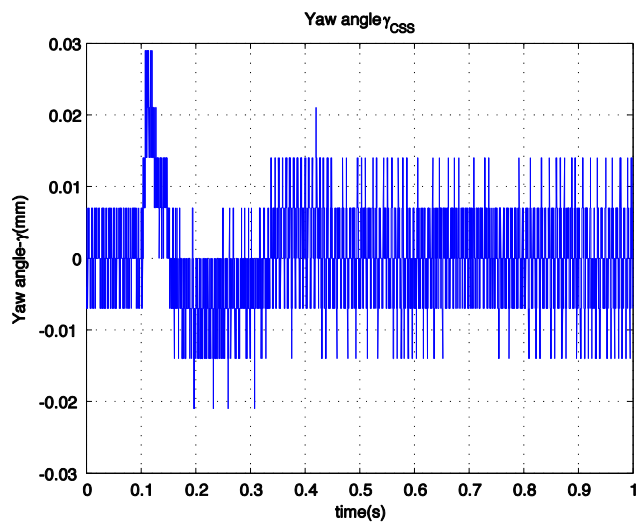


b. Yaw angle response

Figure 7.20 Yaw angle step control



a. Lateral position response



b. Yaw angle response

Figure 7.21 Lateral position step control



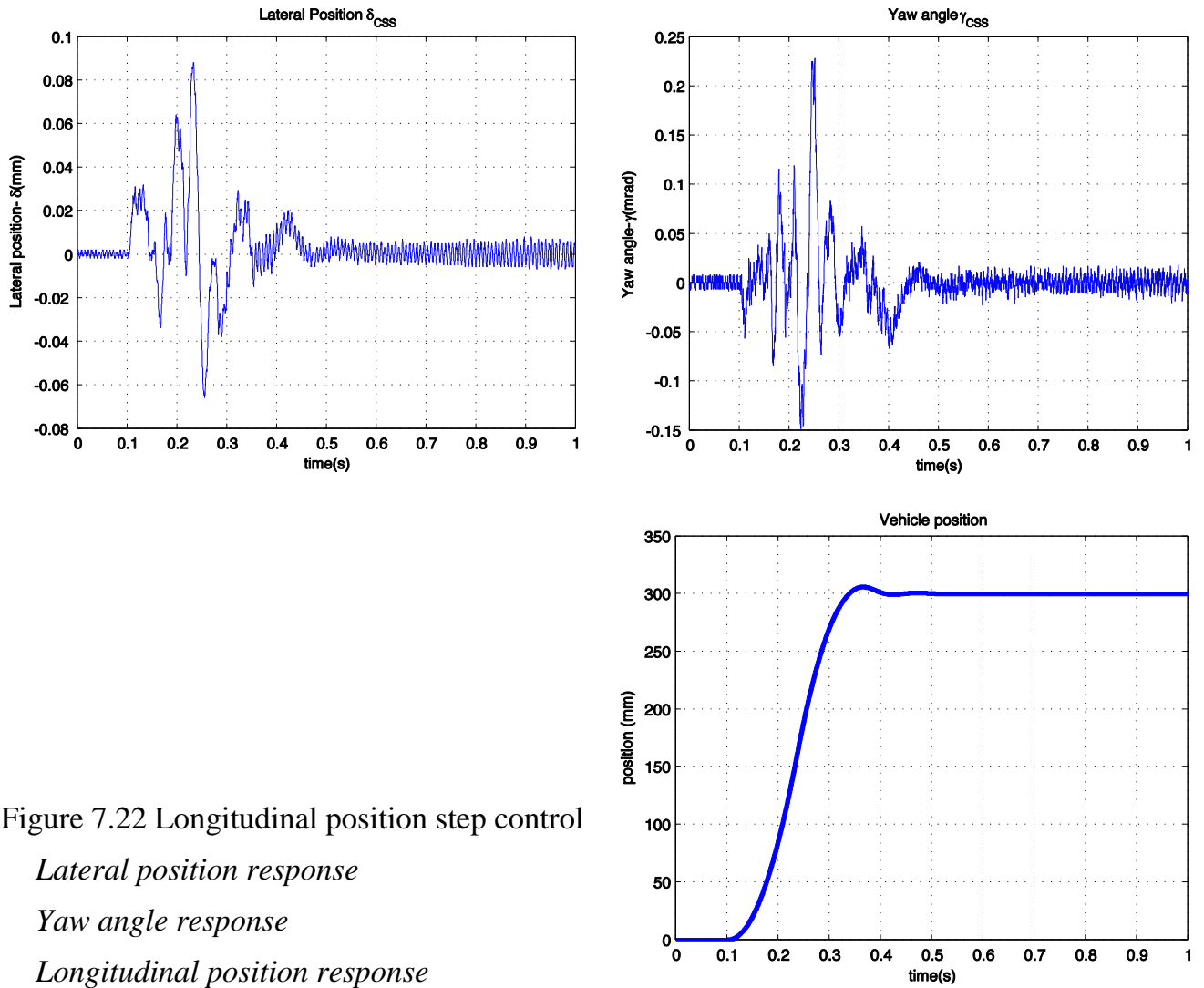


Figure 7.22 Longitudinal position step control

*Lateral position response*

*Yaw angle response*

*Longitudinal position response*

## 8. CONCLUSIONS

To summarize the results of the “magnetic guidance for linear drives” research presented in this thesis, as well as to mention the remaining research problems, the summary and the future work are presented in this chapter.

### 8.1. Summary

In this thesis, an active magnetic guidance for the permanent magnet synchronous linear motors (PMSLM) with long primary was researched. Applications like transport and handling systems in industrial plant would specially profit from this research. The thesis’s idea was the use of an active magnetic guidance for the lateral displacement and the yaw angle, while keeping a mechanical guidance for the vertical displacement. This gives an opportunity to simplify the complicated mechanical assembly significantly without any higher complexity in electromagnetic actuators or control. The active magnetic guidance was proposed with double side long-primary PM SLM. In order to apply the proposed system in multi-mover plant transport and handling systems, the long primaries should be divided into segments. Each segment was driven by a dedicated inverter, which is controlled by a PC based controller.

The prototype based on the proposed idea was constructed and presented in chapter 3. The prototype was realized using commercial PM SLMs from the company Baumüller and commercial inverters from Siemens. The system control method was implemented in a 1.7GHz PC running on Linux Soho operating system. The communication between the PC based controller and the inverters was established using the products developed at our institute.

Based on the proposed structure, the mathematical model of the magnetic guidance system was analyzed. The calculations were based on the assumption of the sinusoidal magnetic model and the synchronous  $dq$ -frame projection. The results were the normal forces and the thrust on the vehicle as the functions of the lateral position  $\delta$ , the yaw angle  $\gamma$  and the primaries’  $dq$ -currents. In order to verify the mathematical calculation, 2D FEM simulations were carried out using Maxwell 2D software from Ansoft company. The system was simulated for different operating points of the vehicle such as in lateral position, longitudinal position and different sinusoidal currents. Finally, the system was validated in a real prototype setup. The results in three cases are quite close together. This confirms that the theoretical

calculations are correct. Consequently, the mathematical model can be used in design calculations of the system's controllers.

The verified mathematical calculations were used in order to design the controllers for the system as presented in chapter 5. The control system used three standard cascade control loops to control the lateral position  $\delta$ , the yaw angle  $\gamma$  and the longitudinal position  $x$  of the vehicle. In addition to the cascade control loops, the decoupling control was suggested to give the improvement in control quality. The control method was then successfully verified in the Matlab Simulink model.

The practical experiments were performed in chapter 6 by implementing the control method on the proposed system. The experiments' results show the successful controls in each independent degree of freedom (DOF) of the vehicle as well as in the three DOFs simultaneously. The control quality was also improved with the implementation of the decoupling control. The successful transmission of the vehicle from one segment to the other segment was presented at the end of the chapter. That confirms the ability to use segmented structure in order to realize a multi-vehicle system as aimed in the target of the study.

In chapter 7, a capacitive sensor for magnetic guidance PM SLMs with long primary was presented. The capacitive sensor is a combination of the lateral position sensor and the yaw angle sensor. The sensor was designed to have the active part mounted on the static area of the system. With the design, the vehicle required no connecting cable for the lateral position and yaw angle measurement. The mathematical calculation and the FEM simulation prove the capacitive sensor's working ability. Consequently, prototypes of the capacitive sensor were incorporated in the experimental setup. The capacitive sensor was installed to the system to supply the feedback signals for the controller. The experimental results show the similar control quality with the capacitive sensor in comparison to the inductive sensor. Therefore, the capacitive sensor can replace the inductive sensor in order to make the vehicle completely passive.

## 8.2. Future work

In order to apply the system to a plant transport and handling systems in industrial manufacturing, some further research has to be done.

Firstly, a new method for the longitudinal position measurement needs to be applied to get a completely passive vehicle. The position measurement can be done by using either optical sensor or incremental sensor, with the encoding header on the

static part of the system. It has been studied and successfully implemented at our institute [52]. One other study of our institute can also be utilized for this case is the use of capacitive sensor [53]. If these suggested methods are applied successfully to the system, the vehicle will totally be passive with no connecting cable.

Secondly, the vehicle control quality, when the vehicle passing the junction between two consecutive segments, has some small perturbation due to the end-effect of the linear motor. That can be reduced with correct compensating currents. Hence, mathematical calculation, FEM simulation and real experimental measurement of that junction area must be studied in order to calculate the correct compensating current for the linear motor.

Finally, the implementation of a multi-vehicle system requires not only the segmented primary of the linear motor but also the segmented measuring sensor. In a multi-vehicle system, each vehicle is controlled to move independently in one segment. That means, each segment needs its own measuring system with three sensing parameters: lateral position, yaw angle, longitudinal position.

## Bibliography

- [1] E. R. Laithwaite. "Linear Electric Machines- A Personal View", *proceedings of the IEEE*, vol. 63, no. 2, February 1975
- [2] R. C. Post. "The Page Locomotive: Federal Sponsorship of Invention in Mid-19th-Century America." *Technology and Culture*, vol. 13, pp. 140–169, 1972
- [3] R. C. Post. *Physics, Patents, and Politics: A Biography of Charles Grafton Page*. Science History Publications: New York, 1976.
- [4] R. C. Post. "Stray Sparks from the Induction Coil: The Volta Prize and the Page Patent." *Proceedings of the IEEE*, pp. 1279–1286, 1976.
- [5] [U.S. Patent 782312](#)
- [6] G. Hugenberg. "Hermann Kemper Pionier der Magnetbahntechnik." *Standort - Zeitschrift für angewandte Geographie*, vol. 25, no. 1, pp. 52–53, 2001
- [7] Linear Induktions Motoren - Mit Volldampf auf der Magnetwelle [http://www.coastersandmore.de/rides/lim/lim\\_lsm.shtml](http://www.coastersandmore.de/rides/lim/lim_lsm.shtml)
- [8] J. Pasanen, P. Jahkonen and S.J. Ovaska. "An integrated digital motion control unit.", *IEEE Transactions on Instrumentation and Measurement*, vol. 40, no 3, pp. 654-657, Jun. 1991.
- [9] T. Masuda, M. Yoshikawa, M. Tawada. "Formulation of elevator door equation of motion." *JSME International Journal Series Dynamics Control Robotics Design and Manufacturing*, vol. 39, no. 2, pp. 279–285, 1996.
- [10] R. Krishnan. "Propulsion with and without wheels." in *IEEE International Conference on Industrial Technology (ICIT)*, vol. 1, no. 2, 2005, pp. 11–19.
- [11] X. Liu, Y.Y. Ye, Z. Zheng. "A novel tubular permanent magnet linear synchronous motor used for elevator door," in *Electrical Machines and Systems, 2007. ICEMS*, Oct. 2007 pp. 801.
- [12] M. Dursun, F. Koc and H. Ozbay. "Determination of Geometric Dimensions of a Double Sided Linear Switched Reluctance Motor." *World Academy of Science, Engineering and Technology*, vol. 70, pp. 282–288, 2010.
- [13] R. Benavides. "Investigation of Control Methods for Segmented Long Stator Linear Drives", PhD. Dissertation, TU Darmstadt, Germany, 2008.
- [14] P. Mutschler. "Comparison of topologies for linear drives in industrial material handling and processing applications," in *7th International Conference on Power Electronics ICPE '07*, 2007, pp. 1027–1032.
- [15] B. Sieber, J. Breil. "New developments for a linear motor system with multiple carriers," in *Int. LDIA2003 Symp.*, 2003, pp. 21–24.

- [16] C. Bosshard. “MagneTrak(c) Paradigmenwechsel im Materialhandling,” in *13. Deutscher Materialfluss-Kongress Innovative Techniken für die Logistik*. vol. 1815 Garching, Germany, 2004, pp. 189–200.
- [17] G. Stöppler. “Segmentierte Langstator-Linearmotoren für die Schnellpositionierung von Werkstückträgern in längsverketteten Montagelinien,” in *SPS/IPC/DRIVES/Electric Automation Systems and Components*, Nürnberg, Germany, 2008.
- [18] N.A. Duffi, R.D. Lorenz, L. Sanders. “High performance LIM based material transfer,” in *Proc. NSF Design and Manufacturing Systems Conference*, Atlanta, GA, Jan. 1992, pp.1027–1030.
- [19] J. Boeij, M. Steinbuch and H. Gutiérrez. “Modelling the Electromechanical Interactions in a Null-Flux EDS Maglev System.” *Electromagnetic Launch Technology*, 12th Symposium, 2004.
- [20] J. Boeij, M. Steinbuch and H. Gutiérrez. “Modeling the Electromechanical Interactions in a Null-Flux Electrodynamic Maglev System.” *IEEE transactions on magnetics*, vol. 41, no. 1, January 2005.
- [21] D. Li and H. Gutiérrez. “Precise motion control of a hybrid magnetic suspension actuator with large travel,” in *Industrial Electronics, 2008. IECON 2008. 34th Annual Conference of IEEE*, Nov. 2008, pp. 2661–2666.
- [22] S.O. Siems and W.-R. Canders. “Experimental investigation of linear and rotatory HTSC bearings for industrial applications.” *Int. Journal of Applied Electromagnetics and Mechanics*, vol. 19, pp. 199–202, 2004.
- [23] C. Navau, A. Sanchez and E. Pardo. “Lateral Force in Permanent Magnet-Superconductor Levitation Systems With High Critical Current.” *IEEE transactions on applied superconductivity*, vol. 13, no. 2, June 2003.
- [24] I.-Y.A Wang and I. Busch-Vishniac. “A new repulsive magnetic levitation approach using permanent magnets and air-core electromagnets.” *Magnetics, IEEE Transactions*, vol. 30 , no. 4 , Part: 2, 1994.
- [25] K. Yoshida, Z. Dai and M. Sato. “Sensor-less Propulsion Control of PM LSM Vehicle with DTC Method,” in *Proceedings. IPEDC*, 2000, pp. 191–196, vol.1
- [26] K. Ben-Yahia and G. Henneberger. “Linear magnetic bearing for high speed machine tools,” in *PCIM 99*, Nürnberg, 1999.
- [27] W. Evers and G. Henneberger. “A New Linear Drive for a Magnetic Levitation Transport System,” in *EPE 99 Lausanne*, 1999.
- [28] D’Arrigo and A. Rufer. “Design of an integrated electromagnetic levitation and guidance system for SwissMetro,” in *EPE 99 Lausanne*, 1999.

- 
- [29] D. Silva and O. Horikawa. "Experimental development of a one degree-of-freedom controlled magnetic linear bearing." *IEEE transactions On Magnetics*, vol. 41, pp. 4257–4260, 2005.
- [30] K. Yoshida, T. Yoshida and K. Noda. "Combined-Levitation-and-Propulsion Control of SLIM Maglev Vehicle on Flexible Guideway," in *EPE2003 Toulouse*, 2003.
- [31] F. Profumo, A. Tenconi, G. Gianolio and K. Gigliotti. "Design and performance evaluation of a PM linear synchronous motor with magnetic guides for industrial applications," in *IEEE-IAS Annual Meeting*, 1999, pp.110–116.
- [32] F. Profumo, A. Tenconi, G. Gianolio and K. Gigliotti. "Parameters and forces of a PM linear synchronous motor with magnetic guides for industrial applications: computed and experimental results," in *IEEE-IAS Annual Meeting*, Rome, 2000, pp.15–20 vol.1.
- [33] P.L. Jansen, L. J. Li and R.D. Lorenz. "Analysis of Competing Topologies of Linear Induction Machines for High Speed Material Transport Systems," in *IEEE-IAS Annual Meeting*, Toronto, 1993, pp. 274–281.
- [34] B. Yang, M. Henke and H. Grotstollen. "Pitch Analysis and Control Design for the Linear Motor of a Railway Carriage," in *Industry Applications Conference*, Chicago, 2001, pp. 2360–2365 vol.4.
- [35] B. Yang, M. Henke and H. Grotstollen. "Control Strategy for a Novel Combined Operation of Long Stator and Short Stator Linear Drive System," in *European Conference on Power Electronics and Applications*, Toulouse, France, 2003.
- [36] A. Pottharst, M. Henke and H. Grotstollen. "Power Supply Concept of the Longstator Linear Motor of the NBP-Test Track," in *EPE-PEMC 2002 Dubrovnik & Cavtat*, 2002, pp. P1-P5
- [37] K. Yoshida, H. Takami, X. Kong and A. Sonoda. "Mass Reduction and Propulsion Control for a Permanent-Magnet Linear Synchronous Motor Vehicle." *IEEE Transactions on Industry Applications*, vol. 37, no. 1, Jan. 2001.
- [38] K. Yoshida and X. Zhang. "Sensorless Guidance Control With Constant Airgap In Ropeless Linear Elevator," in *Power Electronics and Motion Control Conference*, 2004, pp. 772 – 776, vol. 2.
- [39] "MagneTrak®. Paradigmenwechsel im Material-handling. Elektromagnetische Technologie für komplexe Materialflusssysteme," <http://www.translift.ch/>.
- [40] J. Weigel and P. Mutschler. "Acquisition Of A Permanent Magnet Synchronous Linear Motor's Electrical Parameters And Dead Beat Current Control Considering Saturation," in *IEMDC 2003*, Madison Wisconsin, USA, 2003, pp. 791–798.

- [41] J. Weigel and P. Mutschler. “Modelling and control of a permanent magnet linear synchronous motor featuring unbalance and saturation including cross-saturation,” in *IEEE 35th Annual PESC*, Jun. 2004, pp. 2204–2210, vol.3
- [42] J. Weigel and P. Mutschler. “Modellbildung und parameteradaptive hochdynamische Regelung eines permanenterregten Synchronlinearmotors.” PhD. dissertation, TU Darmstadt, Germany, 2004.
- [43] J. Weigel and P. Mutschler. “Enhanced disturbance force rejection due to highly dynamic parameter-adaptive control of saturated PM linear motor,” in *IEEE-IAS 2005*, Hong Kong, Oct. 2005, pp. 723–730 vol. 1.
- [44] R. Benavides and P. Mutschler. “Controlling a System of Linear Drives,” in *IEEE-PESC 2005*, Brazil, Jun. 2005, pp. 1587 – 1593.
- [45] R. Benavides and P. Mutschler. “Compensation of Disturbances in Segmented Long Stator Linear Drives using Finite Element Models,” in *IEEE International Symposium on Industrial Electronics ISIE*, Jul. 2006, pp. 2445–2449.
- [46] R. Benavides and P. Mutschler. “Improved application of resonant controllers for compensation of cogging force ripple in long-stator Permanent-Magnet Linear machines,” in *Optimization of Electrical and Electronic Equipment, OPTIM*, May 2008, pp. 125–131.
- [47] R. Leidhold and P. Mutschler. “Speed Sensorless Control of a Long-Stator Linear Synchronous-Motor arranged by Multiple Sections,” in *IEEE-IECON*, Raleigh, North Carolina USA, Nov. 2005, pp. 1395 – 1400.
- [48] R. Leidhold, R. Benavides and P. Mutschler. “Comparison of control oriented models for the Long Stator Synchronous Motor and their experimental validation,” in *SPEEDAM*, Taormina, May 2006, pp. S22-18 – S22-23.
- [49] R. Leidhold and P. Mutschler. “A Linear Synchronous Motor Model for Evaluation of Sensorless Methods,” in *IEEE - ISIE*, Montreal Canada, Jul. 2006, pp. 2467 – 2472.
- [50] R. Leidhold and P. Mutschler. “Sensorless position-control method based on magnetic saliencies for a Long-Stator Linear Synchronous-Motor,” in *IEEE-IECON 32<sup>nd</sup>*, Paris, Nov. 2006, pp. 781–786.
- [51] R. Leidhold and P. Mutschler. “Implementation of Sensorless Methods in Segmented Long Stator Synchronous Linear Motors,” in *LDIA*, Lille, France, Sept. 2007, pp. 167–168.
- [52] M. Mihalachi and P. Mutschler. “Evaluation of two position acquisition systems for permanent magnet linear motors with passive movers,” in *OPTIM*, May 2008, pp. 37–44.



- [53] M. Mihalachi and P. Mutschler. "Position Acquisition for Long Primary Linear Drives with Passive Vehicles," in *IAS '08*, Oct. 2008. pp. 1–8.
- [54] R. Benavides. "Entwurf eines Kommunikationssystem, Parallel Bussystems auf 485-Basis." Diplomarbeit, TU Darmstadt, 2003.
- [55] <https://rtai.org>
- [56] P. Mutschler. Class lecture, Topic: "Control of Drives." Institute of Power Electronics and Control of Drives, TU Darmstadt, Sep. 2004.
- [57] I. Boldea and S. A. Nasar. *Linear electric actuators and generators*. Cambridge University Press, 1997, ISBN 0-521-48017-5.
- [58] Texas Instrument Europe. "Field Orientated Control of 3-Phase AC-Motors", <http://www.focus.ti.com/lit/an/bpra073/bpra073.pdf> [Feb. 1998].
- [59] Ansys. "Maxwell® Electromagnetic Field Simulation for High-Performance Electromechanical Design," <http://www.ansoft.com/products/em/maxwell/>
- [60] Wikipedia. "Finite element method," [http://en.wikipedia.org/wiki/Finite\\_element\\_method](http://en.wikipedia.org/wiki/Finite_element_method)
- [61] D. Schröder. *Elektrische Antriebe 2*. Springer-Verlag Berlin – Heidelberg – New York, 1995, ISBN 3-540-57610-X
- [62] P. Mutschler. Practical training, Topic: "S2 - AC drive with voltage source inverter (VSI)." Institute of Power Electronics and Control of Drives, TU Darmstadt, Sep. 2003.
- [63] I. Müller. Practical training, Topic: "S3 - Field oriented control." Institute of Power Electronics and Control of Drives, TU Darmstadt, 2003-2004.
- [64] O. Föllinger. *Regelungstechnik – Einführung in die Methoden und Ihre Anwendung*. Hüthig Verlag, Heidelberg, 1994.
- [65] R. Benavides and P. Mutschler. "Control Techniques to Compensate Detent Forces in Segmented Long Stator Linear Motors," in *LDIA*, Lille, France, Sep. 2007, pp. 160-161.
- [66] R. Benavides and P. Mutschler. "Detent force compensation in Segmented Long Stator Permanent Magnet Linear Drives using Finite Element Models," in *12th European Conference on Power Electronics and Applications, EPE 2007*, Aalborg, Denmark, Sep. 2007, pp. DS3.5, topic 10
- [67] R. Benavides and P. Mutschler. "Comparison of field oriented control and indirect flux control applied to segmented long stator linear machine," in *PCIM 2007*, Nürnberg, May 2007, pp. S3d (p.8).
- [68] J. F. Gieras and Z. J. Piech. *Linear synchronous motor: Transportation and Automation Systems*. CRC Press 2000, ISBN: 0-8493-1859-7

- [69] D. Schröder. *Intelligent Observer and Control Design for Nonlinear Systems*. Springer, Berlin – Heidelberg – New York, 2000, ISBN-10: 3-540-63639-0.
- [70] P. Vas. *Vector control of AC machines*. Clarendon Press - Oxford University, New York, 1990, ISBN 10: 0-198-59370-8
- [71] R. Isermann, K. H. Lachmann and D. Matko. *Adaptive Control Systems*. Prentice-Hall, 1993, ISBN-10: 0-131-37456-7.
- [72] U. Tietze, C. Schenk, E. Gamm. *Electronic Circuits: Handbook for Design and Application*. Springer Verlag, 2007, ISBN: 978-3-540-00429-5
- [73] L. K. Baxter. *Capacitive Sensors: Design and Applications*. IEEE Press -1996, ISBN-10: 0-780-31130-2.
- [74] <http://www.magnemotion.com>
- [75] Siemens. *SIMODRIVE 611 digital Drive Converters Configuration Manual*. Feb. 2007.
- [76] M. Mihalachi. “Software Implementation for FVA 445 Project,” Institute für Stromrichtertechnik und Antriebsregelung, TU Darmstadt, Feb. 2008
- [77] P. Khong, R. Leidhold and P. Mutschler. “Magnetic guidance of the mover in a long-primary linear motor” Accepted for *publication in Industry Applications, IEEE Transactions* - electronic publishing, DOI: 10.1109/TIA.2011.2125934, Mar. 2011.
- [78] P. Khong, R. Leidhold and P. Mutschler. “Magnetic guidance of the mover in a long-primary linear motor,” in *IEEE-ECCE 2009*, San Jose, CA Sept. 2009, pp. 2354-2361
- [79] P. Khong, R. Leidhold and P. Mutschler. “Magnetic guiding and capacitive sensing for a passive vehicle of a long-primary linear motor,” in *EPE/PEMC 2010*, Ohrid - Macedonia, Sept. 2010, pp. S3-1 – S3-8.
- [80] P. Khong, R. Leidhold and P. Mutschler. “Capacitive gap and yaw angle sensor for linear drives,” in *IECON 2010*, Glendale – AZ, Nov. 2010, pp. 1240 – 1245.
- [81] Baumüller. *LSE Synchronous Linear Motors Documentation*. Jul. 2002

# APPENDIX A

## Experimental Hardware

Instead of using the commercial products, control and communication hardware in the experimental setup are self-developed products of the institute. The details of the hardware are introduced in following.

### A1. Inverter interface board - IIB

#### A1.1 IIB structure

As mentioned, the inverter interface needs four main functions:

- Generate PWM signals for the power module (IGBT) gates,
- Acquire measured data,
- Communicate with the controller,
- Protect the inverter (over current, over temperature etc.).

Because the setup aims for experimental research, the control system is designed as a central control system in order to simplify data acquisitions and analyses. All the calculations and the regulation tasks are done by a central controller (a PC) instead of a distributed control system (where each inverter module would have one microprocessor controller). This requirement could not be satisfied by any commercial inverter control unit. Therefore, in the experimental setup, each inverter module has one self-developed inverter interface board (IIB) from our institute [54]. The design of the IIB is based on a **Complex Programmable Logic Device (CPLD)** EPM 9320 from Altera. The CPLD has a duty to generate logic function circuits for IIB. Supplements to the CPLD are some other components, i.e. buffers, A/D converters, comparators, transceivers, etc., to generate each specific function. The block diagram of IIB is presented in Figure A1.1.

The PWM signal generating function is mainly implemented by the designed CPLD firmware. The CPLD receives a 40MHz clock from a crystal and generates a 12-bit counter. The counter counts from 0 to 4000 in circulations in order to generate 100  $\mu s$  periods for generating PWM signals. In each period, the rising or falling edges of the PWM signals are produced by comparing the counter value with 12-bit values from the controller. The power of these PWM signals is then amplified in PWM buffers in order to control the IGBT gates.

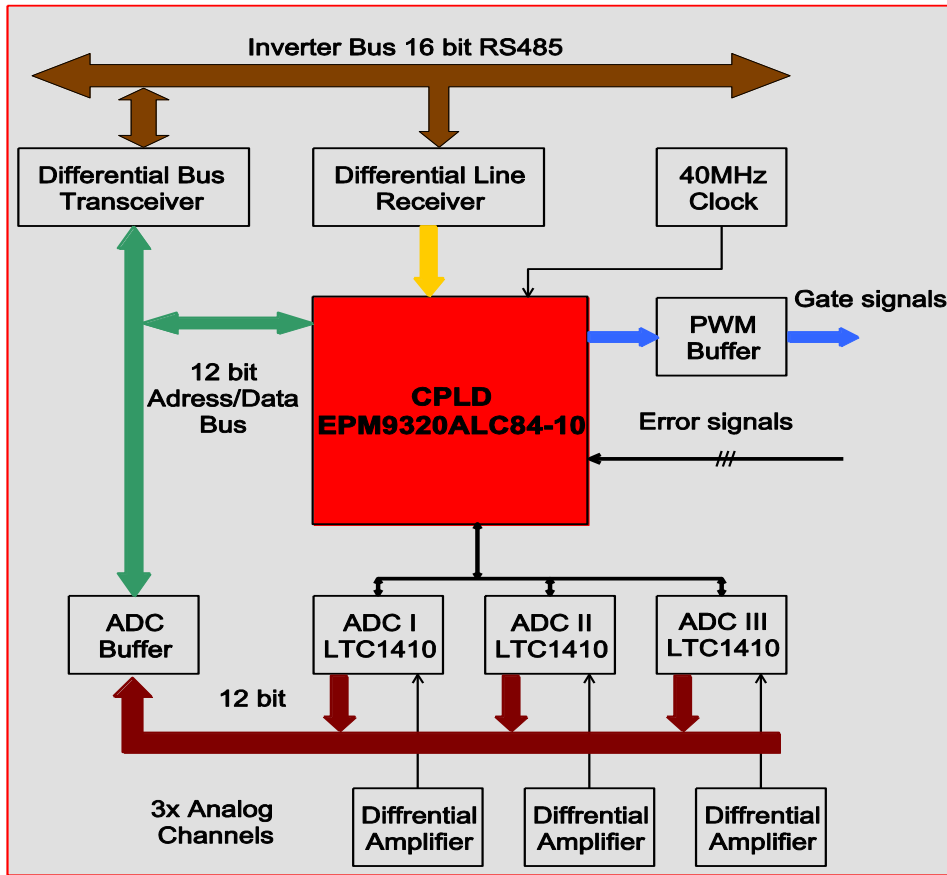


Figure A1.1 Block diagram of Inverter interface board (IIB)

The IIB has three data channels to gather information from sensors for the controller, the data analysis and the system protection. Analogue signals from the sensors are fed to differential amplifiers in order to generate suitable signals for A/D converters. The suitable signals are then converted by 12-bit A/D converters LTC1410 from Linear Technology. After that, the 12-bit converted data are sent to the controller through the communication bus.

Communication between the IIB and the controller is performed by a 16-bit parallel bus according to the RS485 standard. Within the 16 bits, there are 12 bits for address or data de-multiplexing signals. The last 4 bits are synchronous control signals. The communication functions are performed by the CPLD. The CPLD controls the differential bus transceivers and receivers and the other components in order to exchange data with the inverter bus. Each primary section must be independently controlled; therefore each IIB has a separate address to the others stored in the CPLD firmware.

The protection signals used in the IIB include the over current signals, the over temperature signal from the inverter module or the error signal from the rectifier module. All these signals are sent directly to the CPLD in order to process and execute the protection functions.

## A1.2 Modulation in IIB

The modulator is used to generate the switching signals for the IGBTs. The modulator in the experiment setup is implemented in the CPLD of each IIB. The modulator has a 12-bit counter, which counts from 0 to 4000 in  $100\mu\text{s}$ . In running state, the counter is reset to zero when the value reaches 4000, and a reset-procedure is ready. The counter and the reset automat generate a saw-tooth signal as presented in Figure A1.2. In order to generate the IGBT gate signals ( $B_r, B_s, B_t$ ), the counter value is compared with timing values and switching states. The timing values ( $t_r, t_s, t_t$ ) and the switching states are generated by the controller (PC) and sent to the IIB in every  $100\mu\text{s}$ .

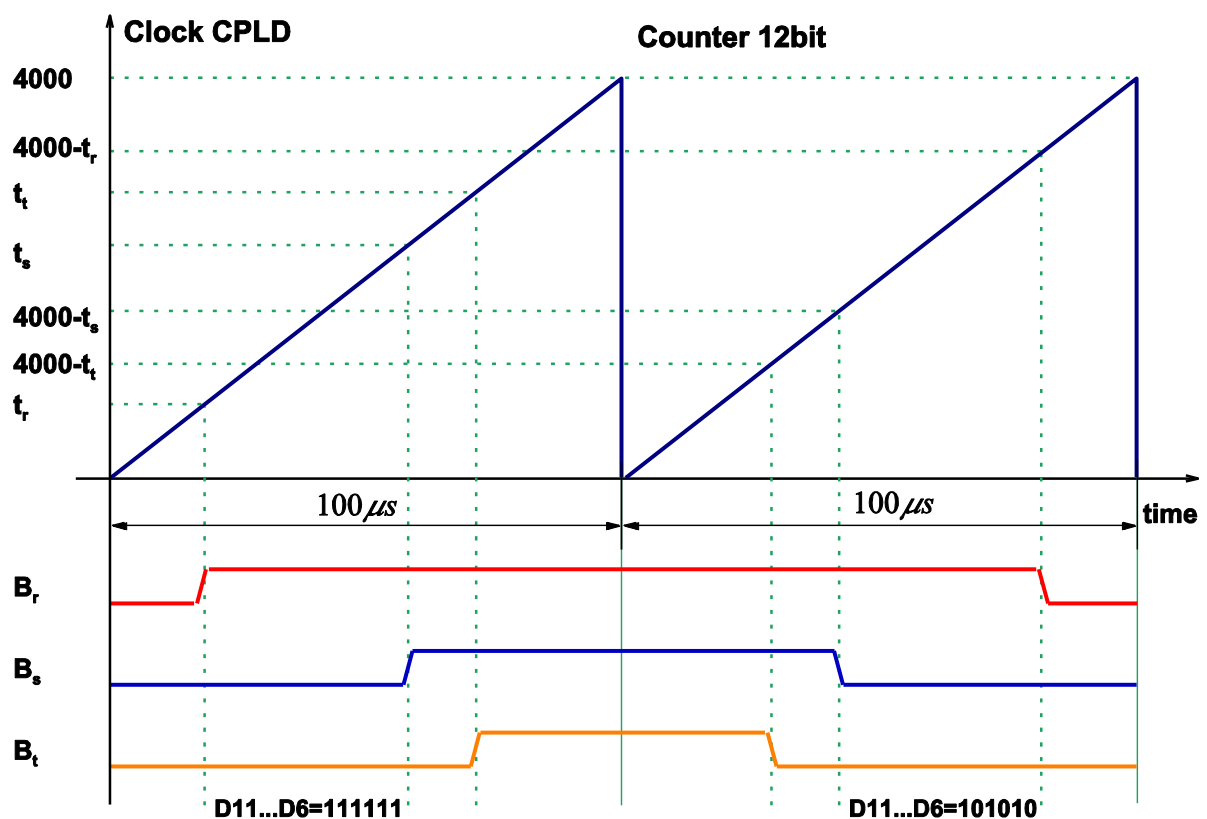


Figure A1.2 Timing diagram of the modulator.

Through the 16-bit communication bus, the IIB is called every  $100\mu\text{s}$ . When the IIB is called with its correct address, it automatically generates a reset-procedure. The procedure brings the IIB back to beginning state of a circle process. This also allows resetting the counter to zero. In a communication period, the switching state and the switching times are also stored in CPLD registers. The switching states are the 6 Bits ( $D6...D11$ ) of the communication bus mentioned in appendix A3. Here, each 2bit determines a switching state in one phase of the IGBT bridge: 11 = above IGBTs on; 10 = below IGBTs on; 0x = no IGBT on. The switching times are three 12-bit data sent after the IIB address in communicating diagram. They carry the timing values

( $t_r, t_s, t_f$ ) for determining the switching states of the three IGBT branches. As presented in the Figure A1.2, each switching circle is generated by two communicating circles. That means the switching frequency of the inverter is 5Khz.

When there is no communication or no call from the VCI, IIB is not addressed. Therefore, the reset-procedure is not generated, and the counter increases to the value of 4090. At that value, the outputs of IIB to IGBT gates are blocked.

## A2. Vehicle control interface - VCI

The communication between PC controller and the other equipment of the experiment system is performed by a Vehicle Control Interface (VCI) card [54][46], shown in Figure A2.1. The VCI has the duty to transmit and receive information from the IIBs. In addition, it acquires longitudinal positions directly from the position sensors. For these duties, the VCI was designed with an Altera Cyclon PQFP240 Field Programmable Gate Array (FPGA) core. There are some other supplements used to combine individual functions of the VCI.

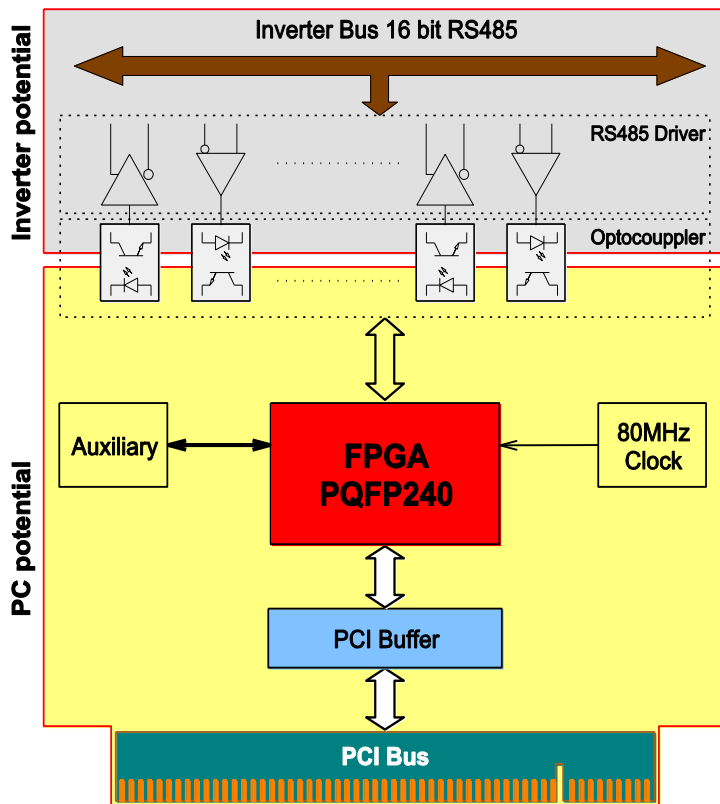


Figure A2.1 Block diagram of VCI board

As the interface card for the controller, the VCI was designed as a bus master for the communication system between the VCI and the IIBs. With this function, the VCI needs to have a clock signal to synchronize all the communicating activities. The synchronous clock is generated by an 80Mhz external crystal oscillator and the designed logic circuit stored in the FPGA. In the designed communicating protocol, one data-transfer period between the VCI with an IIB requires seven synchronous clocks. The frequency of the synchronous clock is

dependent on the number of IIB managed by the VCI, which need to be contacted in one  $100\mu s$  cycle, and the limitation of communicating system. In this experimental

setup, the synchronous clock was 1.44Mhz to generate 20 communicating time slots, for maximum 20 IIBs, per  $100\mu s$ .

The communication between the VCI and the IIBs is implemented by a 16-bit bus using the RS485 standard. Because the signals in the transmitters and the receivers have the same ground potential as the IIBs, the opto-couplers are used to isolate the PC potential and the inverter potential in the VCI board. All the 16-bit signals from the FPGA, including A/D multiplexing signals, the synchronous clock and control signals, are exchanged with the opto-couplers. The output signals from opto-couplers are converted to the RS485 standard.

Information exchanged between the VCI and the PC is transferred through a PCI slot of the PC. The PCI protocol is embedded in the FPGA inside the circuit using a PCI software module supplied by Altera. Input and output signals using the PCI standard are led from the FPGA to buffers. The signals are then connected to the PCI bus of the PC through a PCI standard connector.

With the FPGA, the longitudinal position decoding circuit was also embedded in the VCI board. The 90deg-shifted signals from the incremental position sensor are sent to the VCI through transmitting and receiving auxiliary boards. These signals are decoded to give the longitudinal position of the vehicle.

### **A3. The experimental communication bus**

The communication between a vehicle control interface (VCI) board and inverter interface boards (IIBs) is fulfilled by a 16-bits parallel bus. The bus is implemented following the RS485-Standard (twisted pairs). In the 16-bit signals, there are four signals used as driven Bus-Master signals. The four signals are named CLK, Addr, WR and RD. The other 12 signals are used for addresses or data (timing, switching state, current values) transferring. They are called AD0...AD5 and D6...D11. The Figure A3.1 shows the 16-bit bus signals and their timing diagram.

In transferring processes, each VCI waits for the state  $(clk=1)\&(Addr=1)\&(WR=0)\&(RD=0)$  i.e. the beginning of the first clock cycle (CLK). When the state occurs, the Bus master sends out the signals AD0...AD5. The 6 signals carry an address of a VCI, which the Bus master wants to communicate with it. The state takes  $\frac{3}{4}$  of a clock cycle.

When the control signal WR=1 (at the beginning of the second cycle), the VCI sends the 12 signals AD0...AD5 and D6...D11 to the bus. The WR signal is kept in "1" in four CLK (from 2<sup>nd</sup> cycle to end of 5<sup>th</sup> cycle). In the 2<sup>nd</sup> cycle, the VCI

### A3. The experimental communication bus

transfers on AD0...AD5 the address of the IIB and on D6...D11 the switching state. In the 3<sup>rd</sup>, 4<sup>th</sup> and 5<sup>th</sup> cycle, the VCI must send to the 12-bits timing values  $t_r$ ,  $t_s$  and  $t_t$  on AD0...AD5, D6...D11.

When the control signal RD=1 (at the beginning of cycle 6), the 12-bit signals AD0...AD5, D6...D11 is written by the IIB. The RD signal lasts in 3 CLKs in state "1" (in the 6<sup>th</sup>, 7<sup>th</sup> and 8<sup>th</sup> cycles). In the 3 CLKs, the IIB sends the feedback current values to the controller through AD0...AD5, D6...D11.

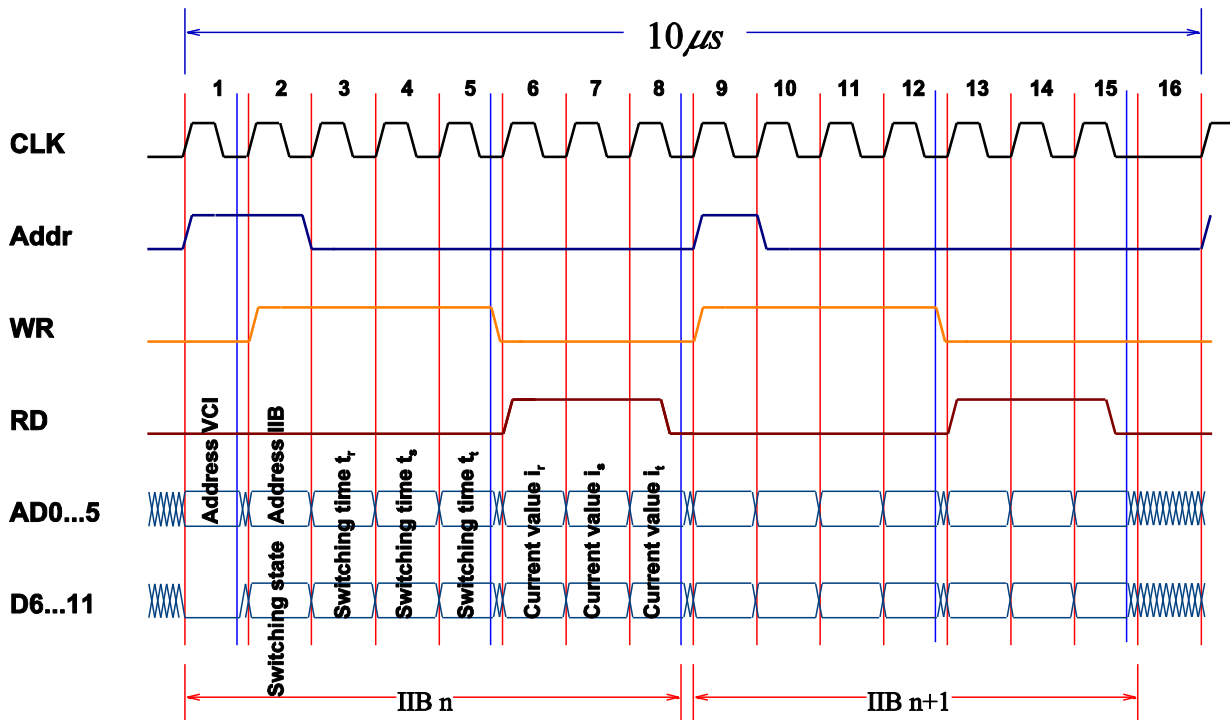


Figure A3.1: Timing diagram of the Bus signals in  $10\mu s$ .

From the 9<sup>th</sup> cycle, the VCI starts a new communication with the next IIB. The communicating process is the same as the previous process. Therefore, the VCI can communicate with two IIBs in one time slot of  $10\mu s$ . The communicating cycle for each IIB is  $100\mu s$ .

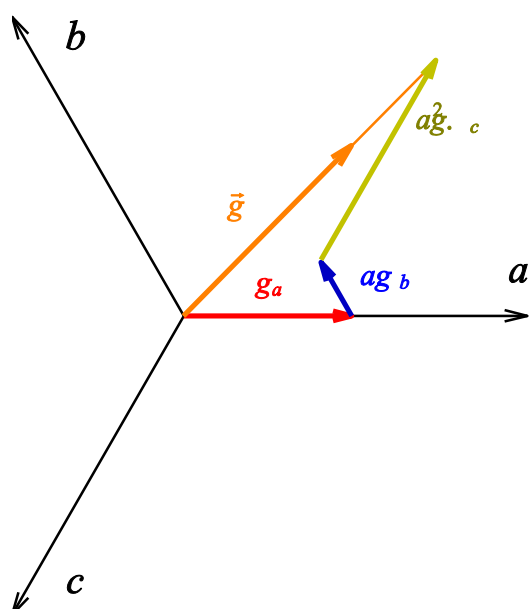


## APPENDIX B

### Controller design

#### B1. The d-q projection

The sets of three phase currents, voltages and fluxes can be described by complex space vectors  $\vec{i}$ ,  $\vec{v}$ ,  $\vec{\Psi}$ . In general, each set of three-phase variables has instantaneous values presented in each axis of the three phase stationary stator coordinates  $g_a$ ,  $g_b$ ,  $g_c$ . If the sum of them is zero, i.e. no zero component, then they can be defined



The space vector is depicted in complex system.

$$\vec{g}_{abc} = \frac{2}{3} g_a + a g_b + a^2 g_c$$

where

$$a = e^{j\frac{2\pi}{3}} = -\frac{1}{2} + j\frac{\sqrt{3}}{2}$$

$$a^2 = e^{j\frac{4\pi}{3}} = -\frac{1}{2} - j\frac{\sqrt{3}}{2}$$

Figure B1.1 The space vector in  $abc$  three-phase system axes

simply by a complex space vector  $\vec{g}$  like in Figure B1.1, where  $a$ ,  $b$  and  $c$  are the three-phase system axes. The space vector  $\vec{g}$  describes the three-phase system [58][70].

The space vector can be also presented simply like an algebraic vector as in (B1.1).

$$\vec{g}_{abc} = \begin{bmatrix} g_a \\ g_b \\ g_c \end{bmatrix} \quad (\text{B1.1})$$

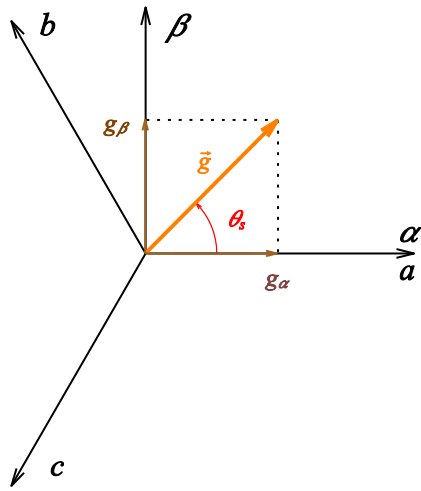
These space vectors can be described neatly in a two dimensional coordinate system, which is called  $\alpha\beta$  stationary reference frame. Assuming that the  $\alpha$  axis of the  $\alpha\beta$  frame aligns with the  $a$  axis of the  $abc$  frame, the description of the space

## B1. The d-q projection

vector in the new reference frame is presented in Figure B1.2. The projection from the three-phase system into the  $\alpha\beta$  two dimensional orthogonal system is presented by the algebraic transformation in equation (B1.2). This  $\alpha\beta$  transformation is in english literature also known as Clarke's transformation or.

$$\vec{g}_{\alpha\beta} = \begin{bmatrix} g_\alpha \\ g_\beta \end{bmatrix} = T_{abc-\alpha\beta} \cdot \begin{bmatrix} g_a \\ g_b \\ g_c \end{bmatrix} \quad \vec{g}_{abc} = T_{\alpha\beta-abc} \cdot \begin{bmatrix} g_\alpha \\ g_\beta \end{bmatrix} \quad (\text{B1.2})$$

$$\text{Where: } T_{abc-\alpha\beta} = \frac{2}{3} \begin{bmatrix} 1 & -\frac{1}{2} & -\frac{1}{2} \\ 0 & \frac{\sqrt{3}}{2} & -\frac{\sqrt{3}}{2} \end{bmatrix}; \quad T_{\alpha\beta-abc} = \begin{bmatrix} 1 & 0 \\ -\frac{1}{2} & \frac{\sqrt{3}}{2} \\ \frac{1}{2} & -\frac{\sqrt{3}}{2} \end{bmatrix}$$



The space vector is depicted in  $\alpha\beta$  frame

$$\vec{g}_{\alpha\beta} = |g|e^{j\theta_s} = g_\alpha + j \cdot g_\beta$$

where

$$g_\alpha = \frac{2}{3} \left( g_a - \frac{1}{2}g_b - \frac{1}{2}g_c \right)$$

$$g_\beta = \frac{2}{3} \left( \frac{\sqrt{3}}{2}g_b - \frac{\sqrt{3}}{2}g_c \right)$$

Figure B1.2 The space vector in  $\alpha\beta$  stationary frame

In order to eliminate the effect of time dependent variable on the system's parameters, a  $dq$  rotational frame is used. The  $dq$  frame in linear drives is electrically fixed to the magnet of the linear motor with the  $d$  axis aligned with the permanent magnet flux. The rotational angle and the speed of the  $dq$  frame are synchronized with the relative motion between the primary and the secondary of the linear motor as described in equations (B1.3).

$$\beta_m = x_0 \frac{\pi}{\tau} = \theta_s - \theta_m \quad \omega_m = \frac{d\beta_m}{dt} = u \frac{\pi}{\tau} \quad (\text{B1.3})$$

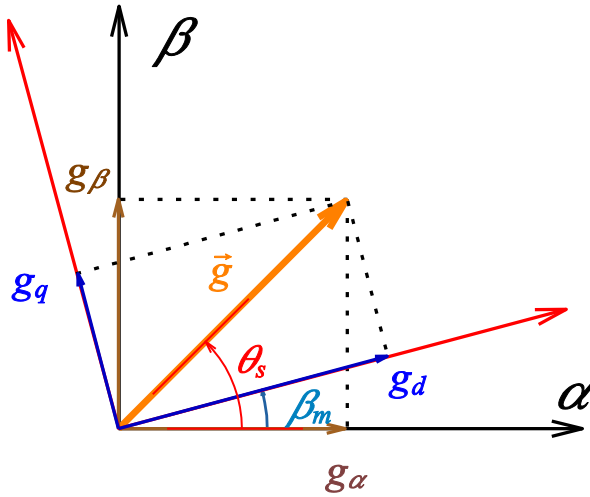
- where:  $\beta_m$  is the angle between  $dq$ -frame and  $\alpha\beta$ -frame,  
 $x_0$  is the displacement between equivalent origin of stationary frame and vector of the PM flux,  
 $u$  is the relative velocity between the magnet and the primary.

The transformation, which modifies a two-phase orthogonal system ( $\alpha\beta$ ) in the  $dq$  rotating reference frame, is also known as Park's transformation. It is presented in Figure B1.3 and is defined by algebraic equations (B1.4).

$$\vec{g}_{dq} = \begin{bmatrix} g_d \\ g_q \end{bmatrix} = T_{\alpha\beta-dq} \cdot \begin{bmatrix} g_\alpha \\ g_\beta \end{bmatrix} \quad \vec{g}_{\alpha\beta} = \begin{bmatrix} g_\alpha \\ g_\beta \end{bmatrix} = T_{dq-\alpha\beta} \cdot \begin{bmatrix} g_d \\ g_q \end{bmatrix} \quad (\text{B1.4})$$

Where:

$$T_{\alpha\beta-dq} = \begin{bmatrix} \cos(\beta_m) & \sin(\beta_m) \\ -\sin(\beta_m) & \cos(\beta_m) \end{bmatrix}; \quad T_{dq-\alpha\beta} = \begin{bmatrix} \cos(\beta_m) & -\sin(\beta_m) \\ \sin(\beta_m) & \cos(\beta_m) \end{bmatrix}$$



The space vector is depicted in  $dq$  frame

$$\begin{aligned} \vec{g}_{dq} &= |g| e^{j(\theta_s - \beta_m)} = |g| e^{j\theta_s} e^{-j\beta_m} \\ &= \vec{g}_{\alpha\beta} \cdot e^{-j\beta_m} \\ \vec{g}_{dq} &= g_d + j \cdot g_q \end{aligned}$$

where

$$\begin{aligned} g_d &= g_\alpha \cdot \cos(\beta_m) + g_\beta \cdot \sin(\beta_m) \\ g_q &= -g_\alpha \cdot \sin(\beta_m) + g_\beta \cdot \cos(\beta_m) \end{aligned}$$

Figure B1.3 The space vector in  $dq$  rotational frame

If the sum of the three-phase component is not zero, a zero component is added. Therefore, the Park's transformation is:

$$T_{abc-dq0} = \frac{2}{3} \begin{pmatrix} \cos(\beta_m) & \cos(\beta_m - \frac{2\pi}{3}) & \cos(\beta_m + \frac{2\pi}{3}) \\ -\sin(\beta_m) & -\sin(\beta_m - \frac{2\pi}{3}) & -\sin(\beta_m + \frac{2\pi}{3}) \\ \frac{1}{2} & \frac{1}{2} & \frac{1}{2} \end{pmatrix} \quad (\text{B1.5})$$

And the inverse Park's transformation is:

$$T_{dq0-abc} = \begin{pmatrix} \cos(\beta_m) & -\sin(\beta_m) & 1 \\ \cos(\beta_m - \frac{2\pi}{3}) & -\sin(\beta_m - \frac{2\pi}{3}) & 1 \\ \cos(\beta_m + \frac{2\pi}{3}) & -\sin(\beta_m + \frac{2\pi}{3}) & 1 \end{pmatrix} \quad \text{B1.6}$$

The transform equation is:

$$\begin{pmatrix} g_a \\ g_b \\ g_c \end{pmatrix} = T_{dq0-abc} \begin{pmatrix} g_d \\ g_q \\ g_0 \end{pmatrix} \quad \text{B1.7}$$

## B2. Transformation of three phase currents

When considering the three-phase currents are functions of a current vector  $\vec{i}$  in the  $dq$ -coordinates, they are defined by:

$$\begin{pmatrix} i_A \\ i_B \\ i_C \end{pmatrix} = T_{dq0-abc} \begin{pmatrix} i_d \\ i_q \\ i_0 \end{pmatrix} \quad \text{B2.1}$$

Where  $i_0 = 0$ , because the experimental setup uses primaries with non-grounded neutral points.

By substituting  $\beta_m$  for  $x_0 \frac{\pi}{\tau}$  in (B1.6), it yields:

$$\begin{pmatrix} i_A \\ i_B \\ i_C \end{pmatrix} = \begin{pmatrix} \cos(\frac{x_0\pi}{\tau}) & -\sin(\frac{x_0\pi}{\tau}) & 1 \\ \cos(\frac{x_0\pi}{\tau} - \frac{2\pi}{3}) & -\sin(\frac{x_0\pi}{\tau} - \frac{2\pi}{3}) & 1 \\ \cos(\frac{x_0\pi}{\tau} + \frac{2\pi}{3}) & -\sin(\frac{x_0\pi}{\tau} + \frac{2\pi}{3}) & 1 \end{pmatrix} \begin{pmatrix} i_d \\ i_q \\ 0 \end{pmatrix} \quad \text{B2.2}$$

Therefore, the three phase currents are:

$$\begin{aligned} i_A &= \cos(\frac{x_0\pi}{\tau})i_a \cos(\theta_m) - \sin(\frac{x_0\pi}{\tau})i_a \sin(\theta_m) = i_a \cos(\frac{x_0\pi}{\tau} + \theta_m) \\ i_B &= \cos(\frac{x_0\pi}{\tau} - \frac{2\pi}{3})i_a \cos(\theta_m) - \sin(\frac{x_0\pi}{\tau} - \frac{2\pi}{3})i_a \sin(\theta_m) \\ &= i_a \cos(\frac{x_0\pi}{\tau} + \theta_m - \frac{2\pi}{3}) \end{aligned} \quad \text{B2.3}$$

$$\begin{aligned}
 i_C &= \cos\left(\frac{x_0\pi}{\tau} + \frac{2\pi}{3}\right)i_a \cos(\theta_m) - \sin\left(\frac{x_0\pi}{\tau} + \frac{2\pi}{3}\right)i_a \sin(\theta_m) \\
 &= i_a \cos\left(\frac{x_0\pi}{\tau} + \theta_m + \frac{2\pi}{3}\right)
 \end{aligned}$$

Derive from (B1.3), it yields

$$\theta_s = \frac{x_0\pi}{\tau} + \theta_m \quad \text{B2.4}$$

Substituting (B2.4) into (B2.3), the three-phase currents are simplified as:

$$\begin{aligned}
 i_A &= i_a \cos(\theta_s) \\
 i_B &= i_a \cos\left(\theta_s - \frac{2\pi}{3}\right) \\
 i_C &= i_a \cos\left(\theta_s + \frac{2\pi}{3}\right)
 \end{aligned} \quad \text{B2.5}$$

### B3 Anti-windup current control

Figure B3.1 shows the block diagram of the implemented current control algorithm, which uses two PI controllers in a  $dq$  reference frame and a Space Vector Pulse Width Modulation (SV-PWM block) to generate the inverters' switching times, in the control system of the linear motor experiment setup [76].

In the control system, the reference input values consist of:

- A current reference vector  $i_m$  with
  - Magnitude of the current vector  $|i_m^*| = \sqrt{i_d^{*2} + i_q^{*2}}$
  - Angle of the current vector  $\angle i_m^* = \arctan(i_d^*, i_q^*)$
- Maximal voltage  $|u_{\max}|$

The current control will be realized in a  $dq$  two-phased reference frame, with the angle  $\beta_m$  between the phase  $d$  of the control reference frame and the phase  $a$  of the three-phased  $abc$  system.

Because of the inverters ability, the output voltage vectors of the inverter are bounded by  $|u_{\max}|$ . This causes the *windup effect* in the PI current control loops when the voltage boundary (presented by a circle with  $|u_{\max}|$  radius in  $dq$ -reference frame) is exceeded. Therefore, general implementation of the PI regulators with anti-windup was used in current control loops of the experimental setup. In the implementation,

the output reference voltage vector is simply confined in side a circle of the given radius.

Table B2.1 defines the variables used in the implementation. The control algorithm is presented in Figure B3.2 and equations (B3.1) ÷(B3.5). This algorithm was inherited from the work of [76] and embedded in the control program of the experimental setup.

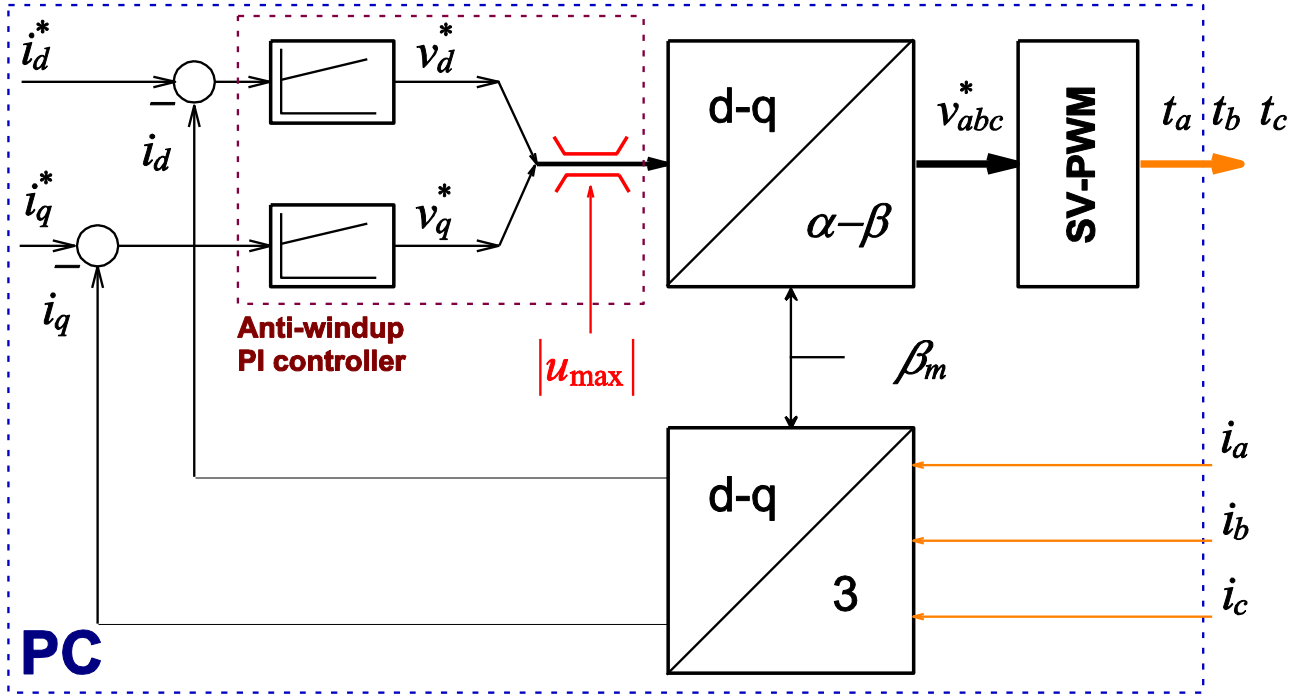


Figure B3.1. Current control block diagram

TABLE B3.1. CURRENT CONTROLLERS' DEFINITIONS

Inputs	Reference vector $i_m^* k$ Measured vector $i_m k$	Auxiliary variables	Output without anti wind-up $v_m k$
Outputs	Manipulated vector $v_m^* k$	Parameters	Sampling time $T_s$
States	Integral component $u_m k$ Control error $e k$		Proportional gain $K_p$ Integral time constant $T_i$ Output limitation $u_{max}$

Control algorithm at a sampling instant  $k$ :

$$e k = i_m^* k - i_m k \tag{B3.1}$$

$$u_m k = u_m k-1 + e k + e k-1 \frac{T_s K_p}{2 T_i} \tag{B3.2}$$

$$v_m k = u_m k + K_p \cdot e k \tag{B3.3}$$

$$v_m^* k = \begin{cases} v_m k ; & \text{if } |v_m k| \leq u_{\max} \\ \frac{v_m k}{|v_m k|} u_{\max} ; & \text{if } |v_m k| > u_{\max} \end{cases} \quad (\text{B3.4})$$

$$u_m k = \begin{cases} u_m k ; & \text{if } |v_m k| \leq u_{\max} \\ v_m^* k - K_P e k ; & \text{if } |v_m k| > u_{\max} \end{cases} \quad (\text{B3.5})$$

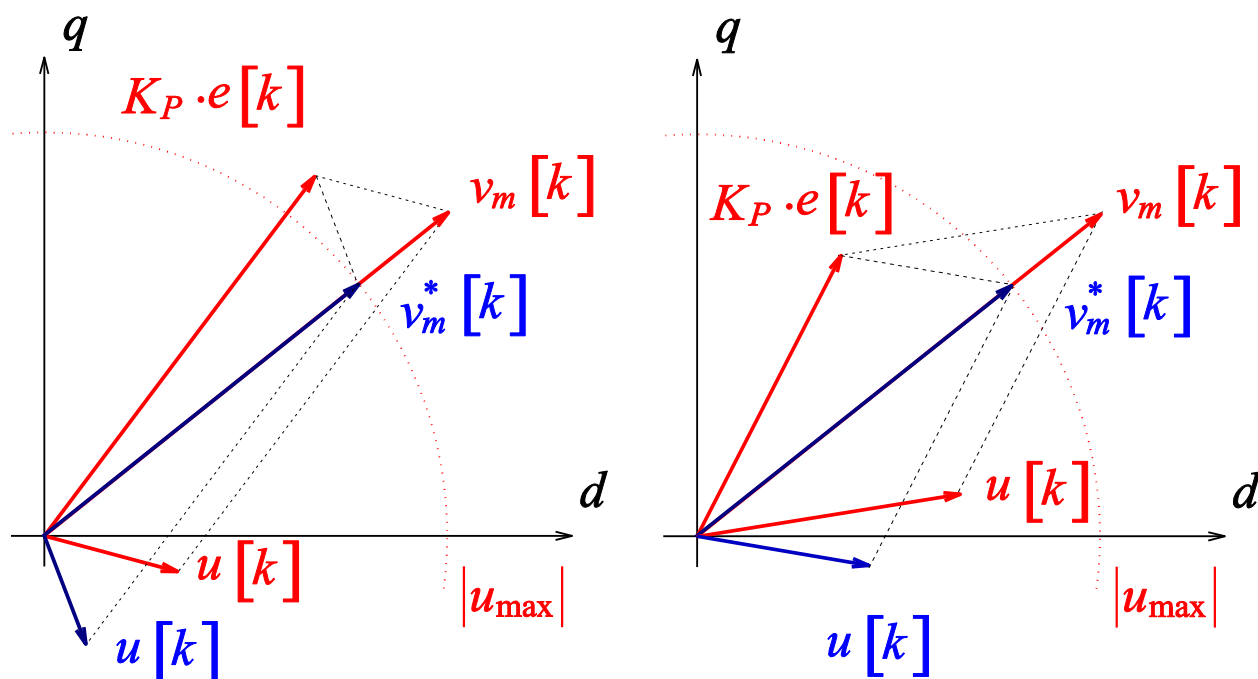


Figure B3.2. PI current controller anti-windup

## B4 Basics of designing controller for drives

In order to design the controller for drives, the transfer function (TF) of a control loop can be presented simply and generally as in Figure B4.1 [56]. In the figure, the control loop includes the controller TF, the plant TF. In there, the TF of the actuator is included in  $F_p$  and the TF of the measuring system for the feedback variable is shifted into  $F_p$  and inversed into  $F_x$ . With that presentation,

the open loop transfer function is  $F_O = F_C F_P = \frac{X}{\Delta X}$ ,

and the closed loop transfer function is  $F_W = \frac{X}{W} = \frac{F_C F_P}{1 + F_C F_P} = \frac{F_O}{1 + F_O}$ .

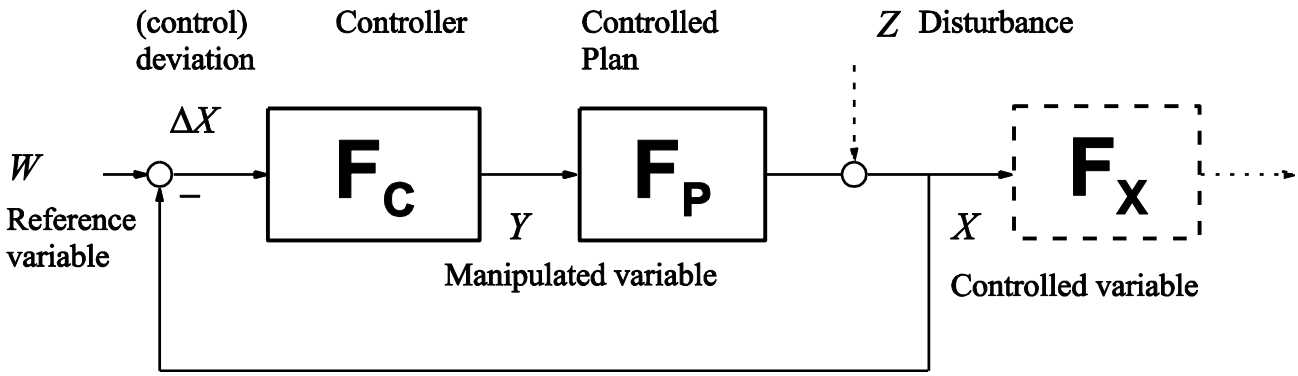


Figure B4.1 General block diagram of a control loop

The desire of the control normally is that

$$x(t) = w(t) \text{ or } X(s) = W(s)$$

$$\Rightarrow F_w(s) = \frac{X(s)}{W(s)} \equiv 1$$

In order to handle the real systems, the designer needs some methods to optimize the controller to get stability, steady state accuracy and good dynamic performance of the control system. In control of drive applications, there are two classical methods of optimisation, which are frequently used; they are “Amplitude Optimum” and “Symmetrical Optimum”.

### B4.1 Amplitude optimum

In the amplitude optimum method, the designing principle is keeping the TF of the control closed loop close to 1 in as large bandwidth as possible i.e.  $|F_w(j\omega)| \approx 1$  in at least a frequency area.

In general, the transfer function of a closed loop can be presented by a Laplace function (B4.1)

$$F(s) = \frac{1}{1 + a_1s + \dots + a_n s^n}; a_0 = 1 \tag{B4.1}$$

Represent the equation in frequency area with  $s = j\omega$  the TF function of the closed loop becomes a complex frequency function.

$$F(j\omega) = \frac{1}{(1 - a_2\omega^2 + a_4\omega^4 - \dots) + j(a_1\omega - a_3\omega^3 + \dots)} \tag{B4.2}$$

If  $|F_w(j\omega)| \approx 1$  then the square of closed loop TF  $|F_w(j\omega)|^2 \approx 1$ . Therefore



$$|F(j\omega)|^2 = \frac{1}{(1 - a_2\omega^2 + a_4\omega^4 - \dots)^2 + (a_1\omega - a_3\omega^3 + \dots)^2} \quad (\text{B4.3})$$

In order to have  $|F_w(j\omega)| \approx 1$  in a large bandwidth, the closed loop TF should be designed with

$$|F_w(j\omega)|^2 = \frac{1}{1 + \omega^2 \underbrace{(a_1^2 - 2a_2)}_{=0} + \omega^4 \underbrace{(a_2^2 + 2a_4 - 2a_1a_3)}_{=0} + \dots + \omega^n a_n^2} \quad (\text{B4.4})$$

$$\begin{aligned} a_1^2 - 2a_2 &= 0 \\ a_2^2 + 2a_4 - 2a_1a_3 &= 0 \\ &\vdots \end{aligned} \quad (\text{B4.5})$$

After optimization, we get:  $|F_w(j\omega)|^2 = \frac{1}{1 + a_n^2 \omega^n} \Rightarrow |F_w(j\omega)| = \frac{1}{\sqrt{1 + a_n^2 \omega^n}}$

Apply the method for control of drive in current control loop and position control loop; the results are presented in follows.

### a. Apply for current control loop with PI controller

The current control loop in control of drive can be simplified and present as a second order lag element (PT2 element) in (B4.5).

$$F_p(s) = \frac{K_p}{(1 + sT_1)(1 + sT_2)} \quad (\text{B4.6})$$

And the TF of PI controller is presented in (A3.6)

$$F_C(s) = K_p \left( 1 + \frac{1}{sT_i} \right) = \frac{K_p}{sT_i} (1 + sT_i) \quad (\text{B4.7})$$

Compensate the higher time constant  $T_1$  of the controlled plan by choosing value of controller  $T_i$  with

$$T_i = T_1 \quad (\text{B4.8})$$

The open loop TF of the system is simplified to

$$F_O(s) = F_C(s) \cdot F_p(s) = \frac{K_p \cdot K_p}{sT_i(1 + sT_2)} = \frac{1}{sa_1 + s^2a_2} \quad (\text{B4.9})$$

With  $a_1 = \frac{T_i}{K_p K_p}$ ;  $a_2 = \frac{T_i T_2}{K_p K_p}$

The closed loop TF of the system will be

$$F_w(s) = \frac{F_o}{1 + F_o} = \frac{1}{1 + sa_1 + s^2a_2} \quad (\text{B4.10})$$

Optimize the TF as in (A3.), we got

$$a_1^2 = 2a_2 \Rightarrow \left( \frac{T_i}{K_p K_p} \right)^2 = 2 \frac{\cancel{K_i} T_2}{\cancel{K_p} \cancel{K_p}} \quad (\text{B4.11})$$

$$\Rightarrow K_p = \frac{T_i}{2K_p T_2} = \frac{T_1}{2K_p T_2} \quad (\text{B4.12})$$

### b. Apply for position control loop with P controller

With the position control loop the plant TF is presented as a PT1 element in series with an integral element as in (B4.13)

$$F_p(s) = \frac{1}{s(1 + sT_1)} \quad (\text{B4.13})$$

And the TF of PI controller is presented in (B3.4)

$$F_c(s) = K_p \quad (\text{B4.14})$$

The open loop TF of the system is simplified to

$$F_o(s) = F_c(s) \cdot F_p(s) = \frac{K_p}{s_i(1 + sT_1)} = \frac{1}{sa_1 + s^2a_2} \quad (\text{B4.15})$$

With  $a_1 = \frac{1}{K_p}$ ;  $a_2 = \frac{T}{K_p}$

Optimize TF, we got

$$K_p = \frac{1}{2T_1} \quad (\text{B4.16})$$

## B4.2 Symmetrical optimum

The design principle of the symmetrical optimum is finding the maximum damping of the control loop system. The optimal damping is the highest phase margin  $\alpha$  of the open loop  $F_o$  at the position that the gain crossover 1 with the crossing frequency  $\omega_{CR}$  i.e. the design method will find the controller parameter that makes  $\omega_{CR} = \omega(\varphi_{\max})$ .

The general speed control in the drive of control can be presented as a IT1 element. Including the PI controller, the speed-control loop is presented in Figure B4.2.

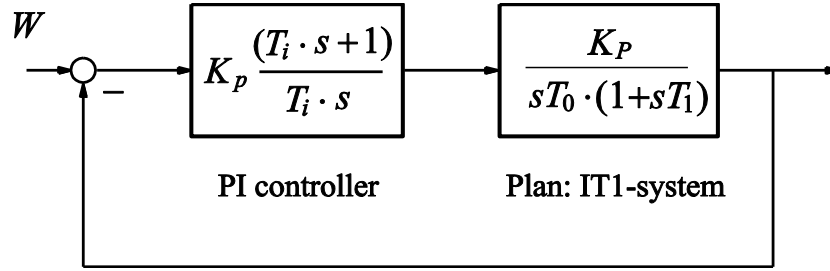


Figure B4.2 General speed-control loop

Therefore, the open loop TF of the speed-control loop can be calculated as in (B4.17).

$$F_o(s) = \frac{K_p K_P (1 + sT_i)}{s^2 T_i T_0 (1 + sT_1)} \quad (\text{B4.17})$$

Presenting in frequency area, we got

$$F_o(j\omega) = \frac{K_p K_P (1 + j\omega T_i)}{s^2 T_i T_0 (1 + j\omega T_1)} \quad (\text{B4.18})$$

The phase shift of the open loop is calculated from the frequency function.

$$\varphi(\omega) = -\pi - \arctan(\omega T_1) + \arctan(\omega T_i)$$

The optimal value of the phase shift  $\varphi(\omega)$  is the root of equation

$$\frac{d\varphi(\omega)}{dt} = \frac{T_i}{1 + \omega^2 T_i^2} - \frac{T_1}{1 + \omega^2 T_1^2} = 0 \quad (\text{B4.19})$$

$$\Rightarrow \omega(\varphi_{\max}) = \frac{1}{\sqrt{T_i T_1}} \quad (\text{B4.20})$$

As the principle desires the open loop TF crossover 1, we have

$$\left| F_o \omega(\varphi_{\max}) \right| = \frac{K_p K_P \sqrt{1 + \omega^2 T_i^2}}{T_i T_0 \omega^2 \sqrt{1 + \omega^2 T_1^2}} = 1 \quad (\text{B4.21})$$

Replace (B3.20) to (B3.21), we got

$$K_p = \frac{T_0}{K_P} \frac{1}{\sqrt{T_i T_1}} \quad (\text{B4.22})$$

In order to make  $|F_w(j\omega)|$  stay close to 1 for a wide frequency range, the close loop TF of the speed control loop is analysis.

$$\begin{aligned}
 F_w(s) &= \frac{F_o}{1 + F_o} = \frac{K_p K_P (1 + sT_i)}{s^2 T_i T_0 (1 + sT_1) + K_p K_P (1 + sT_i)} \\
 &= \frac{1 + sT_i}{1 + sT_i + s^2 \frac{1}{K_p K_P} T_i T_0 + s^3 \frac{1}{K_p K_P} T_i T_0 T_1}
 \end{aligned} \tag{B4.23}$$

Presenting in frequency area

$$F_w(j\omega) = \frac{1 + j\omega T_i}{1 + j\omega T_i - \omega^2 \frac{1}{K_p K_P} T_i T_0 - j\omega^3 \frac{1}{K_p K_P} T_i T_0 T_1} \tag{B4.24}$$

To make  $|F_w(j\omega)| \approx 1$  we have to make the denominator ( $|D(j\omega)|$ ) of  $|F_w(j\omega)|$  close to 1. In another words, we have to make  $|D(j\omega)|^2 \approx 1$ .

$$\begin{aligned}
 |D(j\omega)|^2 &= \left(1 + \omega^2 \frac{1}{K_p K_P} T_i T_0\right)^2 + \left(\omega T_i - \omega^3 \frac{1}{K_p K_P} T_i T_0 T_1\right)^2 \approx 1 \\
 |D(j\omega)|^2 &= 1 + \omega^2 \underbrace{\left(T_i^2 - 2 \frac{T_i T_0}{K_p K_P}\right)}_{\stackrel{!}{=}0} + \omega^4 \underbrace{\left(\left(\frac{T_i T_0}{K_p K_P}\right) - 2 \frac{T_i^2 T_0 T_1}{K_p K_P}\right)}_{\stackrel{!}{=}0} + \omega^6 \underbrace{\left(\frac{T_i T_0 T_1}{K_p K_P}\right)^2}_{\stackrel{!}{=}1} = 1
 \end{aligned}$$

Solve the set of two equations, the result is

$$T_i = 4T_1 \tag{B4.25}$$

## APPENDIX C

# Fundamental of electromagnetic field in synchronous linear motors

## C1. Review of electromagnetic field theory

In order to review the knowledge of the electromagnetic field theory, the basic laws of electricity are repeated in this appendix by a set of equations called Maxwell's equations and some other derived equations from them [57].

The force  $F$  acting on a charge  $q$  moving with a velocity  $u$  in an electric field  $E$  and in magnetic field  $\mathcal{B}$  is given by the Lorentz force equation.

$$\vec{F} = q \vec{E} + \vec{u} \times \vec{\mathcal{B}} = \vec{F}_E + \vec{F}_B \quad (\text{C1.1})$$

The electric field intensity  $E$  and the magnetic field  $\mathcal{B}$  can be defined from (C1.1) by the following equations:

$$\vec{F}_E = \Delta q \cdot \vec{E} \quad (\text{C1.2})$$

$$\vec{F}_B = \Delta q \cdot \vec{u} \times \vec{\mathcal{B}} \quad (\text{C1.3})$$

The potential difference  $dV$  between two points separated by a distance  $dl$  is defined as

$$dV = -\vec{E} \cdot d\vec{l} \text{ or } \vec{E} = -\vec{\nabla}V \quad (\text{C1.4})$$

The total magnetic flux  $\phi$  can be expressed from the magnetic flux density  $\mathcal{B}$  as

$$\phi = \int_s \vec{\mathcal{B}} \cdot d\vec{s} \quad (\text{C1.5})$$

where the integral is over a surface  $s$ .

The electromotive force ( $EMF$ ) is induced in a closed circuit following the Faraday's law when the magnetic flux  $\phi$  linking the circuit changes. With a  $N$ -turn coil closed circuit, the induced  $EMF$  is given by

$$EMF = -N \frac{d\phi}{dt} \quad (\text{C1.6})$$

From equation (C1.4), the  $EMF$  can be defined as

$$EMF = \oint \vec{E} d\vec{l} \quad (C1.7)$$

If consider  $N = 1$ , then from (C1.5) to (C1.7) it follows that

$$\oint \vec{E} d\vec{l} = -\frac{\partial}{\partial t} \int_s \vec{B} \cdot d\vec{s} \quad (C1.8)$$

The relationship between given currents and resulting magnetic field is expressed by Ampere's circuital law. The law gives the relationship between the magnetic field intensity  $\mathcal{H}$  and the current  $I$  as following

$$\oint \vec{\mathcal{H}} \cdot d\vec{l} = I \quad (C1.9)$$

If  $J$  is the surface current density, then (C1.9) can be rewritten as

$$\oint \vec{\mathcal{H}} \cdot d\vec{l} = \int_s \vec{J} \cdot d\vec{s} \quad (C1.10)$$

In order to obtain complete information reading the various field quantities, in addition to the equations in this appendix certain auxiliary relations are also useful. These relations are as following.

Ohm's law: For a conductor of conductivity  $\sigma$ ,

$$\vec{J} = \sigma \cdot \vec{E} \quad (C1.11)$$

where  $J$  is surface current density, and  $E$  is electric field intensity.

Permittivity: The electric field intensity and the electric flux density in a medium are related to each other by

$$\vec{D} = \varepsilon \cdot \vec{E} \quad (C1.12)$$

where  $\varepsilon$  is called the permittivity of the material.

Permeability: The magnetic field intensity and the magnetic flux density in a material are related to each other by

$$\vec{B} = \mu \cdot \vec{\mathcal{H}} \quad (C1.13)$$

where  $\mu$  is called the permeability of the medium.

## C2. Permanent Magnet in PMLSM

As presented in the previous appendix, the magnetic flux density  $\vec{B}$  and the magnetic field intensity  $\vec{\mathcal{H}}$  in free space are related by the constant  $\mu_0$  known as the permeability of free space [57]:

$$\vec{B} = \mu_0 \cdot \vec{\mathcal{H}} \quad (C2.1)$$

and  $\mu_0 = 4\pi \times 10^{-7}$  (H/m)

Within a material, the equation (C1.13) is modified to describe a magnetic phenomenon different from that occurring in free space:

$$\vec{B} = \mu \cdot \vec{H}, \quad \mu = \mu_R \mu_0 \quad (\text{C2.2})$$

where  $\mu$  is termed permeability and  $\mu_R$  relative permeability, a non-dimensional constant.

Permeability in a material medium must be further qualified as applicable only in regions of homogeneous (uniform quality) and isotropic (having the same properties in any direction) materials. In materials not having these characteristics,  $\mu$  become a vector. Finally, note that for some common materials, equation (C1.13) is nonlinear, and  $\mu$  varies with the magnitude of  $B$ . This leads to several sub-definitions of permeability related to the well-known nonlinear  $B$ - $H$  characteristic of material, as shown in Figure B1. C2.1.

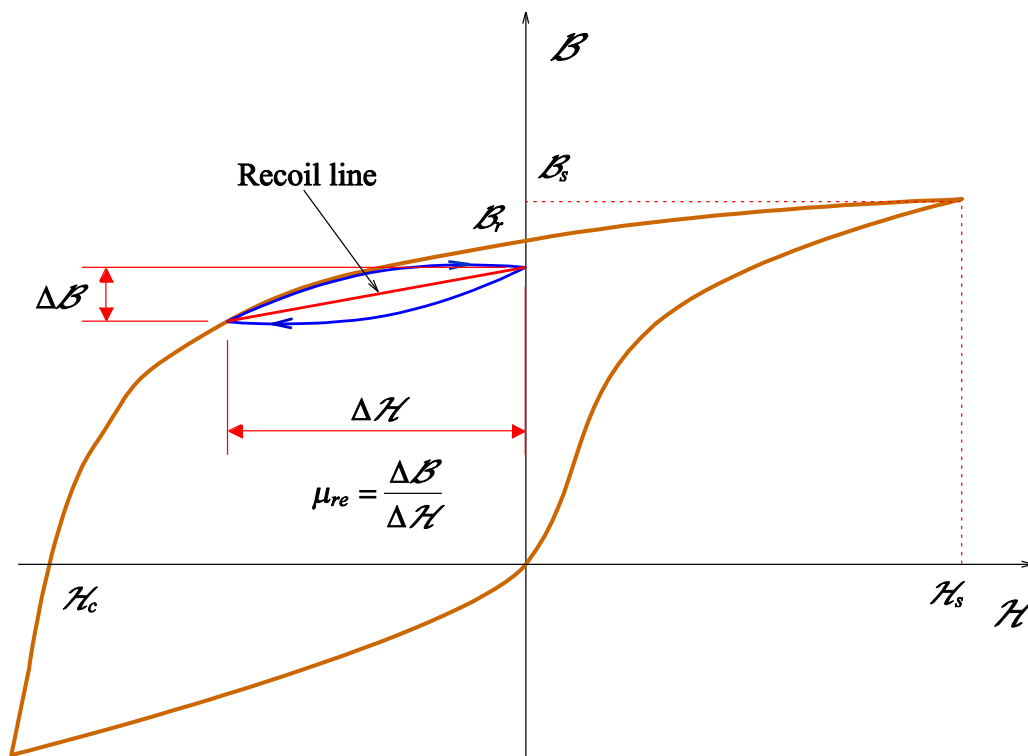


Figure C2.1 Demagnetization curve, recoil loop and recoil magnetic permeability of a PM

Nowadays, PMs made of high-energy rare-earth are almost invariably used in synchronous motors to obtain large thrust (torque)/weight and thrust (torque)/power input ratios. Such magnets are characterized by large remanent flux densities  $B_r$  and large coercive forces  $H_c$ , as shown in Figure C2.2. Their recoil permeabilities  $\mu_{re}$  are in the range 1.02 to 1.18  $\mu_0$ . A typical high-energy product PM, which is isotropic, has a linear demagnetization characteristic of the algebra's form

C2. Permanent Magnet in PMLSM

$$\mathcal{B}_M \approx \mathcal{B}_r + \mu_{re} \mathcal{H}_M \tag{C2.3}$$

Consequently, such a PM can be replaced by an equivalent MMF,  $\mathcal{M}_{PM}$ , given by

$$\mathcal{M}_{PM} = \mathcal{H}_c h_m \tag{C2.4}$$

where  $h_m$  is magnetic thickness, and  $\mathcal{H}_c$  is coercive force. This equivalent (fictitious) MMF is located in air with  $\mu_{re} \approx \mu_0$ , and may be in the form of a current sheet. Such the equivalent is used with analytical methods to obtain field distributions in the PMLSM of this thesis.

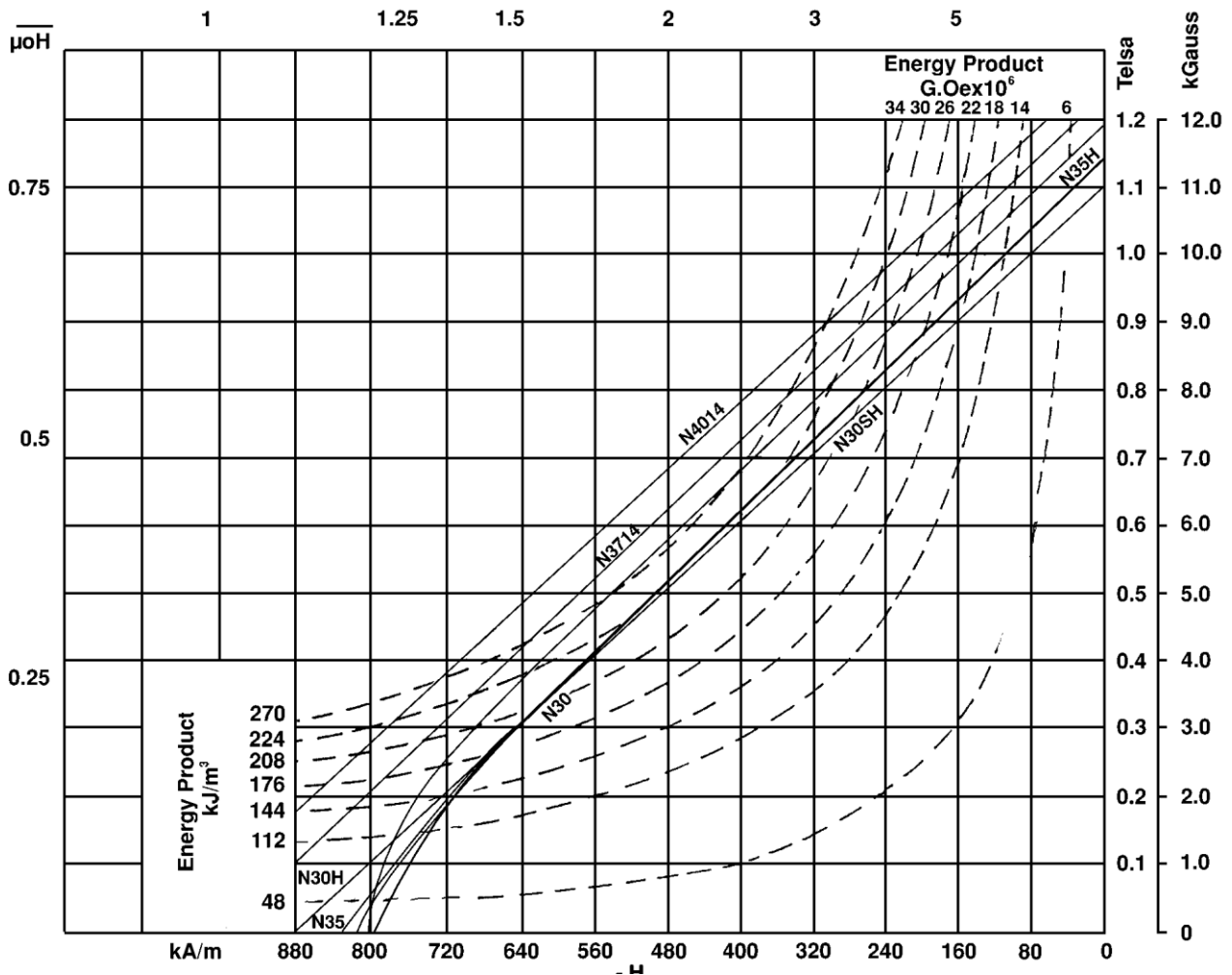


Figure C2.2 BH-characteristics of some rare-earth magnets.



# Curriculum Vitae

## Personal data

Name: **Phong C. Khong**

Date of birth / place: 10.04.1978 / Hanoi – Vietnam

Family status: Married, One child

## Education and Career

1984-1989: Primary school Duc Giang

1989-1993: Junior high school Duc Giang

1993-1996: Senior high school Nguyen Gia Thieu

1996-2001: Study for diploma's degree of Electrical engineering at Hanoi University of technology

2001-2003: Study for master's degree of Electrical engineering at Hanoi University of technology.

2001-2007: Assistant at the Department of Automation for Mining and Petroleum Factory, Hanoi University of Mining and Geology.

Since 2007: Studying for PhD degree at the Department of Power electronic and control of drives, Technical university of Darmstadt.

## Publication

- [1] P. Khong, R. Leidhold and P. Mutschler. "Magnetic guidance of the mover in a long-primary linear motor," *Industry Applications, IEEE Transactions – electronic publishing*, DOI: 10.1109/TIA.2011.2125934, March 2011.
- [2] P. Khong, R. Leidhold and P. Mutschler. "Magnetic guidance of the mover in a long-primary linear motor," in *ECCE 2009. IEEE*, San Jose, CA Sept. 2009, pp. 2354–2361.
- [3] P. Khong, R. Leidhold and P. Mutschler. "Magnetic guiding and capacitive sensing for a passive vehicle of a long-primary linear motor," in *EPE/PEMC 2010*, Ohrid-Macedonia, Sept. 2010, pp. S3-1 – S3-8.
- [4] P. Khong and P. Mutschler.: "Capacitive gap and yaw angle sensor for linear drives," in *IECON 2010*, Glendale, AZ Nov. 2010, pp. 1240–1245.
- [5] P. Khong, R. Leidhold and P. Mutschler. "Active magnetic guidance for material handling systems based on linear motors," in *LDIA 2009*, Incheon-Korea, Sep. 2009.